ULTRASOUND ATTENUATION IN THE UNCONVENTIONAL SUPERCONDUCTOR Sr_2RuO_4

by

Christian Lupien

A thesis submitted in conformity with the requirements
for the degree of Doctor of Philosophy
Graduate Department of Physics
University of Toronto

ABSTRACT

Ultrasound Attenuation in the Unconventional Superconductor Sr_2RuO_4

Christian Lupien
Doctor of Philosophy
Graduate Department of Physics
University of Toronto
2002

Sr_2RuO_4 is an unconventional superconductor with a critical temperature of 1.5 K. It is highly two-dimensional and of a similar crystal structure as the high-T_c cuprates. In contrast to the cuprates it is believed to be a triplet superconductor. The generic symmetry of the order parameter is p-wave with a full gap in all directions. However recent measurements of heat capacity, penetration depth, thermal conductivity and NMR lattice relaxation time have shown power-law temperature dependences indicative of nodes in the gap.

In order to locate the position of these nodes, we performed ultrasound attenuation measurements. At low temperature, changes in the ultrasound attenuation are electronic in origin. When performed at low frequency, in the hydrodynamic limit, the electronic attenuation is proportional to the electron viscosity which is a tensor of rank four. Hence there are six independent elements of which three describe all the in-plane sound modes. A difference in the temperature dependence between these modes can reveal the position of nodes in some cases.

We measured the attenuation of four in-plane modes and one out-of-plane mode. Together they describe four of the viscosity components. Our first observation is that the normal state in-plane viscosity is highly anisotropic. Transverse waves polarized in the plane are a thousand times less attenuating when they propagate along the [100] direction than along [110].

In the superconducting state, the T dependence of the attenuation follows a power-law down to 40 mK, or $T_c/30$. This confirms the presence of nodes in the gap. We also observed some anisotropy in the amplitude and exponent of the low temperature power-laws. This anisotropy is weak suggesting horizontal line nodes instead of vertical line nodes. The best fit to the entire data was obtained with the model of Zhitomirsky and Rice in which horizontal line nodes are present only on two of the three Fermi surfaces, the third one being fully gapped. If this agreement is confirmed by careful calculations, then it would represent compelling evidence for the identification of the gap symmetry.

To my parents

ACKNOWLEDGEMENTS

The work presented in this thesis has benefited from the help of many people. First I would like to thank my supervisor, Louis Taillefer, for is guidance and support. He suggested the projects I worked on and gave me a lot of freedom in carrying it out. He also provided me with many opportunities to meet and interact with other physicists through many conferences and a month spent in Grenoble. I must also thank the other members of my committee, Bryan Statt and Michael Walker, for the guidance they provided.

Many post-docs helped me during the years. Rob Hill worked hard in getting the lab set up and running again after the move from McGill. He provided lots of help for the thermal conductivity experiments and in running the dilution refrigerator. He also had many insightful comments about low temperature techniques and the data analysis. My project on ultrasound attenuation was made possible with the invaluable help of Andrew MacFarlane. We shared all of the work which allowed the lengthy set of experiments to be completed in a reasonable length of time. Cyril Proust provided help on both experiments, especially with his expert skills at making good contacts and bounds. He also lightened my load as a system administrator. I am also very grateful that he read drafts of this thesis and provided many useful comments.

Low temperature experiments are very demanding on time so sharing the work is essential. I must thank the other graduate students of the group, Etienne Boaknin, David Hawthorn, Johnpierre Paglione, and Michael Sutherland, for their help in keeping the equipment running, for all those questions and discussions that provided me with fresh views of problems and for inciting me to improve my data analysis programs.

I am grateful to Andrei Stratilatov and then Hongfei (Harry) Zhang for their help with the X-ray machine, cutting samples and using the ovens. Our group consumed huge quantity of cryogen but thanks to the work of Robert Henderson we never ran out. I must thank people of the machine shop for their work in making sample mounts and numerous other objects. The graphics shop was of great help in making a very professional looking poster. At McGill, I must thank Robert Gagnon for his help in mounting samples.

A lot of the work was done with a home built ultrasound spectrometer, constructed at McGill. I must thank Brett Ellman for the design and Anders Sune Vang-Pedersen for its construction and a job well done. This was the first real experiment for the equipment and it worked well.

The first year of my Ph. D. was spent at McGill University. It was a very enjoyable time thanks to many people people: Mark, Stéphane, Mikko, Johan, Mary, Philip, Van,

Graham, Jeremy, Tiago and Robert. Work in the lab, the struggles with the fridge and the summer school organisation I shared with May Chiao, fellow student and friend. She was also present during my stay in France and introduced me to many people which made my stay very enjoyable.

I have had many fruitful discussions with theorist. Among them I should list Matthias J. Graf, Daniel F. Agterberg, Marcel Franz, and Peter J. Hirschfeld. In particular I had very useful interactions with the local group of Michael Walker, his student Michael Smith and post-doc Kirill Samokhin. They obtained interesting results to help describe my experiments.

Good crystals were essential to my experiments. Therefore I must thank Yoshiteru (Yoshi) Maeno for providing such wonderful Sr_2RuO_4 crystals and Z. Q. Mao for growing them. Yoshi also provided many useful discussions. The ultra-pure crystals of YBCO were provided by the group of Doug A. Bonn and Walter N. Hardy at UBC and grown by Ruixing Liang. They also provided interesting discussions.

Working long days and nights in the lab could be lonely but I was not alone. In the lab next door Zahra-Sadat Yamani also had those crazy schedules. I thank her for all the work breaks (dinners, movies) and all the interesting discussions.

Work in the lab or on the computer does not provide much physical exercise. In order to remain healthy I must thank all the people I played sport with. I must thank the physics ultimate team, the Field Operators, and the TUC teams the Cut Backs as well as Discord and especially Erica Bird who introduced me to the game. There is also the volleyball team, Quantum Leaps, which Daniel Côté organized. Finally Jessica Mondia who also organized the volleyball and the street hockey.

I need to thank the funding agencies that helped me financially along the way. These were the Natural Sciences and Engineering Research Council of Canada (NSERC), the Fonds pour la Formation de Chercheurs et l'Aide à la Recherche (FCAR) of Québec, the Walter C. Sumner foundation, and the Canadian Institute of Advanced Research (CIAR). Additional support was provided by the university of Toronto and the department of physics at McGill university.

Finalement j'aimerais remercier ma famille pour leur support et leurs bons soins lorsque j'avais besoin de vacances.

CONTENTS

FIGURES AND TABLES

FIGURES

TABLES

1

INTRODUCTION

The phenomenon of superconductivity was discovered almost 100 years ago by H. Kamerlingh Onnes [1] in 1911. Below a critical temperature T_c of 4 K the electrical resistance of mercury suddenly disappeared. The same effect was also observed in other metals with different critical temperatures. Later on, in 1933, W. Meissner and R. Ochsenfeld [2] discovered that accompanying the zero conductivity was a perfect diamagnetism (now known as the Meissner effect), i.e. the superconductor expels all magnetic field[1]. These two effects, zero conductivity and the Meissner effect, are two traditional hallmarks of superconductivity. After these discoveries some phenomenological models were proposed to describe these and other characteristics. The London equations in 1935 [3] described the electromagnetic response of a superconductor. Combined with a two-fluid model [4] were the electrons are separated in two parts, the superconducting ones and the normal ones, the temperature dependence of some of the response could be described. Pippard proposed a nonlocal extension to the London equations in 1953 [5]. The Ginzburg-Landau (GL) theory of 1950 [6] describes the behavior of a superconductor near the critical temperature using Landau's general theory of second-order phase transitions. It introduced a complex order parameter and could described spatially-varying orders. This makes it a powerful tool and like the other phenomenological models is still used to described data in some limits and to provide some understanding of phenomena. But no microscopic theory had hitherto been able to explain the inner workings of superconductivity.

In 1957, Bardeen, Cooper, and Schrieffer, proposed what is now known as the BCS theory of superconductivity [7]. It finally provided a microscopic explanation of the phenomenon. Later, this theory was shown to be equivalent to the GL theory close to the critical temperature [8]. This BCS theory described superconductivity as the condensation of pairs of electrons, called Cooper pairs, with a binding energy coming

---

[1] This Meissner effect works until a critical field is reached. Above this field the sample is either no longer superconducting (the normal state) or is in the mixed state of superconductivity.

from the electron-phonon interaction. The change of energy of the condensed electrons was described by an energy gap. Supplying an energy greater than twice this gap to the condensate would be enough to break a pair and produce two excitations called quasi-particles. These quasiparticles then behave somewhat like the normal component of the two-fluid model, while the condensate — being in a gapped ground state — is mostly inert. The presence of the gap resulted in activated (exponential) behavior at low temperature in most of the properties (heat capacity, ultrasound attenuation, etc) which explained the previous observations.

This theory was a major change in thinking in condensed matter physics. It required a different approach to the problem. A lot of progress in solid state physics had been achieved until then by perturbing the free electron model, or simplified band models. The difficulty with this approach is that even if the perturbation that produces superconductivity is small the result is a total rearrangement of the electrons. Correlations between pairs of electrons appear and this cannot be obtained by perturbing the simple electron models [9, Chapter 1]. The leap that was taken was to recognize the importance of the coherence of the pairs and to include that in the model by defining a new ground state that could describe the pairs and the free electron in the limit of no coherence. With this new ground state the calculations could finally be performed and provided a very good description of the experimental data. Therefore, single-electron theory with perturbation was not sufficient to describe superconductivity and some tools of many-body physics such as second quantization and/or field theory were required to solve this problem. This also showed that superconductivity is a macroscopic effect of quantum physics. All the condensed electrons are in a coherent superposition and can be described by a wave function with a certain phase. This macroscopic quantum fluid exhibits interference in effects such as in SQUID (superconducting quantum interference device).

A similar trick of finding the proper ground state to describe a problem as been used more recently to solve the problem of the integer quantum Hall effect [10, 11]. There the problem also required a leap of imagination to come up with a proper starting point to allow a solution. It is always possible to write down the full Hamiltonian of a solid state system, which simply contains the various electromagnetic interactions between ions and electrons with their kinetic energies. But with all the particles in the system interacting with each other it is not possible to solve it without making approximations. In doing those approximations something is lost which cannot be recovered by a small perturbation. For superconductivity, it was the coherence between the electrons. One cannot deduce from the original Hamiltonian that this coherence is the important thing to keep for superconductivity. Someone had to guess that this was the key ingredient to solve the problem. So even if the original unsolvable Hamiltonian contained everything it does not guide us in picking the proper route in solving the complicated problems that involve many-body interactions.

Coming back to our story, by the end of the 1960s, with the help of the BCS theory with its electron-phonon coupling and of the GL theory, there was a general sentiment that the story of superconductivity was nearing its conclusion. For example, in the two volume book *Superconductivity* edited by Parks [12], which was a comprehensive review of the field in 1969, the preface began with:

> During the preparation of this treatise one of the authors commented that it would be “the last nail in the coffin [of superconductivity].” While we may hope this is unduly pessimistic, it is clear that the field is well advanced in maturity and sophistication. ...

Superconductors started being used as superconducting magnets and as SQUIDs in very sensitive devices to measure magnetic fields. The aim was then to find materials with the highest possible critical temperature and field. This search culminated with Nb_3Ge, with $T_c = 23$ K and which is used in magnets to produce fields of about 20 T. It was believed that much higher critical temperature were improbable.

At the beginning of the 1970’s, the BCS theory was adjusted to explain the superfluidity that was discovered in ^{3}He below 1.3 mK [13]. It required a different pairing mechanism than the electron-phonon interaction of superconductors. In this case, the attraction was provided by spin fluctuations [14]. Also the fermions in this case combined not in pairs without net spin (singlet state) but in pairs with a net spin of one (triplet state). Being a superfluid instead of a superconductor, but also a spin triplet state, produced some interesting differences and a more complicated model but the BCS theory in its general form did describe the behavior of the superfluid. For example, in some parts of the phase diagram the gap would not be a constant for all directions. In some particular direction the gap would be zero, which is called a node, and this would replace the low temperature exponentials (in the heat capacity for example) by power laws because thermal energy can easily excite quasi-particles around the nodes.

At the end of the 1970’s and the beginning of the 1980’s two new classes of superconductors were discovered: the heavy fermions (such as $CeCu_2Si_2$, UPt_3, UBe_{13}, ...) [15, 16] and the organic superconductors (such as the TMTSF and BEDT-TTF families) [17, 18]. These became known as unconventional superconductors as they quickly raised the possibility that pairing did not proceed with phonons and the order parameter did not have the usual s-wave symmetry (with a nodeless gap). For example UPt_3, showed power laws at low temperature and multiple superconducting phases. This was therefore a metallic analog of superfluid ^{3}He. These materials had relatively low critical temperatures (about 1 K for the heavy fermions and 1D organics and 10 K for the 2D organics). This totally changed in 1986 when $La_{2-x}Sr_xCuO_4$ was discovered [19] (commonly known as LSCO), with a T_c of about 40 K. This was only the first of a new class of superconductors now called the high-T_c or the cuprates. Very soon after the initial discovery, at the beginning of 1987, $YBa_2Cu_3O_{7-\delta}$ (also a high-T_c commonly known as YBCO) was seen to be superconducting at about 90 K [20, 21, 22]. This broke the barrier of liquid nitrogen (77 K) for the first time. This has many implications for the technological use of superconductors because liquid nitrogen is much cheaper than the liquid helium required for devices using low-T_c superconductors. Liquid nitrogen also has a much larger latent heat so it evaporates more slowly and is therefore easier to use. This discovery has also had a huge impact for theories because such a high T_c needed some revision of the previous thinking about maximum T_c and many other ideas. The highest T_c of this class is currently that of $HgBa_2Ca_2Cu_3O_8$ at 133 K (up to 164 K under pressure of 30 GPa) discovered in 1993 [23, and references therein]. The best studied compounds of the high-T_c cuprates are LSCO, because it is easily doped from insulator to a non-superconducting metal, BSCCO, because it is very easy to cleave and is therefore favored for surface measurements and YBCO, because it has provided the cleanest and purest samples.

The discovery of the class of high-T_c superconductor started a frenzy of investigation with over 100,000 research papers published over the past 15 years describing experiments on different compounds and various proposed theories. Initial measurements suggested conventional behavior except for the high critical temperature but as the sample quality improved this started to change. Power law started to be observed at low temperature and other new effects were seen. These materials are all two-dimensional (to different degree) and superconductivity is believed to occur in planes of copper and oxygen of which they are made (hence the name cuprates). Also similarly to the heavy fermions and organic superconductors, cuprates have a proximity to a magnetic phase. The high-

T_c behavior changes upon hole doping and they become anti-ferromagnetic insulators at low enough doping. Some heavy-fermions show coexistence of anti-ferromagnetic order with superconductivity and the the organics can show magnetic behavior like spin-density waves or antiferromagnetic order with applied pressure.

This shows interesting similarities between these compounds and theories are often applied to more than one class. But no microscopic theory has yet been able to fully explain any of these materials. In part this is because these systems are more complicated than the conventional superconductors. In particular even the normal state of the high-T_c is not properly understood. Since most theories (like BCS) implicitly start from a well-known normal state (*i.e.* a Fermi liquid), this is an additional difficulty.

The discovery of new superconductors did not end with the cuprates. In the mid 1990's another material was added, Sr_2RuO_4 [24]. It was discovered in 1994 and is part of the class of ruthenates but is the only superconducting material of this class. However, the other materials like $SrRuO_3$ and $Sr_4Ru_2O_7$, show magnetic behavior, not unlike what is seen in the other classes. Sr_2RuO_4 was already synthesized in 1959 [25]. It was also used in 1992 as a substrate to grow thin films of the high-T_c YBCO [26]. That is because it has the same crystal structure as LSCO but with ruthenium taking the role of the copper, and the lattice dimensions were very close to those of YBCO (within 1.3%). Then in 1994 good crystals of Sr_2RuO_4 were synthesized for the purpose of looking for superconductivity in an isostructural material to the high-T_c, but without copper. At last, superconductivity was discovered but with a very low critical temperature of only 1 K [24]. Furthermore, it was quickly observed that the superconductivity was easily destroyed by impurities. Since that time, samples of higher quality have been produced and approach the maximum T_c of this material, estimated to be 1.5 K.

Similarly to what happened in the case of high-T_c and heavy fermions, as the sample quality improved, the experimental results changed. Initial measurements were not accessing the intrinsic behavior of the material but were strongly affected by impurities; for example huge residual terms were seen in heat capacity. As the impurities were removed in better samples, the intrinsic properties of the sample was uncovered and a new behavior became apparent; for example the residual linear term in the heat capacity disappeared and power laws are now easily observed in various properties. Having better samples eventually helps the theorist because they have a more stable set of data on which to base their theory, otherwise they need to guess the intrinsic behavior which is a difficult and uncertain task.

It would save a lot of time and energy if the initial measurements were done on pure samples but the difficulties of crystal growth with peculiarities different in every compound implies that crystals start with low quality and then improve over time. This was the case for silicon in the 1950's at the begin of the semi-conducting revolution and is still the case today. The conventional superconductors were not sensitive to impurities so they partially escaped this problem but the new classes of superconductors have a much stronger dependence on disorder and crystal quality therefore becomes important. This was crucial for the heavy-fermion UPt_3 were totally new behavior was seen on pure samples (multiple superconducting transitions) and for Sr_2RuO_4 where there is no superconducting phase unless the sample is very clean. Once clean samples are obtained it is then possible to add impurities in a controlled way and then theories should be able to account for the observed behavior.

The initial interest in Sr_2RuO_4 was because of its similarity in structure to the high-T_c but it soon became clear that it was actually quite a different type of superconductor. Besides its low critical temperature and strong sensitivity to impurities, it is close to a ferromagnetic phase and not to antiferromagnetism like in the high-T_c. It also has a conventional normal state well described by Landau's Fermi liquid theory (which is a starting point of the BCS theory). The initial results were immediately indicative of unconventional behavior but different from the high-T_c and more like the behavior of superfluid ^{3}He. In other words it looked like a spin-triplet superconductor, as proposed early on (in 1995) by Rice and Sigrist [27] and by Baskaran [28]. The initial proposal identified a state with constant gap without any nodes. Like the cuprates, it is also a 2D system so it looked like a simple system, having spin-triplet superconductivity and a well known normal state that theorists could describe easily. Therefore it attracted many theorists who applied their previous theories of the heavy fermions, superfluid ^{3}He or even some aspects of high-T_c to this material. Experiments also started and luckily very good samples became available quite soon. Experimental results seem to indicate that it is indeed a spin-triplet superconductor. But results since 1998 also suggest the presence of nodes in the gap because of observed power laws in the temperature dependence at low temperature. This invalidates the simple initial models and opens a new list of possibilities.

More and more experiments have seen power laws and some are trying to identify their position. This is looking at the gap structure. For this, low temperature measurements are required because the identification of the nodes is done by exciting only the low energy quasi-particles present around the nodes. The behavior of the material is controlled by those quasiparticles and in turn these are controlled by the position in space where the nodes are situated and also by the way the gap approaches zero around the nodes (the angular dependence of the amplitude of the gap). A probe sensitive to the quasiparticles will give information about the gap structure and if the probe has angular dependence or if the nodes can be affected in unequal way, information about the position of the nodes can be obtained. The second way is seen for example by measuring the thermal conductivity and rotating a magnetic field around the sample, which can change the occupation of nodes in particular directions with respect to the field. An example of the first technique would be the angular dependence of tunneling or ultrasound attenuation.

Ultrasound attenuation has been used since the 1950's to measure the angular dependence of the gap in conventional superconductors and also to obtain very useful information about the gap structure of unconventional superconductors like UPt_3 [29, 30]. The measurement entails sending a pulse of sound in a crystal and observing the amplitude of the echoes of the pulse bouncing back and forth on the crystal surface. The decay of the amplitude provides the attenuation and this is done in the 100 MHz range hence the name "ultrasound". At low temperature, changes in this decay are due to electrons and this is strongly affected by superconductivity. The advantage of this technique is that at very high frequency (GHz) it is highly angle-dependent and only senses quasi-particles in a restricted volume of space. This volume is moved by changing the direction of propagation. At lower frequency, it does not have as strong an angular dependence since it is then related to a tensor of rank 4 but it still provides some angular sensitivity. This sensitivity is a result of the freedom to select both a direction of propagation and polarization for the sound waves. For example, in the plane of a tetragonal system, the attenuation at lower frequency will have three independent components accessible by changing both the direction of propagation and polarization of the sound waves.

In this thesis, we present a study of ultrasound attenuation in Sr_2RuO_4 aimed at discovering the position of the nodes. This experiment was initiated because gap structure is an important question to answer and also because this technique was shown to be very powerful in the case of UPt_3. This technique was also applied to the high-T_c in the beginning of 1990s but was not able to clarify the gap structure at the time. The problem in the case of the high-T_c was the small sample dimensions (the good crystal are usually thinner than 100 μm) and the higher temperature which complicates the results by adding other sources of attenuation. These are not a problem for Sr_2RuO_4 since high quality crystals of mm size are available and the critical temperature is low enough (1.5 K) so that other sources of attenuation are not a complication.

The story of superconductivity is still evolving. Very recently, organic insulators like undoped C_{60} or pentacene have been made metallic and superconducting at temperatures as high as 52 K (for C_{60}) by applying a large electric field [31, 32, 33].[2] This requires very pure sample to prevent electrical breakdown and is another example of the need of always better samples.

Also this year a new superconductor, MgB_2, has been discovered with $T_c = 39$ K [35]. Its critical temperature is not high compared to the high-T_c but it is interesting to note that it was missed during the initial search of high temperature superconductor of the 1970s. The reason for that is that this binary compound cannot be made using the same techniques that were used to produce all the other compounds. This new material is attracting a lot of attention because it is currently believed to be a conventional superconductor but with a very high-T_c and could become important for commercial use.

---

[2] Very recently C_{60} as been made superconducting at 117 K by chemically stretching the lattice [34].

2

THEORY OF ULTRASOUND ATTENUATION

In this chapter we look at the theory of sound waves in an elastic media and the calculation of ultrasound attenuation.

We use the symbol $\mathbf{v}$ for a vector with components v_i where i is the index of the component which can be 1, 2 or 3 or equivalently x, y or z (some vectors will have 6 components so the subscripts will then stand for 1, 2 … 6). The length of a vector ($|\mathbf{v}|$) is simply denoted as v. A unit vector in the direction of ($\mathbf{v}/v$) is denoted as $\hat{\mathbf{v}}$ and has components $\hat{v}_i$. A Greek index is not a vector component but stands for different vectors. The 3 unit vectors in a Cartesian coordinate system are listed as $\hat{\mathbf{x}}_\sigma$ and are $\hat{\mathbf{x}}$, $\hat{\mathbf{y}}$ and $\hat{\mathbf{z}}$. So combining the above conventions $\mathbf{v} = v_1\hat{\mathbf{x}} + v_2\hat{\mathbf{y}} + v_3\hat{\mathbf{z}}$. The vector $\mathbf{r}$ is reserved for the position of points in real space and can have components x_1, x_2, x_3 or simply x, y z. Repeated indices in a formula are summed over. A second rank tensor is represented as $\mathbf{C}$ with elements C_{ij}.

2.1 *Elastic theory*

Let us begin with a survey of continuum elastic theory. Only the main results will be presented. For a proper derivation and a full development of the theory, many books on the subject exist (see for example [36]). We will assume that the material is neither piezoelectric nor pyroelectric because such materials introduce complications we are not interested in.

The theory is described in terms of a displacement vector field $\mathbf{u}$ which is defined at all points $\mathbf{r}$. We take $\mathbf{r}$ to be a continuous variable over all space but in a crystal it would be a discrete variable specifying the position of the unit cells. When an elastic deformation is applied to a medium, a point originally at $\mathbf{r}$ moves to $\mathbf{r}+\mathbf{u}(\mathbf{r},t)$. Obviously the effect of a constant $\mathbf{u}$ is just a translation of the whole medium. This does not produce any internal forces (stress) in the crystal. Only actual deformations of the crystal will have that effect. These deformations (strain) are given by the space derivative of $\mathbf{u}$, *i.e.* by $\partial u_i/\partial x_j$. In general $\mathbf{u}$ can be large as a uniform translation of the object suggests. Another example would be a long and thin wire held at one end. The wire can then be bent so that the the displacement at the other end is larger than the width of the wire. Therefore care must be taken in theories not to assume a small $\mathbf{u}$ if that is not appropriate.

In classical mechanics, the force F of a spring on a mass is related to the displacement from equilibrium x and a spring constant k by $F = -kx$. This is Hooke's law and the force is in such a direction as to return the system to equilibrium ($x = 0$). It is derivable from a harmonic potential energy of $U = \frac{1}{2}kx^2$. Hooke's law can be generalized to a continuous elastic medium and we obtain

$$\sigma_{ij} = C_{ijkl}s_{kl} \tag{2.1}$$

where σ_{ij} are the stress tensor components, C_{ijkl} are the elastic stiffness constants (or elastic moduli) which form the 4^{th} rank tensor $\mathbf{C}$, and s_{kl} are the resulting strain tensor components. This is valid only for a small strain but since in a crystal the strain at which a deformation becomes inelastic is very small, Hooke's law remains valid for all elastic deformations (by elastic we mean that the work is reversible). We will only consider homogeneous samples so the elastic constants are independent of position and only depend on the material. The above equation can be inverted to give $s_{kl} = S_{ijkl}\sigma_{ij}$ where S_{ijkl} are the elastic compliance moduli and is given by $\mathbf{S} = \mathbf{C}^{-1}$. Before discussing the symmetries of these variables and the exact definition of s_{ij} let us give some physical description of these parameters. First the strain s_{ij} is the deformation of the medium and depends on the space derivative of $\mathbf{u}$ as mentioned above. It is therefore a unitless parameter that describes the change of shape of the microscopic unit volume. Considering the unit volume to have the shape of a cube, then the diagonal elements s_{11}, s_{22} and s_{33} represent a change of length along the 1, 2 and 3 direction of the cube, respectively. These actually change the volume of the cube. The other components conserve the volume of the cube. For example s_{12} represents a relative displacement of the two faces of the cube which are normal to 1 in the 2 direction. It is a pure shear deformation. Therefore the change in volume dV depends on the trace of $\mathbf{s}$, i.e. $dV/V = s_{ii}$. The stress σ_{ij} is the force per unit area (pressure) along the direction j applied to a surface of the cube which is normal to i. It therefore has units of pressure (Pa) and similarly for the C_{ijkl}, which are usually given in GPa.[1] It is the force that a unit element applies to its neighboring

---

[1] Older literature will often list the elastic constants in Dyne/cm^2 = 0.1 Pa. The constants are often around 10^{12} Dyne/cm^2=100 GPa.

element. Hence a sample with uniform stress with only diagonal elements must have a uniform pressure P on the surfaces to be static. Therefore a hydrostatic pressure P means that the strain is $\sigma_{ij} = -P\delta_{ij}$, where δ_{ij} is a delta function which is equal to 1 if $i = j$ and 0 otherwise. The sign is because the pressure is applied to the medium while the stress is the force of the medium on its surrounding.

The energy per unit volume (U) of a particular deformation is written as

$$U = \frac{1}{2} C_{ijkl} s_{ij} s_{kl}. \tag{2.2}$$

Considering the rotational invariance of the energy and other symmetry considerations, the following symmetries exist for the C_{ijkl}:

$$C_{ijkl} = C_{klij} = C_{jikl} = C_{ijlk} \tag{2.3}$$

and permutations of the above. This brings the number of independent components for the tensor from 81 down to 21. Similarly the stress tensor can be shown to have $\sigma_{ij} = \sigma_{ji}$ and therefore it is symmetric with 6 independent components. Finally the strain tensor can also be written in a symmetric fashion

$$s_{ij} = \frac{1}{2}\left(\frac{\partial u_j}{\partial x_i} + \frac{\partial u_i}{\partial x_j}\right) \tag{2.4}$$

then $s_{ij} = s_{ji}$ and it also has only 6 independent components.[2]

In order to take advantage of all these symmetries, the following notation is introduced for the stress

$$\begin{gathered} \sigma_1 = \sigma_{11},\ \sigma_2 = \sigma_{22},\ \sigma_3 = \sigma_{33}, \\ \sigma_4 = \sigma_{23} = \sigma_{32}, \quad \sigma_5 = \sigma_{13} = \sigma_{31}, \quad \sigma_6 = \sigma_{12} = \sigma_{21} \end{gathered} \tag{2.5}$$

and for the strain

$$\begin{gathered} s_1 = s_{11},\ s_2 = s_{22},\ s_3 = s_{33}, \\ \tfrac{1}{2}s_4 = s_{23} = s_{32}, \quad \tfrac{1}{2}s_5 = s_{13} = s_{31}, \quad \tfrac{1}{2}s_6 = s_{12} = s_{21} \end{gathered} \tag{2.6}$$

and C_{ijkl} (and S_{ijkl}) is converted to a symmetric tensor C_{mn} (S_{mn}) where $ij \rightarrow m$ and $kl \rightarrow n$ according to $11 \rightarrow 1$, $22 \rightarrow 2$, $33 \rightarrow 3$, $23 = 32 \rightarrow 4$, $13 = 31 \rightarrow 5$ and $12 = 21 \rightarrow 6$. With these notations eqn. (2.1) becomes $\sigma_m = C_{mn} s_n$ where m and n range from 1 to 6 and eqn. (2.2) becomes $U = \frac{1}{2} C_{mn} s_m s_n$. This conversion simplifies the language by lowering the rank of the tensors but it increases the dimensions from 3

---

[2] The symmetric version of s_{ij} is not always used. Sometimes only the $s_{ij} = \frac{\partial u_j}{\partial x_i}$ is used because it makes proofs simpler. This does not cause any problems since C_{ijkl} contains the necessary symmetry.

to 6. It also introduces some factors of 2 and loses some of the power of the full tensor notation. We will use both notations depending on convenience.

Symmetries of a system reduce the number of independent elements of the elastic tensor from 21. We will be interested in a tetragonal system and therefore we will have only 6 independent components (C_{11}, C_{33}, C_{12}, C_{13}, C_{44} and C_{66}) and $\mathbf{C}$ can be written:

$$C_{ij} = \begin{pmatrix} C_{11} & C_{12} & C_{13} & 0 & 0 & 0 \\ C_{12} & C_{11} & C_{13} & 0 & 0 & 0 \\ C_{13} & C_{13} & C_{33} & 0 & 0 & 0 \\ 0 & 0 & 0 & C_{44} & 0 & 0 \\ 0 & 0 & 0 & 0 & C_{44} & 0 \\ 0 & 0 & 0 & 0 & 0 & C_{66} \end{pmatrix}. \tag{2.7}$$

The compliance tensor S_{mn} has the same symmetry. In a cubic system only 3 components are independent and the additional restrictions are $C_{12} = C_{13}$, $C_{33} = C_{11}$ and $C_{44} = C_{66}$. Finally, an isotropic medium as only 2 elements and, on top of the restrictions for a cubic system, it has $C_{66} = \frac{1}{2}(C_{11} - C_{12})$ which for the compliance tensor implies $S_{66} = 2(S_{11} - S_{12})$.

Before going to the dynamics of the system let us relate other parameters often used in elastic theory to the elastic constants. We will restrict ourselves to an isotropic system. The deformation energy can be written as $U = \frac{1}{2}\lambda s_{ii}^2 + \mu \sum_{ij} s_{ij}^2$ which defines the Lamé coefficients λ and μ (which is also called the modulus of rigidity or shear modulus). These are the coefficients of the two independent scalars that can be formed from a symmetric second rank tensor (squared sum of diagonal elements and sum of elements squared). Relating to the elastic constants for an isotropic system, then $\lambda = C_{12}$ and $\mu = C_{66} = \frac{1}{2}(C_{11} - C_{12})$.

For a cubic or isotropic system we have $S_{11} = (C_{11} + C_{12})/[(C_{11} - C_{12})(C_{11} + 2C_{12})]$, $S_{12} = -C_{12}/[(C_{11} - C_{12})(C_{11} + 2C_{12})]$ and $S_{44} = 1/C_{44}$.

The modulus of extension (or Young's modulus) is $E = L\frac{\partial P}{\partial L}$, where L is the length of the sample and the pressure P is applied along the length of the sample. If we assume the force is along the 1 direction than it is equivalent to $E = \sigma_1/s_1$ and since we applied the force so that only σ_1 is non zero then $s_1 = S_{11}\sigma_1$ and therefore $E = (S_{11})^{-1}$. Keeping the same stress the Poisson ratio[3] σ is defined to be the ratio of the perpendicular deformation to the longitudinal one, i.e. $\sigma = -s_2/s_1 = -s_3/s_1$ and is given by $\sigma = -S_{21}/S_{11}$. These

---

[3] The Poisson ratio σ will not be confused with the stress because it has no indices.

definitions work for a crystal of any symmetry but for cubic or isotropic system, we have $E = \frac{(C_{11}-C_{12})(C_{11}+2C_{12})}{C_{11}+C_{12}}$ and $\sigma = C_{12}/(C_{11}+C_{12})$.

A last parameter is the modulus of hydrostatic compression B (or Bulk modulus) which is the inverse of the compressibility (coefficient of hydrostatic compression) K, $K = 1/B = -\frac{1}{V}\frac{\partial V}{\partial P}$. In this case the pressure is uniformly applied so $\sigma_{ij} = -P\delta_{ij}$. As seen above $dV/V = s_{ii}$, so $K = 3(S_{11}+2S_{12}) = 3/(C_{11}+2C_{12})$ and $B = \frac{1}{3}(C_{11}+2C_{12})$ for a cubic or isotropic system.

Now we can study the dynamics of the system. The equation of motion for the system can be derived among other techniques from a Lagrangian and using Hamilton's principle [37, Chap 22]:

$$\rho\frac{\partial^2 u_i}{\partial t^2} = C_{ijkl}\frac{\partial^2 u_l}{\partial x_j \partial x_k}. \tag{2.8}$$

where ρ is the density. These are 3 equations indexed by i. This is equivalent to $ma_i = F_i$ from classical mechanics. The force on each volume element is the difference in stress on opposite faces of the cube element. This is why the force is the space derivative of the stress. This equation possesses solutions of the form $\mathbf{u} = u\hat{\mathbf{e}}\exp(\mathrm{i}\omega t - \mathrm{i}\mathbf{q}\cdot\mathbf{r})$, where $\hat{\mathbf{e}}$ is a unit vector in the direction of the motion of the atoms and is the polarization vector of the wave, $\omega = 2\pi f$ for f the wave frequency, and $\mathbf{q}$ is the wave number with $\hat{\mathbf{q}}$ being the wave propagation directions and $q = 2\pi/\lambda$ using the wavelength λ. This is a wave equation. With this definition of $\mathbf{u}$, then

$$\rho\omega^2\hat{e}_i = C_{ijkl}q_j q_k \hat{e}_l = C_{ijkl}q^2\hat{q}_j\hat{q}_k\hat{e}_l \tag{2.9}$$

This is an eigenvalue problem for a matrix $C_{ijkl}\hat{q}_j\hat{q}_k/\rho$. The eigenvalues are $v_S^2 = \omega^2/q^2$ and the eigenvectors are the polarization vectors. Because the matrix is symmetric there is always a solution with 3 eigenvalues and 3 eigenvectors ($\hat{\mathbf{e}}$) which are orthogonal. The v_S's are both the phase velocity (ω/q) and the dispersion ($d\omega/dq$), also called group velocity, and represent the sound velocity in the material. It can be written as

$$v_S = \sqrt{\bar{C}/\rho} \tag{2.10}$$

where $\bar{C} = C_{ijkl}\hat{q}_i\hat{q}_j\hat{e}_l\hat{e}_k$ is the particular combination of elastic constants for that sound wave. Of course eqn. (2.9) must first be solved to find the possible $\hat{\mathbf{e}}$ for a particular $\hat{\mathbf{q}}$.

When the propagation direction of the sound wave $\hat{\mathbf{q}}$ is along a high symmetry axis then one of the polarizations is parallel to $\hat{\mathbf{q}}$ and the other two are perfectly perpendicular to it. The parallel one is called a longitudinal wave and represents a density wave through

$\mathbf{q}$	$\hat{\mathbf{e}}$	$\bar{C}$
[100]	[100]	C_{11}
[110]	[110]	$\frac{1}{2}(C_{11}+C_{12}+2C_{66})$
[001]	[001]	C_{33}
[100]	[010]	C_{66}
[110]	$[1\bar{1}0]$	$\frac{1}{2}(C_{11}-C_{12})$
in-plane	[001]	C_{44}
[001]	[100]–[110]	C_{44}
[100]–[001]	[010]	Combination of C_{66} and C_{44}
[110]–[001]	$[1\bar{1}0]$	Combination of $(C_{11}-C_{12})$ and C_{44}
in-plane	in-plane	Combination of C_{11}, C_{12} and C_{66}
[100]–[001]	[100]–[001]	Combination of C_{11}, C_{33}, C_{44} and C_{13}
Any	Any	Combination of all 6 elements

Table 2.1: List of polarization and the corresponding linear combination of elastic constants for a tetragonal symmetry $\bar{C}$. The top part shows pure longitudinal (first 3) and transverse modes. The bottom part show the quasi modes (both longitudinal and transverse for each). [001] is the c-axis which is the axis of 4-fold symmetry. A range indicates all direction between the 2 vectors, for example [100]–[001] represents all directions in the a–c plane of the crystal.

the material while the other two are transverse waves and represent shear waves. When the direction of propagation is not along a direction of high enough symmetry then the waves are not perfectly parallel or perpendicular anymore but they often are very close and will be described then as quasi-longitudinal and quasi-transverse.

In a crystal the motion of the ions can be quantized and the wave excitations are then known as phonons. There are actually $3P$ phonon modes in a crystal, where P is the number of atoms per unit cell. Three of the modes have a linear dispersion at small q and going to $\omega = 0$ at $q = 0$. These are called acoustic modes and are the quantized version of the sound waves from elastic theory at small q. The other modes are called optical modes and depend on the relative motion of atoms within the unit cell. The acoustic modes are when all the atoms move in a similar way because the acoustic $q = 0$ mode corresponds to a translation of the whole crystal (this is the reason why the energy is 0). The presence of the acoustic modes is a result of broken translational symmetry of the crystal. The $q = 0$ mode is the Goldstone mode. From now on, sound waves and phonons will always refer to the acoustic branch only unless otherwise noted.

The sound wave is a harmonic oscillator. It has a constant energy (E) which is shared between kinetic and potential energy. The total energy can therefore be written as the maximum in kinetic energy and no potential energy, or vice-versa:

$$E = \begin{array}{ll} \rho\frac{1}{2}\left(\frac{du}{dt}\right)^2_{\max} = \frac{1}{2}\rho\omega^2 u^2 & \text{(from kinetic energy)} \\ \frac{1}{2}(C_{ijkl}s_{ij}s_{kl})_{\max} = \frac{1}{2}q^2u^2\bar{C} & \text{(from potential energy).} \end{array} \tag{2.11}$$

Other solutions to the sound wave equation can be obtained at the crystal surface by applying proper boundary conditions. These solutions are called surface waves because the displacement vector amplitude decays exponentially away from the surface. We are interested in sound waves in the bulk so we will not discuss these surface waves further.

Sound frequencies above the audible range of the human ear (20 Hz – 20 kHz) are called ultrasound while frequencies below the audible range are infrasound. We will use frequencies from 1 MHz to 600 MHz and will therefore use the term ultrasound interchangeably with sound.

2.2 Ultrasound attenuation of metals

The wave solution from the previous section describes a sound wave traveling in the sample at a velocity v_S and with a constant amplitude. In a real system the amplitude will actually decrease because of dissipation from many sources. This decrease of intensity of the wave is the sound attenuation. Instead of postulating a solution to the wave equation with a constant amplitude we write:

$$\mathbf{u} = u\hat{\mathbf{e}}\exp(\mathrm{i}\omega t - \mathrm{i}\mathbf{q}\cdot\mathbf{r} - \tfrac{1}{2}\alpha\hat{\mathbf{q}}\cdot\mathbf{r}) \tag{2.12}$$

where $\alpha = \alpha(\mathbf{q}, \hat{\mathbf{e}})$ is the sound attenuation. The factor of 1/2 is introduced because the attenuation is the decay of *energy* in the sound wave. The energy (or intensity) of the wave is related to the square of the amplitude which explains the factor of 1/2.[4] Here the attenuation is given per unit length (m^{-1}). Is is also possible to write it per unit time then the added term is $\exp(-\frac{1}{2}\alpha_t t)$ and is related to the other attenuation through the sound velocity by $\alpha_t = \alpha v_S$ assuming v_S is not affected strongly by the dissipation which is usually the case. Yet another form for the attenuation is given per wave number, $\alpha_q = \alpha/q = \alpha\lambda/2\pi$, which is often used for theoretical calculation. It is the attenuation

---

[4] The literature sometimes uses the definition of alpha in terms of amplitude and is therefore $\alpha/2$.

constant for propagation through one wavelength (up to a factor of 2π) and is useful because $\alpha_q \ll 1$ for any sound wave that propagates any significant distance relative to λ. Otherwise a wave description is not valid. Related to this definition is the use of logarithmic decrement which is the logarithm of the amplitude change over a cycle. It is given by $\delta = (\alpha/2)\lambda$.

When the solution, eqn. (2.12), is inserted in the original wave equation, eqn. (2.8) the result is to replace q_i with $q_i - \frac{1}{2}\mathrm{i}\alpha$ in eqn. (2.9) but the solution sets $\alpha = 0$ because that equation does not have any dissipation term. Following Landau and Lifshitz [36, section 29] we introduce a dissipation term to the wave equation. This can be derived from a dissipation function $\mathcal{F} = -\frac{1}{2}\mathbf{F}\cdot\mathbf{v}$ [38] if the dissipation force is linear in velocity. This requirement is generally observed. Therefore the wave equation with dissipation is:

$$\rho\frac{\partial^2 u_i}{\partial t^2} = C_{ijkl}\frac{\partial^2 u_l}{\partial x_j \partial x_k} + F_i \tag{2.13}$$

where F_i could also include other extra non-dissipative forces. Upon inserting the solution eqn. (2.12) the above equation becomes:

$$\rho\omega^2\hat{e}_i = C_{ijkl}\hat{q}_j(q - \frac{1}{2}\mathrm{i}\alpha)\hat{q}_k(q - \frac{1}{2}\mathrm{i}\alpha)\hat{e}_l - \frac{F_i}{u} = \underline{C}_i(q^2 - q\mathrm{i}\alpha - \frac{1}{4}\alpha^2) - \frac{F_i}{u} \tag{2.14}$$

where we use the short hand $\underline{C}_i = C_{ijkl}\hat{q}_j\hat{q}_k\hat{e}_l$. The eigenvectors along the high symmetry directions don't change but the eigenvalues change and become complex. In general the eigenvectors will also change but to first order we assume they don't. If we decompose the dissipation force into a real and imaginary part ($F_i = uq^2(R_{ij} + \mathrm{i}Z_{ij})\hat{e}_j$) and also assuming α is small then we can write the general solutions as [39]:

$$\alpha = -q\frac{Z_{ij}\hat{e}_j}{\underline{C}_i} \tag{2.15}$$

$$\frac{\Delta v_S}{v_{S0}} = \frac{v_S - v_{S0}}{v_{S0}} = \frac{-\alpha^2}{8q^2} - \frac{R_{ij}\hat{e}_j}{2\underline{C}_i} \tag{2.16}$$

where v_{S0} is previously defined velocity before only from the elastic constants, eqn. (2.10), and Δv_S is the change in velocity because of extra forces F_i.

Therefore one way to calculate the attenuation is to find the dissipation force. With the dissipation is associated a change in sound velocity but it is usually unmeasurably small and other sources of velocity change will dominate.

The formal definition of the attenuation is

$$\alpha_t = \alpha v_S = \frac{\text{energy dissipated per time}}{\text{instantaneous energy in system}} = \frac{\frac{1}{T}\int_0^T dt\ \Re(\mathbf{F})\cdot\Re\left(\frac{\partial\mathbf{u}}{\partial t}\right)}{E} = \frac{\frac{1}{2}\Re\left(\mathbf{F}^*\cdot\frac{\partial\mathbf{u}}{\partial t}\right)}{E} \tag{2.17}$$

where $T = 2\pi/\omega$ is the period of oscillation $\Re$ is to take the real part of the complex number and * is the complex conjugate operator. We can also use the result that the work done by the dissipative force is $2\mathcal{F}$ [38, chapter 1]. This can be shown to give the same result as above.

The wave equation is basically the result of a damped harmonic oscillator. So the same results apply here. For example the Q factor is defined as

$$Q = \omega_r \frac{\text{instantaneous energy in system}}{\text{energy dissipated per time}} \tag{2.18}$$

where the r subscript means the resonance of a forced damped harmonic oscillator. By similarity with eqn. (2.17) we can immediately write $\alpha_t = \omega/Q$. When the attenuation is small this can be approximated by $Q = f_r/\Delta f$ where f_r is the resonance frequency and Δf is the full frequency width at half-maximum of the intensity. In this case we obtain $\alpha = 2\pi\Delta f/v_S$.

Finally, when considering quantum mechanical calculations what is obtained is the collision rate of the phonons $\Gamma = -\Im(\Sigma)/\hbar$ from the imaginary part ($\Im$) of their self-energy (Σ) [40, section 4.1 and 5.8D]. This is related to the phonon lifetime $\tau = 1/2\Gamma$,[5] which in turns gives the attenuation: $\alpha_t = \alpha v_S = 1/\tau = -2\Im(\Sigma)/\hbar$.

2.2.1 Sources of attenuation

Sound attenuation has many sources. The most obvious one is scattering of sound from crystal defects. These can range from cracks in the crystal to voids in the crystal. In this category we can also include variations of the elastic constants and of the density of the material. These can be difficult to calculate and estimate but they are temperature independent to first order. They are mostly dependent on geometry but can also dependent on the elastic anisotropy. Since the elastic constants are typically not strongly temperature dependent (especially at low temperature) and so the anisotropy is almost constant and does not yield much temperature dependence from this source of attenuation.

Another source of attenuation is the phenomenon of mode conversion on crystal surfaces. At a surface, because of the boundary conditions, an incident pure mode can be reflected into a combination of transverse and longitudinal waves. This conversion depends on the anisotropy of the elastic constants (therefore it depends on the orientation

---

[5] The factor of 2 is by definition. Γ is the relaxation rate of the Green's function (G) while the life-time is obtained from the decay of the probability $|G|^2$ of a state. In a way τ is related to the decrease in intensity and Γ with the decrease in amplitude.

of the surface with respect to the crystal axis) and it also depends on the polarization direction of the incoming wave. The reflected waves (longitudinal and transverse) propagate at an angle dependent on the elastic constants which is therefore not necessarily the same angle as the incoming wave: $\sin\theta_{in}/\sin\theta_{out} = v_{in}/v_{out}$ for v a sound velocity. Conversion is avoided when the incoming wave is purely longitudinal and arrives perpendicular the the surface or when the incoming wave is purely transverse with the polarization parallel to the surface. Otherwise conversion occurs and this implies a loss of amplitude in the incoming mode and some attenuation which should be temperature independent to first order.

In a magnetic material the phonons can interact with the spins and yield attenuation. In particular you can have interaction with spin-waves or nuclear spins. Another source of attenuation is the motion of the magnetic domain walls under the influence of the sound wave. The system we will study is non-magnetic so we are not concerned with this type of interactions.

Until now we have assumed the crystal to be perfectly harmonic. This implies that there are no interactions between phonons. In an actual crystal there is always some anharmonicity and this leads to phonon-phonon interactions which give another source of attenuation. This particular source of attenuation varies quickly at low temperature, as T^4 or higher power in insulators. In metals, it is small and it will be shown to be small in our case even in the superconducting state. It is given by $\alpha = \gamma^2\omega_s^2\kappa T/\rho v_S^5$ where γ is the Grüneisen parameter (order 1) and κ is the thermal conductivity of the phonons. That equation is valid if $\omega\tau \ll 1$ for τ the phonon lifetime. Above that, the attenuation gets smaller by a factor $(3\pi/4\omega\tau)$ [41, pages 307–327].

Crystals are never perfect and they will contain defects. Dislocations are such a defect. They produce attenuation. Estimating the amplitude is not easy because it is hard to know the actual density and the type of dislocations present in a crystal. Dislocations are produced during crystal growth, and when a crystal is strained past its elastic limit. The frequency response of the sound attenuation from a dislocation is a resonance curve. We are mostly below the resonance where the frequency dependence is quadratic. Its temperature dependence is complicated. Part of it is an activated behavior (*i.e.* an exponential curve). Another part is linear in temperature or at least monotonically increasing.[6] The attenuation can also be strain amplitude dependent

---

[6] The increase can end at higher temperature where an additional resonance can produce the Bordoni peak [41, section 48]. If present this peak occurs around the Debye frequency so in the 100 K range.

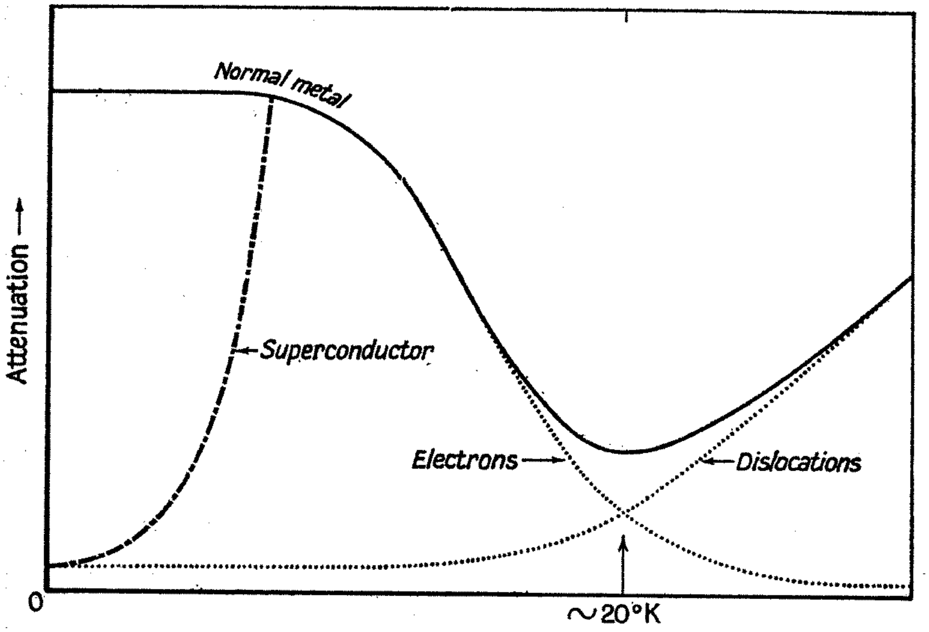

Figure 2.1: Sketch of attenuation in a generic metal from [42]. Note that the dislocation becomes relatively unimportant below about 20 K.

because with enough strain some of the pinning sites can be broken. In metals this source of attenuation is not important at low enough temperatures fig. (2.1).

When a longitudinal sound wave travels through a medium, the local density variations produce changes in temperature. These temperature variations setup a flow of heat which will result in attenuation. This is the thermoelastic effect and is present only for longitudinal waves since transverse waves do not setup the necessary temperature gradients. It is given by $\alpha = \omega^2\beta^2\kappa T/\rho v_S C_p^2$ where β is the linear thermal expansion coefficient and C_p is the heat capacity per unit mass at constant pressure. In metals this is smaller than the other sources of attenuation and is not considered further.

Finally, the last source of attenuation we consider is the interaction between phonons and conduction electrons. This contribution can be large at low temperature and can have a large temperature dependence, especially when crossing a superconducting transition. In the next few sections we will describe this interaction further since it is the one we are interested in.

Among all the interactions we surveyed, only the electronic attenuation shows temperature dependence at low temperature. The others are either temperature independent (crystal defects, mode conversion), don't apply to our samples, are small and/or are gapped at low enough temperatures. Hence the idea is to measure the sound attenuation at low temperature and any temperature variation is then attributed to the electrons. The approximation is typically valid at temperatures below 10 K (see fig. (2.1)). This therefore extracts the temperature dependent part of the electronic ultrasound attenuation. It is important to note that the absolute value of electronic attenuation (including the constant part) cannot be extracted because other sources of constant attenuation cannot be estimated (and technical considerations add other sources of constant attenuation as will be seen later).

2.2.2 Length and time scales for the attenuation

We want to calculate the electronic sound attenuation. On general grounds, we must consider two different regimes depending on the characteristic lengths of the system. For lengths, we have the unit cell dimension $a \sim$Å, the wavelength of the sound $\lambda \sim \mu$m (in the 100 MHz range), and the electron mean free path $\ell \sim \mu$m (for very clean crystals, smaller otherwise).

The time scales of the problem are the electron scattering time τ_e which is related to the mean free path by the electron velocity v_f (*i.e.* $\ell = v_f \tau_e$), and the period of the sound wave, which is the inverse of the frequency, with $1/f \sim 10^{-9}$ s for a large frequency of 1 GHz. Since electron velocities are usually around 100 km/s, then $\tau_e \sim 10^{-11}$ s for very pure crystals ($\ell = 1$ μm) or smaller.

In general, ultrasound attenuation experiments are limited to frequencies below a few GHz. Therefore we will always be in the limit where $\omega\tau_e \ll 1$. More pertinent are the different length scales. The wavelength will always be larger than the lattice size. To have $\lambda \approx a$ requires unattainable frequencies. Also this is one of the assumptions in elastic theory so that continuum physics for the sound wave is a good approximation to the real system with a lattice structure. Thus we are left with the comparison between ℓ and λ. These have the same magnitude and their relative size defines two behaviors. The comparison is often done in terms of $q\ell$ where $q = 2\pi/\lambda$ is the wavevector of the phonons. When $q\ell \ll 1$ (*i.e.* $\ell \ll \lambda$), then we are in the hydrodynamic limit. In this limit the electrons suffers many collisions over the spatial extent of the wave. These collisions bring the electron back in equilibrium with the local position of the lattice. Viewed from the lattice, the electrons behave as a viscous fluid that is dragged along with the slow moving sound wave. What will cause attenuation in that regime is the viscosity of the electrons. In the other limit, $q\ell \gg 1$, the collisions happen rarely and can be considered localized with respect to the wavelength. This is referred to as the quantum limit (also called the collisionless limit). Calculations can be done assuming collisions between an electron and a phonon. Therefore depending on the value of $q\ell$ different calculation techniques can be applied. It is also possible to use more general calculations which can give the general solution and describe the cross over between the two regimes.

A final comparison is between the velocity of the sound wave and that of the electrons. Sound waves travel at about 5 km/s so that usually $v_S/v_f \ll 1$. This ratio relate the units of time to length, $\omega\tau_e = (v_S q)(\ell/v_f) = q\ell(v_S/v_f)$, which explains why $\omega\tau$ is not the important parameter. One exception is the class of materials called heavy fermions, where one can have $v_S/v_f \sim 1$.[7] In that case care must be taken in theories when the wavelength gets short.

2.2.3 Simple calculations of attenuation

We have already seen that the stress is related to the strain by the elastic constants, $\sigma_{ij} = C_{ijkl}s_{kl}$. In the hydrodynamic limit, we can add a relation between stress and the time derivative of the strain

$$\sigma_{ij} = \eta_{ijkl}\frac{\partial s_{kl}}{\partial t} \tag{2.19}$$

This introduces η, the viscosity tensor. It is sometimes called dynamic or absolute viscosity (as opposed to kinematic vicosity[8]) and it is given in units of poise (P=g/cm s, sometimes Ps) or in the MKS system by Pa s (kg/m s) where 1 poise = 0.1 Pa s. It has the same symmetries as the elastic tensor. It is a characteristic of the long wavelength response of the system and is independent of frequency (in the limit we are interested in). The viscosity is the proportionality constant between a uniformly changing strain and the resulting stress (or equivalently momentum transfer) across a plane. It can come from interactions between particles but even without them you have some viscosity. For example an ideal gas between 2 horizontal plates moving at different velocity will setup a vertical pressure proportional (by the viscosity) to the velocity gradient. This is because on average particle crossing a horizontal plane from a lower to higher velocity region have a smaller momentum than particles crossing the other way. Hence a momentum transfer occurs from the faster to slower region. A time rate of change of momentum is, by Newton's second law, equal to a force so that our momentum transfer is equal to the strain. Typical values of viscosity for fluid is about 0.01 poise for water at room

---

[7] Another are the semiconductors but we are not interested it these.

[8] Kinematic viscosity is given by the dynamic viscosity divided by the density and is given in units of stokes (St = cm^2/s).

temperature, 0.9 poise for olive oil and 14.9 for glycerin.

When inserting the standard wave solution we have

$$\sigma_{ij} = \mathrm{i}\omega\eta_{ijkl}s_{kl} \tag{2.20}$$

so the viscosity can be seen as the complex part of a general elastic constant $C'_{ijkl} = C_{ijkl} + \mathrm{i}\omega\eta_{ijkl}$. Inserting $\mathbf{C}'$ instead of $\mathbf{C}$ into eqn. (2.13) and rearranging it we can obtain $F_{ij} = -uq^2\omega\eta_{ijkl}\hat{\mathbf{q}}_j\hat{\mathbf{q}}_k\hat{\mathbf{e}}_l[(\alpha/q)+\mathrm{i}]$ to lowest order in α. Using this result we can immediately write the attenuation (see section 2.2):

$$\alpha = \frac{q^2}{\rho v_S}\eta_{ijkl}\hat{e}_i\hat{q}_j\hat{e}_k\hat{q}_k = \frac{\omega^2}{\rho v_S^3}\eta_{ijkl}\hat{e}_i\hat{q}_j\hat{e}_k\hat{q}_k. \tag{2.21}$$

With that equation we can use, for example, the electronic viscosity for a free electron gas, obtained from kinetic theory [43]. Similarly to the definition for elastic constants there are bulk viscosities and shear viscosities. For a free electron gas, the shear viscosity is simply written $\eta = \ell Nm\bar{v}/3$ where N is the number of electrons per unit volume, m is the electron mass, ℓ is the electron mean free path and $\bar{v} = 3v_f/5$ is the average electron velocity.[9] The bulk viscosity is the resistance of the medium to changes in density. Using kinetic theory [42, section 4.7] it can be shown to be zero in the special case of a free electron gas. In general the bulk viscosity is non-zero. We can than combine this viscosity and eqn. (2.21) to obtain

$$\alpha_T = \frac{\omega^2}{5\rho v_T}\ell Nmv_f, \tag{2.22}$$

for transverse sound waves with velocity v_T and

$$\alpha_L = \frac{4\omega^2}{15\rho v_L}\ell Nmv_f, \tag{2.23}$$

for longitudinal waves with velocity v_L. Note that in this limit the attenuation depends on the square of the frequency and is proportional to the mean free path. The electronic conductivity (σ) is also proportional to ℓ so within the current approximation $\alpha \propto \sigma$.

In the other limit, $q\ell \gg 1$, we consider electron-phonon collisions. Conservation of energy requires that $\varepsilon_{\mathbf{k}+\mathbf{q}} - \varepsilon_{\mathbf{k}} = \hbar\omega_q$, where $\varepsilon_{\mathbf{k}}$ is the energy of an electron with crystal moment $\mathbf{k}$, $\mathbf{q}$ is the phonon wave number and $\omega_{\mathbf{q}}$ is its frequency. The phonon $\mathbf{q}$ is small so the electron energy difference can be expanded into $\varepsilon_{\mathbf{k}+\mathbf{q}} - \varepsilon_{\mathbf{k}} = \hbar\mathbf{q}\cdot\mathbf{v}_{\mathbf{k}}$

---

[9] For a free electron gas $(v)_{(avg)} = \frac{3}{4}v_f$ and $(v^2)_{(avg)} = \frac{3}{5}v_f^2$ hence using $\bar{v} = 3v_f/5$ is more valid when considering a constant scattering time τ than a constant mean free path since $\ell = v\tau$. But this is a minor error considering the level of approximation [42, section 12.2]. The current choice matches with more detailed calculations.

where $\mathbf{v_k} = (1/\hbar)\partial\varepsilon_\mathbf{k}/\partial\mathbf{k}$ is the semi-classical electron velocity for a wave packet centered around $\mathbf{k}$. Therefore the energy conservation reduces to

$$\mathbf{q} \cdot \mathbf{v_k} = \omega_\mathbf{q} = v_S q \tag{2.24}$$

This requires the projection of the electron velocity along the direction of propagation to be the same as the sound velocity. In other words, the only electrons that attenuate the wave are those which are surfing with the wave (staying synchronized with it). As mentioned before the ratio of sound velocity to electron velocity is usually very small, so that the electrons that take part in the interaction are those traveling almost perpendicular to the sound wave. It is a general result that in this regime the attenuation is linearly dependent on the frequency and independent of the electron mean free path [44]. The calculation of the attenuation can be done using the electron-phonon interaction but this does not provide any attenuation for transverse waves in that regime.[10] That is because for transverse waves the electron-phonon interaction is zero perpendicular to the propagation. But the electrons also interact through the electro-magnetic field which must be added to the electron-phonon interaction in this regime.

Between the two limits, slightly more complicated calculations are needed. These can given insight into the crossover from $q\ell \ll 1$ to $q\ell \gg 1$. Here we only quote the results obtained by Pippard [45] for both longitudinal and transverse waves of a free electron system:

$$\alpha_L = \frac{Nmv_f q}{\rho v_L (q\ell)} \left(\frac{1}{3} \frac{(q\ell)^2 \tan^{-1}(q\ell)}{(q\ell) - \tan^{-1}(q\ell)} - 1 \right) \tag{2.25}$$

$$\alpha_T = \frac{Nmv_f q}{\rho v_T (q\ell)} \frac{(1-g)}{g}; \quad g = \frac{3}{2(q\ell)^2} \left(\frac{(q\ell)^2 + 1}{(q\ell)\tan^{-1}(q\ell)} - 1 \right) \tag{2.26}$$

In fig. (2.2) we show the frequency dependence of these two functions. Both have quite a similar frequency dependence. At $q\ell = 1$ they deviate by 17% from the ω^2 dependence expected in the hydrodynamic regime (for low frequency). This deviation quickly gets smaller at lower frequency so that at $q\ell = 0.5$ it is already only 5%.

Many techniques can be employed to calculate the attenuation. As pointed out by Blount [46], energy is first transfered from the sound wave to the electron, and then from the electron to an energy reservoir. The attenuation can be obtained by looking at the first energy transfer or the second. Among possible calculation techniques, field theory

---

[10] This statement is only true for a free electron gas. In general the electron-phonon interaction can have additional terms which are non-zero perpendicular to the direction of propagation.

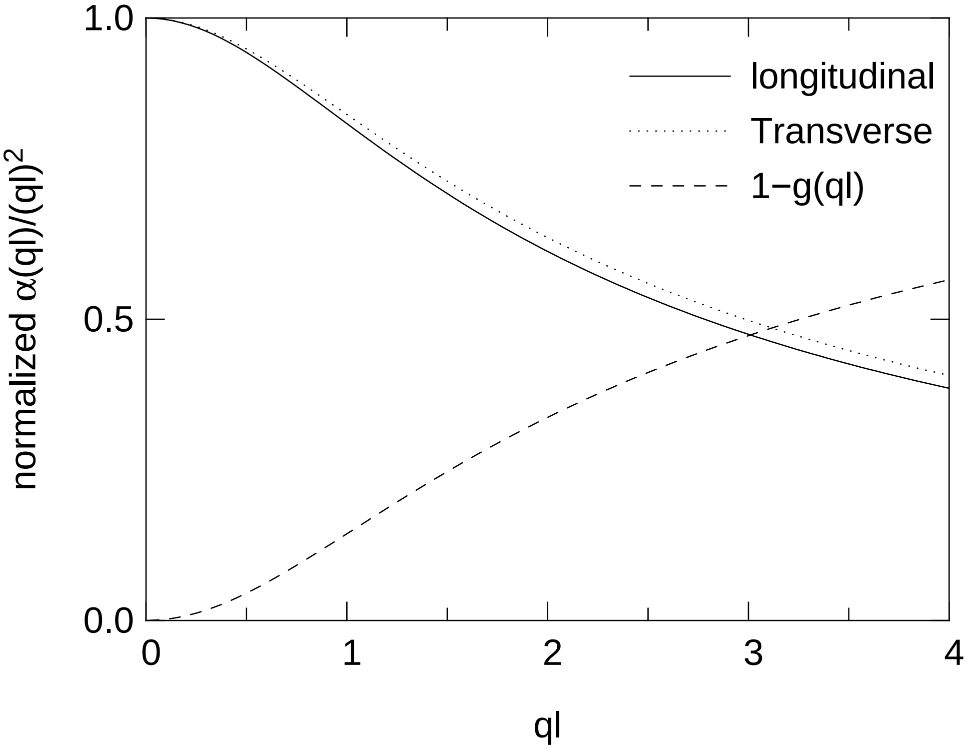

Figure 2.2: Frequency dependence express in terms of $q\ell$ for the longitudinal and transverse mode of a free electron system (see eqn. (2.25) and eqn. (2.26). The curves are normalized to give 1 in the hydrodynamic limit (a factor of $(q\ell)^2$ is divided out). The third curve $(1-g)$ represent the relative jump of attenuation at the superconducting transition for transverse waves (section 2.5.2).

can be used to calculate the phonon lifetime [47, 48]. But a large segment of the literature uses Boltzmann transport theory with varying approximations. In the next section we will use such a technique.

2.3 Deformation theory

Following the derivation of Khan and Allen [48], we will now proceed in calculating the viscosity (hence the attenuation in the hydrodynamic limit) for a general crystal.

Before we start, lets review some fundamentals of solid state physics and band theory. The solution of the Schrödinger's equation of one electron in the periodic potential of the ions gives energies $\varepsilon_{\mathbf{k},n,\sigma}$ parametrized by a band index n which are integers, by the crystal momentum $\mathbf{k}$ and by the spin σ. The crystal momentum is also periodic according the the reciprocal lattice vectors $\mathbf{K}_\sigma$. A crystal is defined by 3 lattice vectors $\mathbf{G}_\sigma$, where $\mathbf{G}_\sigma \cdot \mathbf{K}_\mu = 2\pi\delta_{\sigma\mu}$. The potential energy is periodic in any linear combination of the $\mathbf{G}_\sigma$. To simplify the description, we will drop the n and σ indices (so $\mathbf{k}$ includes all 3 variables). Because of the Pauli principle only one electrons can occupy an energy eigenstate. The number of electrons per state is given by the Fermi-Dirac distribution:

$$f(\varepsilon_{\mathbf{k}}) = \frac{1}{1+\exp((\varepsilon_{\mathbf{k}}-\mu)/k_BT)} \tag{2.27}$$

where we have introduced the chemical potential μ, the temperature T and the Boltzmann constant $k_B = 1.38 \times 10^{-23}$ J/K. At absolute zero temperature, the function is equal to 1 when $\varepsilon_{\mathbf{k}} < \mu$ and 0 otherwise. Therefore the bands are filled up to an energy μ and the locus of points where $\varepsilon_{\mathbf{k}} = \mu$ represents the Fermi surface. Some bands can be completely filled or empty and they will not participate in the calculations. Only the partially filled bands are important. If more than one band is partially empty then the Fermi surface is made of multiple sheets. The value of μ is set by the total number of electrons N implicitly from

$$N = \sum_{\mathbf{k}} f(\varepsilon_{\mathbf{k}}) = 2\sum_{\mathbf{k},n} f(\varepsilon_{\mathbf{k},n}) \tag{2.28}$$

where in the second equality we have expanded $\mathbf{k}$ and the factor of 2 is because of the electron spin. The energy range of μ or the Fermi energy is given by the bandwidth of the bands crossing the Fermi energy. In most materials this is in the eV range. This should be compared to the thermal energy k_BT which is 25 meV at room temperature and much smaller at low temperature (0.09 meV at 1 K). Therefore only a small volume of k-space around the Fermi surface has its distribution modified by temperature, and only this volume is active in the calculation of most quantities. This is why the Fermi surface is a very useful concept. The semi-classical theory consists of wave packets of electrons with crystal momentum around $\mathbf{k}$ and moving at a velocity $\mathbf{v_k} = (1/\hbar)\partial\varepsilon_{\mathbf{k}}/\partial\mathbf{k}$ where $\hbar = 1.05 \times 10^{-34}$ Js is Plank's constant divided by 2π. The variation of the crystal momentum $\mathbf{k}$ is given by the applied forces (the internal forces due to the potential are incorporated in the energy dispersion). Finally, for a free electron gas $\varepsilon_k = \hbar^2k^2/2m = mv_k^2/2$.

With these results we can now define a deformation potential

$$D_{ij} = \lim_{s_{ij}\to 0} \frac{\varepsilon(k_i - s_{ij}k_j, s_{ij}, \mu(s_{ij})) - \varepsilon(k_i, 0, \mu(0))}{s_{ij}} \tag{2.29}$$

where we use s_{ij} as a strain. The energy here is defined with respect to the chemical potential which can vary with the strain. The $\mathbf{k}$ points are also modified by the strain. This is done so that a point on the Brillouin zone boundary remains on the Brillouin zone boundary after a deformation (the Brillouin zone is a particular choice of the reciprocal unit cell which is periodic in $\mathbf{G}_\sigma$). There are many other definitions of a deformation potential (without the renormalization of the $\mathbf{k}$ or the $\mu(s_{ij})$ dependence) but the one defined above will prove to be the appropriate one for the calculation of attenuation. The renormalization of the $\mathbf{k}$ points comes about because in real space the lattice vectors under strain become $G_{\alpha i} + s_{ij}G_{\alpha j}$. Keeping changes only linear in s_{ij}, this implies that the reciprocal lattice vectors change to $K_{\alpha i} - s_{ij}K_{\alpha j}$. This deformation potential has the property that

$$0 = \sum_{\mathbf{k}} D_{ij} \left(\frac{-\partial f}{\partial \varepsilon_{\mathbf{k}}} \right) \tag{2.30}$$

which is a consequence of charge conservation.

The attenuation is then calculated by considering the Boltzmann transport theory. That theory is an equation that describes the evolution of the non-equilibrium electron distribution function $F(\mathbf{k}, \mathbf{r}, t)$ which depends on momentum, position and time. The Boltzmann equation is:

$$\left(\frac{\partial}{\partial t} + \frac{d\mathbf{r}}{dt}\frac{\partial}{\partial \mathbf{r}} + \frac{d\mathbf{k}}{dt}\frac{\partial}{\partial \mathbf{k}} \right) F(\mathbf{k}, \mathbf{r}, t) = \left. \frac{\partial F}{\partial t} \right|_{\text{coll}} \tag{2.31}$$

The distribution function F is written as

$$F(\mathbf{k}, \mathbf{r}, t) = f_{\text{LE}}(\mathbf{k}, \mathbf{r}, t) + \frac{-\partial f}{\partial \varepsilon_{\mathbf{k}}} \psi(\mathbf{k}, \mathbf{r}, t) \tag{2.32}$$

where ψ is then a function giving the deviation from local equilibrium (f_{LE}).

The term on the right, in eqn. (2.31), is a collision term that tends to bring the distribution back to local equilibrium, and can be written as

$$\left. \frac{\partial F}{\partial t} \right|_{\text{coll}} = - \left(\frac{-\partial f}{\partial \varepsilon_{\mathbf{k}}} \right) \sum_{\mathbf{k}'} C_{\mathbf{k}\mathbf{k}'} \psi_{\mathbf{k}'} \tag{2.33}$$

where $C_{\mathbf{k}\mathbf{k}'}$ is introduced as a scattering operator. In what is called the relaxation time approximation the collision term is replaced by a single time constant τ so that

$$\sum_{\mathbf{k}'} C_{\mathbf{k}\mathbf{k}'} \psi_{\mathbf{k}'} = \frac{\psi_{\mathbf{k}} - (\psi)_{\text{avg}}}{\tau} \tag{2.34}$$

where the average value of $\psi_{\mathbf{k}}$ over the Fermi surface, $(\psi)_{\text{avg}}$, is used to satisfy particle conservation. It can be shown to go to zero. Therefore the relaxation time approximation reduces to $C_{\mathbf{k}\mathbf{k}'} = \delta_{\mathbf{k}\mathbf{k}'}/\tau$. It represents the effective decay time needed to remove the deviation, to restore equilibrium.

The local equilibrium is not the straight Fermi distribution. It is given by

$$f_{\mathrm{LE}}(\mathbf{k},\mathbf{r},t) = f\left[\varepsilon(\mathbf{k} - m\mathbf{v}_{\mathrm{ion}}(\mathbf{r})/\hbar) + D^{\mathrm{ep}}_{ij}s_{ij}(t)\right] \tag{2.35}$$

where $v_{\mathrm{ion}} = \partial\mathbf{u}/\partial t$ is the velocity of the ions and m is the free electron mass. This is a standard Fermi distribution but as seen from a reference frame moving with velocity v_{ion} (a kind of Doppler shift) and with energy surfaces distorted by $D^{\mathrm{ep}}_{ij}s_{ij}$. The presence of the velocity is called the collision drag effect. It appears because energy conservation for the collisions is valid only in the moving frame of the lattice. If considering impurity scattering, after a collision the electron will have an average velocity equal to the impurity which is being moved by the lattice. The deformation potential, $\mathbf{D}^{\mathrm{ep}}$, is not the same as the one introduced before. This one is related to the electron-phonon part of the Hamiltonian. It is also related to $\mathbf{D}$ by

$$D^{\mathrm{ep}}_{ij} = D_{ij} + m v_{\mathbf{k}i} v_{\mathbf{k}j}. \tag{2.36}$$

This last relation was proven only in the case of a rigid ion model and of a deformable ion model [49, 50] but suggests it could have a more general applicability. The equation for the local equilibrium distribution function looks reasonable but to know exactly what mass to use and which deformation potential is not obvious. This was discussed by Holstein [51] Blount [46] and by Khan and Allen [48].

We are considering the low frequency limit so instead of considering an oscillating strain we can consider a strain that is changing at a constant rate. Then the Boltzmann equation can be shown to reduce to

$$D_{ij}(\mathbf{k})\frac{ds_{ij}}{dt} = \sum_{\mathbf{k}'} C_{\mathbf{k}\mathbf{k}'}\psi_{\mathbf{k}'} \tag{2.37}$$

with a solution

$$\psi_{\mathbf{k}} = \sum_{\mathbf{k}'}(C^{-1})_{\mathbf{k}\mathbf{k}'}D_{ij}(\mathbf{k}')\frac{ds_{ij}}{dt}. \tag{2.38}$$

Now to find out the viscosity we must find what stress this distribution produces. Then the term in the stress which is proportional to ds_{ij}/dt is the viscosity (see eqn. (2.19)).

For a system in equilibrium the stress is given by the derivative of the free energy with respect to the strain. This is a generalization of $P = -\partial F/\partial V$ that relates pressure to the volume derivative of the Helmholtz free energy. So the stress can be written as

$$\sigma_{ij} = \sum_{\mathbf{k}} f_{\mathbf{k}}\frac{\partial\varepsilon_{\mathbf{k}}}{\partial s_{ij}}. \tag{2.39}$$

Assuming this formula still applies when the electrons are out of equilibrium we replace $f_{\mathbf{k}}$ by $F_{\mathbf{k}}$ and keep only σ_{ij}^D the term proportional to ds_{ij}/dt and we obtain

$$\sigma_{ij}^D = \sum_{\mathbf{k}} D_{ij} \frac{-\partial f}{\partial \varepsilon_{\mathbf{k}}} \psi_{\mathbf{k}} \tag{2.40}$$

Finally combining eqn. (2.38) and eqn. (2.40) we arrive at the result that

$$\eta_{ijkl} = \sum_{\mathbf{k}\mathbf{k}'} \frac{-\partial f}{\partial \varepsilon_{\mathbf{k}}} D_{ij}(\mathbf{k})(C^{-1})_{\mathbf{k}\mathbf{k}'} D_{kl}(\mathbf{k}') \tag{2.41}$$

A similar result was obtained by Pippard [44] using a different technique. This result is also similar to the formal answer for the electrical conductivity using the same formalism

$$\sigma_{ij}^{\text{elect.cond.}} = e^2 \sum_{\mathbf{k}\mathbf{k}'} \frac{-\partial f}{\partial \varepsilon_{\mathbf{k}}} v_{\mathbf{k}i}(C^{-1})_{\mathbf{k}\mathbf{k}'} v_{\mathbf{k}'j} \tag{2.42}$$

In both the electrical conductivity and the viscosity the temperature dependence is contained only in the scattering operator C_{ij} since both the deformation potential $D_{ij}(\mathbf{k})$ and the electron velocity $\mathbf{v}(\mathbf{k})$ are characteristics of the material and don't vary over the energy scale defined by the temperature. The scattering operator is not necessarily the same for both equations[11] but even if it is the same it could give a different τ in the relaxation time approximation because the deviations from equilibrium ($\psi_{\mathbf{k}}$) are different. But assuming the relevant τ are the same, the viscosity (hence the attenuation) is proportional to the electrical conductivity. This relation has been observed to hold in many experiments. But it is not an exact equality. As Pippard [44] and Steinberg [39, 52] point out, if the scattering time is made up of different parts like impurity and phonons scattering or intra-band and inter-band[12], the combination cannot be easily cast into a single equivalent τ that is the same in both conductivity and viscosity. But the overall shape is still expected to be qualitatively similar.

So the picture is as follows. A long wave length strain (so that $q\ell \ll 1$) that travels through a sample both moves the lattice around and can change the shape of the Fermi surface. The electrons will try to follow this change but their state is only updated after a collision. There is a delay τ between the collisions so that the electron energy distribution is not the same as the local equilibrium and the electron energy must be modified on each

---

[11] It is the same when considering impurity and phonon scattering [48].

[12] Inter-band scattering can be important for longitudinal modes because the density wave can change the occupation of states in different bands. On the other hand inter-band scattering is usually not important for transverse waves since there is no density change and the band occupation is unaffected. [45].

collision. This energy change comes from the impressed sound wave and is the reason why the wave's amplitude decays.

The same formalism can be use to cover both the hydrodynamic and the quantum regime. In the latter case, the time dependence of the strain and the effect of the induced electrical field must be considered. The induced electrical field is the mechanism through which an electron at high frequency is dragged towards equilibrium. As long as $\omega\tau \ll 1$, the electric field can be obtained by assuming the induced electrical current cancels the ionic current and using Maxwell's equation (the current is canceled so that no charge imbalance is produced). The field does not produce dissipation for longitudinal waves because it is along the direction of propagation and the electrons doing the dissipation are perpendicular to this propagation. But it is very important for the attenuation of transverse waves. For longitudinal waves the electric field is produced by the charge imbalance (from the density wave) to cancel the ionic current and maintain the charge neutrality. It is a feedback mechanism which must be driven by a small error in neutrality but for $\omega\tau \ll 1$ the errors is very small and does not modify the results. For transverse waves the electric field is produced from the ionic current which induces a magnetic field that produces the transverse electric field. Hence it requires an electromagnetic coupling. The magnetic field itself has negligible effect on the distribution function and is not considered directly as an additional force. But it is important (especially when considering superconductor) in that it is the intermediary that provides the transverse electrical field.

The calculations shown above are done in a reference frame moving with the lattice. This introduces the deformation potential as a fictitious force that pushes the electron out of equilibrium. The deformation potential in a static strain keeps the electron in local equilibrium but when the deformation is time-dependent it cannot bring the electron quite into local equilibrium [44]. This small error dependent on the deformation potential is the source of the fictitious force. There is also a force from an electrical field. The electrical field is calculated so that under the influence of both deformation potential and electrical field there is no local current or charge that develops. In the hydrodynamic limit, this gives a force from the electrical field much smaller than from the deformation potential and that was assumed above. This is because at low frequency collisions occur many times during a cycle which keeps the electron in step with the ions. At high frequency, the collisions don't occur often enough and it is the electric field that must then keep the electron moving with the ions.

The attenuation can be viewed as a transfer of energy from the applied sound wave to the electron system, or from the electron system to the heat reservoir. Looking at the electron system, the effect can be seen as the increase of their energy during a cycle, or a loss of this energy through collisions. The collisions bring the electrons back to equilibrium and dump the extra energy into the heat reservoir. Looking at the energy increase of the electron we can understand the frequency/scattering dependence of the attenuation. At low frequency the electrons are accelerated by the deformation potential. This increase is limited in amplitude by the scattering length, since the electron travels a fraction $\ell/\lambda \sim q\ell \ll 1$ of the cycle between collisions. As the frequency is increased the force from the deformation potential increases (quadratically in frequency) but the length of action of the force is constant and related to ℓ. This gives an attenuation that depends on the square of the frequency and linearly on the mean free path. But at high frequency, $q\ell \gg 1$, the increase in energy during a cycle is no longer limited by the scattering. In this case the electrons will suffer at least a full cycle of the force so that averaged over a full cycle the energy change is related to the deformation potential only (quadratic in frequency). But only electrons moving in phase with the ions (so that they oscillate at the same frequency as the sound wave) will give the maximum energy change. This restriction of phase space is about inversely proportional to frequency. Therefore in this regime the attenuation is independent of mean free path and linear in frequency as was mentioned before. At higher frequency not only the deformation potential but also the electrical field must be looked at. It has the same dependence at high frequency (at low frequency it is killed by the scattering) as the deformation potential and is important for transverse waves.

The calculation can also be done in the lab (rest) frame instead of with the moving lattice. In that case the only force acting on the electron is the electric field (no fictitious force from the deformation potential). When using this formalism the electron can put energy back into the sound wave and this must be removed from the energy loss of the electrons to obtain the dissipated energy. This correction is related to the collision drag effect [46, 53] but is small at low frequency and often neglected.[13] In the previous formalism, the correction is automatically included. It also separates the problem into two forces, which provides an easier description of the attenuation and is easier to extend away from the free electron system.

---

[13] The collision drag effect still enters the problem because it gives the local equilibrium towards which relaxation occurs. It is needed at all frequencies.

2.4 Attenuation and sound velocity in a magnetic field

When a magnetic field is present, an additional force is applied to the electron. The attenuation is approximately proportional to the electrical conductivity without a field and one might expect that this will still be the case. This would produce a field dependence of the attenuation similar to the field dependence of the conductivity. This effect as been observed.

There is also an additional effect due to the magnetic field. An additional term is added to the Boltzmann equation that can be large. It was first calculated for liquid metal [54]. It depends on the magnetic force applied to a moving charge. As was mentioned above, in the absence of a magnetic field the electronic current is adjusted to compensate the ionic current. When the field is applied the electronic current will be modified and this will lead to an additional source of attenuation separate from the one due to the electron viscosity.

We will calculate this attenuation (and the effect on velocity) using the formalism of section 2.2. Therefore we need to find the dissipative force Z [55, 56, 57]. In the presence of the magnetic field we have a new force:

$$\mathbf{F}_m = \mathbf{j} \times (\mu_0 \mathbf{H} + \mu_0 \mathbf{h}) \tag{2.43}$$

where $\mathbf{j}$ is the electrical current, $\mu_0 = 4\pi \times 10^{-7}$ is the permeability of free space, H is the applied field and h is the induced field from the current.

We want to express $\mathbf{j}$ and $\mathbf{h}$ in terms of the displacement vector. To do that we use Maxwell's equations:

$$\mathbf{j} = \boldsymbol{\sigma} \left[\mathbf{e} + \mu \mathbf{v} \times (\mathbf{H} + \mathbf{h})\right] \tag{2.44}$$

$$\nabla \times \mathbf{e} = -\mu \frac{\partial (H + h)}{\partial t} \tag{2.45}$$

$$\nabla \times (\mathbf{H} + \mathbf{h}) = \mathbf{j} \tag{2.46}$$

where μ is the material permeability and $\mathbf{e}$ is the electrical field induced by the sound wave.

This can be solved by assuming $h \ll H$, that $\mathbf{h}$, $\mathbf{j}$ and $\mathbf{u}$ all have the same time and space dependence ($\exp(\mathrm{i}\omega t - \mathrm{i}\mathbf{q} \cdot \mathbf{r})$) and keeping track of the components of the conductivity tensor (in case there is anisotropy). We assume the conductivity only has the diagonal components (σ_{11}, σ_{22}, σ_{33}). Since H is time independent and spatially uniform, care must be taken not to assume $h \ll H$ before taking a derivative on it. We also assume the displacement vector $\mathbf{u}$ is not affected to first order by the magnetic field.

Then the following results are obtained assuming propagation along a high symmetry axis which we take as z and get, for a longitudinal wave:

$$\mathbf{F}_m = -\mu q^2 \mathbf{u} \left(\frac{H_x^2}{1 - \mathrm{i}\beta_x} + \frac{H_y^2}{1 - \mathrm{i}\beta_y} \right) \tag{2.47}$$

and for a transverse wave (polarization along x):

$$\mathbf{F}_m = -\mu q^2 \mathbf{u} \left(\frac{H_z^2}{1 - \mathrm{i}\beta_y} \right) \tag{2.48}$$

where $\beta_i = \omega / \sigma_{ii} \mu v_S^2$ (v_S is the sound velocity). We have dropped the force component not along the original displacement. It occurs only if $H_x H_z$ or $H_y H_z \neq 0$ for longitudinal and $H_z H_x \neq 0$ for transverse waves and induces a displacement of the opposite type (transverse or longitudinal). This induced displacement is smaller than the original one and will only produce a second order effect, as was assumed at the beginning.

Inserting these expressions in eqn. (2.15) and eqn. (2.16) we obtain the effect on the attenuation and velocity for longitudinal waves:

$$\alpha_L = \frac{(\mu/\mu_0)^2}{\rho v_L} \left(\frac{\sigma_{xx} \beta_x^2 (\mu_0 H_x)^2}{1 + \beta_x^2} + \frac{\sigma_{yy} \beta_y^2 (\mu_0 H_y)^2}{1 + \beta_y^2} \right) \tag{2.49}$$

$$\frac{\Delta v_L}{v_L} = \frac{\mu}{2 \mu_0^2 \rho v_L^2} \left(\frac{(\mu_0 H_x)^2}{1 + \beta_x^2} + \frac{(\mu_0 H_y)^2}{1 + \beta_y^2} \right) \tag{2.50}$$

and for transverse waves:

$$\alpha_T = \frac{(\mu/\mu_0)^2}{\rho v_T} \left(\frac{\sigma_{yy} \beta_y^2 (\mu_0 H_z)^2}{1 + \beta_y^2} \right) \tag{2.51}$$

$$\frac{\Delta v_T}{v_T} = \frac{\mu}{2 \mu_0^2 \rho v_T^2} \left(\frac{(\mu_0 H_z)^2}{1 + \beta_y^2} \right) \tag{2.52}$$

Therefore if $\beta \ll 1$ or if β is a constant, the change in sound velocity is expected to be quadratic. When β is larger and for the attenuation, the field dependence can be more complicated because the conductivity could also be field dependent. But at small field this dependence should be small and a quadratic field dependence of the attenuation is expected. Note that it may be very small.

2.5 Superconductivity

We now turn to the behavior of the ultrasound attenuation in the superconducting state. we start by describing conventional superconductivity and then look at ultrasound attenuation. We then go on to describe unconventional superconductors.

Element/Compound	T_c (K)	H_c/H_{c2} (mT)
Al	1.17	10.5
In	3.41	28.2
Sn	4.47	30.5
Ta	4.47	83
Pb	7.20	80.3
Nb	9.25	200
Nb-Ti	10.3	14.8 max.
Nb_3Sn	18.0	22

Table 2.2: List of some conventional superconductors from [58, 59]. Nb and the compounds below are all type II superconductors (with H_{c2}).

2.5.1 Introduction to conventional superconductivity

We begin by describing conventional superconductivity. By conventional we mean superconductors well understood in terms of the BCS theory as described in 1957. The term will be made clearer once we describe the unconventional superconductors.

Before describing the BCS theory we must describe what is a superconductor. As the name implies it is a material that has no resistance to electrical current. This state of superconductivity exists below a critical temperature T_c which is always (at least until now) below room temperature and usually in the 1–20 K range (for conventional superconductors). In terms of phase transition, the superconducting state is reached from the normal state by a second order transition. Examples of superconductors are given in table (2.2) with their critical temperatures and critical fields.

Another phenomenon attached to the superconducting state is the perfect diamagnetism, which occurs in the Meissner state, below a critical field H_{c1}. In this state the field penetrates the sample over a distance λ called the penetration depth. This can range from 10^2 Å to 10^3 Å well below T_c. In this layer superconducting currents are automatically setup to cancel the external field inside the sample so that $B = 0$ in the bulk of the material. This is more than just a consequence of the perfect conductivity. Cooling a sample in a magnetic field through the superconducting transition will set up the Meissner state, while in a perfect conductor no electric current is set up since the magnetic field is time independent. Above another critical field, H_{c2}, the superconducting state cannot exist anymore and the material reverts to the normal state.

The superconducting state cannot be explained in terms of a small perturbation from the free electron system. It requires an attractive interaction between the electrons so that they form pairs. These electron pairs then condense into a ground state. This is similar to Bose-Einstein condensation as in ^{4}He or in a dilute gas of atoms. Pairs of electrons (which are fermions) behave as bosons but these bosons are not point particles. This is an important difference compared to the Bose-Einstein condensate. The electron pairs in a superconducting condensate are separated by an average distance called the coherence length ξ. In conventional superconductors this is typically about 10^3 Å.

The ratio of λ and ξ defines two types of superconductors. For $\lambda \ll \xi$ it is a type I superconductor. In that case $H_{c1} = H_{c2} = H_c$ where H_c is a thermodynamic critical field and $(\mu_0 H_c)^2/2$ represents the amount of energy the superconducting condensate saves over the normal state. In this case, the calculation of electrodynamics requires non-local corrections because the electrons are correlated over a large region ξ.[14] In the opposite limit, $\xi \ll \lambda$, it is a type II superconductor and $H_{c1} < H_c < H_{c2}$. In this case no particular effect is seen at H_c but it still represents the thermodynamic energy in the superconducting state. Here local electrodynamics work well. The exact change between type I and type II is precisely defined by the Ginzburg-Landau theory. For type II superconductors in a field H between the two critical fields, a region called the mixed state, the field penetrates the sample with lines of magnetic flux called vortices (so the region is also called the vortex state). The magnetic field is maximum at the center of the vortex and the field decays away from it on the scale of λ. The integrated flux from a vortex is quantized and is given by $\phi_o = h/2e = 2.07 \times 10^{-15}$ Wb, where h is Planck's constant and $-e$ is the electron charge (1.602×10^{-19} C). Only vortices with a single quanta are energetically favored. At the core of the vortex, the superconducting state is destroyed over a distance ξ. In this sense, the core of the vortex is similar to the normal state. Increasing the applied magnetic field increases the number of vortices. The upper critical field H_{c2} can be seen as the field where vortices get so close that the cores touch and no superconducting state remains. Therefore $H_{c2} \propto 1/\xi^2$. The calculations for the lower critical field, H_{c1}, are more complicated and depend on the energetics of a vortex: condensation energy is lost because of the normal cores but energy is saved because of the magnetic field. Hence it depends on both λ and ξ. In a type I superconductor it

---

[14] The non-local corrections are modified by the electron mean free path when $\ell \ll \xi$, the dirty limit. Otherwise when $\xi \ll \ell$, the clean limit, only ξ is the important parameter.

is never favorable to have a vortex so there is no mixed state. In the mixed state (of a type II superconductor) the vortices organize themselves into a two dimensional array. The most energetically favorable array tends to be hexagonal but disorder can remove the long range order of this array.

Let us get back to the coupling between electrons mentioned above. For a conventional superconductor, this coupling is through the electron-phonon interaction. An electron moves much more rapidly than the ions can respond because it is so much lighter. The ions are attracted by the passage of an electron and move closer but this response is slow. Therefore after some time delay they will have moved enough to create a region of local charge that can attract another electron at the same site. This electron has interacted with the previous one through the polarization of the lattice, *i.e.* through the phonons. The interaction is delayed in time. During that time, the first electron will have moved a distance of the order of ξ.

Hence there is an interaction between electrons and it is attractive. To solve the problem of superconductivity we must make the bold step of assuming that the electrons actually pair up, in a state of opposite momenta and opposite spin. These pairs then condense and have a lower energy than the normal state. The condensate is inactive with respect to many probes. Pairs of the condensate can be broken up by thermal energy or other sources and these excitations are called quasiparticles. These quasiparticles are what is measured in most experiments.

We now develop the BCS results following Tinkham [60]. We define the BCS ground state as

$$|\psi\rangle = \prod_{\mathbf{k}} (u_{\mathbf{k}} + \nu_{\mathbf{k}} c^{\dagger}_{\mathbf{k}\uparrow} c^{\dagger}_{-\mathbf{k}\downarrow} |0\rangle \tag{2.53}$$

where $|u_{\mathbf{k}}|^2 + |\nu_{\mathbf{k}}|^2 = 1$ and $c^{\dagger}_{\mathbf{k}\sigma}$ ($c_{\mathbf{k}\sigma}$) is the creation (destruction) operator of an electron in state $\mathbf{k}$ and with spin σ. Then $|\nu_{\mathbf{k}}|^2$ is the probability that the $(\mathbf{k}\uparrow, -\mathbf{k}\downarrow)$ pair is occupied and $|u_{\mathbf{k}}|^2$ that it is unoccupied. This state has no fixed number of electrons, so it is like a grand canonical ensemble and an additional requirement fixes the average number of particles $N = \sum_{\mathbf{k}} 2|\nu_{\mathbf{k}}|^2$. We start from a Hamiltonian

$$H = \sum_{\mathbf{k}\sigma} \varepsilon_{\mathbf{k}} c^{\dagger}_{\mathbf{k}\sigma} c_{\mathbf{k}\sigma} + \sum_{\mathbf{kl}} V_{\mathbf{kl}} c^{\dagger}_{\mathbf{k}\uparrow} c^{\dagger}_{-\mathbf{k}\downarrow} c_{-\mathbf{l}\downarrow} c_{\mathbf{l}\uparrow} \tag{2.54}$$

where $V_{\mathbf{kl}}$ is the effective interaction between the electrons. This equation is too hard to solve in general because the potential requires four operators. To avoid this, a mean field approximation is done by replacing a pair of operators with its average and assume this difference is small. That is done by introducing the function

$$\Delta_{\mathbf{k}} = -\sum_{\mathbf{l}} V_{\mathbf{kl}} \langle c_{-\mathbf{l}\downarrow} c_{\mathbf{l}\uparrow} \rangle \tag{2.55}$$

where $\langle A \rangle$ is the average of A with all states weighted by their thermal distribution, *i.e.* $\langle A \rangle = \sum_n \langle \psi_n | A | \psi_n \rangle \exp(-E_n/k_B T) / \sum_n \exp(-E_n/k_B T)$. With this the mean-field Hamiltonians H_M is

$$H_M = \sum_{\mathbf{k}\sigma} \varepsilon_{\mathbf{k}} c^\dagger_{\mathbf{k}\sigma} c_{\mathbf{k}\sigma} - \sum_{\mathbf{k}} \left(\Delta_{\mathbf{k}} c^\dagger_{\mathbf{k}\uparrow} c^\dagger_{-\mathbf{k}\downarrow} + \Delta^*_{\mathbf{k}} c_{-\mathbf{k}\downarrow} c_{\mathbf{k}\uparrow} - \Delta_{\mathbf{k}} b^*_{\mathbf{k}} \right) \tag{2.56}$$

where we introduced $b_{\mathbf{k}} = \langle c_{-\mathbf{k}\downarrow} c_{\mathbf{k}\uparrow} \rangle$, often called anomalous average. All the averages in ( ) are zero in the normal state because the states $-\mathbf{k}\downarrow$ and $\mathbf{k}\uparrow$ are uncorrelated. But a superconductor is expected to have these two states correlated which makes the averages non-zero.

The next step is to make a transformation to new operators ($\gamma_{\mathbf{k}0}$ and $\gamma_{\mathbf{k}1}$) defined by

$$c_{\mathbf{k}\uparrow} = u^*_{\mathbf{k}} \gamma_{\mathbf{k}0} + v_{\mathbf{k}} \gamma^\dagger_{\mathbf{k}1} \tag{2.57}$$

and

$$c^\dagger_{-\mathbf{k}\downarrow} = -v^*_{\mathbf{k}} \gamma_{\mathbf{k}0} + u_{\mathbf{k}} \gamma^\dagger_{\mathbf{k}1}. \tag{2.58}$$

The operator $\gamma_{\mathbf{k}0}$ ($\gamma_{\mathbf{k}1}$) creates the particle state $\mathbf{k}\uparrow$ ($-\mathbf{k}\downarrow$) from the pair ($\mathbf{k}\uparrow, -\mathbf{k}\downarrow$) and leaves the other part unoccupied. Those excitations are a mixture of hole and particle. Using these new operators allows to diagonalize H_M if the condition $\Delta^*_{\mathbf{k}} v_{\mathbf{k}} / u_{\mathbf{k}} = E_{\mathbf{k}} - \varepsilon_{\mathbf{k}}$ is satisfied[15] where we introduced $E_{\mathbf{k}} = (\varepsilon^2_{\mathbf{k}} + |\Delta_{\mathbf{k}}|^2)^{1/2}$. The Hamiltonian can now be written as

$$H_M = \sum_{\mathbf{k}} (\varepsilon_{\mathbf{k}} - E_{\mathbf{k}} + \Delta_{\mathbf{k}} b^*_{\mathbf{k}}) + \sum_{\mathbf{k}} E_{\mathbf{k}} (\gamma^\dagger_{\mathbf{k}0} \gamma_{\mathbf{k}0} + \gamma^\dagger_{\mathbf{k}1} \gamma_{\mathbf{k}1}). \tag{2.59}$$

The first term is a constant that represents the condensation energy at $T = 0$. The other term is that of quasi-particle excitations with an energy $E_{\mathbf{k}}$. It can be shown that the BCS ground state is the vacuum state for the $\gamma_{\mathbf{k}}$ operators. The minimum energy of the excitations is fixed by $\Delta_{\mathbf{k}}$, so this function is called the energy gap. It must be solved self-consistently.

---

[15] The u and ν can be expressed as $|\nu_{\mathbf{k}}| = 1 - |u_{\mathbf{k}}| = \frac{1}{2}\left(1 - \frac{\varepsilon_{\mathbf{k}}}{E_{\mathbf{k}}}\right)$. The overall phase of $\nu_{\mathbf{k}}$, $u_{\mathbf{k}}$ and $\Delta_{\mathbf{k}}$ are arbitrary but related because $\Delta^*_{\mathbf{k}} \nu_{\mathbf{k}} / u_{\mathbf{k}}$ is a real number. Without any loss of generality then $u_{\mathbf{k}}$ can be chosen to be real and positive then $\nu_{\mathbf{k}}$ and $\Delta_{\mathbf{k}}$ have the same phase.

The function $\Delta_{\mathbf{k}}$ was defined before but now we can write the equation in a form that can be solved implicitly:

$$\Delta_{\mathbf{k}} = -\sum_{\mathbf{l}} V_{\mathbf{kl}} b_{\mathbf{l}} = -\sum_{\mathbf{l}} V_{\mathbf{kl}} \left\langle 1 - \gamma^{\dagger}_{\mathbf{l}0}\gamma_{\mathbf{l}0} - \gamma^{\dagger}_{\mathbf{l}1}\gamma_{\mathbf{l}1} \right\rangle = -\sum_{\mathbf{l}} V_{\mathbf{kl}} \frac{\Delta_{\mathbf{l}}}{2E_{\mathbf{l}}} \tanh \frac{E_{\mathbf{l}}}{2k_B T} \tag{2.60}$$

where we used $\left\langle \gamma^{\dagger}_{\mathbf{l}n}\gamma_{\mathbf{l}n} \right\rangle = f(E_{\mathbf{k}}) = (1 + \exp(E_{\mathbf{k}}/k_B T))^{-1}$. This is the gap equation.

To go any further the potential must be defined. The usual definition is to assume a very simple potential:

$$V_{\mathbf{kl}} = \begin{cases} -V & \text{if } |\varepsilon_{\mathbf{k}}| \text{ and } |\varepsilon_{\mathbf{l}}| \leq \varepsilon_c \\ 0 & \text{otherwise} \end{cases} \tag{2.61}$$

where we introduced an energy cut off ε_c which is related to the Debye energy of the crystal for electron-phonon interaction. This potential is independent of direction and of energy (except for the cutoff) and yields an isotropic gap $\Delta_{\mathbf{k}} = \Delta$. Solving the gap equation at $T = 0$ gives

$$\Delta(0) = \frac{\varepsilon_c}{\sinh[1/N(0)V]} \approx 2\varepsilon_c \exp(-1/N(0)V) \tag{2.62}$$

where $N(0)$ is the density of states of the normal state at the Fermi surface and the last step is justified in the weak-coupling limit $N(0)V \ll 1$. Similarly, solving the gap equation for the temperature that brings Δ to 0 provides the critical temperature T_c:

$$k_B T_c = 1.13\varepsilon_c \exp(-1/N(0)V) \tag{2.63}$$

Therefore in the weak coupling BCS theory the zero temperature gap and critical temperature are related by

$$\frac{\Delta(0)}{k_B T_c} = 1.764. \tag{2.64}$$

Despite the crude approximations many conventional superconductors have approximately this value for the ratio. This is one of the results which showed that the BCS theory probably had all the necessary ingredients. For the actual temperature dependence of the gap, one needs to solve the implicit equation. The result is shown in fig. (2.3). From that graph it is seen that the gap can be considered as the order parameter for the superconducting state.

Many calculations require a knowledge of the density of states in the superconducting state $N_S(E)$. If we relate it to the normal state density at the Fermi surface $N_N(0)$, it can be shown that

$$\frac{N_S(E)}{N_N(0)} = \frac{d\varepsilon}{dE} = \begin{cases} \frac{E}{\sqrt{E^2-\Delta^2}} = \frac{E}{|\varepsilon|} & (E > \Delta) \\ 0 & (E < \Delta) \end{cases} \tag{2.65}$$

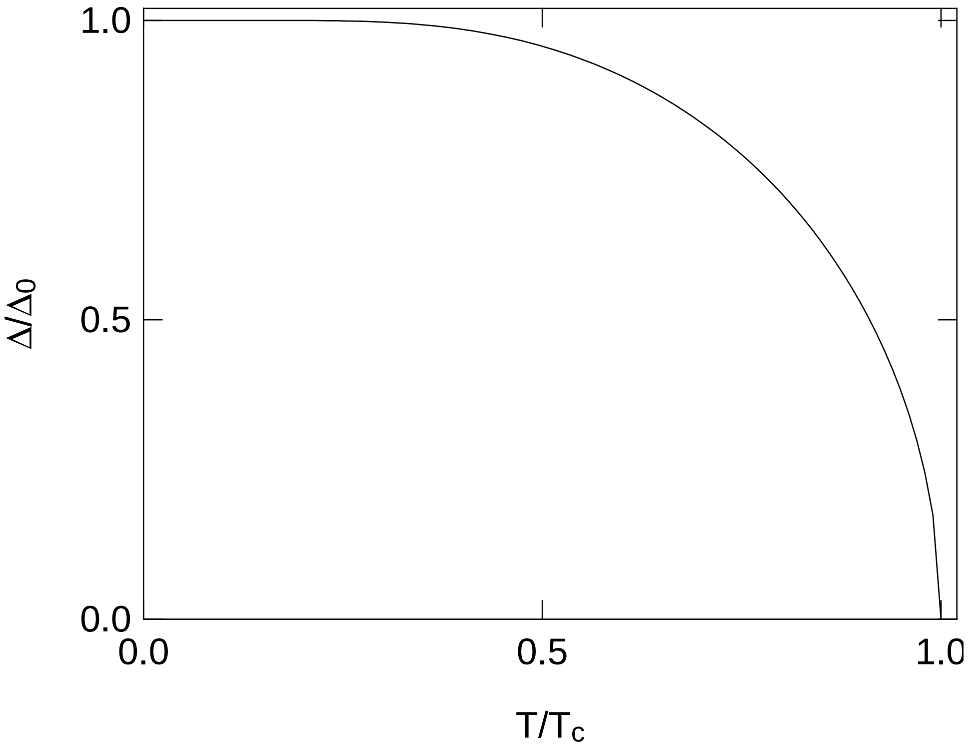

Figure 2.3: Temperature dependence of the BCS gap. For weak coupling $\Delta_0 = 1.764 k_B T_c$.

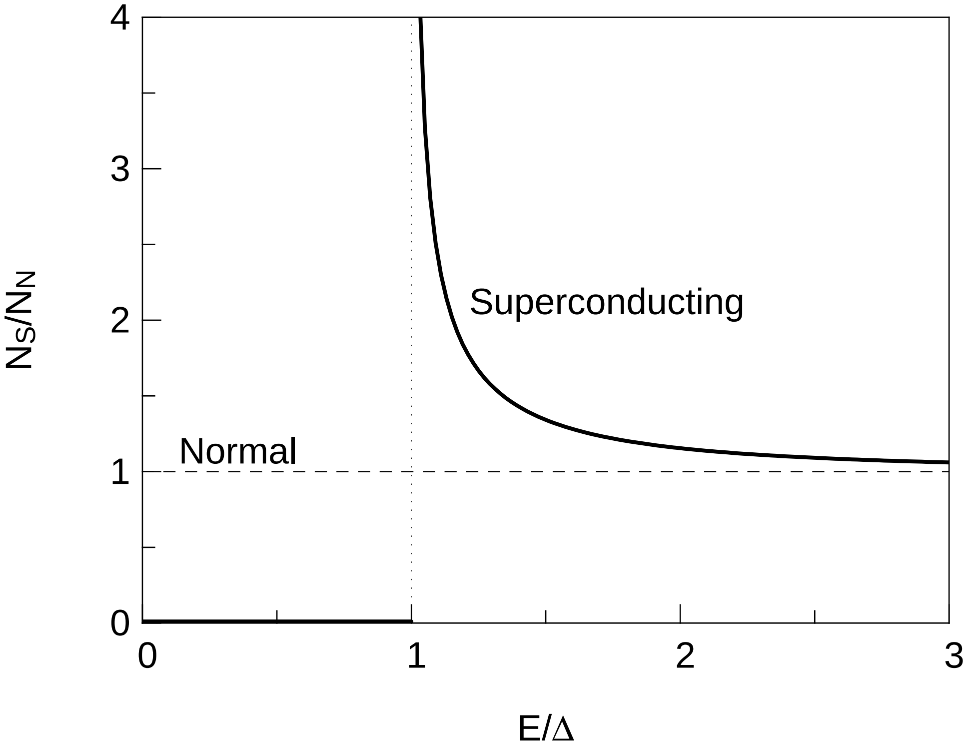

Figure 2.4: Density of states for an isotropic gap compared to the normal state. The energy is given in terms of the gap Δ. Note that there is no DOS below $E = \Delta$ in the superconducting state.

The result is valid for an isotropic gap and is shown in fig. (2.4).

A final parameter that is needed for the calculation of many transport parameters is the scattering time $\tau_S(E)$ in the superconducting state. We want to express it in terms of the normal state scattering time τ_N. We assume scattering is from non-magnetic[16] impurities so that we have elastic (energy conserving) collisions. The mean free path (ℓ) from impurities is related to the distance between impurities so we could expect it to stay the same in the superconducting state as it is in the normal state. With this assumption then

$$\ell = v_f \tau_N = v_S(E)\tau_S(E) = \tau_S(E)\frac{\partial E}{\partial \mathbf{k}} = \tau_S(E)\frac{\partial E}{\partial \varepsilon}\frac{\partial \varepsilon}{\partial \mathbf{k}} = \tau_S(E)\frac{|\varepsilon|}{E}v_f, \tag{2.66}$$

so that

$$\frac{\tau_S(E)}{\tau_N} = \frac{E}{|\varepsilon|} = \frac{E}{\sqrt{E^2-\Delta^2}}. \tag{2.67}$$

A better and more general treatment of this problem is to consider $1/\tau_S$ to be proportional to the number of states available to scatter into multiplied by the coherence factor for scattering (ε^2/E^2 in our case) [61]. So we can write $\frac{1}{\tau_S(E)} = \frac{1}{\tau_N}\frac{N_S(E)}{N_N(0)}\frac{\varepsilon^2}{E^2}$ i.e. $\tau_S(E)/\tau_N = E/\varepsilon$ which is the same result as above.

2.5.2 Attenuation in conventional superconductors

All the ingredients necessary to calculate the ultrasound attenuation in the superconducting state of a conventional superconductor have now been seen. We start by the definition of the deformation potential eqn. (2.29) and write

$$D^S_{ij} = \frac{\partial E}{\partial s_{ij}} = \frac{\varepsilon}{E}D^N_{ij} + \frac{\Delta}{E}\frac{\partial \Delta}{\partial s_{ij}} \tag{2.68}$$

where S stands for superconducting state and N for normal state and we assume the scattering is isotropic. This is obtained by assuming the condensate does not produce any attenuation and we just need to look at the quasiparticle excitations. We can drop the second term because the energy scale of the deformation potential D^N_{ij} is of the order of the Fermi energy while the gap is much smaller. Therefore we have $D^S_{ij} = D^N_{ij}\varepsilon/E$.

So the viscosity in the hydrodynamic limit is given by

$$\eta_{ijkl} = \sum_{\mathbf{k}} D^S_{ij}(\mathbf{k})\tau_S(E)D^S_{kl}(\mathbf{k})\left(\frac{-\partial f}{\partial E}\right) = \sum_{\mathbf{k}} D^N_{ij}(\mathbf{k})\tau_S(E)D^N_{kl}(\mathbf{k})\left(\frac{\varepsilon}{E}\right)^2\left(\frac{-\partial f}{\partial E}\right) \tag{2.69}$$

---

[16] Magnetic impurities are not discussed because they have a pair-breaking effect, *i.e.* they tend to destroy the superconductivity.

Now we turn the sum into an integral over surfaces of constant energy Ω so $\sum_{\mathbf{k}} = 2\int dk^3/8\pi^3 = \int dE \int d\Omega/4\pi^3\,|\partial E/dd\mathbf{k}|$, where the 2 is because of the spins, and we get

$$\eta_{ijkl} = \int dE\tau_S(E)\left(\frac{-\partial f}{\partial E}\right)\int d\Omega D^N_{ij}(\mathbf{k})D^N_{kl}(\mathbf{k})\frac{\sqrt{E^2-\Delta^2}}{E}\frac{1}{4\pi^3\hbar v_N(\mathbf{k})}. \tag{2.70}$$

where we used

$$\left|\frac{\partial E}{\partial \mathbf{k}}\right| = \frac{\partial E}{\partial \varepsilon}\left|\frac{\partial \varepsilon}{\partial \mathbf{k}}\right| = \frac{|\varepsilon|}{E}\hbar v_N(\mathbf{k}) \tag{2.71}$$

and v_N is the electron velocity in the normal state. For an isotropic system it can be approximated by v_f.[17] We also have that $\tau_S(E) = \tau_N E/\sqrt{E^2-\Delta^2}$. Now the derivative of the Fermi function ensures that only values of E within about k_BT of the Fermi surface will show in the result. Since the normal state deformation potential should be independent of energy over that range, the surface integral is independent of energy. To remove its effect we then take the ratio of normal state over superconducting state $\alpha_S/\alpha_N = \eta_S/\eta_N$ and we finally obtain

$$\frac{\alpha_S}{\alpha_N} = \frac{2\int_\Delta^\infty dE\left(\dfrac{-\partial f(E)}{\partial E}\right)}{2\int_0^\infty d\varepsilon\left(\dfrac{-\partial f(\varepsilon)}{\partial \varepsilon}\right)} = \frac{-f(\infty)+f(\Delta)}{-f(\infty)+f(0)} = 2f(\Delta) \tag{2.72}$$

(remember that $f(0) = 1/2$). This result was obtained by [62, 63].

This simple result $\alpha_S/\alpha_N = 2f(\Delta)$ was initially obtained for longitudinal waves in the quantum limit using coherence factors [7]. In fig. (2.5) we compare the curve with data measured on Nb. The standard derivation [7][60, section 3.9.1] uses the coherence factors but in the above derivation they were not needed (see also comments in [63, 64]), it can be obtained directly from the function E, so ultrasound attenuation is not a test of the coherence factors in the low frequency limit. But the fact that both limits give the same answer is a result of the self-consistency of the BCS theory.

The demonstration above works for all wave types in the hydrodynamic limit. As mentioned above it is also obtained for longitudinal modes in the quantum limit. But it does not work for transverse waves in the quantum limit. The reason is that the coupling goes through an electromagnetic wave which is killed in the superconducting state because of the Meissner effect. The transverse electric field is zeroed because of the

---

[17] In an isotropic system the surface integral of eqn. (2.70) can be written as $\int \frac{d\Omega}{\hbar v_f}(\cdot) = N^N(0)\int d\Omega(\cdot)/\int d\Omega$, *i.e.* an average of $(\cdot)$ over the surface Ω, where $N^N(0) = \Omega/\pi^2 v_f$ (Ω is the k-space area) is the normal state density of states at the Fermi surface obtained from $N^N(E) = \int d\Omega/4\pi^3|v_N(E)|$.

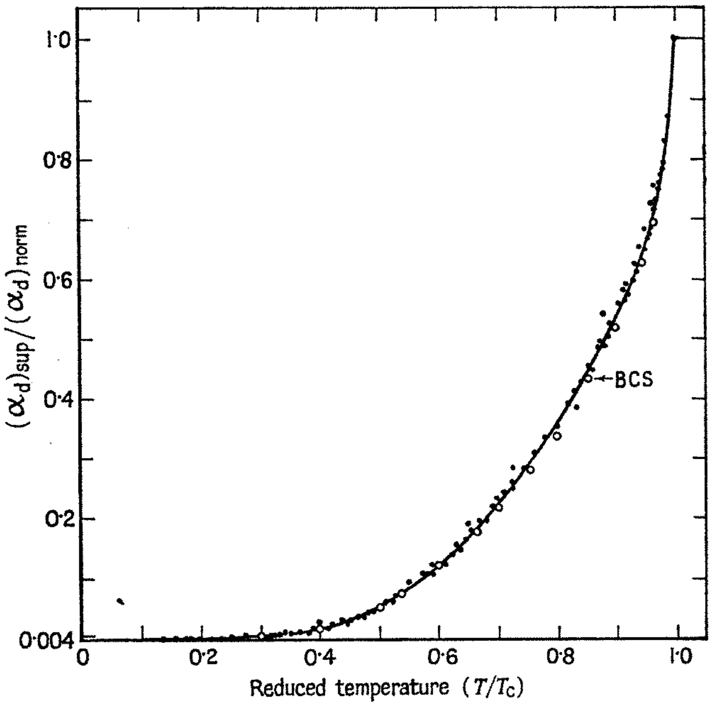

Figure 2.5: Ultrasound attenuation in Nb ($T_c = 9.16$ K) compared to BCS result with $2\Delta_0 = 3.63k_BT_c$ (from [42]).

supercurrent response. This produces a sudden decrease of attenuation when crossing the transition. This drop gets bigger as the frequency gets larger. The drop $\Delta\alpha_S$ at T_c is related to the normal state attenuation α_N by $\Delta\alpha_S/\alpha_N = 1 - g$, where the function g was introduced before and gives $1 - g = 0.14$ for $q\ell = 1$. What is left after the drop does follow the BCS curve but is smaller (proportional to g).

So in general the attenuation always follows the above equation except that for transverse waves in the quantum limit there is an additional jump at T_c which depends on the frequency. The longitudinal electrical contribution that can be present in longitudinal waves does not provide attenuation at high frequency and is there to keep local charge neutrality, i.e. adjust the local electron density. Around $q\ell \sim 1$ it enters the attenuation but its effect is not changed by the presence of superconductivity and so there are no steps for longitudinal modes [63]. What happens is that the supercurrent can cancel the ionic current and remove that part of the electric field but the part that adjusts the density for charge neutrality cannot be canceled by supercurrents. And this is the only part modifying the attenuation for longitudinal waves.

In a superconductor there is an additional energy that comes into play, the gap. This energy is much greater than the frequencies used for the hydrodynamic regime but it is possible to reach it. When the phonon energy reaches the gap energy then a new phenomenon should come into play. The phonons are able to break Cooper pairs and this provides a new source of attenuation. As the energy of the phonons keeps increasing then the effect of the superconducting state disappears since the energy dispersion of the electrons is the same [65], *i.e.* when $\hbar\omega > \Delta$.

2.5.3 Unconventional superconductivity

The most frequent definition of unconventional superconductivity is that additional symmetries are broken in the superconducting state. The superconductivity always breaks gauge symmetry. That is the only broken symmetry for a conventional superconductor. Unconventional superconductors will usually break a crystal symmetry.

The theory of unconventional superconductors [66] is similar to what was described in section 2.5.1. The main difference is that the potential is expanded in a set of basis functions for the irreducible representations of the group. For an isotropic Fermi liquid this means the basis function can be the spherical harmonic functions Y_{lm} where l is the total angular momentum and goes from 0 and up while m is the z component of the angular momentum and ranges from $-l$ to l. Similarly to what is used in atomic physics, the various l are given letter names as s, p, d, f, $\ldots$, for $l = 0$, 1, 2 and 3, $\ldots$, respectively. For a crystal of a particular symmetry group the basis functions will be different from these spherical harmonics but often the same language of s, p, d $\ldots$ is used.

The other modification to the above description is to relax the restriction that electrons couple in a singlet state. Therefore electrons are allowed to couple in a triplet state. Since electrons are fermions the overall electronic wavefunction must be antisymmetric (odd) and this limits the possible combinations of orbital and spin wavefunctions. For an isotropic system and a spin-singlet state, only the even l states are allowed (i.e. $l = 0$, 2, 4 $\ldots$), while for spin triplet only the odd ones are allowed (i.e. $l = 1$, 3, 5 $\ldots$).

The separation between spin triplet and singlet is only possible if the electron spin is a valid quantum number. This is true as long as spin-orbit coupling is minimal. When it is strong, the separation is not possible in terms of the electron spin wavefunction but there is usually a possible separation in terms of pseudo-spin.

The gap function is expanded in the same basis functions. For spin-triplet the gap is usually written has a vector $\mathbf{d}$. For weak spin-orbit coupling the components of $\mathbf{d}$ represent pairs with the no component of the spin angular momentum along that direction. For example d_z is the pairing for electron having total spin angular momentum $S = 1$ and a z component of $S_z = 0$.

As long as the gap is unitary ($d_i d_j^* = \delta_{ij}$) then the energy of the quasiparticles is given by

$$E = \sqrt{\varepsilon^2 + |\mathbf{d}|^2} \tag{2.73}$$

which is the same as for the conventional superconductor except that Δ can have some angular dependence and can also be a vector ($\mathbf{d}$). A non-unitary gap complicates the inversion and includes (weak) spin polarization effects [67, 68].

The basis functions can be part of a multidimensional representation. Then instead of $\mathbf{d}$ we have $\eta_1\mathbf{d}_1 + \eta_2\mathbf{d}_2$ for a two dimensional order parameter. The two order parameters are η_1 and η_2 and they can lead to a phase diagram with multiple superconducting phases. This can also lead to a broken time-reversal symmetry when the order parameters have different complex phase. This manifest itself as an internal magnetic field that appears near defects and surfaces in the superconductor.

With a lower symmetry, the gap function can be forced to be zero in some particular directions. These zeroes are nodes and in this case are imposed by symmetry. It is possible to have nodes in other places and they will be called accidental nodes. The distinction is important because the symmetry imposed nodes are fixed and cannot move around while the accidental ones can adjust their position in response to some control variable.

For example, for spin singlet we show four different gap fig. (2.6). The first one is an isotropic gap, called the s-wave gap. The last one breaks the symmetry of the crystal by having lobes with different polarity. It is the d-wave gap. The other two are called extended s-wave and they don't break any additional symmetries but they possess nodes. According to the definition at the beginning of this section they are then conventional superconductors.

We have given the standard definition of unconventional superconductor but the term can be used more generally as "superconductors that are not understood". This can come from breaking any of the assumptions of the simple theory of BCS superconductor. It could be because the interaction between electrons is not due to electron-phonon but from some other source (spin fluctuation, electron-electron interactions, . . .). It can be because there are nodes in the gap. It can be because the coupling is spin triplet, that

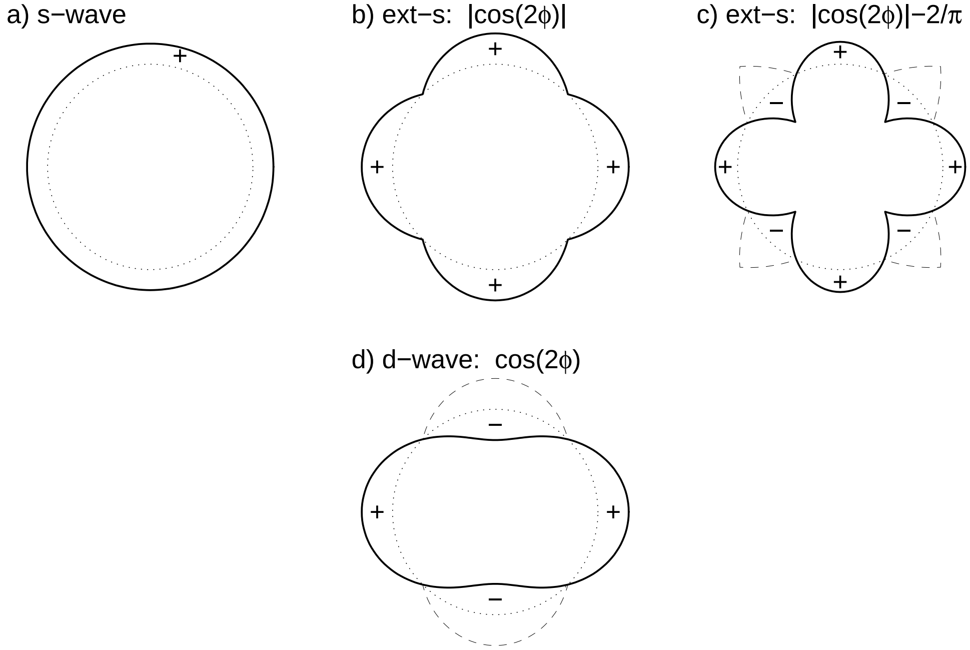

Figure 2.6: Sketch of a) s-wave, two extended s-wave in b) and c), and of a d-wave gap in d). The Fermi surface is shown has the dotted line while the gap is shown has the displacement away from the surface and is shown in the solid line. The dash line is the result of taking the absolute value of the gap; note the similitude between b) and d). The $+/-$ represent the gap polarity.

additional symmetries are broken. It could also be because the phenomenon cannot be described by the current BCS framework.

What is often needed is the density of states and the relaxation time. But unlike for conventional superconductors many results are possible here and the density of states and the amplitude of the gap can be affected by impurities even if they are not magnetic. This can be understood because impurities tend to remove any anisotropy. This will force a gap where the nodes are fixed by symmetry to decrease in amplitude until the superconducting state is killed passed a critical impurity scattering rate. For an isotropic state (like fig. (2.6a)) there is no anisotropy to be removed. For an extended s-wave that just touches (like in b)), the nodes disappear as soon as some impurities are added. While the one in c) will show an intermediate behavior. As the impurities are added, the nodes will move around until all the anisotropy is removed and a constant gap is left. In that case there is a possible state where the average gap turns out to be zero, that state will behave under impurity doping similarly to the d-wave gap but it is a very specific case.

The presence of nodes will produce power laws in the density of states in general.

These power laws influence most measured quantities which will also show power law instead of exponential behavior. Often the node is a line which then produces a linear density of states, $N(E) \sim E$ at low energy. On the other hand a point node with linear dispersion produces a square dependence of the density of states, while a point node with quadratic dispersion also produces a linear density of states.

This pure power law behavior is expected only in samples without impurities. The presence of impurities will modify that behavior at low energy. The scattering strength from the impurities is described in terms of the phase shift δ of the scatterer. A small strength $\delta \ll 1$ is called the Born limit and the large strength $\delta = \pi/2$ is called resonant impurity scattering. These two have quite a different effect on the density of states and the scattering time. The effect of the impurity is to produce a constant density below an energy scale γ called the impurity bandwidth. For Born scattering $\gamma = 4\Delta_0 \exp(-\pi\Delta_0/2\Gamma_N)$, while for unitary scattering it is $\gamma \sim \sqrt{\Gamma_N \Delta_0}$ up to logarithmic corrections [69].[18] We have introduced Γ_N as the normal state scattering rate and these results were derived for a $d_{x^2-y^2}$ state which has line nodes, and assuming a small impurity concentration.[19] The residual density of states at zero energy is $N_N(0) = \gamma/\Gamma_N$ in the Born limit and $N_N(0) = \Gamma_N \gamma \sim \sqrt{\Gamma_N/\Delta_0}$ in the unitary limit. Obviously the impurity bandwidth and the residual density of states are small in the case of Born scattering but large for unitary scattering. So the impurity bandwidth is mostly attainable when the scattering is strong. To obtain the density of states below γ and the change in T_c because of impurities the problem (gap) must be solved self-consistently including the effect of the impurity. That is done using Green's function techniques [66, 61, 70].

The basic idea is that the impurities will reduce the anisotropy of the gap. Then if the gap still has nodes the point of crossing is widen from a point to a finite area so that you obtain a certain fraction of states similar to the normal state (since $\Delta = 0$ for them). The resonant impurity scattering is much more efficient at reducing the gap and making the nodes wider than Born scattering.

As long as the impurities do not affect T_c too much, the density of state is only modified below $\sim \gamma$. Above that self-consistency is not required and the result is independent of impurity density and scattering phase shift. The scattering time also needs to be

---

[18] In the unitary limit, the full result under the current approximation is $(\gamma/\Delta_0)^2 = (\pi\Gamma_N)/[2\Delta_0 \ln(4\Delta_0/\gamma)]$.

[19] The small impurity concentration requirement can be given as $\Gamma_N(1 + c^2) \ll \Delta_0$ where c depends on the phase shift, $c = \cot(\delta)$.

extracted from the self-consistent calculations below γ but above that range, and contrary to the density of states, the scattering time is quite sensitive to the impurity phase shift. On a state with nodes, Born scattering produces lifetimes that tend to increase (diverge) at low energy while unitary scattering produces lifetimes that get smaller. Transport measurement depend on the density of states and scattering time among other variables. Therefore even without considering self-consistent effect, and for all $T < T_c$, a gap with nodes will have quite a range of behavior for transport measurements depending on the impurity phase shift [71]. For unitary scattering the curves mostly decrease towards zero as the temperature is lowered but for Born scattering they often stay around the normal state value.[20]

2.5.4 Angular dependence of the attenuation

As described in the previous section, an important difference with unconventional superconductors is the non-trivial angular dependence of the gap function. Ultrasound attenuation is a tool to look at this dependence. It is easy to see that in the quantum limit, because of the energy conservation, only a line on the Fermi surface perpendicular to the direction of propagation produces the attenuation. Therefore by propagating longitudinal waves at different angles in a sample at very high frequency and fitting the curve to the BCS expression to extract the gap amplitude, the angular dependence can be extracted. This was done in Sn for example and the result is shown in fig. (2.7). The gap extracted is somewhat of an average over the line on the Fermi surface.

It is not always possible to use those high frequencies. Then we are limited to the hydrodynamic regime were the angular dependence is not as strong. For example, in the plane of a tetragonal material we only have three independent tensor elements for the viscosity. Any measurement will be a combination of these. This is not enough to extract a full angular dependence like in the quantum limit but can give some very useful information.

For that we rewrite the attenuation we extracted before without assuming any particular form for the scattering time or the angular dependence of the gap. It is easy to

---

[20] With the same approximation as above, for a $d_{x^2-y^2}$ gap, the energy dependence (ω) of the scattering time τ is given by $\tau^{-1}(\omega) = (1/\omega)(\pi^2\Gamma_N\Delta_0)/[2\ln^2(4\Delta_0/\omega)]$ in the unitary limit and by $\tau^{-1} = \omega(4\Gamma_N/\pi\Delta_0)\ln(4\Delta_0/\omega)$ in the Born limit. This is valid for $\gamma < \omega \ll \Delta_0$. Note that the low energy density of states of a $d_{x^2-y^2}$ (above γ) is $N \sim \omega$ so for the unitary scattering $N\tau \sim \omega^2$ while for Born scattering it is $N\tau \sim 1$.

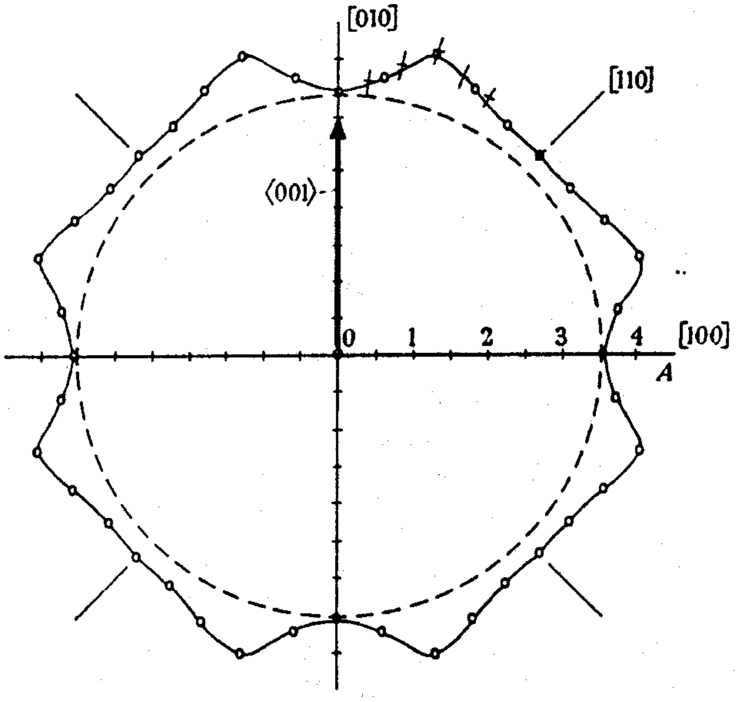

Figure 2.7: Anisotropy of the gap in Sn from ultrasound attenuation measured in the quantum limit (after [72]). The plot shows $2\Delta(0)/k_BT_c$.

get

$$\frac{\alpha_S}{\alpha_N} = \frac{\displaystyle\int dE\tau_S(E)\left(\frac{-\partial f}{\partial E}\right)\int \frac{d\Omega}{v_N(\mathbf{k})}\frac{\sqrt{E^2-|\Delta|^2}}{E}D^N_{ij}(\mathbf{k})D^N_{kl}(\mathbf{k})}{\displaystyle\int d\varepsilon\tau_N\left(\frac{-\partial f}{\partial \varepsilon}\right)\int \frac{d\Omega}{v_N(\mathbf{k})}D^N_{ij}(\mathbf{k})D^N_{kl}(\mathbf{k})}. \tag{2.74}$$

Simple theories use this formula with the deformation potential replaced by the free electron one: $D_{ij} = mv_f^2\frac{1}{d}\delta_{ij} - mv_iv_j$ where d stands for the dimensions of the electron gas [73, 74]. The function $D_{ij}D_{kl}$ has some directions where it goes to zero. On the other hand, when an unconventional superconductor has nodes, the low temperature behavior is controlled by the gap region around the node. Therefore in general those nodes will control the attenuation and produce small power laws because many quasiparticles are available to scatter the sound. But if the zero of the deformation potential occurs at the same place as the node in the gap, then they can't control the attenuation as well. In this case the node are said to be "inactive", while in the previous case they were "active".

For example the free electron deformation potential for transverse waves has zeroes in the direction of propagation and along the direction of polarization. Therefore the zeroes are at 90° from each other. For a gap with line nodes separated by 90° it is then

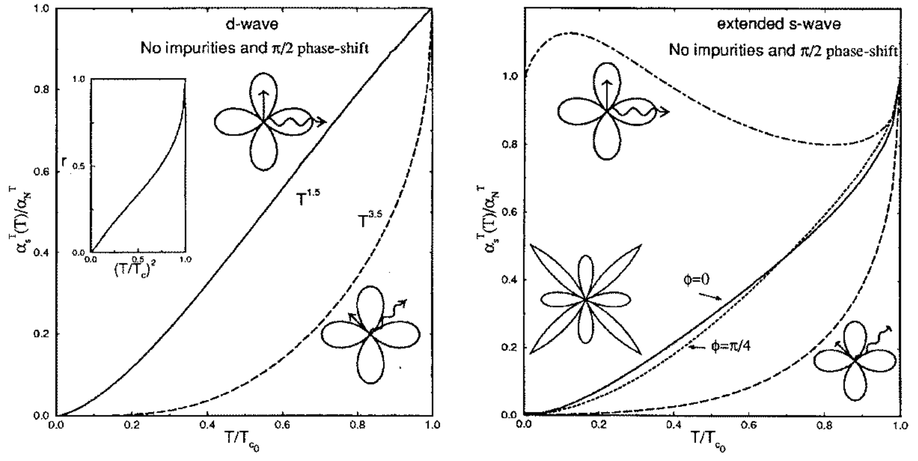

Figure 2.8: Theoretical angular dependence of ultrasound attenuation of transverse waves for a d-wave gap (on the left) and for extended s-waves, $|\cos(2\phi)| - A$, (on the right) from [73]. For the extended s-wave, the gap with 4 nodes has $A = 0$ and the one with 8 nodes has $A = \pi/2$. The diagram show the direction of the sound propagation and polarization with respect to the nodes. The inset shows the ratio of the 2 modes for the d-wave (note the power of 2 difference).

possible to "activate" or "inactivate" them by a rotation of the propagation by 45°. The anisotropy in power laws this produces is usually T^2, i.e. the "inactive" nodes have a power law which is T^2 stronger than the "active" one. This is sketched in fig. (2.8). If the nodes in the gap are not separated by 90° (like for a general extended s-wave) all the nodes cannot be simultaneously made "inactive" and the angular anisotropy of the attenuation will be weak.

The above equation is not accurate for longitudinal waves. In that case an additional terms shows up which is related to vertex corrections of microscopic theories [75]. In the case of transverse waves, after angular integration, this gives zero so it applies only to longitudinal waves. For an even parity orbital state and if the scattering is neither Born nor unitary it is possible that yet another term needs to be added to the formula [71]. Both of these terms come from the interaction between the gap anisotropy, the scattering time and the shift $\psi_{\mathbf{k}}$ of the distribution function. In a way it makes $(\psi)_{\text{avg}}$ non-zero which forces the inclusion of off-diagonal terms ($\mathbf{k} \neq \mathbf{k}'$) into the $C_{\mathbf{k}\mathbf{k}'}$ scattering operator (see eqn. (2.34)).

Finally, like many other measurements, the attenuation will depend on the type of impurity scattering (Born or unitary). When nodes are present the shape of the curve is strongly dependent on the phase shift of the scattering. There might not even be any temperature range were power laws are observable (especially for Born scattering).

Therefore ultrasound attenuation in the hydrodynamic regime, while not being the best regime to measure the angular dependence of the gap, is quite sensitive to some particular gap geometries. So it can be a good tool if some of those geometries are expected in a material. We should note that the description above was based on the free electron deformation potential. This deformation potential does not necessarily apply. But what is required is knowledge of the position of the zeros in the potential and some of those zeros are required by symmetry [76]. With some or all of the zeros position of the potential known then a similar discussion as above (active/inactive) can then be done.

2.5.5 Sound velocity near T_c

The elastic constants, and therefore the sound velocity, are sensitive to a phase transition. A structural transition obviously affects the constants but the superconducting state also produces a change.

This is because the elastic constants are obtained from the free energy by a second derivative, as for specific heat. Therefore on crossing the superconducting transition it is possible to obtain a discontinuity in the elastic constants and a change in the slope of the temperature dependence [77, section 11.6] [78]. But these changes are usually very small, on the order of parts per million (ppm).

The step is given by

$$\Delta C_{ij} = C_{ij}^S - C_{ij}^N = -\frac{\Delta C_e}{T_c}\frac{\partial T_c}{\partial s_i}\frac{\partial T_c}{\partial s_j} \tag{2.75}$$

where ΔC_e is the specific heat jump at the transition. So the jump depends on the first derivative of the critical temperature with the strain. For a single component order parameter there is no step for the pure shear elastic modulus because $\partial T_c/\partial s_i = 0$ for $i = 4, 5, 6$. This is a consequence of expanding the free energy linearly in the s_i, the change in energy should be the same irrespective of the sign of the shear strain and this forces it to be zero. For a multi-component order parameter, this is no-longer forced [79]. The change in slope is given by

$$\left.\frac{\partial C_{ij}^S}{\partial T}\right|_{T_c} - \left.\frac{\partial C_{ij}^N}{\partial T}\right|_{T_c} \approx \frac{\Delta C_e}{T_c}\frac{\partial^2 T_c}{\partial s_i s_j} \tag{2.76}$$

Hence it depends on the second derivative of the critical temperature with the strain.

This behavior of the elastic constants can be used to map out the superconducting transition, *e.g.* as a function of magnetic field or pressure. This was done in UPt_3 where multiple superconducting phases exist and allowed a mapping of the transitions over the entire phase diagram [80, 79, 81, 82, 83].

3

EXPERIMENTAL TECHNIQUE AND ANALYSIS

In this chapter we describe the experimental technique and the data analysis procedure. We then describe a test of the system using tantalum, a conventional superconductor.

The experimental setup is made up of two parts. The cryomagnetic system and the ultrasound spectrometer. For a recent review of the experimental technique in ultrasound attenuation, see [84]. This book also provides techniques for accurate sound velocity measurements.

3.1 Cryomagnetic systems

In order to reach the low temperatures needed for the experiments we used two different cryomagnetic systems. The first one is an ^{3}He system which was used for initial testing because of its quick turn around time (a couple of hours). But since it did not reach low enough temperatures, most of the final experiments were in a dilution refrigerator which has a much longer turn around time (more than a day). For low temperature techniques (cooling, materials, etc), see [85, 86, 87, 88].

3.1.1 ^{3}He system

Most of the preliminary tests and some of the results were obtain using a Heliox system from Oxford Instruments which is a ^{3}He cryostat. This system is used in a dewar filled with liquid helium (^{4}He) and surrounded by a liquid nitrogen jacket to lower the boil off of liquid helium. The dewar also contains a superconducting magnet of NbTi and Nb_3Sn of 52 mm of inner bore which can reach 16 T at 4.2 K, the boiling point of liquid helium at atmospheric pressure. When the helium in the bath is cooled to its lambda transition (see below), the magnet can be used up to 18 T (which requires 115 A of current supplied by the PS 120 power supply). During an experiment, the dewar requires daily transfers of liquid helium (about 15 liters) and of liquid nitrogen.

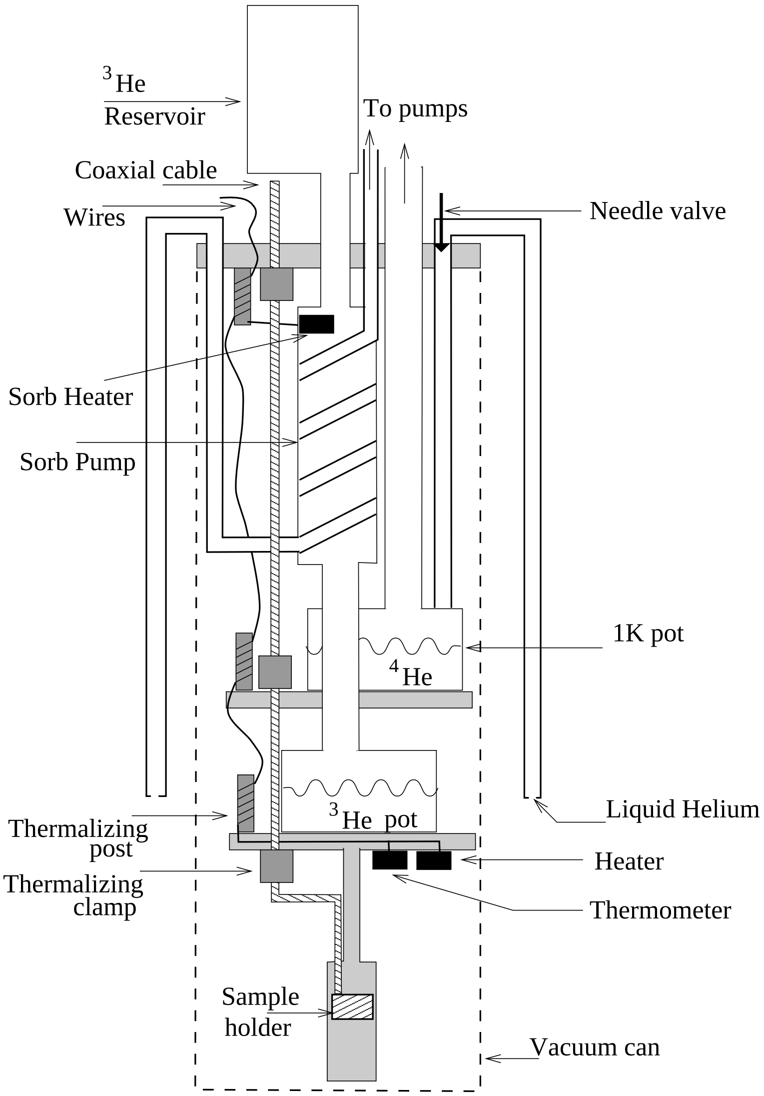

Figure 3.1: Schematic of the ^{3}He system insert.

The cryostat cooling is obtained by a closed system where the ^{3}He gas is successively condensed into a pot and then pumped (see fig. (3.1)). The pumping reduces the pressure which controls the temperature of the liquid/gas system. Therefore by controlling the pumping speed the temperature of the ^{3}He pot is adjusted from as low as 300 mK to about 1.6 K. Above that the temperature is changed by applying heat from a resistive heater directly to the pot and sample stage. The 1.6 K limit is set by the temperature of a continuous fill ^{4}He pot which is used to condense the ^{3}He.[1] This other pot siphons some regular helium from the main bath (dewar) and an external pump is used to reduce the pressure and cool it. But because this is regular ^{4}He it reaches a temperature of

---

[1] The boiling point of ^{3}He at atmospheric pressure is 3.2 K.

about 1.4–2 K (depending on the pumping speed, and flow of He from the dewar). The different temperature reached with the two isotopes is a result of their different weight and statistics. The ^{3}He atom is a fermion so that there is only 1 atom per state because of the Pauli principle. So it has a Fermi surface, and a Fermi energy which controls its behavior. Because of this, models such as the Landau Fermi liquid theory (used for electron gas) also applies to ^{3}He. One difference is that the atoms are not charged so the concept of charge flow (conductivity) and superconductivity don't apply. This is replaced by particle flow and superfluidity. The superfluid transition in ^{3}He occurs below 3 mK. This is to be contrasted with ^{4}He which is a boson. Therefore any number of atoms can be in a given state. In particular, there can be a microscopic number of atoms in the ground state. That is referred as a Bose-Einstein condensation and also produces a superfluid. This transition occurs at 2.2 K and is often called the lambda transition (because of the shape of the heat capacity anomaly).

This system is a closed circuit because ^{3}He is very expensive and must not be lost. Having a closed system also makes the system easier to use. The pump for the ^{3}He is a sorb pump which is either cooled by flowing liquid ^{4}He from the main bath (dewar), which makes it pump and cool the ^{3}He, or it is heated up by a resistive heater to regenerate and expulse the absorbed ^{3}He so that it can be condensed in the pot. A single cycle could last up to 20 hours but because of the wiring and other sources of heat load it lasts around 4 hours. To start a cycle the ^{3}He must be recondensed in the pot. This process is automated by the computer and the base temperature can be reached in about 20 min. We usually opted for fitting a full temperature sweep in a single cycle by adjusting the density of points (temperature step) and the averaging (the time per point, see section 3.2.3) instead of breaking it in multiple segments. This usually provided a high enough density of points, especially considering most of the sweeps in this system were for exploration. At higher temperature (above 1.6 K), the system is in continuous mode and it no longer imposes time restrictions.

Below the ^{3}He pot, which is the coldest point, there is a tail of copper that is attached. Samples are placed at the other end where they are in the middle of the magnetic field of the superconducting magnet. The field is in the direction of the tail. Copper is used because it is a very good thermal conductor so that the sample is effectively at the same temperature as the pot. The diameter available to mount a sample is 35 mm.

Two thermometers are used for temperature control. They are both situated on the ^{3}He pot away from the maximum of the magnetic field. At low temperature (below

1.7 K) we use the 470 Ω Speer resistor which only has a rough calibration. For higher temperatures we use the 500 Ω carbon glass resistor (CGR) which was calibrated by Oxford Instruments. Both of these thermometers have a small magnetoresistance so they don't produce large errors when a magnetic field is applied. These thermometers are measured by an Oxford Instruments Intelligent Temperature Controller (ITC 503) which adjusts the temperature by heating the sorb pump or the ^{3}He pot depending on the temperature range.

The temperature obtained from those thermometers is enough for temperature control but is insufficient otherwise. This is because at low temperature the thermometer is not calibrated. Also around 2 K, where the calibrated CGR is used, it is very noisy and shows some sensitivity to the power dissipated in the heater (200 Ω wire wound resistor) which is physically very close. Above 4 K this is no longer a problem and the CGR can be used but most of our experiments are done below 2 K. Therefore we calibrated, from 0.3 K to 4 K, a couple of 1 kΩ RuO_2 chip resistors (Phillips SMD precision ship resistor model RC12H) against a calibrated RuO_2 from Oxford Instruments. These thermometers were then installed close to the attenuation mount. Two wires were attached to both ends of the resistor and we performed standard 4 probe resistance measurements using a Linear Research LR-700 AC resistance bridge. The bridge was fitted with an 8 channel multiplexer which also allowed us to measure other resistances at the same time, for example other thermometers or some resistivity samples. The measured resistance of the RuO_2 thermometers is then converted to temperature using our calibration and are used as the temperature scale for the attenuation measurements.

At low temperature (below 1.6 K) and high temperature (above 2 K) the temperature control was good and automatic. In between, the system required some adjustments which could not be automated. Therefore the temperature control in that region was often defective which produced some holes in the temperature sweeps.

3.1.2 Dilution refrigerator

The other system is an Oxford Instruments Kelvinox 300 ^{3}He–^{4}He dilution refrigerator.[2] This is a continuous system that can reach 10 mK and stay there for days or weeks. It fits in a dewar similar to that of the ^{3}He system described in the previous system. The dewar is also fitted with a superconducting magnet (bore diameter of 52 mm) but this

---

[2] The Kelvinox 300 has a minimum cooling power of 250 μW at 100 mK.

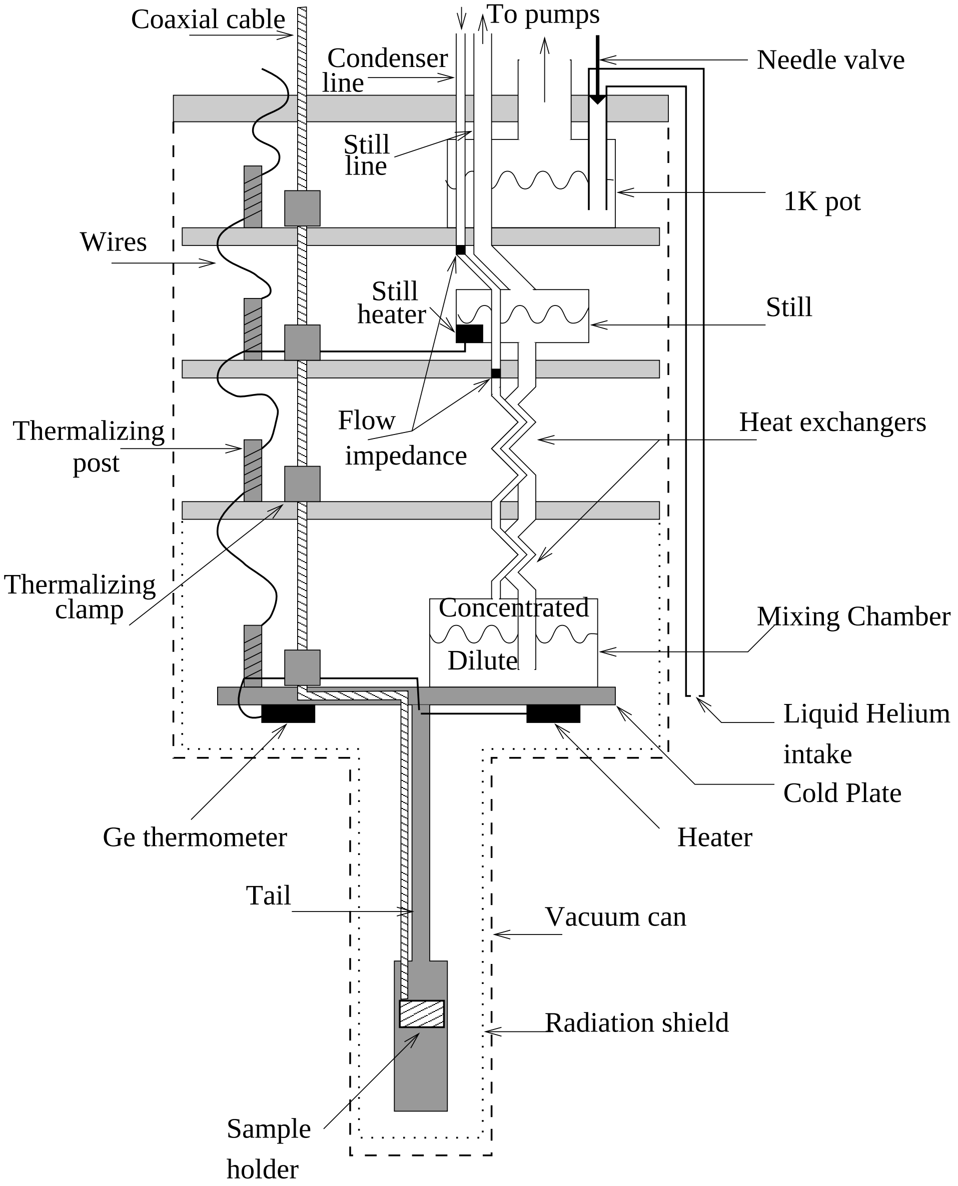

Figure 3.2: Schematic of the dilution refrigerator insert.

one reaches 13 T at 4.2 K and 15 T at 2.2 K (which is 113 A supplied by a PS-120 power supply). In addition it produces a compensated zone where the field is maintained at 0 T. That zone is were the main thermometer, a calibrated Lakeshore Ge sensor (GR-200A-30), is positioned. This thermometer is very sensitive to magnetic field, but being in the compensated zone means we still obtain the proper temperature irrespective of the intensity of the field at the sample. The dewar requires daily transfer of liquid helium (about 20 liters) and of liquid nitrogen.

The cooling is provided by mixing ^{3}He into ^{4}He inside the dilution unit (see fig. (3.2)).

At low temperature, because of quantum effects and their fermion and boson statistics, the mixture separates into an almost pure ^{3}He phase which floats onto a dilute phase (containing about 6% of ^{3}He). By removing ^{3}He atoms from the dilute phase, it forces a net flow of atoms in the dense phase to cross the phase boundary into the dilute phase to keep the mixture in equilibrium. This cools the mixture in a similar way as pumping on the gas above a liquid lowers its temperature. The removal of the ^{3}He from the dilute phase is obtained by pumping on the still which is heated in order to increase the evaporation rate. At the right temperature, about 0.7 K, mostly ^{3}He will evaporate and this gas is pumped away. Contrary to the ^{3}He system described above, here the system is continuous. The gas circulates in external sealed pumps. It is then returned, through a condenser line to the mixing chamber where the phase boundary is situated and were the cooling occurs. Since the gas coming from outside is warm it is liquefied and precooled by a ^{4}He pot (around 1.5 K, similarly to the Heliox). But this is still very hot, while the gas coming out the other end is relatively cold. If both were connected to the mixing chamber it would be inefficient and this is avoided by having good heat exchange between the liquid going to and from the mixing chamber. At low temperature, thermal contact between a liquid and a solid is not very good because of the Kapitza resistance. It is the result of impedance mismatch between the phonons in the solid and liquid. This is a problem both in the heat exchanger and the mixing chamber and is corrected by using sintered metal powders which have the purpose of increasing the area of contact.

This is a more complicated system than the previous one. Many pumps are needed and the ones through which the mixture travels need to be sealed. This is for two reasons. First the mixture is expensive since it contains ^{3}He and its volume is adjusted for the particular geometry of the system. The second reason is that in order to control the flow of the mixture in the system, which controls the cooling power, there is an impedance in the condenser line. This impedance can easily be plugged by any solid impurity in the liquid. This impurity could come from solid air that leaks into the close circuit and is another good reason why the pump needs to be sealed. Of course there is additional cold traps along the closed circuit which are designed to remove such impurities.

The mixing chamber is attached to a copper plate. Copper is used here again because it is a good thermal conductor and therefore stays at a uniform temperature. This plate is where the heater and Ge thermometer are mounted and is in the middle of the field compensation zone. Below this plate is attached a copper tail. The other end of this tail is in the middle of the magnetic field and is where the samples are mounted. The available diameter to mount a sample is 30 mm, which is slightly smaller than for the ^{3}He system. Therefore a mount designed for the dilution refrigerator, fits in both systems.

The temperature control uses a LR-700 resistance bridge to measure the Ge sensor which ranges from 90 kΩ at 40 mK to 23 Ω at 4.2 K. The signal is used by a TS-530 temperature controller from RV-electronikka to supply heat to the mixing chamber plate. The thermometer calibration is valid from 40 mK up to 5 K which sets the range of temperature used in experiments (the refrigerator can get colder). Below 1 K the temperature control is stable and automatic. Temperature sweeps in this range usually last from 8–12 hours in order to provide a large enough density of points and it allows two sweeps per day. The system is not designed to be used above 1 K but for our experiments we needed sweeps at least up to 1.5 K and preferably up to 4 K. In this regime the unit requires many manual adjustments as the temperature is changed and ends up with all the mixture out of the system. To restart another sweep it must then be recondensed. All these steps cannot be automated and are time consuming so it is not done for all the sweeps. Most will be up to 1 K only. A small fraction will cover the full temperature range.

At low temperature, the system can be affected by radio frequency signals. These can warm up sensors such as thermometers and samples and this would prevent making measurement in that low temperature regime. In order to avoid those difficulties the dewar and the measuring electronics are enclosed in a shielded room (a Faraday cage) that attenuates those interfering signals.[3] The computer, which is outside the cage, controlling those devices with a GPIB interface is electrically decoupled by the use of an optical fiber GPIB extender. The electronic devices present in the cage are not as noisy as a computer but they also produce some noise so we have extra filters on the top of refrigerator on most of the wiring (excluding coax for ultrasound attenuation).

3.1.3 Wiring

The measurements all rely on using electrical signals. Therefore lots of wires are required in the cryostat between room temperature and the sample. For all the resistance measurement and heaters which all deal with DC or very low frequency (<100 Hz) signals, we used twisted pairs. The twisting is to remove pick up of EM field. The material for

---

[3] The shielded room was essential for measurements when the lab was situated at McGill University in Montréal since we were on a fourth floor and very close to a strong emitting antenna. At the University of Toronto, the lab is in the basement and further away from any antenna so the room is not as necessary but it still provides a nice controlled environment.

the wire needs to be chosen carefully. Copper can be used when both ends of the wire are at the same temperature, like along the tail. Otherwise the large thermal conductivity of copper will cause large heat leaks and force the use of very thin wires. In this case, wires such as phosphor-bronze or manganin are more thermally and electrically resistive, so they limit heat leaks. When possible, superconducting wires provide the best result since they have no electrical resistance but a large thermal resistance. But they can only be use in a section which is always below the critical temperature (about 10 K for the usual NbTi wires) so they are used only on a section of the dilution refrigerator. It is also important to thermalized the wires at many different stages in the system. This is done by coiling the wires around a copper bobbin which is screwed to a stage. Thermalizing is necessary so that the thermal load from warmer stages is not all dumped at the lowest stage.

For the ultrasound measurement what is needed is coaxial cables because the frequencies are in the 100 MHz range. Again the material needs to be chosen carefully. An additional restriction is that not all coaxial cables work at low temperature. Some can fail because of thermal contraction or their impedance can change as a function of temperature. We used both semi-rigid and flexible coaxial cables from Lakeshore which have an impedance of 50 Ω and are known to work at low temperature. The simplest setup would be to use a single type of wire from top to bottom but this is not flexible enough. The cryomagnetic systems are not used only for the ultrasound measurement and the configuration must be changeable. Therefore we used a combination of the semi-rigid and flexible wires. The connection between the segments is done with the help of Microdot connectors. A problem is attaching the cables to the connectors. This cannot be done easily without introducing some impedance mismatch. This will produce some reflection and therefore attenuate the signal and depends on the cable length and the frequency. The cable also produces attenuation because of its resistance.

To have as much amplitude as possible we use the flexible coaxial cable (which has a small resistance) between room temperature and the first stage of both setup and along the tails. The first segment dumps some heat into the liquid helium and this will increase the boil off rate. But we only have two cables and this increase of boil off is relatively small. In between we use the semi-rigid cable which is more resistive. Similarly to the other wiring it is thermalized at the different stages. We accomplish this by squeezing the cables between two copper plates which are screwed on the stages. In this section of the dilution refrigerator we also had some superconducting coaxial cables. But only the core was superconducting, the shield was in stainless steel and provided a strong attenuation. So we replaced them with the semi-rigid coax which did not attenuate as much.

The connections to the outside of the cryostat was done using SMA connectors. We used some hermetically sealed ones on the dilution refrigerator. For the ^{3}He system we used some regular connectors[4] which we sealed with some Eccobond 286 epoxy. This is much cheaper but does not always work.

Finally the connection to the transducer on the sample is usually done by connecting a small gold wire from the transducer to a copper pad besides the sample which is also attached to the coaxial cable. This contact is done in the open without any shielding. This is enough for most experiments, since we used a reflection technique (see below) which uses just one cable. To use a transmission technique which requires a cable connected on both ends of the sample, better care is needed to shield the wiring. One way to achieved this is to enclose the sample into a container that separates both ends. This is needed to prevent cross-talk between the cables which would interfere with a measurement in transmission mode or generally when two transducers and cables are attached to the sample.

3.2 Pulse echo technique

The technique we used is the pulse echo technique. The basic idea is to send a pulse of sound in a sample. This pulse of sound travels through the sample and bounces on the surfaces. The pulse will then be seen as a series of echoes detectable at one of the sample surfaces. The pulse amplitude decays as it travels through the sample and this is seen as a decay in the echo amplitude as a function of time or travel length.

3.2.1 Sample

To use this technique puts constraints on the sample characteristics. The pulses need to be long enough to include at least a few cycles of the frequency. With frequencies around 100 MHz this implies that 10 cycles are included in a pulse length of 1 μs. A pulse that is too short will not provide a clean excitation at the reference frequency. Another way to view the problem is that, as the pulse length (τ) is shortened, the frequency spectrum of the signal pulse is made wider; the bandwidth is approximately $1/\tau$. If it gets to wide,

---

[4] Not all connectors work. We found that the model 901-9892-RFX of SMA connector from Amphenol worked properly.

a larger range of frequencies get excited by the pulse which can interfere with a proper measurement.

This restriction on the pulse length is then translated into a restriction in sample length (L). This is because the echoes need to be separated into distinct pulses so the travel time (t_L) through the sample must be longer than the pulse length, i.e.

$$\tau < t_L = \frac{2L}{v_S} \tag{3.1}$$

where L is the length of the sample (the factor of 2 is because the detection is at one end and requires two traversals of the sample) and v_S is the sound velocity for the mode excited (transverse or longitudinal). Because sound velocities are in the order of 5 km/s, and assuming pulse length of 1 μs this implies a requirement of sample length of a few millimeters. If this is not possible, the basic technique shown here will not work. One way around this is to reduce the pulse length by going to much higher frequencies (microwave range – GHz).

It is also necessary to have the two surfaces where the sound is to be bouncing to be as parallel and as flat as possible. The flatness requirement is to insure specular reflection (like in a mirror) from the surface. For this to occur the surface roughness must be smaller than the wavelength of the sound. At 100 MHz and for a velocity of 5 km/s this represent a wavelength of 50 μm. Therefore a polish finish on the surface of 1 μm or better (like optical quality finish) are good enough for those frequencies. If the polish is not good enough the sound waves will suffer a diffuse scattering, so that a large fraction of the signal will not come back along the incoming direction and will be seen as a source of attenuation.

The parallelism requirement is necessary because otherwise the signal does not come back to the same location. But even more important is that a small misalignment will produce an interference effect [89]. This is because parallel paths will have slightly different lengths so that over the surface of the transducer the phase of the signal can sometimes average to zero depending on the propagation length and frequency. This problem becomes worse as the frequency is increased and can produces zeros in the detected signal as a function of time.

The transverse dimensions need to be large enough so that a transducer can be attached. The size of the transducer does have effects. A perfect transducer would produce a nice plane wave but real transducers suffer of diffraction effects. These effects are worse at lower frequency and for smaller transducers. It produces a dispersion of the sound wave that is more like spherical wave than a plane wave. Because the size of the beam of sound increases this produces a loss of sound intensity in the detector. But also the signal will suffer different propagation length, like for parallelism effect, and some interference effects also result. These effects were studied by Papadakis [84, and references therein]. The sideways dispersion of the signal has an additional complication when the perpendicular dimensions of the sample are considered. As the signal expands it will eventually hit the sides and, depending on the geometry, it can be reflected back toward the center in a coherent way and produce additional dependence of the amplitude of the echoes versus time. This effect can be calculated for simple geometry like cylindrical or rectangular samples [90] and shows it can have a strong effect on the measurements.

The effects we just mentioned (parallelism, diffraction and side effects) are geometrical effects that will destroy the simple exponential decay expected from the sample but should mostly be independent of temperature at low-T.[5] It is important to limit their effect, and to apply corrections when an absolute value of the attenuation is needed. In our case we are only interested in the electronic part of the attenuation. Its absolute value cannot be extracted from the overall attenuation because the other sources of attenuation cannot be estimated or extracted. Therefore we only need a relative measurement and those problems are not critical. But if possible they must be avoided because the will reduce the amplitude of the signal and shorten the number of echoes that are observable.

3.2.2 Transducers and bonds

As will be seen in the next section, what the electronics provide is an electronic pulse at a particular frequency and the detection system also requires an electrical signal. Therefore we must find a way to turn electrical signal into a mechanical signal — a sound wave — and also to do the opposite, *i.e.* turn the mechanical signal back into an electrical signal. This is most easily done using a piezoelectric transducer. Quartz as been used extensively but in our case we use $LiNbO_3$. It is possible to use other materials or other effects such as the magnetostriction.

To turn the electrical wave into a particular sound wave, the piezo-electric material must be cut in a particular way. The direction in which it is cut and the position of the electrodes produce different motions in the crystal and this depends on the piezo-electric parameters. The transducer will also have a resonant frequency defined by the shape

---

[5] These effects mostly depend on geometry, which is temperature independent at low-T (very little thermal contraction) and the sound velocity which also varies very little at low temperature.

of the transducer. Often the dimension of interest is the thickness of the transducer. Then the resonance frequency occurs when half of the sound wavelength corresponds to the transducer thickness. This relation is derived from boundary conditions when both surfaces are free to move [91]. These same boundary conditions also provide resonances at all the odd harmonics of the original resonance frequency f_o. Therefore as long as the transducer surfaces are prepared properly to allow those higher frequencies, which is called an overtone finish, the transducer can be excited into resonance at f_o, $3f_o$, $5f_o \ldots$ The resonance frequency gets larger as the transducer thickness is smaller. Without the overtone finish the surface will provide dissipation and the resonance amplitude will be much smaller than with the finish as the frequency is increased. The maximal conversion of electrical energy to sound sound wave occurs at the resonances. Therefore to optimize the signal, we try to be as close as possible to resonance but sometimes the bond quality is not good and being too close to resonance produces a lot of ringing[6] and we are forced to stay away from it. But you cannot go to far away from the resonance because then the signal becomes much too small. How far you can go depends on the Q value of the transducer and this depends on the material, the particular process the transducer was made and also how the transducer is mounted onto the sample. The more loading the bond and lead attachment produce the smaller is the Q value which means the resonance peak is wider. The loading can also shift the resonance frequency. Therefore the signal amplitude at resonance is not as large but it is easier to find and going away from resonance does not lower the amplitude as quickly. When using a transmission mode experiment (see later) which requires two transducers, special care needs to be taken so that the transducers resonances match. This is more easily achieved by mounting them the same way and minimizing the loading.

For our measurements we used very thin $LiNbO_3$ transducers with overtone polish and a fundamental resonant frequency of 30 MHz. The transducers were circular in shape with a diameter of 2 mm (0.078 inch). They have coaxial gold electrodes with a center electrode of 0.75 mm (0.030 inch) in diameter and the grounding electrode, on the other face, was wrapped around the edge and formed an outer circle on the top of the transducer. This permitted to make both the active and grounding contacts on the top of the transducer. The contacts to the electrode were done with silver epoxy or a small

---

[6] Ringing is often caused by a bad bond (see below). It is a transducer that continues oscillating at its resonance frequency for a certain amount of time after the excitation pulse is finished. Even if the pulse is not at the resonance frequency, its bandwidth can be large enough to excite the resonance.

amount of solder. When using solder, care must be taken not to apply too much pressure or too much heat which can break the very thin transducers. To excite longitudinal waves we used 36° Y-cut crystals [92]. It actually produces quasi-longitudinal wave but the polarization is very close to a pure mode. The angle between the propagation and polarization direction is 2.7°. For transverse modes we used 41° X-cut crystals which gives pure transverse modes. The direction of propagation is marked by lines on the transducers or a flat segment on the edge.

We mentioned a few times the bonding of the transducer to the sample. This is an essential but difficult process. The transducer produces mechanical motion from the electrical signal and vice-versa but this mechanical motion needs to be transfered back and forth between sample and transducer. This bonding layer must be thin, uniform, allow transverse waves if necessary and strong enough to last throughout the experiment. At room temperature this is not too difficult. If transverse waves need to be propagated, the coupling agent need to sustain transverse wave so it should not be a liquid. For room temperature tests we have used crystals of Phenyl Salicylate (Salol) and Phenyl Benzoate (both from Aldrich). These compounds become liquid at 45°C and 70°C respectively. The liquid can be put between transducer and sample and then cooled below the solidification temperature. Then the solidification is initiated usually by approaching a small crystal to the liquid. This bond then supports both longitudinal and transverse waves, is very easy to make and to remove by melting the compound again or dissolving it in acetone. Many other compounds can be use similarly.

The above bond works at room temperature and allows some characterization of the sample (sound velocity, does it transmit sound at all or has big voids or a large intrinsic attenuation at room T?) But what we really want is to make measurements at low temperature. This is where things get complicated. In fact it is an art and a certain dose of luck is required because the probability of success will rarely be anywhere close to 100%. The problem is that the thin layer of bonding agent must connect the piezo-electric transducer with its particular thermal contraction coefficient to the sample with another thermal contraction coefficient. So a bond that works at room temperature will usual suffer strong stress and can break when cooling down. Also the cooling method, such as the cooling rate, the presence of exchange gas, etc, will influence the bond quality. One way around this problem is to make a stronger bond. In this case the bond can be permanent with glues or epoxy or even with solder if the sample is wetted by the solder (for example indium). The other way is to have a material that is liquid at room temperature and solidifies at much lower temperature were a large part of the contraction will have occurred. This should lower the stress on the coupling compound, for example 4-methyl 1-pentene with a melting point of -153°C is sometimes used. But since it is a liquid it might be necessary to have a setup that allows the application of pressure on the transducer during cooldown to keep the bonding layer thin and uniform.

The literature contains many possible coupling agents, some as exotic as honey. We tried honey, glycerol (also called glycerin, m.p. of 18°C), vacuum grease (Dow Corning high vacuum grease) and a few other compounds like silicon rubber (clear Silicone II sealant from GE) which is a more permanent bond, but obtained the best result with an optical coupling compound (we used an old Dow Corning 20-057 which is superseded by Q2-3067). This is a non-permanent bond that can be cleaned off using an organic solvent such has petroleum ether and an ultrasound cleaning bath. Moderately fast cooldown also seemed to produce more reproducible results probably because the bonding layer would solidify at a lower temperature. The bonds were made by putting a very small amount of the compound on the sample. Then the transducer is gently placed on this, moved slightly and oriented properly. To make the bond thin and uniform, a weight is applied on the transducer for a couple of hours. The coupling tests were performed by putting the sample in liquid nitrogen (77 K) because at that temperature most of the thermal contraction is finished. This kind of test works as long the ultrasound attenuation at liquid nitrogen temperature is not too large so that echoes can be observed. This was the case for our samples of Sr_2RuO_4.

Both the bond and the transducer can remove energy from the sound wave and provide additional attenuation. This is a reason to keep the bond thickness small. The loss in the transducer is from mechanical (sound attenuation) and because a small amount of energy is transformed in electrical energy and sent to the electronics. Also interference effect between the wave hitting the sample face, the bond-transducer interface and the free face of the transducer can affect the frequency dependence of the total attenuation. These effects will be temperature independent at low T (at least to first order because the sound velocity changes very little).

3.2.3 Electronics

The spectrometer to produce the pulse and detect the amplitude of the echoes is a home-built heterodyne system. This basically means that the final detection is done internally at a fixed frequency. The overall design is taken from [93]. It was constructed

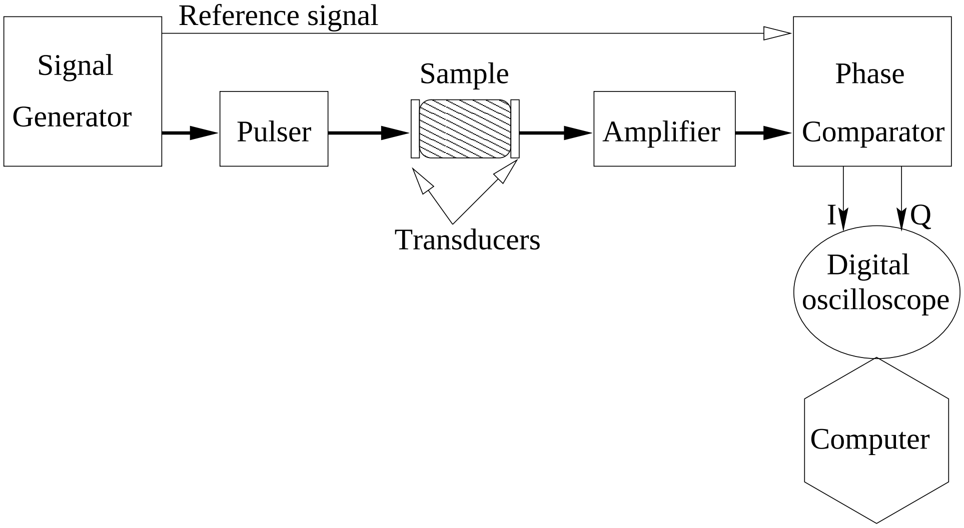

Figure 3.3: Simplified schematic of setup to measure ultrasound attenuation.

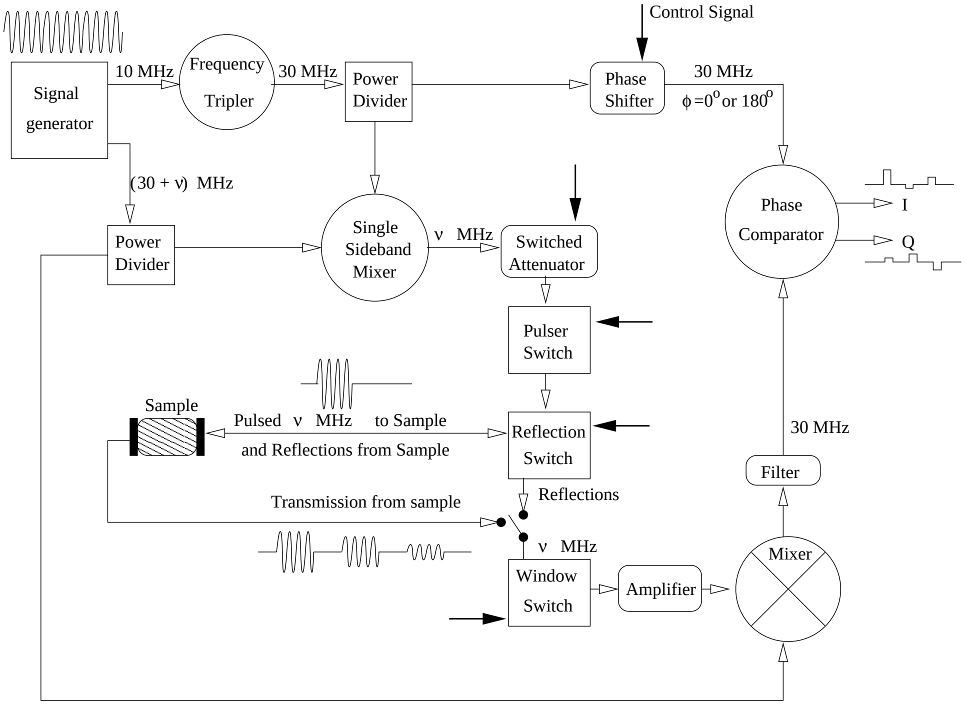

Figure 3.4: Detailed schematic of ultrasound measuring setup. Everything shown is contained in the spectrometer box except for the sample and the signal generator.

by assembling rf components like mixers and amplifiers that can be bought (from Mini Circuits, Merrimac and others) as seal boxes with connectors. Therefore it is a matter of choosing the components with the required characteristics and connecting them in the needed geometry. Overall the components were selected to work up to 500 MHz and generally have a 50 Ω impedance.

Fig. (3.3) shows the simplified diagram of the setup and fig. (3.4) shows a more detailed diagram of the setup. From the simplified diagram we see the basic operation of the system. A continuous source of high frequency signal (10-500 MHz), a Hewlett Packard E4423B (250 kHz – 1GHz), is chopped into short pulses of sound which are brought to the transducer on the sample. The transducer converts the electrical signal into a pulse of sound. This pulse of sound travels in the sample and the same transducer (reflection) or another one (transmission) converts the sound wave of the echoes back into an electrical signal. This signal is amplified and the envelope of the pulses is extracted and captured by a digital oscilloscope, a Tektronix TDS 520C (bandwidth of 500MHz and acquisition rate of 1 Gs/s). The scope also performs some averaging. Finally the data is transfered to the computer where additional averaging can be performed and the data is saved. The computer also controls other instruments to change the temperature and the magnetic field and to measure additional sensors.

In the detailed diagram, fig. (3.4), all the circles are devices built at least in part with a mixer. A mixer is a very common device in RF circuits so before looking at the details of the setup let us describe what is a mixer and how it works. As the name implies they mix two signals. The mixing is done by multiplying the two signals. Assuming the input signals are at a particular frequency $\omega = 2\pi f$, they have the following time dependence: $A\cos(\omega t + \phi)$ where A is the amplitude of the signal and ϕ is the phase of signal. A mixer multiplies two signals so we obtain:

$$A_1\cos(\omega_1 t)A_2\cos(\omega_2 t + \phi_2) = A_1 A_2 \left(\cos(\phi_2)\frac{\cos\left[(\omega_1+\omega_2)t\right] + \cos\left[(\omega_1-\omega_2)t\right]}{2} \right.$$
$$\left. - \sin(\phi_2)\frac{\sin\left[(\omega_1+\omega_2)t\right] - \sin\left[(\omega_1-\omega_2)t\right]}{2}\right) \quad (3.2)$$

where the subscript represent the two waves and we set $\phi_1 = 0$ to simplify the result (without loss of generality). It just implies we fixed the time reference t so that the phase of one signal is zero. Often in a mixer there is a reference wave and it is natural to make that simplification. As is seen the result of a perfect mixer is waves at the sum and difference of the original frequencies. It also produces both an in-phase (cos) and out of phase (sin) components. The identification of in-phase and out-of phase is just a definition in this case because there is no reference signal at the same frequency.

This description of a perfect mixer shows its utility. It can be used with filtering to move the center frequency of a signal to a higher or lower frequency. It is possible to even move the amplitude of a certain frequency all the way to 0 Hz, *i.e.* to a DC signal. This is called demodulation and is what happens in an AM radio signal where the carrier is removed by tuning the radio station to leave only the amplitude modulation. A real mixer will mostly behave in this way but because the way to obtain mixing at high frequency is to use non-linear elements (usually diodes), additional harmonics of the signal are produced and some of the incoming signal can also leak from input to output. These characteristics can be important.

Coming back to the spectrometer we see that what it uses is the RF signal from the signal generator which we write as $\nu+30$ MHz, where ν is the frequency sent to the crystal and the presence of the 30 MHz will soon be explained. We also use the reference signal from the generator. This is a 10 MHz signal with a squarish shape. From the diagram it can be seen that this 10 MHz is turned into a 30 MHz sine wave using a frequency tripler (a combination of mixers and filters to remove the unwanted harmonics). This 30 MHz is then used internally as the reference for the extraction of the signal at the end. The signal sent to the sample is obtained from the $\nu + 30$ MHz wave by removing the 30 MHz using a single side band mixer. This is a mixer designed to select either the sum or difference in frequency. Here we pick out the difference and obtain just ν. This signal amplitude is adjusted, with some manually switchable extra attenuators to decrease the output amplitude (separate 4, 8 and 16 dB attenuators). It is then pulsed using signals from a home built circuit. This pulser can select the pulse length from 80 ns to 16 μs and also the repeat rate of the pulses from 7 Hz to 6.5 kHz. The repetition rate was set to 40 Hz because that was the maximum rate at which the oscilloscope could perform averaging. A faster rate would put more power into the sample without increasing the data gathering speed. A slower rate would reduce the power but also slow down the data taking. To change the power we used the attenuator instead. This pulse of ν signal then goes through a switch which sends the signals out to the crystal. The output amplitude without attenuation is of the order of 1 V.[7] With a repeat rate of 40 Hz and a pulse length of 1 μs this sends a maximum power of 0.8 μW. The actual power converted into sound is much smaller because of losses due to impedance mismatch in the cabling, the transducer itself has the wrong impedance and only a fraction of the electrical energy is converted into mechanical energy.

The reflection switch is used when the same transducer crystal is used for excitation

---

[7] This 1 V is often given as 13 dBm. The dBm unit the is ratio of amplitude or power in dB with 1 mW as a reference. For a circuit based on 50 Ω impedance (like ours) then 0 dBm (1 mW) is 0.05 V and 13 dBm (1 V) is 20 mW.

of sound wave and the detection of the echoes. This is called the reflection mode. In this mode the signal comes back through the same cable but must be directed to the detection electronics. This is the purpose of the switch. The pulsing circuit produces an additional signal that controls the time when the switch connects the output cable to the detection circuit and also the length of this connection. The start of the switch needs to be adjusted to allow the excitation pulse to go through while allowing the first echo to be detected. Sometimes the transducer can be resonating a little and some extra time after the excitation must be given before connecting the detection circuit to prevent overloads. This could eat up some of the first echo and happens when the transducer is not well bonded. The length of the switching needs to be adjustable to allow the next pulse to go through. It is usually set to its maximum. In the other mode when separate transducers are used for excitation and detection, the transmission mode, this is not a problem.

In order to prevent overload of the detection circuit an additional switch (the window) is used as the first step of the detection circuitry. This is turned on by the same signals used for the previous switch (with some delay) and is used to keep the detection circuit disconnected until the time where the input signal is under control. The settings for this are called the window control and can be set up to 150 μs. This is necessary because the next step is to amplify the signal with a RF amplifier. These devices, when overloaded by a signal larger than their specification, get saturated and take a long time (many μs) before coming back to normal operating behavior. Since the excitation signal is much larger than the expected amplitude of the echoes it is essential to avoid overload which would prevent the measurement of the first few echoes.

The amplifier provides a gain of about 20 dB (×10). But they are not operational amplifiers with nice and stable gain. The gain is slightly frequency dependent but also depends on the temperature of the device and can drift slightly over time. This must be taken into account when analyzing the data.

After amplification then the signal is mixed with the original $\nu + 30$ MHz and filtered to move the frequency of the echo signal back to 30 MHz. This signal is then mixed with the internal 30 MHz reference with a phase comparator. The reference goes through a switch and power divider that allows its phase to be changed by 180°. The utility of this we will discussed later. The phase comparator is a combination of mixers, filters and other components to extract an in-phase (I) and an out of phase (Q) envelope of the incoming pulses. It basically outputs the amplitude of the $\cos(\omega t + \phi)$ and $\sin(\omega t + \phi)$

components. The ω is $2\pi 30$ MHz and the phase shift (ϕ) is the same for both components in a perfect comparator. A real comparator can have a slight angular error which could affect some of the data and can also extract signal at harmonics of the 30 MHz. Therefore the output is cleaned up by additional filtering (5 MHz low pass, not shown on diagram) and the envelope which has a relatively small bandwidth is then amplified by a variable gain amplifier (×30, ×90, ×300, ×600, also not shown) separately on both channels to obtain the final output which can be digitized. This last step of amplification needs to handle the rise time of the pulses which after filtering is in the 200 ns range at best so it is built with fast op-amp used for television signals. These op-amp circuits produce a gain which is much more stable then the RF amplifier and they are setup to remove some of the anisotropy between the two output channels of the phase comparator. In all the path between the phase comparator and the oscilloscope, the circuit is made as symmetric as possible between the two channels to prevent time delays between them. This includes choosing two short cables of the same length between spectrometer and scope and the shifts are then less than a couple of ns and have no effect on the data.

A problem with the circuitry is that the background is not completely flat. The switches leak a small signal that takes a relatively long time to settle. This is a problem because the actual measured signal is also very small. This sloping background complicates the analysis. But a way to avoid this problem is to switch the phase of the reference. This does not change the shape of the background but does change the polarity of all the echoes. Therefore by taking the difference between the two states of the phase shifter, the background is made flat and the echoes are kept. This circuit was added during the experiments but most of the data described later was taken while using this circuit. With or without this circuit the signal is averaged using the scope and the computer to remove the random electrical noise (but it has no effect with coherent noise like acoustical noise). The final curve saved by the computer usually contains from 1000 to 10000 averages. The selection is a compromise between noise, the time per points (10000 averages takes about 4 min) and the stability of the system. For example, the averaging is usually shorter (2000) for the ^{3}He system because we try to do the experiment during a single condensation cycle which limits the time available. Therefore a shorter averaging allows a higher density of points.

In summary, the electronic system uses a continuous wave generator which it turns into short pulses of sound with adjustable amplitude, pulse length and repetition rate. The detection is then performed in a certain time interval (window) by performing amplification, extracting the I and Q envelope of the echoes (removing the high frequency component) which is finally amplified some more. Care must be taken in the measurement that some other frequency than expected can leak in the system and the RF amplifier are prone to drifts. This is a problem at high frequency because, we used transducer with 30 MHz fundamental resonance frequency and at high frequency the signal are small and a leaking 30 MHz can then be seen. To avoid this a high pass filter is added in the path to and from the sample to remove the 30 MHz. Also the phase comparator can make an error in the angle but this is not a big problem for this type of measurement.

3.3 Other techniques

Many variations on the pulse echo techniques exist. Many of them are specialized in improving the accuracy and precision of velocity measurements [94, chapter 2]. Some techniques, such as the use of buffer rods, allow the measurement to high temperatures where the transducer would fail. There are also specific techniques for measurements in the microwave regime.

A slightly different technique is the resonant ultrasound spectrometer. In this technique a weakly bonded transducer excites normal modes of vibration (resonances) in the sample. When the sample geometry is well known and simple (parallelepiped) the resonance frequencies can be calculated from the elastic constants. The inversion from frequencies to elastic constants is possible for moderately simple shapes. For this to work well, most resonance frequencies must be detected. Therefore other resonances, such as the transducer resonance, must be avoided so this technique is used at low frequency, usually below 10 MHz. Special care needs to be taken so that the sample is not loaded by the transducer and that the resonances are intrinsic to the sample. Also in order to excite the largest possible number of different modes, the transducer needs to be installed at a position of low symmetry which is most often the corners of the sample. As the frequency is increase, more and more modes are observed and eventually it becomes impossible to separate individual modes and this yields another practical limit to the usable frequency. This implies stricter requirements on the geometry of the sample.

This RUS technique leads directly to the elastic constants and can be quite sensitive since frequency measurements are very precise. It is possible to use it at low temperature. This technique can also be used to extract the attenuation from the width of the resonance peaks. The attenuation obtained in this way is for the particular resonance mode that is excited at a particular frequency. Therefore there is not much control of frequency, polarization and propagation. Also because of the restriction to low frequency this is not a very sensitive technique for the electronic source of attenuation.

3.4 Data analysis

Section 3.2.3 described what is obtained from the experiment: an averaged time dependence of the echoes signal in the I and Q channels. But we must avoid some technical problems like background drift.

The first step in the analysis is to convert the I, and Q signals into amplitude A and phase ϕ. The amplitude will be used to obtain the attenuation and the phase will be used to obtain the sound velocity changes. Assuming pure I and Q signals, then the conversion is simply

$$A = \sqrt{I^2 + Q^2}; \quad \phi = \tan^{-1}(Q/I). \tag{3.3}$$

But the real system, because of limitations of the electronics, is not perfect. The I and Q channels are not exactly 90° apart and, what is even worse, both channels have possibly large and unequal offsets which means that they have non-zero output even for a signal with $A = 0$. The first problem (phase error) is not too important. As will be seen later, the phase usually changes very little with temperature (or field) so even if there is an error, it will modify the absolute amplitude of an echo but it will not change its relative dependence on temperature (or field). The measured phase will also have its absolute value modified but again, we are only interested in the changes in the phase. So as long as it is small the offset due to the phase error produces no bad side effect.

The actual effect can be estimated as follows. Let y' (Q) and x' (I) be the measured values, extracted by the phase comparator from $\sin(\omega t)$ and $\cos(\omega t + \delta)$ respectively where δ is the angle of the phase error. The corrected x and y (perfectly perpendicular) are then given by $y = y'$ and $x = (x' - y' \sin(\delta))/\cos(\delta) \approx x' - y'\delta$ where the last part is given to first order in δ. Using this we can relate the measured, A' and ϕ' (obtained from eqn. (3.3) using $I = x'$ and $Q = y'$), and the corrected one, A and ϕ. To first order in δ we get $A = A'(1 - (x'/A')(y'/A')\delta)$ and $\phi' = \phi + \delta y'^2/A'^2$. Assuming a realistic error of 1° ($\delta = 0.017$ rad), and since $x'/A' = \cos(\phi') \leq 1$ and $y'/A' = \sin(\phi') \leq 1$, the measured phase is modified by less than 1° and the measured amplitude by less than 2%.

The other, more important problem, is the effect of the background drifts. During the averaging of a channel the background offset moves due to noise and due to general drift of the electronics. One source of drifts is the effect of temperature variation on the operating condition of RF components. These effect do not distort the echo signal but they shift it. For data acquisitions well separated in time, *e.g.* curves at different temperatures, the background drift can be relatively large. Because of this non-zero and changing background the amplitude is not calculated properly. If we assume an offset x_o (only on one channel for simplicity) on a pure signal x, y then the measured amplitude without considering the effect of the offset would be $\sqrt{(x-x_o)^2+y^2}$ instead of $\sqrt{x^2+y^2}$. When the main signal becomes small ($x, y \sim x_o$), the amplitude will be distorted and, as the signal gets even smaller, the amplitude will saturate to $|x_o|$ instead of going to zero. This will distort and saturate the attenuation curves when a signal with a large attenuation makes echoes almost disappear. In the other limit of large amplitude but very small changes, the amplitude with the offset is given by $A - xx_o/A = A(1-(x/A)(x_o/A))$ (where $A = \sqrt{x^2-y^2}$). This is a small rescaling of the amplitude. But what we will be concerned with is the temperature (or field) variation of this A. When it is small, it can be of the same size as the corrections due to the background noise and drift. Since the noise and drift also change, they will distort the measurements and are a source of systematic errors.

The background offset will also influence the phase. In a similar way as for the amplitude, large amplitude swing will distort and saturate the phase. In this case the phase saturates to 0° (signal only along x). A drifting background on a weakly varying amplitude also disrupts the measurement since the measured phase is then given by $\phi + yx_o/A^2$ where $\phi = \tan^{-1}(y/x)$. The phase usually changes by very small amounts so that the systematic effects due to drifts can be very large. Another effect of the offset is that it provides a coupling between amplitude and phase. Therefore a strongly varying amplitude will produce a change in the measured phase even if the real phase is constant.

Because of the problems described above, it is important to remove as much as possible the background offset and its drift, especially in the limits of very large and very small amplitude variations. As will be seen later we have measured data in both of these limits. The background removal must be done before the amplitude and phase are calculated. We achieve that by removing the average of the data in-between echoes. It is possible to fit the background to a linear or to a higher polynomial curve in order to remove some possible curvature of the background but it is unnecessary when using the phase shifting circuit (see section 3.2.3). For the averaging we select the flattest time segments between echoes. Therefore the space between the first couple of echoes is often removed from the average since they are often very noisy because of acoustical noise and of ringing of the transducer. As many segments as possible are used in order to lower the statistical error of the average. This procedure is good at making the offset amplitude small. But where this is needed the most, *i.e.* to prevent saturation for large variations of the amplitude of the signal, it can suffer from systematic errors because the whole echo spectrum changes so drastically. On the other hand this procedure is very good at removing the background drift, especially in the case of small amplitude variations. This is because the signal shape changes very little except for the variation in offset, which is then easy to detect.

An effect we have not mentioned yet is the effect of slightly different gains in the two measurement channels. Let us say the measured x is replaced by $x' = (1+k)x$, then the measured amplitude is $A'/A = (1 + kx^2/A^2) = 1 + k\cos^2(\phi)$ to first order in k. Therefore if k is small, say 2% (our setup should be better than that), it would give a relative error in amplitude which is at most 2%. Also the correction is affected only if the phase changes by a large amount (∼90°). Similarly the effect on the phase is $\phi' - \phi = yxk/A^2 = k\sin(2\phi)/2$ which produces an error of at most 1.2° (for $k = 2\%$). Therefore this effect can contaminate the attenuation from large changes in the phase (which is rare) and it can rescale the angular dependence by at most 2%. So in general this is not a source of problems.

After correcting the Q and I signal by removing the background drift and offset, the amplitude and phase can be extracted using eqn. (3.3). Therefore we have A and ϕ and we must extract the attenuation and the changes in velocity. The top panel of Fig. (3.5) and Fig. (3.6) show examples of the extracted amplitude. The first information that can be obtained from this is the absolute value of the sound velocity. This is extracted from the echo spacing and can be determined roughly as the time difference between the rise (or fall) of two echo pulses. Let us call this time difference t_{n-m}, where the subscripts n, $m = 1, 2, \ldots,$ identify the echo number. Therefore the sound velocity is $v_S = 2L(n-m)/t_{n-m}$ where L is the length of the sample and the factor of 2 is because the sound travels a distance $2L$ for each echo (it goes through the sample, reflects at the other end, then comes back). Most sound velocities are around 5 km/s (=mm/μs). Using this technique, absolute sound velocities can be determined with errors of a few %. Other techniques can do much better but in our experiments we are not interested in very accurate sound velocities.

To proceed further we average the amplitude and phase of each echo and write them as A_n and ϕ_n, where the corresponding time is $t_n = n\Delta t + t_o$. We have introduced Δt, the

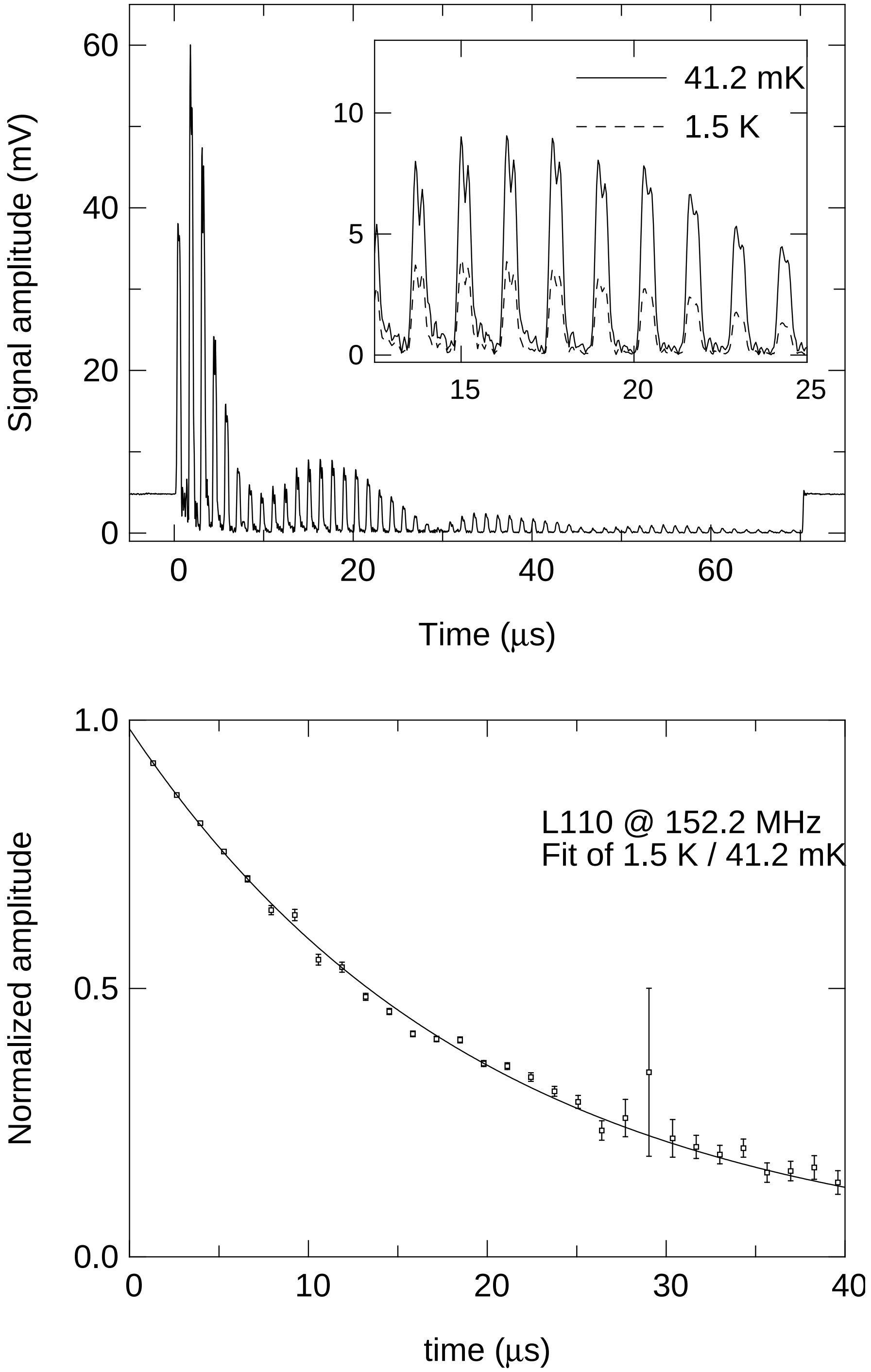

Figure 3.5: The top panel shows the echo amplitude for the L110 mode (see table (5.2) for a description of the mode). Before 0 μs and after 70 μs (echo 52) the step is an effect of the electronic window. The excitation pulse leaks through the electronic and is seen as a pulse at 0 μs. The inset shows a zoom of some echoes and their temperature dependence. The bottom panel is an exponential fitting example of the ratio of the 2 temperatures shown in the inset. The ratio removes the strong pattern on the attenuation. See also fig. (3.6).

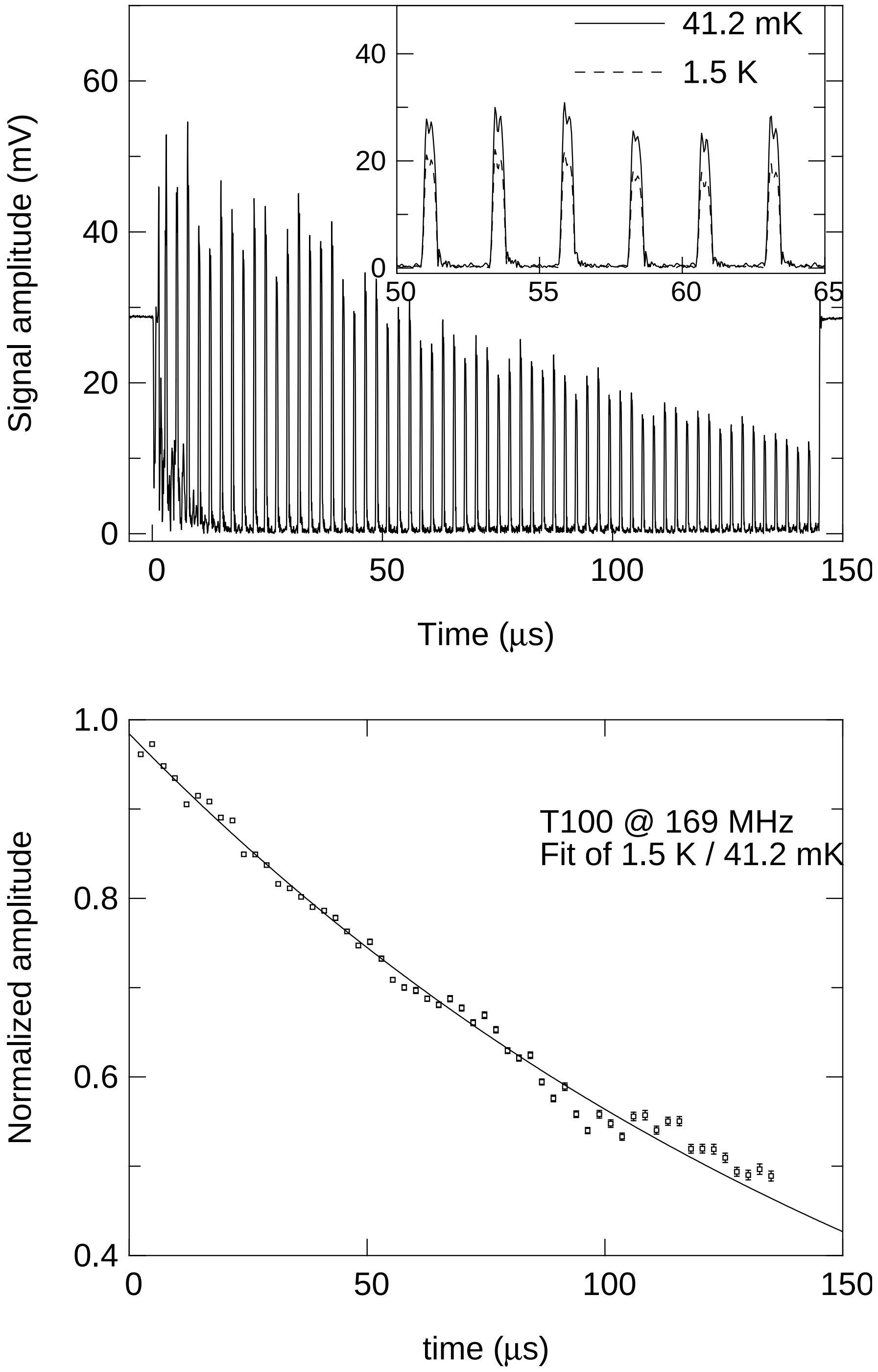

Figure 3.6: See fig. (3.5) for a description of this graph. Here it is for the T100 mode with 59 echoes before the window closes (at 140 μs). In this case the attenuation is much weaker and the amplitude is more exponential.

echo spacing (related to the sound velocity, $\Delta t = 2L/v$), and the origin of time t_o which should be zero for the reflection mode of measurement and $-\Delta t/2$ for the transmission mode. It should be noted that this time scale does not correspond exactly to that of the oscilloscope because its time origin depends on the triggering circuit which uses the rising edge of the pulse trigger signal and this signal suffers different delays in the electronics than the main signal (which must travel all the way to the cryomagnetic system and back). The averaging of the echoes is done in the center of the echo over a small window in order to avoid the sharp edges of the pulse. Instead of first calculating A and ϕ and then performing the averages it is possible to do the inverse, *i.e.* calculate the averages of the Q and I signals first and then proceed to calculate A_n and ϕ_n from these. This procedure does not give the exact same A_n and ϕ_n, but for clean signals the difference in the temperature (or field) dependence of both the amplitude and the phase is very minor. Therefore we generally use the first method of calculating A_n and ϕ_n, *i.e.* we calculate A and ϕ first and we average last.

To extract the attenuation, the obvious technique would be to just fit A_n vs t_n to an exponential curve $C\exp(-\alpha t/2)$ where C is an arbitrary constant and the factor of 2 is because the attenuation α is defined in terms of energy. But this is not a good approach because the curves can be modified by diffraction and imperfect parallelism among other effects which add a structure to the signal (see top panel of fig. (3.5)). However, this additional structure should be temperature independent. There is also another problem coming from the electronics. The gain of the amplifiers is not absolutely stable and can drift over time. If the gain changes during the averaging time, the shape of the signal is not affected and the gain can be replaced by an average gain. We can combine these effects by writing the signal amplitude as a function of temperature[8] (T) as

$$A(t,T) = G_T S(t) C \exp(-\alpha_T t/2) \tag{3.4}$$

where we write G_T for the drifting gain, $S(t)$ for the overall structure of the curve and α_T for the attenuation. The attenuation can be divided into the electronic part $\alpha_e(T)$, which is temperature dependent, and the attenuation from other sources which is temperature independent α_b. This function contains many unknowns and it is impossible to fit using it directly. One way to simplify it, is to take the ratio of one echo with respect to a

---

[8] For simplicity we use the temperature as the control variable. It can equally well be the magnetic field or any other external parameter.

reference temperature (T_r), and to take the natural logarithm,

$$\log_e\left(\frac{A_n(T)}{A_n(T_r)}\right) = \log_e(A_n(T)) - \log_e(A_n(T_r)) = -(\alpha_T - \alpha_{T_r})\frac{t_n}{2} + \log_e\frac{G_T}{G_{T_r}}. \tag{3.5}$$

The result is in neper (Np). This is the same as taking the natural logarithm of the amplitude and to look at its deviation as the temperature is changed away from T_r. This simple ratio removes most of the factors in $A(t, T)$ except for the drifts in gain. Instead of just taking a natural logarithm the decay is usually given in dB/cm and would be obtained in this case as $-20\log_{10}(A_n(T)/A_n(T_r))/(t_n v_S)$.[9] The conversion between the above units is 1 dB = $20\log_e 10$ Np = 8.686 Np. Because the gain drifts are still present, this analysis is not very useful and therefore it is rarely used unless only one or two echoes are observable. In such cases, no other kind of analysis is possible and the gain drift must be controlled as much as possible. This can be achieved partially by doing quicker experiments and by keeping the instruments at a fix temperature.

To remove the effect of a drifting gain we can take the difference of the logarithm from two different echoes. If we introduce $R_n(T) = A_n(T)/A_n(T_r)$ then we have

$$\log_e(R_n(T)) - \log_e(R_m(T)) = -(\alpha_T - \alpha_{T_r})\frac{t_n - t_m}{2} \tag{3.6}$$

This expression only contains the time and the attenuation and it is not affected by the other parameters including the gain drift. The decay in dB/cm is obtained as $-20(\log_{10} R_n - \log_{10} R_m)/(v_S t_{n-m})$. This expression can be used in general and provides the change in the attenuation away from T_r. Replacing the R_n by A_n in the previous equation we obtain:

$$\log_e(A_n(T)) - \log_e(A_m(T)) = -\alpha_T\frac{t_n - t_m}{2} + \log_e S(t_n) - \log_e S(t_m). \tag{3.7}$$

This expression would provide the absolute total attenuation (not the absolute electronic attenuation) if the structure factor was absent, $S(t) = 1$, or at least if $S(t_n) = S(t_m)$. The expression in eqn. (3.6) can be seen as the difference of eqn. (3.7) between a temperature T with respect to a reference temperature T_r. We are only interested in the changes of attenuation, not in the absolute value, so both eqn. (3.6) and eqn. (3.7) are then equivalent.

---

[9] The definition of dB (or 0.1 bel) is $20\log_{10} R_A$ for R_A a ratio of amplitudes and $10\log_{10} R_E$ for R_E a ratio of energies (or intensities). Both definitions give the same number assuming $R_E = R_A^2$ and is one reason for its usefulness.

The last two equations produce proper results but they only use a small fraction of the data (two echoes only). To improve on this in order to decrease the noise, we can fit an exponential to $R_n(T)$. Remember that $R_n(T) = G_T/G_{T_r} \exp((\alpha_T - \alpha_{T_r})t_n/2)$. Therefore we can fit to

$$C \exp(-kt) + D. \tag{3.8}$$

The C, k and D variables are all free parameters of the fit. But treating all three as free parameters does not work well usually. So either C or D must be held fixed. Looking at the expression for R_n it is seen that we should set $D = 0$. This is what is usually done. We included D because it could be useful when echoes become very small in amplitude in case the background subtraction did not work well. But in most cases where this could be useful, the attenuation is so large that not many echoes are available so that this is not the best analysis anyway. Without the D, the above fit is equivalent to a linear fit of $\log_e R_n$. The fitting procedure for the general exponential fit, which is a non-linear function, is the Levenberg-Marquardt algorithm [95]. In order to deal automatically with data points having a larger statistical errors (smaller amplitude), we perform a weighted fit where the weight is obtained from the standard errors. The errors are estimated from a constant voltage amplitude noise on the echoes[10] and converting that into an error on R_n (including the effect of the reference temperature). This will put more weight on the echoes with a higher amplitude and automatically disregards points from the fit with very small amplitude, like for a node in the structure factor or for late time echoes (see fig. (3.5) and fig. (3.6)). It is also usually necessary to restrict the range of echoes used for the fit. The first few ones are often affected by coherent acoustical noise and the very late echoes can be too small and noisy anyway. The constant C will absorb the variation of gain and k gives the time decay constant (*i.e.* the attenuation). This algorithm works because we remove the extra structure of the attenuation by dividing the amplitude with a reference temperature. For this to work well and to keep the noise as small as possible, the reference temperature must be selected with some care. It should be a curve with the largest possible echo amplitude (usually the lowest temperature data in the superconducting state) and it should not have any obvious systematic errors (*i.e.* it should have the same shape as the other curves). This first requirement is easy to satisfy by looking at the amplitude data. The second is not a problem also, it just requires to avoid bad data points (like a really unstable temperature). This data analysis procedure

---

[10] The voltage statistical noise after 2000 averages is usually around 0.05 mV.

is the one used whenever possible.

We have just described the analysis of the amplitude to obtain the attenuation. A similar description can be done for the phase. The phase ϕ (in radians) depends on the frequency f (or $\omega = 2\pi f$) of the sound wave, the path length of the sound in the sample l and the sound velocity v_S as

$$\phi = 2\pi\frac{l}{\lambda} = \omega\frac{l}{v_S} \tag{3.9}$$

where $\lambda = v_s/f$ is the wavelength of the sound wave. The absolute phase cannot be determined since the measured value is modulo 2π. Even if the spectrometer could keep track of the total phase, it would depend not only on the sample, but also on the delays in the cables and the response of the electronics. Therefore we are only interested in the changes in phase. The change can be caused by a variations in either the frequency, the length or the velocity. Since we fix the frequency for the measurement, f cannot be giving changes in ϕ. But length and velocity could be changing so we change them to $v + \Delta v$ and $l + \Delta l$ and we can write

$$\Delta\phi = \omega\left(\frac{\Delta l}{v} - \frac{l\Delta v}{v^2}\right) = \omega\frac{l}{v}\left(\frac{\Delta l}{l} - \frac{\Delta v}{v}\right). \tag{3.10}$$

The changes in length are due to thermal contraction, are small and usually tend to disappear below liquid nitrogen temperature (77 K). Therefore at low temperature (below liquid helium, 4.2 K) there should be no more changes in length and the variations in phase should come from changes in velocity. So we drop the Δl term and we finally have

$$\frac{\Delta v}{v} = -\Delta\phi\frac{v}{\omega l} = -\Delta\phi_n\frac{1}{\omega t_n} = -\frac{1}{\omega}\frac{\partial\phi}{\partial t} \tag{3.11}$$

From this it is easy to see that the change of phase is linearly increasing in time since the relative change of velocity is a constant (dependent on temperature or field). The gain drift of the spectrometer that caused trouble for the attenuation analysis does not show up in this analysis. Here the problem could be a varying overall phase shift in the circuit. Of course this assumes a perfect decoupling between ϕ and A. This is not necessarily the case. When the amplitude changes a lot, this can shift the phase slightly, especially if the background is not properly removed. In those cases, extracting valid information from the phase might be very difficult. In rare occasions it is the phase that changes a lot and not the amplitude. In these cases the sound velocity is easily extracted and it is the sound attenuation that can be contaminated.

Assuming a change in velocity of 1 ppm (part per million), a sound frequency of 100 MHz and the echo time of 10 μs, this translates into a change in phase of 0.4°. This is a measurable change in angle. Hence at higher frequencies and using late echoes it is possible to see changes in the sound velocity with a sensitivity of order 1 ppm.

To extract the sound velocity variation, what is needed is the slope $\partial\phi/\partial t$. The first approximation would be to use just one echo and write

$$\partial\phi/\partial t = \frac{\phi_n - \phi_{nr}}{t_n} \tag{3.12}$$

where we use ϕ_{nr} to be the phase of echo n at a reference temperature or field. This will provide the changes of velocity from the reference point. It should be noted again that the measured ϕ_n are defined modulo 2π. Therefore the above formula could result in jumps of 2π. But it is possible to identify and remove these as long as the density of T-points is high enough so that the phase change between points is kept below π.

This single echo analysis is not affected by the gain drift and provides a good analysis. It is also possible to take the difference in phase between two echoes. This removes the effect of a varying overall phase in the electronics or the cables (possibly because of changes in the level of cryogens). But these use only a fraction of the data. Therefore, similarly to the exponential fit done for the amplitude, a linear fit of $\phi_n - \phi_{nr}$ versus t_n can be done. Here again a weighted fit automatically takes care of using the data properly. This linear fit provides the slope which is proportional to the sound velocity changes and a constant which is related to the drifts of the overall phase.

3.5 Tantalum

In order to check that the whole procedure from cables and electronics to data analysis was working properly, we performed a test on a conventional superconductor. We obtained a sample of tantalum from Prof. J. M. Perz. Ta is a type I superconductor with a weak-coupling BCS gap. It measured 6.00 mm along the direction of propagation. Quartz shear transducers (20 MHZ) were already bounded on both ends of the sample using indium solder but we only used one (reflection mode).

Our sample had a critical temperature (T_c) of 4.40 K and a critical field (H_c) of 75 mT which are in reasonable agreement with literature values [59]. The attenuation data is shown in fig. (3.7). The curve was obtained by fitting

$$\alpha_S(T) = A + 2f[\Delta(T/T_c, \Delta_0)](\alpha_N(T) - A)B \tag{3.13}$$

where A and B are free parameters adjusting the offset and amplitude of the fit respectively. The function $f(x) = 1/[1 + \exp((x - \mu)/k_BT)]$ is the Fermi-Dirac distribution.

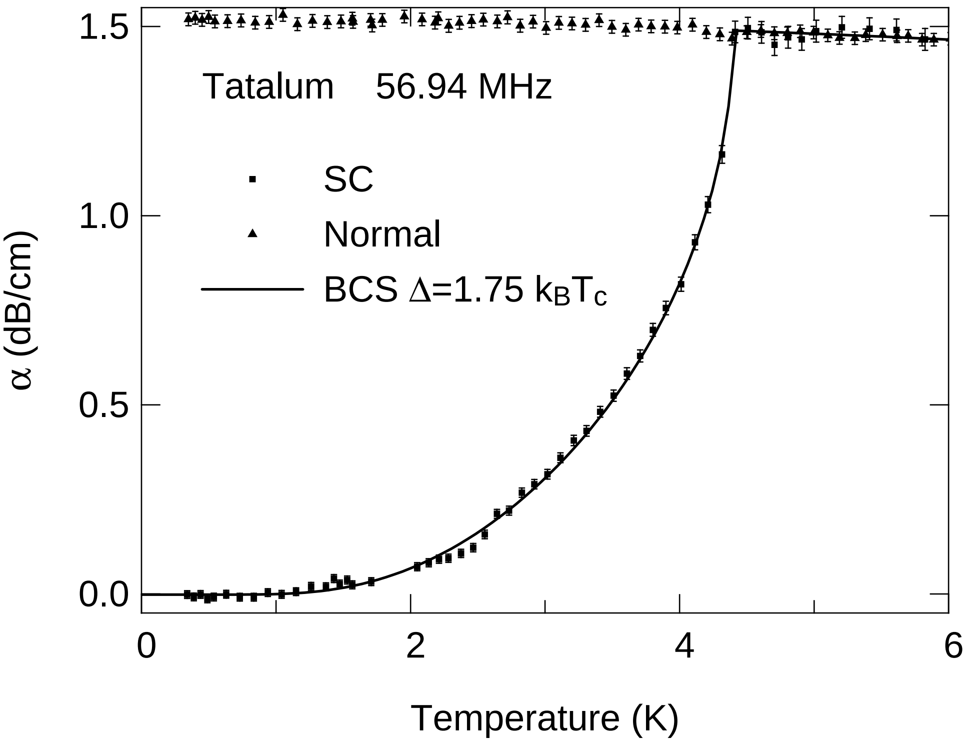

Figure 3.7: The attenuation of tantalum for both the superconducting state (no applied field) and normal state (0.75 T). The curve shows the result of a BCS fit to α_S/α_N. The gap found is $\Delta = 1.75 \pm 0.02$, very close to the simple BCS result (1.764 k_BT_c).

The temperature dependence of the gap is assumed to be the standard BCS curve with an amplitude at $T = 0$ given by Δ_0 in units of k_BT_c which is a also a free parameter (weak coupling BCS has $\Delta_o = 1.764 k_BT_c$). The function $\alpha_n(T)$ is a fit to the normal state attenuation which has a very weak temperature dependence for this sample. Finally the critical temperature can also be left as a free parameter. With all parameters free we obtain the following values: $B = 1.00 \pm 0.01$, $T_c = 4.40 \pm 0.01$ K and $\Delta_0 = 1.75 \pm 0.02$. This is in good agreement with the weak coupling BCS result and with previous experiments [96].

The measurement shown in the graph was performed at 56.94 MHz. Using a density of 16.65 g/cm^3 and the measured sound velocity of 4.26 km/s, the amplitude at T_c of 1.49 dB/cm translates as a viscosity of 3.44 poise. We obtained a similar value (3.6 poise) for a temperature sweep at 132.2 MHz, which implies we where in the hydrodynamic limit were the simple BCS result applies for transverse waves. We also performed a field sweep at 350 mK. It showed no change until 50 mT where it quickly reached the normal state value at 75 mT (which we define has H_c).

Therefore both the experimental setup and the data analysis work correctly and give the expected results. Hence we can use this system with confidence in order to extract information about Sr_2RuO_4.

4

$\mathrm{Sr_2RuO_4}$

Since the discovery of superconductivity in Sr_2RuO_4 in 1994 [24], many experiments have been done. Initially the crystal quality was not high enough to measure the intrinsic superconducting properties. It is possible to understand the modification to the intrinsic properties that impurities and defects produce, but this can be complicated especially when the behavior of pure crystals is not known. Therefore the initial measurements were fine for the normal state, but gave some confusing results for the superconducting state. For a recent introduction to Sr_2RuO_4, see [97].

4.1 Normal state

The initial interest in this material was because it is the first superconductor that has the same structure as the high-T_c superconductor $(La,Sr)_2CuO_4$ but without copper (see [25, 26, 98, 99] for Sr_2RuO_4 crystal structure). Both have the perovskite structure (see fig. (4.1)) and similar crystal lattice parameters (see table (4.1)). Both systems are of the D_{6h} (I4/mmm) crystal symmetry group. It is a body-centered tetragonal lattice. The body center means that the unit cell repeats with a shift of half a unit cell in the plane and along the z-axis. The conventional tetragonal unit cell therefore contains 2 units of Sr_2RuO_4. It basically has planes of RuO_2 instead of CuO_2 which are the site of superconductivity. The other components provide structural stability and doping to make the plane conducting.

But contrary to $(La,Sr)_2CuO_4$ it does not have a structural transition at low temperature and is very stable. Many refinements by neutron scattering down to low temperatures have been unable to detect any change in structure [100, 101, 102, 103, 104, 105].

Also contrary to the high-T_c, the normal state is easily reachable (since as will be seen later, the superconductivity is very fragile) and looks like a 2D Landau Fermi liquid. A Fermi liquid is a system where the characteristics can be matched to that of a free electron gas. One of the effects of interactions, *e.g.* electron-electron, is to renormalize

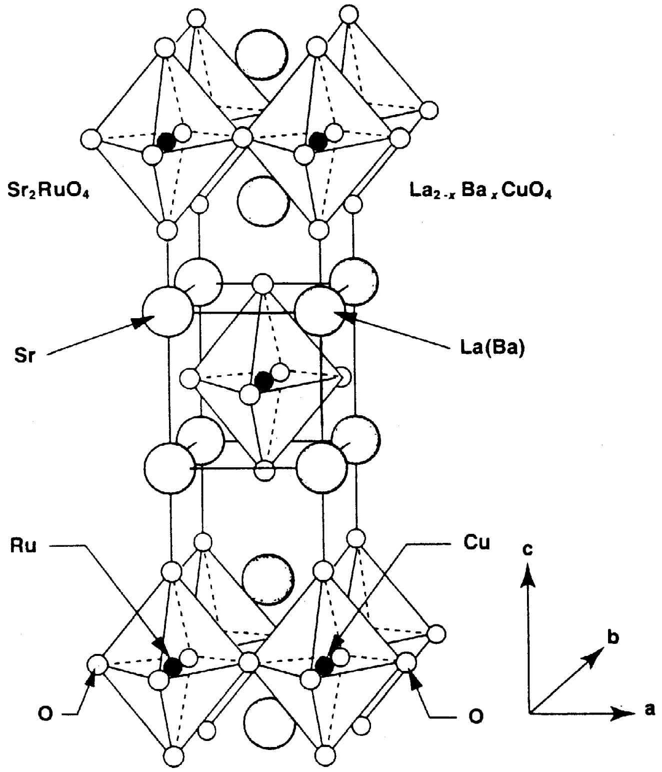

Figure 4.1: Crystal structure of Sr_2RuO_4 and of the isostructural high-T_c superconductor $(La,Sr)_2CuO_4$.

Parameter	Sr_2RuO_4	$La_{2-x}Sr_xCuO_4$
$a = b$ (Å)	3.8628	3.78
c (Å)	12.7204	13.23
ρ (g/cm^3)	5.954	7.03
M (g/mol)	340.31	400.2
V (cm^3/mol)	57.16	56.93

Table 4.1: Lattice parameters and density of Sr_2RuO_4 at 2 K from [102]. It has a body-centered tetragonal structure. The approximate values for LSCO are taken from [59], choosing $x = 0.1$ for ρ and M.

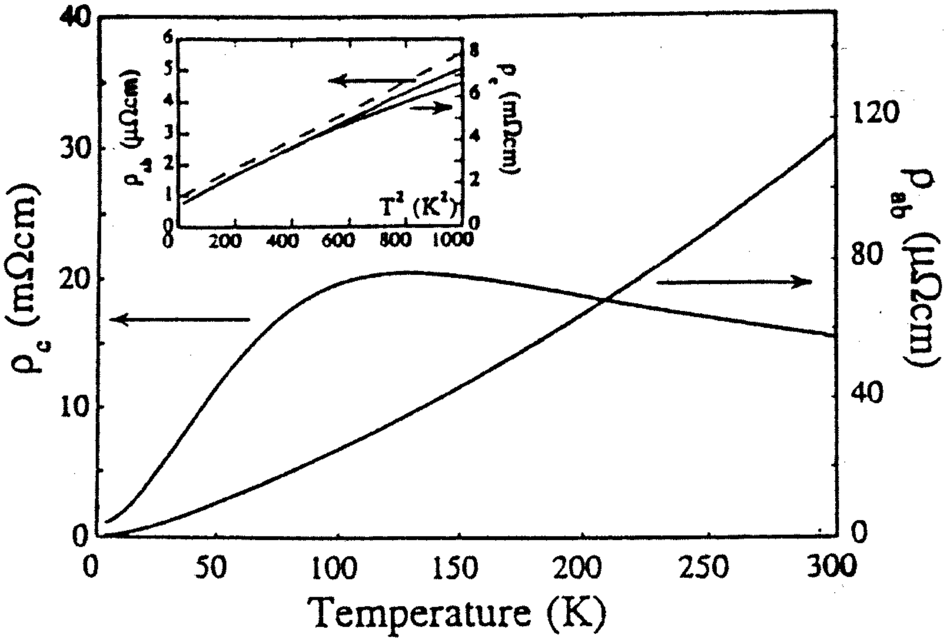

Figure 4.2: Resistivity of in-plane and c-axis resistivity. The inset shows the low temperature T^2 behavior (from [106]).

the mass and other constants of the free electron model. The first evidence of Fermi liquid behavior is that the temperature dependence of the resistivity is quadratic at low temperature (fig. (4.2)) [107] as is expected from a Fermi liquid with electron-electron interactions. It is seen both for the in-plane and out of plane resistivity of Sr_2RuO_4. The resistivity also demonstrates the anisotropy of this material. The out-of-plane resistivity is 1000 times larger than the in-plane resistivity. Resistivity measurements up to 1300 K have been done and show that Sr_2RuO_4 becomes a bad metal at high temperature [108], similarly to the high-T_c. The mean free path becomes less than the lattice spacing but the resistivity still increases with temperature while standard conduction processes would show saturation.

The normal state can be described microscopically by the Fermi Surface. In samples of high enough purity the surface can be measured by magnetic oscillations, in particular the de Haas-van Alphen and the Shubnikov-de Haas effects [110, 112]. Combining such measurements with calculations of Fermi surfaces using LDA [113, 114] (see [115] for a tight-binding approximation) the geometry of the surface is obtained. There are three sheets which come from the three Ru orbitals: xy, xz and yz. The xy orbital has a strong 2D character and produces a cylindrical Fermi surface called γ. The other two

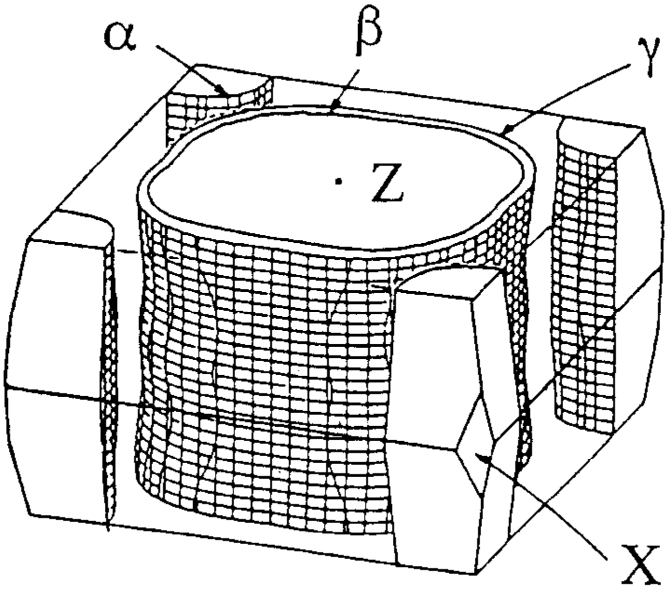

Figure 4.3: Fermi surface of Sr_2RuO_4.

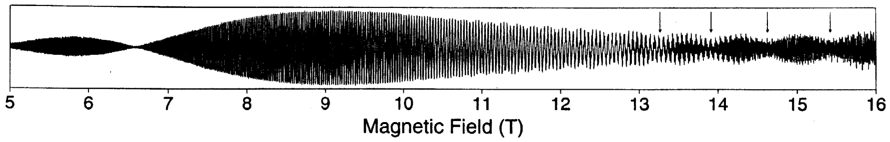

Figure 4.4: Example of dHvA data from [109]. Note the modulation of the amplitude (beats) which are used to extract warping information.

orbitals have more of a 1D character but they hybridize together in order to form two squarish cylinders called α and β. One is centered on the origin and is an electron pocket like the γ. The other is on the corner of the Brillouin zone and is a hole pocket (see fig. (4.3)). The sum of the occupied volume in k-space is twice the unit cell volume. This is another way of saying that there are four free electrons per unit cell (2 spins per state). The dHvA measurements were refined by looking closely at the beating and angular dependence [109]. Fig. (4.4) shows an example of the field sweep taken showing the beating in the signal. From this, the 3D warping of the Fermi surface is obtained. All these values provide an accurate view of the Fermi surface and the effective mass. The effective mass represents the k dependence of the energy surface and provides a measurement of the average Fermi velocity around the surface. The data for the three sheets is shown in table (4.2).

Parameter	α	β	γ
Type	Hole	Electron	Electron
F (kT)	3.05	12.7	18.5
Volume (% of BZV)	10.8	45.7	66.7
Average k_f (Å^{-1})	0.302	0.621	0.750
$\Delta k_f/k_f$ (%)	0.21	1.3	<0.9
Cyclotron mass m_c^* (m_e)	3.4	7.5	14.6
$v_f = \hbar k_f/m_c^* m_e$ (km/s)	103.	95.9	59.5
Band mass (m_e)	1.1	2.0	2.9

Table 4.2: Measured and calculated Fermi surface parameters for Sr_2RuO_4 from dHvA measurements obtained from [110] (the masses are from [111]). F are the observed dHvA oscillation frequencies. The volume is given as a fraction of the Brillouin zone volume (BZV). $\Delta k_f/k_f$ represents the 3D warping of the cylinders (see [109] for a more detailed study of the warping) and v_f is an averaged Fermi velocity on the surface. The band masses are from band structure calculations.

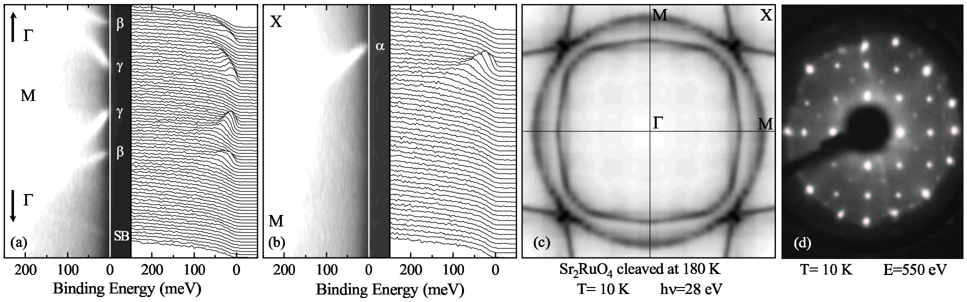

Figure 4.5: Fermi surface from angle-resolved photoemission spectroscopy [121]. Energy distribution curves along different directions are shown in panel a) and b). The intensity at the Fermi energy (one method of extracting the Fermi surface) is in panel c). In panel d) a LEED pattern shows the surface quality.

Other techniques that extracted Fermi surface information from magnetic field effects are angle-dependent magnetoresistance [116] and oscillations in the elastic constants [117, 118]. Also cyclotron resonance was used to extract somewhat different effective masses [119] which is attributed to strong electron-electron interactions.

Using this Fermi surface, reasonable values of the heat capacity, the resistivity, the Hall effect and the susceptibility can be calculated [112, 120]. A comparison of measured and calculated effective masses yields a renormalization of 3–5.

Additionally the Fermi surface can be seen using the technique of angle-resolved photoemission spectroscopy (ARPES). In that technique a high-energy photon (10's of eV) is sent into the sample. This photon penetrates at most a couple of layers in the material and ejects an electron. By detecting the electron direction and energy, and since we can assume the electron was restricted to the 2D planes of the material, the momentum and energy of the original electron can be calculated. The energy is related to the Fermi energy which is obtained from a standard reference (usually gold) which is in electrical contact with the sample. The Fermi energy is seen from the Fermi function discontinuity which is identifiable even at higher temperature. What is observed is that the scattering intensity as a function of momentum and energy shows peaks. These come from the quasi particles which are built up of the detected electrons. The peaks show the positions of the energy bands. Bands crossing the Fermi energy define the locus of the points of the Fermi surfaces. The result of such a map from ARPES for Sr_2RuO_4 is shown in fig. (4.5), where all three sheets are seen. This technique as been used successfully in the high-T_c's to look at the Fermi surface of those materials where dHvA and similar techniques have not been successful yet. It was also used to look at the superconducting gap and even its angular dependence. This is not yet possible in the case of Sr_2RuO_4 since the gap is too small. The best energy resolution of that technique is currently a couple of meV while the gap in Sr_2RuO_4 is smaller than 1 meV.

The impressive results from this technique needs to be checked against certain caveats. As mentioned above the best results are obtain for 2D systems because then the reconstruction of the kinematics can be fully done. The measurement provides two angles for the direction of the outgoing particle which can be mapped to two components of the momentum in 2D. But the technique is sensitive only to the first few layers of material and is therefore very sensitive to surface conditions. This was seen in this material where initially the analysis of the data was made complicated because of the appearance of many artifacts [122, 123, 124, 111]. Some of these even made one of the electron pockets look like a hole pocket instead. It is now believed that these artifacts were the result of surface states and surface reconstruction which produced shadow bands [121] and not from the effect of surface ferromagnetism [125]. A lot of these extraneous effects can be removed by different treatments of the surface, like cleaving at high temperature (180 K). Because the ARPES result can be compared with many other techniques, Sr_2RuO_4 is a good tool to understand similar effect observed in the high-T_c materials where the comparison with other techniques such as the dHvA effect has not been possible.

This material does not show ferro- or antiferro-magnetism. But similarly to most of the other unconventional superconductors (high-T_c, heavy fermions, organics) it is also close to a magnetic phase. Some compounds in the same family are ferromagnetic such as $SrRuO_3$ while others are antiferromagnetic insulators (AFI) like Ca_2RuO_4 [126]. Doping studies have been done for example on $Ca_{2-x}Sr_xRuO_4$ where the AFI phase is present below $x = 0.2$ and the magnetism seems to be tuned by structural effect [127, and references therein]. Structural effects also play a role in $Sr_2Ir_{1-x}Ru_xO_4$ which is a weakly ferromagnetic insulator at $x = 0$ [128, 129]. $Sr_2Ru_{1-x}Ti_xO_4$ shows localized magnetic moments as the substitution of the non-magnetic Ti is increased [130]. Under pressure $Sr_3Ru_2O_7$ becomes ferromagnetic [131] while without applied pressure it shows metamagnetism; it behaves as a Fermi-liquid except in certain field ranges where it becomes a non-Fermi liquid [132]. These all suggest that Sr_2RuO_4 may be close to a magnetic instability of the ferro- or antiferro-magnetic type. In fact, resistivity measurements under pressure show a crossover that could be due to magnetism [133]. Also Ru and O NMR show that the spin susceptibility is enhanced over the band structure calculations [134, 135, 136], which is due to spin fluctuations. O NMR additionaly show a connection of the spin fluctuations to the anomalous charge transport at high temperature [137]. Neutron scattering measurements have not observed ferromagnetic spin fluctuations, but they observed significant incommensurate spin fluctuations at $\mathbf{q}_0 = (\pm 0.6\pi/a, \pm 0.6\pi/a, 0)$ [138, 139]. This was expected from theory because of Fermi surface nesting around that vector [140]. The normal state spin fluctuation spectrum has been studied further theoretically in [141, 142, 143] and a recent article combines the NMR and neutron experiment and attempts to give a coherent view of spin fluctuations in Sr_2RuO_4 [144]. The ruthenates have interesting magnetic behavior and in particular it is believed that spin fluctuations in Sr_2RuO_4 play an important role in the superconductivity.

4.2 Superconducting state

In the previous section it was seen that the normal state is understandable in terms of a Landau Fermi-Liquid picture and is well characterized. This gives a nice reference state to use in theoretical work, for example the BCS theory should be applicable. This relative simplicity helped the early theoretical developments. As such, soon after the discovery of the superconductivity of Sr_2RuO_4 [24], there were proposals by Rice and Sigrist [27] and Baskaran [28] that Sr_2RuO_4 was an analogue of superfluid ^{3}He. They therefore

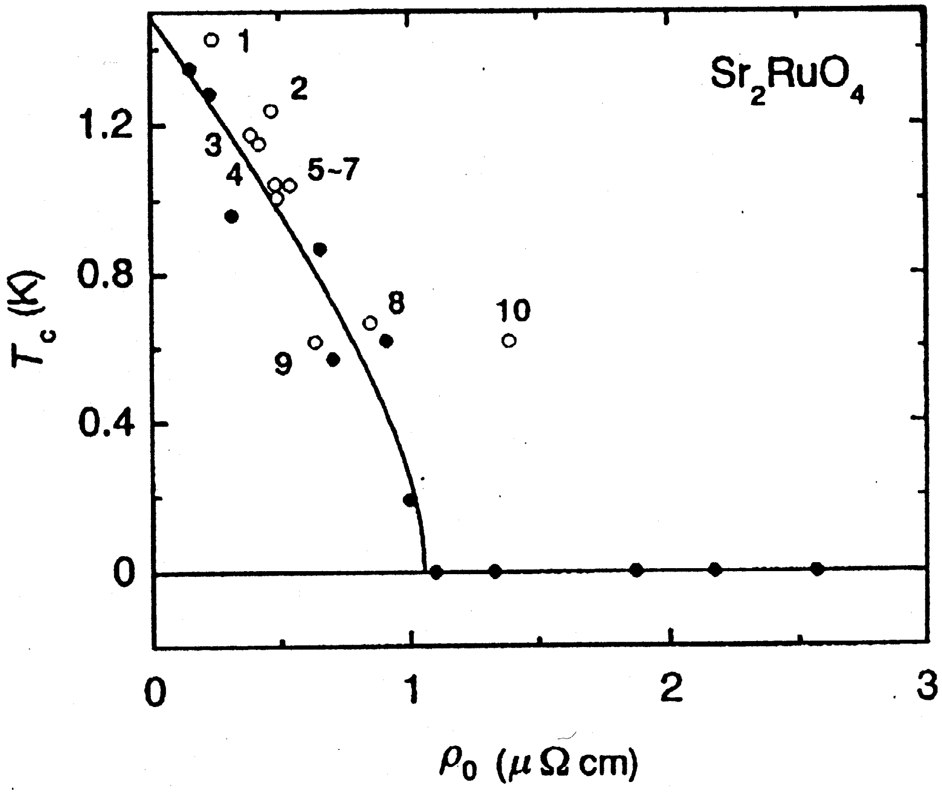

Figure 4.6: Impurity dependence of T_c of Sr_2RuO_4. The residual (0 K) resistivity is used to parameterize the impurity concentration (from [145]).

predicted this was a spin-triplet superconductor and proposed many order parameters with p-wave structure. This would obviously make this superconductor unconventional and also quite different from the high-T_c which are spin singlet and d-wave. It actually looks more like the heavy fermion superconductor UPt_3, but might be simpler because it is two-dimensional and spin-orbit coupling is not as strong.

The initial measurement of resistivity and susceptibility that showed the superconductivity also showed that this material was very sensitive to impurities. For example the dependence of the critical temperature on impurity concentration is shown in fig. (4.6) [146, 145]. For the impurity concentration, the residual resistivity is used which is the temperature independent part (at low temperature) of the resistivity and is obtained by applying a magnetic field large enough to make the sample normal and/or by extrapolating from higher temperature. This kind of dependence cannot be explained in terms of an isotropic gap if the impurities are non-magnetic. As was mentioned before the effect of the impurities is to remove anisotropy in the gap function, so no effect is seen if the gap is already isotropic. Of course magnetic impurities have a large effect on the superconducting state because they have a pair breaking effect; magnetism does not mix with conventional superconductors. But if the superconductor has anisotropy then even non-magnetic impurities will have an effect on the gap. Therefore this sensitivity to non-magnetic impurities suggests unconventional superconductivity. These measurements also showed the intrinsic critical temperature to be around 1.5 K. Samples with such a T_c are now available but for the first few years measurement were done on sample with a T_c of around 1 K.

Note however that transition temperatures around 3 K have been observed. These are due to Ru lamellae inclusions in the sample which enhance T_c [147] and modify other properties like H_{c2} [148]. The presence of this "3 K" phase depends on the crystal growth conditions [149] and should be avoided in order to measure the intrinsic properties of Sr_2RuO_4.

Most theories for the superconductivity in Sr_2RuO_4 rely on spin fluctuations as the important interaction for the pairing. Conventional superconductors rely on phonons and this leads to the isotope effect. Changing some atoms in the crystal with a heavier or lighter isotope changes the phonon spectrum slightly and this in turn changes the critical temperature. In the case of Sr_2RuO_4, even if the pairing is from spin fluctuations, phonons can still have an effect on the superconductivity. The isotope effect for Sr_2RuO_4 was measured and a sign reversal was observed in high-quality crystals [150]. This cannot be explained by simple theories and might require both pair-breaking and anharmonic phonon effects to be taken into account.

4.2.1 Evidence for spin-triplet p-wave pairing

Because of the initial prediction of spin-triplet p-wave superconductivity in this material, most measurements were initially focused on trying to see if this was the case. A consequence of spin-triplet is that the spin-susceptibility could be temperature independent in some cases contrary to spin-singlet superconductors. The pairing in spin singlet forces the susceptibility of the electron pairs to be zero. It is not possible for them to sustain a polarization without breaking pairs. Therefore the susceptibility in that case is expected to drop to zero below T_c. In a spin-triplet, pairs are formed of the same spin and polarization can be obtained by changing the occupation of pairs along the field and opposite to the field. This is the same effect as in the normal state and so no significant change is expected if the field is aligned in a direction to allow this behavior. This is

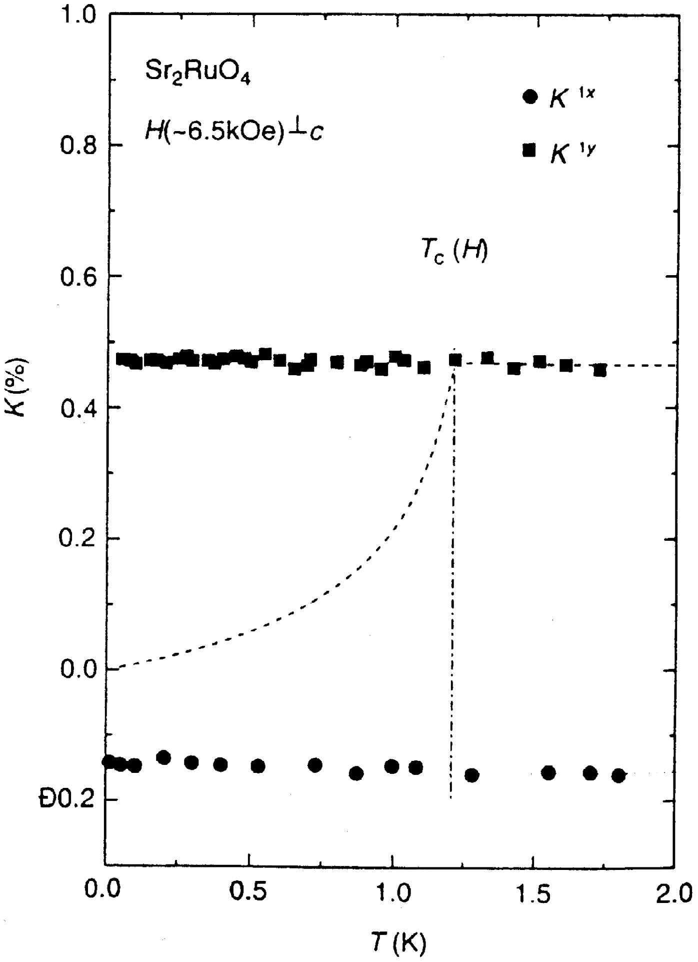

Figure 4.7: Temperature dependence of the ^{17}O Knight shift of Sr_2RuO_4 for two different sites [151]. The line is the expected behavior for a singlet *d*-wave gap. The lack of change at T_c is indicative of spin-triplet pairing.

the behavior that was observed for Sr_2RuO_4 as seen in fig. (4.7). In that experiment the field was in-plane and the susceptibility was obtained from the NMR Knight shift of the ^{17}O nucleus [151]. Similar results have been obtained for the ^{99}Ru nucleus [152] and from neutron scattering experiments [153]. The identification of spin triplet by this technique rests on the conclusion that the lack of change is due to the triplet nature. Another possible reason would be that spin-orbit coupling is so strong that the electron spin is not a good quantum number. It is believed this is not the case in this material [154]. To increase this belief the field applied perpendicular to the planes would be interesting because then it should show some temperature dependence but since the critical field along that direction is so much smaller (70 mT instead of 1.5 T) it is not possible to do

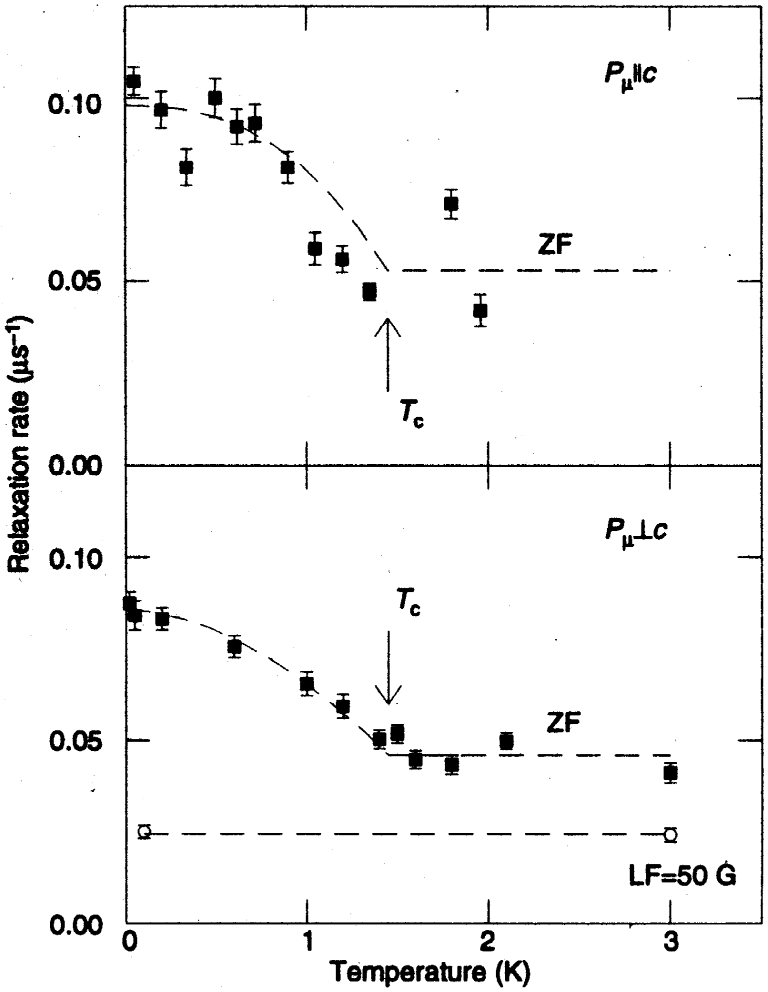

Figure 4.8: μSR relaxation rate as a function of temperature for Sr_2RuO_4 [155]. The increase below T_c is related to the appearance of a magnetic field which is indicative of time-reversal symmetry breaking.

those kind of experiments.

Another magnetic probe of superconductivity is muon spin relaxation (μSR). In that technique, spin polarized muons are implanted in the sample. These muons live for a short period of time and sample the local magnetic field where they are implanted by having their spin rotate. When the muon decays, it emits a positron preferentially in the direction of the muon spin. From a time histogram of the muons which decay (10^7) in a particular direction, the internal field distribution can be obtained. For most order parameters, the time reversal symmetry (TRS) is conserved and no magnetic field is expected to appear as the sample becomes superconducting. But for states where the TRS is broken, it is possible that an internal magnetic field is produced. TRS breaking requires a multi-component order parameter and is possible for some unitary states ($\Delta_i\Delta_j^* \propto \delta_{ij}$) and for all non-unitary states. The magnetic field produced by TRS breaking in the bulk is usually too small to measure but at defects, impurities and/or domain walls it can become measurable [66, chapter 15][155]. What was observed in $\mathrm{Sr_2RuO_4}$ under zero applied field is the spontaneous appearance of a small randomly distributed magnetic field [155], as shown in fig. (4.8). A possible source for a small magnetic field besides a gap with TRS breaking would be the appearance of a magnetic state at the same temperature but this is ruled out by measurements in impure crystals ($T_c = 1$ K) which show the same coincidence of magnetic field and superconducting state. More complicated explanations can be used but the simplest one is that the magnetic field is the result of a superconducting order with TRS breaking.

According to the previous two experiments, and considering the tetragonal symmetry of $\mathrm{Sr_2RuO_4}$, a two-component order parameter spin triplet gap of the E_u type is the most probable. Assuming the gap is strongly two-dimensional, we have the representation (k_x, k_y) and the order parameter, stable at low temperature, which breaks TRS is $k_x \pm \mathrm{i}k_y$, i.e. the two-component order parameter (η_1, η_2) is (1, $\pm$i). We call this the p-wave gap. The amplitude of this gap is isotropic so thermodynamic measurements that depend on the gap amplitude should provide the same results as for s-wave superconductors, i.e. exponential behavior for the heat-capacity, thermal conductivity, ultrasound attenuation, penetration depth and others is expected. As we will see this is not the case. Even if the amplitude of this gap is the same as for a s-wave, its response to impurities is very different. As we mentioned before in section 2.5.3, an effect of impurities is to remove gap anisotropy. In the case of a s-wave gap, impurities have no effect since the gap is already isotropic. In the case of the p-wave, there is a continuously changing complex phase around the Fermi surface. This anisotropy cannot be removed without destroying the superconducting order. The effect of impurities on the p-wave state was explored theoretically and results in a suppression of the gap, a suppression of T_c and the appearance of a residual density of states at zero energy [156]. These effects will modify measurable quantities. In particular, the residual DOS will be seen as a residual linear term in the low temperature heat capacity.

The presence of a multi-component order parameter has other effects. In a Ginzburg-Landau expansion of the Free energy, which is valid close to the transition, the energetics of different vortex arrays can be compared. This was done and it predicted a square structure and it also predicted a distinctive field distribution [157, 158] around the vortices. The vortex structure was then observed with neutron scattering to agree with this. Spin-polarized neutron scattering is a magnetic probe in reciprocal space but the resulting spectrum can be Fourier transformed to obtain the real space field distribution [159, 160, 161].

The anisotropy of the vortex structure is related to the anisotropy of the upper critical field. The measurements show an in-plane anisotropy of about 3% at low temperature (0.35 K) [162]. The [110] direction has a larger critical field than the [100] direction. Of course, because of the 2D character of the system, the critical field in the [001] direction is much smaller. At low temperature, the critical field in the plane is about 1.5 T while it is about 0.075 T along the c-axis. This in-plane anisotropy is small and changes sign at higher temperature and smaller field. This behavior was not expected by theory and could be the result of accidental cancellation between the different bands [163]. The anisotropy is very sensitive to the direction of the field. A small misalignment of the field out of plane (0.6°) removes this anisotropy. The sign is also opposite to what was needed for the vortex structure. All of these observations seem to be explained by an extension of the work of Agterberg [157] where the effect of induced non-unitary gap order is added [68]. This additional source of anisotropy becomes important at high field and low temperature. It also relies on some spin-orbit coupling to break the degeneracy of some of the possible order parameters.

Another effect of a multi-component order parameter is the possibility of multiple superconducting phases in Sr_2RuO_4 [157]. This is the case in superfluid ^3He and also in UPt_3. Since the order parameter for Sr_2RuO_4 seems to be a two-component order parameter it could support new superconducting phases. In the other compounds, these phases are accessed in different field, temperature or pressure regimes. Measurement of heat-capacity [164], thermal conductivity [165] and indirectly by AC susceptibility [162, 166] in Sr_2RuO_4 with the magnetic field aligned in the plane suggest the presence of a new phase very close to H_{c2}. This new phase is very sensitive to field alignment; 3° is enough to remove it for the thermal conductivity measurement and 0.5° for the susceptibility [166] (1° for the heat capacity [164]).

4.2.2 Evidence of nodes in the gap

As we just mentioned this gap does not explain the measured thermodynamic parameters. Power laws have been observed in many properties. The first power laws were observed in the specific heat [164]. The roughly quadratic dependence of the specific heat with

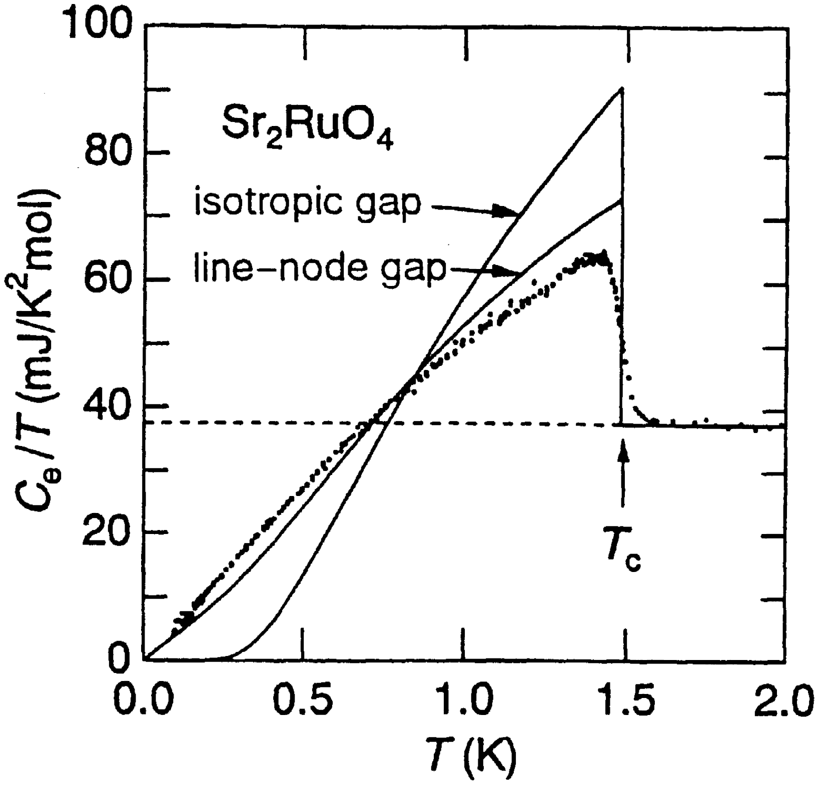

Figure 4.9: Electronic heat capacity of a high-quality single crystal of Sr_2RuO_4, from [164]. The phonon heat capacity has been subtracted.

temperature suggests the presence of a line of nodes, as shown in fig. (4.9). For a very pure sample, the residual term (the extrapolation of C_e/T to 0 K) is small. But it was observed to grow very quickly with impurities; for $T_c = 1.38$ K, the residual term is already 37% of the normal state [167, 168, 169]. A large residual term is also observable in the thermal conductivity of a dirty sample [170] and gets smaller in purer samples [171, 165].

Then measurements of the penetration depth reveals a T^2 or T^3 behavior depending on sample purity [172]. This technique was one of the key measurements for the high-T_c in order to identify the order parameter. The presence of a line of nodes should produce a linear dependence of the penetration length in the clean limit ($\xi \ll \ell$) and a T^2 dependence in the dirty limit ($\ell \ll \xi$). The authors suggests that the inconsistency between line nodes and the power law observed in Sr_2RuO_4 may be explained in terms of nonlocal dynamics [173]. This is because in the case of Sr_2RuO_4, the coherence length is much longer than in the high-T_c and this leads to the effect of non-local electrodynamics.

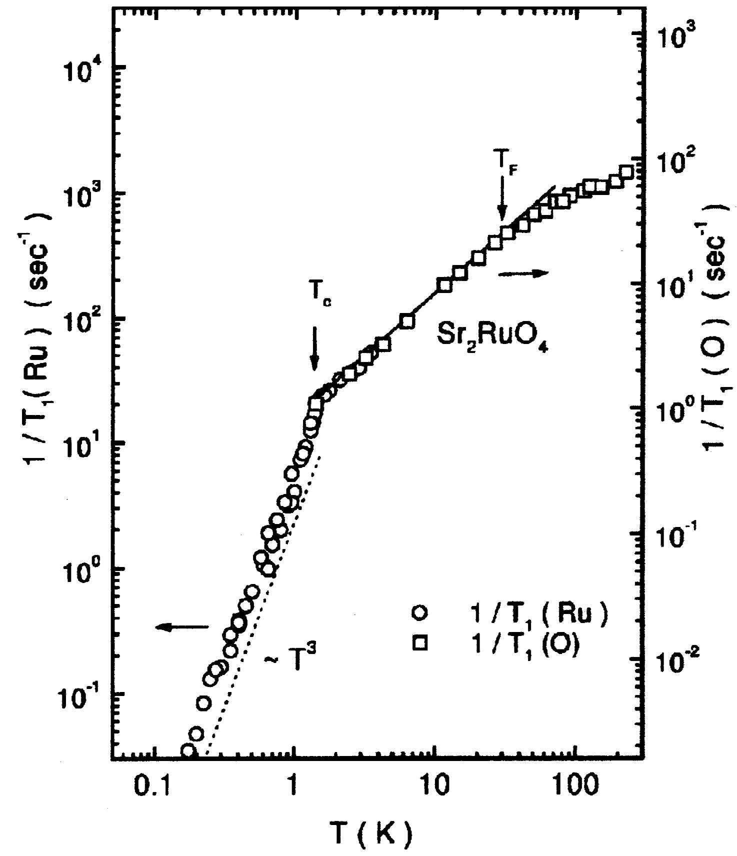

Figure 4.10: Relaxation rate from Ru-NQR from [174].

The group who did the experiments tried to test this idea but failed possibly because the anisotropy of the penetration depth masked the intrinsic behavior. In any case this experiment does show the presence of power laws even if the actual powers are not fully understood.

Another measurement that showed power laws is the nuclear spin-lattice relaxation rate ($1/T_1$). The NQR $1/T_1$ measurement is not affected by the Cooper pairs and so depends on the quasiparticles. It is affected by the coherence factors and should produce a peak just below T_c for s-wave superconductors (the Hebel-Slichter peak) and an exponential behavior at lower temperature. In the case of Sr_2RuO_4, no peak was observed and at low temperature a T^3 power law was measured while in the normal state it is a T^1 power law characteristic of a Fermi liquid, as seen in fig. (4.10) [174, 136]. This difference of T^2 can be explained by a line of nodes in the gap. It is similar to what is observed in the heavy-fermion superconductor UPt_3.

Thermal conductivity is another probe that shows power laws but the data does not

Parameter	along the ab plane	along the c-axis
T_{c0} (K)	1.50	
γ_N (mJ/K^{2}mol)	37.5	
$\Delta C_e/\gamma_N T_{c0}$	0.74	
Θ_D (K)	410	
$\mu_0 H_{c2}(0)$ (T)	1.50	0.075
$\mu_0 H_c(0)$ (T)	0.0194	
$\mu_0 H_{c1}(0)$ (T)	1.0×10^{-3}	5.0×10^{-3}
$\xi(0)$ (Å)	660	33
$\lambda(0)$ (Å)	1.8×10^3	3.7×10^4
$\kappa(0)$	55	2.7

Table 4.3: Anisotropic superconducting parameters of Sr_2RuO_4 (mostly from [176]). T_{c0} is the optimal T_c (from [146]. γ_N is the electronic specific heat coefficient ($C_e/T = \gamma_N$) in the normal state and $\Delta C_e/\gamma_N T_{c0}$ is the specific heat jump at T_c as a fraction of the normal state value [164]. Θ_D is the Debye temperature (taken from [167]) and corresponds to a phonon cubic term of the heat capacity of 0.19 mJ/K^{4}mol. $\mu_0 H_{c2}(0)$, $\mu_0 H_c(0)$ and $\mu_0 H_{c1}(0)$ are the upper, thermodynamic and lower critical field at $T = 0$ K respectively. $\xi(0)$, $\lambda(0)$ and $\kappa(0)$ are the coherence length, the penetration length and the Ginzburg-Landau parameter at $T = 0$ K respectively.

reach very low temperature. We will discuss another aspect of the thermal conductivity experiments in the next section. The ultrasound attenuation also shows power laws, as our results will make evident. Another group has measured the attenuation of one of the modes [175] and the sound velocity of a couple of modes [117, 118]. Their results will be discussed and compared to ours in the next chapter.

In table (4.3) we list many of the characteristic parameters of Sr_2RuO_4 we have discussed so far and some other ones.

4.3 Theories and order parameters

Since the beginning, it has been suggested that spin fluctuations are the microscopic interaction that gives rise to superconductivity in this material. Initial focus was on ferromagnetic spin fluctuations [177, 178]. More recently focus is given to anisotropic antiferromagnetic spin fluctuations, in particular the incommensurate fluctuations seen in neutron scattering, and models lead to triplet superconductivity over a certain range

Gap name	$\mathbf{d}(\mathbf{k})$	Sketch
p-wave	$\Delta_0\hat{\mathbf{z}}(k_x - \mathrm{i}k_y)$	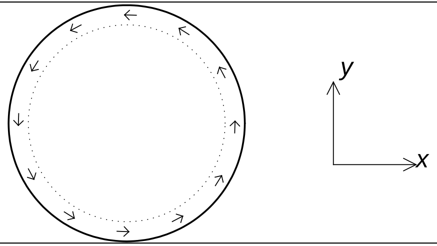
f-wave ($f_{x^2-y^2}$)	$\Delta_0\hat{\mathbf{z}}(k_x - \mathrm{i}k_y)(k_x^2 - k_y^2)$	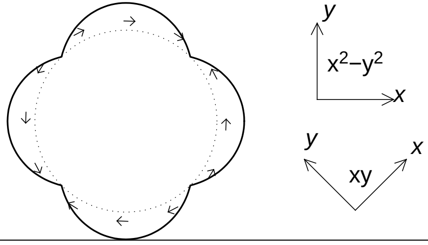
f-wave (f_{xy})	$\Delta_0\hat{\mathbf{z}}(k_x - \mathrm{i}k_y)(k_xk_y)$	See above
horizontal node	$\Delta_0\hat{\mathbf{z}}(k_x - \mathrm{i}k_y)(\cos(ck_z) + a_0)$ $\lvert a_0\rvert < 1$	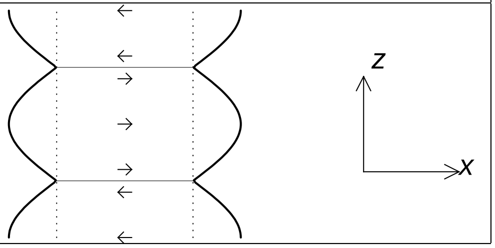

Table 4.4: List of some possible gap structure for Sr_2RuO_4 based mostly on [187]. The arrows on the drawings represent the complex phase of the order parameter. Note that the horizontal gap is plotted on the zx plane and that $a_0 = 0$ was used.

of parameters but the details vary [140, 179, 180, 181, 182, 183, 184]. However, before the mechanism can be ascertained, we must discover what is the order parameter structure. There has been many discussions of possible symmetries, limited to those consistent with the crystal point group symmetry.

Early predictions by Rice and Sigrist [27] (which also listed some possible gaps) and by Baskaran [28] pointed to triplet superconductivity. Then because of the large residual heat capacity initially observed, some attention was given to the non-unitary states that pair up only half the electrons [67, 185] (both gave lists of possible gaps). Another model to explain the large residual heat capacity was the orbital dependent superconductivity proposed by Agterberg *et al.* [186]. As we mentioned above, it considers different gap amplitudes on the different Fermi surfaces. A more recent survey concentrated on gaps with line nodes (horizontal and vertical) allowed by the symmetry groups [187].

To limit the number of states in our description, let us only pick some of the states that show TRS breaking and are odd-parity (triplet). These states will then satisfy automatically the results of the μSR and Knight shift experiments. We obtain the states listed in table (4.4), which are all also unitary ($\Delta_i \Delta_j^* \propto \delta_{ij}$) and have a single $\mathbf{d}$ component pointing out of the plane. Therefore the spins are in the plane.[1] The first state, the p-wave, is the only one without nodes. The f-wave states have vertical line nodes on the diagonal ($f_{x^2-y^2}$) or along the crystal axis (f_{xy}) of the unit cell. In general the p-wave and f-wave can mix like $d_f + \mathrm{i}\gamma d_p$, γ being a real number. This is because they are from the same symmetry group [187, 188]. This mixing removes the nodes. To have a pure f-wave then requires a microscopic theory to explain the absence of the p-wave gap but no such theory is known. Therefore the f-wave gaps cannot be justified by symmetry group arguments alone and for that reason its nodes are qualified as accidental. Nonetheless they are an easy way to modify the p-wave gap to include line of nodes and are also attractive because of their similarity with the high-T_c gap ($d_{x^2-y^2}$). The last state in the table, as the name implies, has horizontal line nodes situated at $k_z = \pm \cos^{-1}(-a_0)/c$ (hence the restriction $|a_0| < 1$ for the existence of nodes). It comes from the first two odd components of a Fourier series along the c-axis and is a simple way to move away from two dimensions.

The thermodynamic and transport properties of these states (and others) have been studied to some extent. The p-wave heat capacity, thermal conductivity, superfluid density, nuclear spin lattice relaxation rate and their dependence on unitary impurity scattering were studied in [156] and in the same formalism the sound attenuation was calculated in [156]. The heat capacity, thermal conductivity and London penetration depth of the orbital-dependent model were calculated in [186] and the effect of impurities (Born limit) on the heat capacity was studied in [189]. The heat capacity, thermal conductivity and sound attenuation of the f-wave states were studied with both unitary and Born impurity scattering in [74]. The heat capacity and thermal conductivity were also compared to the p-wave and orbital-dependent model. The gap with horizontal line nodes presented in the table has not been studied but a related gap structure, the 3D f-wave model defined by Maki and Yang [190], was studied for thermodynamics in [190, 191] and compared to the usual f-wave and a nodal p-wave in [192]. The 3D f-wave is a proposed structure for the heavy-fermion UPt_3 and has a *horizontal* node at $k_z = 0$

---

[1] This is because the components of $\mathbf{d}$ represent Cooper pairs which have zero spin projection along that direction (assuming weak spin-orbit coupling so that spin is a valid quantum number).

($\mathbf{d} = \Delta_0 \hat{\mathbf{z}} k_z (k_x + \mathrm{i}k_y)^2$). The nodal p-wave is based on the anisotropic p-wave introduced in [178] but with strong enough angular anisotropy that the gap has nodes (similar to extended s-wave). The sound attenuation and thermal conductivity of the 3D f-wave state were compared to the other f-wave states in [193]. The field dependence of the ultrasound attenuation of the f-wave states and horizontal line nodes has been studied in [194]. Many models described so far can achieve good fits to the the heat capacity but they cannot reproduce the convex shape of the data. A recent model proposed by Zhitomirsky and Rice [188] can reproduce this shape and it will be described further when discussing the ultrasound data in section 5.3.

To be able to close in on the symmetry gap any further, it is required to find the position of the line of nodes. Possible techniques for this are tunneling measurements which can even provide information on the phase dependence of the gap. Andreev reflection from Pt-Sr_2RuO_4 point contact [195] measurements and critical current measurements between Sr_2RuO_4 and a conventional superconductor [196, 197] are consistent with a spin-triplet p-wave order parameter. Additionally, tunneling through the Ru inclusions of the “3 K” phase suggest that that phase is also unconventional [198].

Another way to detect the phase variation of the gap is by observing a vortex with a *half*-quantum of flux. This was described theoretically for the heavy-fermions [199] but applies to any unconventional superconductor. If the order parameter changes sign it is possible to get a half-flux even in no magnetic field. This was observed in the high-T_c by a tri-crystal experiments where the combination of three crystal boundaries at different angles frustrates the order parameter and allows such a half flux quantum to sit at the corner [200, and references therein]. It was one of the crucial experiments in identifying their order parameter ($d_{x^2-y^2}$). In superconductors with multi-component order-parameters it is possible to have domain walls in a crystal that separate different orders. At these domain walls, a half-flux vortex could nucleate. Therefore looking for half-flux quantum with a technique like a SQUID microscope is a way to observe phase changes in the gap. The detection can be helped by constructing samples with a particular geometry and characteristics.

The gaps based on $\hat{\mathbf{z}}(k_x \pm \mathrm{i}k_y)$ have a non-zero orbital angular momentum ($L_z = \pm 1$). This introduces some form of chirality in the superconductor. The chirality produces such effects as a spontaneous Hall effect [201], but it is predicted to be small and as not been observed so far.

Another possible tool is to examine the perturbation produced by a single impurity on the superconducting state. This can be done using scanning tunneling spectroscopy. This technique has been used on the high-T_c with interesting results [202, 203]. No such experiments have been published so far in $\mathrm{Sr_2RuO_4}$ but theoretical predictions for p-wave and f-wave have been done [204].

It is also possible to use thermal conductivity in a magnetic field. By measuring the dependence of the thermal conductivity as a function of the direction of the magnetic field in the plane it is possible to see the angular dependence of the gap. Theoretical predictions for different gap structures have been done considering zero temperature and no vortex scattering [192] and also relaxing these restrictions to finite temperature and some vortex scattering [205]. For vertical line nodes this would produce a four-fold angular dependence of the thermal conductivity. The phase of this signal would indicate if the nodes are along the crystal direction or on the diagonal. Under certain conditions of field and impurity scattering it is possible for the four-fold dependence to change sign as the temperature is raised [205]. The result of those experiments is that no strong angular dependence was detected [206, 207]. The residual dependence was explained in terms of the anisotropy of the upper critical field. The result is then that the line nodes are not vertical but most probably horizontal. This null result is in contrast to successful observation of a four-fold term for the high-T_c superconductors such as YBCO [208, 209], in the organic superconductor κ-$\mathrm{(BEDT\text{-}TTF)_2Cu(NCS)_2}$ [210] and in the heavy-fermion $\mathrm{CeCoIn_5}$ [211]. Therefore the null result in $\mathrm{Sr_2RuO_4}$ looks convincing for the absence of vertical line nodes. But it requires a magnetic field and the interpretation depends on the proper calculation of the amplitude of the effect including temperature, vortices and impurities. All of these tend to reduce to amplitude and it is possible that in $\mathrm{Sr_2RuO_4}$ the amplitude was smaller than the measurement sensitivity.

Another technique is ultrasound attenuation and this is the one we chose and the results are presented in the next chapter. Some prediction for the p-wave [212] gap and the f-wave [74] were proposed and calculation for the 3D f-wave has been done and compared to other gaps [193]. In particular the position of vertical line nodes for possible f-wave states should give distinctive behavior for longitudinal and transverse waves along the axis and the diagonals, as see in fig. (4.11).

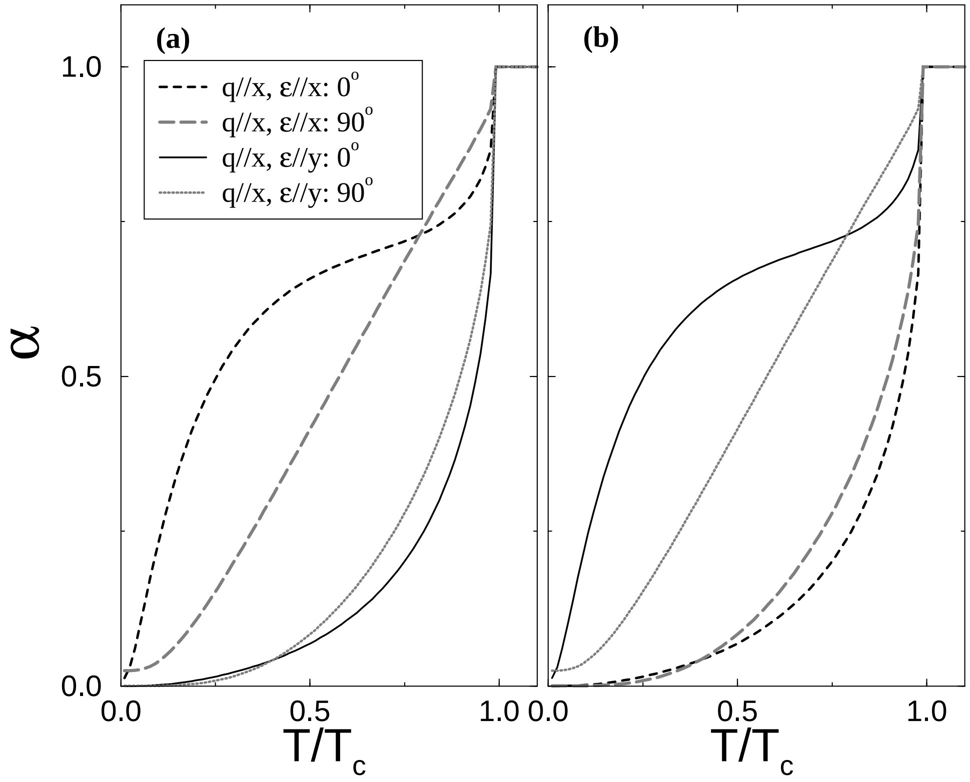

Figure 4.11: Calculation of the attenuation anisotropy for the f_{xy}-wave gap from [74]. In a) the calculation are done for the x axis along the crystal axis, while in b) it is along the crystal diagonal (in plane rotation of 45°). The angle represent the phase shift of the impurity scattering: 0° for Born and 90° for resonant scattering.

5

ULTRASOUND ATTENUATION AND VELOCITY OF Sr_2RuO_4

In this chapter we discuss the measurement and analysis of ultrasound attenuation and velocity in Sr_2RuO_4. The initial objective for this experiment was to see if nodes in the gap function indeed exist and if so find their position on the Fermi surface.

5.1 Sample characterization

The experiments that will be described shortly have been performed on a sample obtained from Prof. Y. Maeno at Kyoto University. The crystal (C121Ba) was grown by Z. Q. Mao using a floating zone method that employs an image furnace to reach the high melting point (∼2200°C) [149]. It was annealed at 1500°C in air for 72 hours. It was about 5 cm long with a cross section varying between 2.5 mm and 3.5 mm. The long dimension of the crystal was not aligned with any particular direction. It was about 7° out of the plane and 18° away from the *a*-axis. The *c*-axis was roughly along the shortest dimension of the cross-section. The slight misalignment of the *c*-axis produced a step-like structure all along the surface of the sample during crystal growth.

Fig. (5.1) shows the susceptibility of the original crystal. It has a T_c of 1.336 K obtained from the peak of the derivative. The small width of transition (about 0.05 K) shows it is a very homogeneous sample. Also, no so called "3-K" phase was detected. This crystal was then cut into multiple samples using a spark-cutter. They were attached onto a goniometer and aligned using Laue X-ray back reflection. Then the goniometer with the sample still attached was transferred to the spark-cutter where two parallel cuts were performed. The sample faces where then polished, finishing with a 1 μm diamond suspension. The sample alignment was then checked again using the Laue system and the face parallelism was estimated using a sensitive comparator.

Table (5.1) shows the different samples obtained from the original sample. The critical temperatures were extracted from the onset of change in the attenuation measurement. Sample S1 was cut along the length of the original crystal and was used for the initial

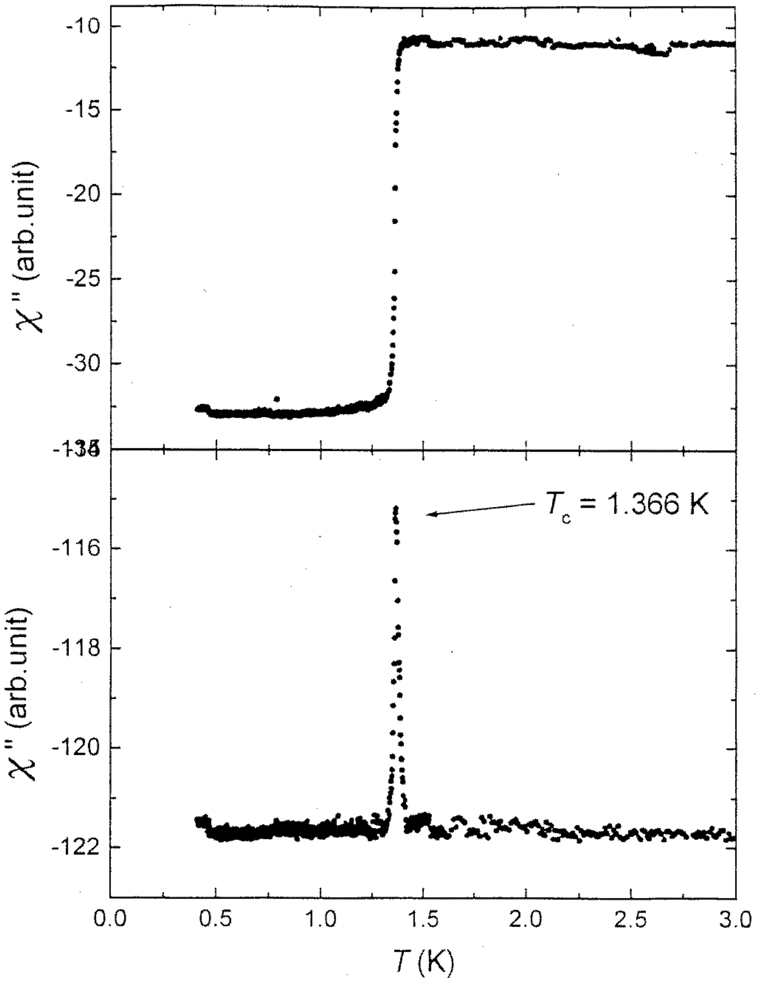

Figure 5.1: Susceptibility of the original Sr_2RuO_4 crystal (C121Ba) as measured by the group of Prof. Y. Maeno.

Sample name	Direction	Length (mm)	T_c (K)	Comment
S1	~18° in plane	5.61	1.44	Unaligned sample
S2	[100]	4.23	1.43	misaligned by 2.2°
S3	[110]	4.23	1.41	
S1'	[100]	3.98	1.44	Recut and polish of S1

Table 5.1: List of samples cut from the original C121Ba crystal.

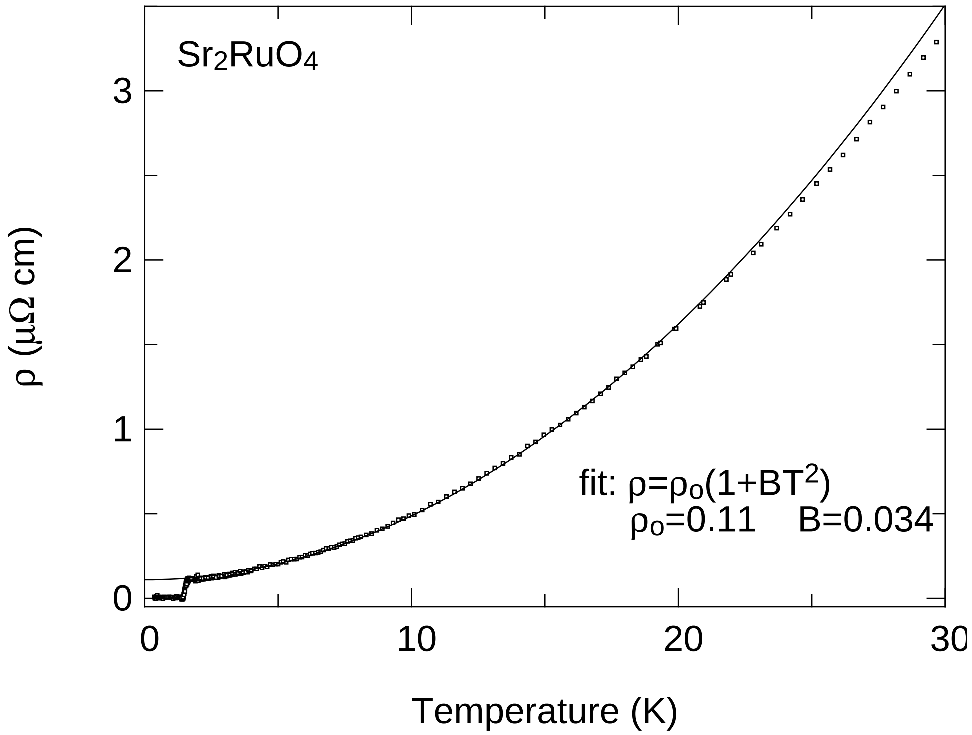

Figure 5.2: Resistivity of C121Ba Sr_2RuO_4 sample. The line is a fit to the expected T^2 behavior.

tests. S2 and S3 were then cut to be along the a-axis ([100]) and along the diagonal ([110]) of the crystal structure. It was subsequently observed that the S2 sample was misaligned in the plane by 2.2°. As will be seen later, this misalignment is much too large considering the strong anisotropy of this material. Therefore we reoriented and recut S1 in order to obtain a better sample which is called S1'. The alignment of that sample was checked and is $0.25 \pm 0.05°$. The alignment of S3 is not as critical and was measured to be better than 0.4°.[1]

The critical temperatures are not exactly the same as the one obtained from susceptibility mainly because it is a different measurement technique, but it could also partially be due to the different cryogenic system used (Kyoto and Toronto) which can have slightly different thermometer calibrations. The different critical temperatures between the S1, S2 and S3 samples were all measured in our dilution refrigerator. The difference between S1 and S2 is not significant but S3 is smaller. It is therefore slightly less pure and this should be kept in mind when comparing the measurements between samples.

Another sample was cut from the original crystal to measure the resistivity. It was

---

[1] The out-of-plane misalignment of S1' is also about 0.25° while for S3 it is 0.5°.

shaped into a square needle of dimensions[2] 5.00 × 0.10 × 0.16 mm by spark cutting and some polishing. The length of the needle was along the crystal *ab*-plane. Electrical contacts were then made on the sample using silver epoxy. In order to lower the electrical contact resistance, the epoxy was applied and then baked in flowing oxygen at 500°C for one hour. Wires were then attached to these contacts, again using silver epoxy. Because the sample has a highly anisotropic resistance, $\rho_c/\rho_{ab} \sim 1000$ at low temperature, the contacts were placed on the face parallel to the *c*-axis. In effect, the planes were shorted together. The contact resistances were less than 50 mΩ at room temperature. The room temperature value of the resistivity was 97 $\mu\Omega$ cm. Fig. (5.2) shows the low temperature resistivity curve. The line is $\rho = \rho_o + AT^2 = \rho_o(1 + BT^2)$ and provides a good fit to the data with $\rho_o = 0.11$ $\mu\Omega$cm and $A = 0.0037$ $\mu\Omega\,\mathrm{cm/K}^2$ ($B = 0.034$ K^{-2}). This is the expected behavior for Sr_2RuO_4 (see section 4.1) and is a result of Landau Fermi liquid theory. This sample has a RRR (residual resistance ratio) with respect to room temperature of about 880, which implies it is a very clean crystal. From the residual resistivity we can obtain the impurity limited mean free path using data from the dHvA experiments [112]. This resistivity of 0.11 $\mu\Omega$cm gives $\ell = 0.95$ μm. We will use this value later to estimate the frequency at which the sound wavelength is equal to ℓ ($q\ell \sim 1$).

We can list all the measurable sound modes according to the available crystals. This is done in table (5.2) where we introduce the naming convention we will use throughout the rest of the thesis. The letter L or T identifies the mode as either purely longitudinal or purely transverse. The digits identify the propagation direction of the sound wave, which at the same time identifies the sample used. For the 100 modes it could be S2 or S1' but when the sample is not specified it will always be S1'. We also identify the effective elastic constant (see also table (2.1)) for the mode. The measured velocity is obtained from the echo spacing and the sample length. It is accurate to about 2% except for the L001 mode which is less accurate. All the values except for L001 were measured at low temperature (below 4 K). The L001 mode was measured at room temperature and no attenuation was obtained. It was performed on a segment of the original crystal which had *c*-axis faces as a result of cleaving. These faces provided a sample length of 1.97 mm (less than half of the other lengths) and since this was a longitudinal mode (higher sound velocity) it was difficult to separate the echoes and therefore required very short pulses. This still permitted an estimate of the sound velocity but was not good enough for an

---

[2] The voltage contact separation is 3.69 mm which gives a geometric factor of 4.3×10^{-4} cm.

Sound mode	Propagation	Polarization	$\bar{C}$	Sound velocity (km/s)	Sample
L100	[100]	[100]	C_{11}	6.28	S1'
T100	[100]	[010]	C_{66}	3.30	S1'
L110	[110]	[110]	$\frac{1}{2}(C_{11}+C_{12}+2C_{66})$	6.41	S3
T110	[110]	$[1\bar{1}0]$	$\frac{1}{2}(C_{11}-C_{12})$	2.94	S3
T100c	[100]	[001]	C_{44}	3.41	S1'
T110c	[110]	[001]	C_{44}	3.39	S3
L001	[001]	[001]	C_{33}	6.35 (RT)	—

Table 5.2: We list the definition for the different sound modes measured. L and T identify the mode as either longitudinal or transverse; the digits identify the propagation direction. All the sound velocities (km/s=μm/s) were obtained at low temperature using the echo spacing except for L001. For L001 the velocity was obtained at room temperature. The sample used for L001 was a segment of the original crystal which had c-axis faces from cleaving (length of propagation 1.97 mm). The velocity are accurate to about 2% except for L001 which is less accurate.

attenuation measurement.

The sound velocities can be combined with the previously measured mean free path to obtain the frequencies at which $q\ell = 1$. For the longitudinal modes $v_L \approx 6.35$ km/s which implies $f \sim 1.1$ GHz while for the transverse modes $v_T \approx 3$ km/s implies a more restrictive $f \sim 500$ MHz. This sets the upper limit for the hydrodynamic regime where $q\ell \ll 1$.

It is possible to convert the sound velocities to elastic constants using $\bar{C} = \rho v_S^2$ where $\rho = 5.95$ g/cm^3 is the density (see table (4.1)). The result is shown in table (5.3). Most of the values are obtained from the sound wave which is composed of a single elastic constant. This leaves out C_{12} which is extracted from various combinations of velocities (hence the range of values). C_{13} is undefined because it requires the measurement of an impure mode which we did not do. C_{44} is an average of the measured sound velocities. C_{33} is the only value obtained at room temperature (the others are all at low temperature). In the last column we also show the results obtained from resonant ultrasound spectroscopy performed at room temperature by Johnpierre Paglione on a small parallepiped sample cut out from the original crystal. The difference between the two measurements comes in a large part from the different temperatures at which they were done. Some of the elastic

Elastic constant	From velocity (GPa)	From RUS (GPa) at RT
C_{11}	233	233 ± 2
C_{12}	124–131	106 ± 2
C_{13}	—	71.3 ± 2.0
C_{33}	238 (RT)	208 ± 2
C_{44}	68.2	65.84 ± 0.07
C_{66}	64.3	61.35 ± 0.03

Table 5.3: Elastics constants extracted from the sound velocity at low temperature (except for C_{33}, RT stands for room temperature) and a resonant ultrasound spectroscopy measurement at room temperature by J. P. Paglione. The conversion used a density of 5.95 g/cm^3.

constants, such as C_{12}, change a lot between room temperature and low temperature as was observed by Matsui *et al.* [117, 118]. The relative sizes of the elastic constants are not too far from what is expected for an isotropic material (which have only two independent elastic constants, see section 2.1). This can also been seen by the small anisotropy of the longitudinal and transverse sound velocities.

5.2 Normal state attenuation

Having characterized the sample we are now ready to look at the ultrasound attenuation. Before we study the attenuation in the superconducting state we need to make sure the measured data represents the intrinsic electronic attenuation and is not due to another source of attenuation or to systematic errors. We also need to identify whether the data is in the hydrodynamic limit or not.

We begin by looking at the amplitude of the signal in the normal state. In fig. (5.3) we show the viscosity for the four measured in-plane modes (L100, T110, L110 and T100). We plot the viscosity, $\eta = \alpha\rho v_S^3/\omega^2$ (see eqn. (2.21)), instead of attenuation because it is more directly related to the theory for the hydrodynamic limit. It doing so it removes the frequency and velocity dependence of the attenuation and allows comparison of transverse and longitudinal modes together. In fig. (5.4) we show the viscosity for the T1x0c modes which we will discuss separately. In table (5.4) we list the amplitude of the different modes at T_c in terms of viscosity and of attenuation in dB/cm and in dB/(cm GHz^2). These numbers can be used for general comparisons and also to see how large or small

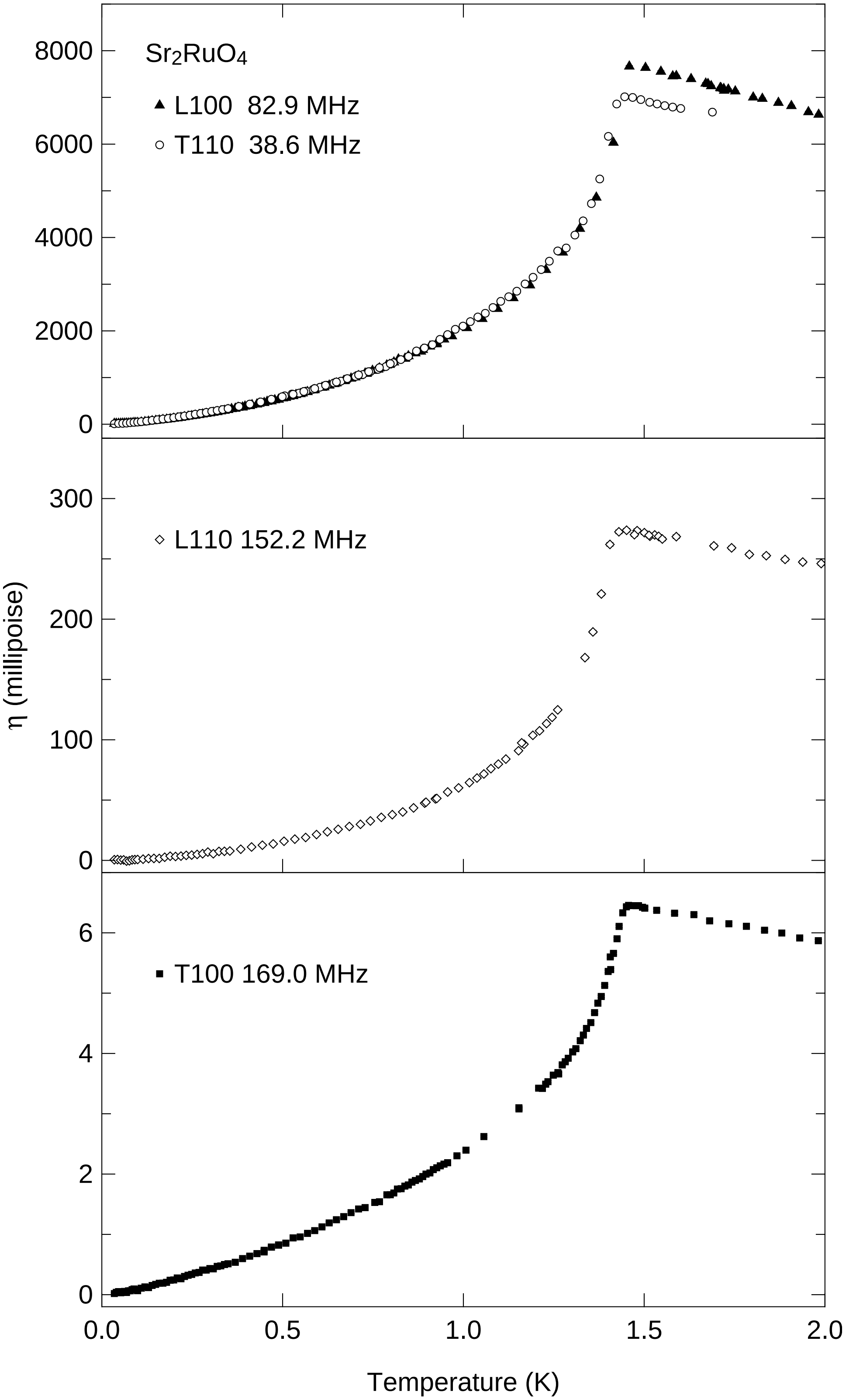

Figure 5.3: Viscosity of the in-plane modes of Sr_2RuO_4.

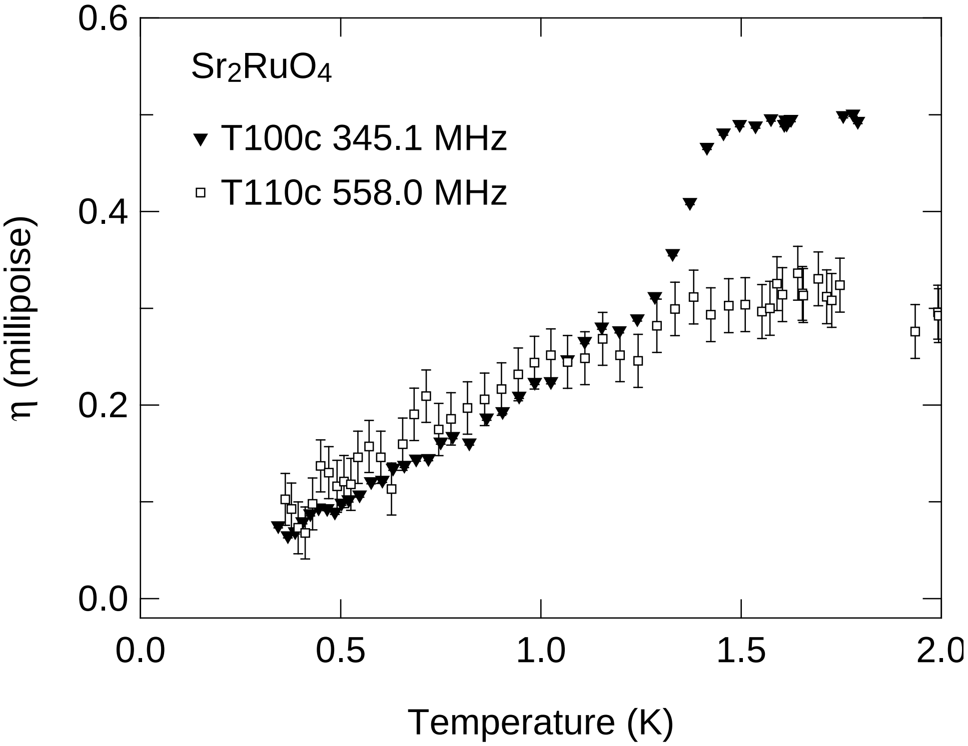

Figure 5.4: Viscosity of the c-axis polarized transverse mode of Sr_2RuO_4.

was the actual change (in dB/cm) at the measuring frequency. Note in particular the smallness of the T100 mode and especially the T100c mode.

Since the measured attenuation is relative, it is important to specify how the origin of the graphs was obtained. We have extrapolated the low temperature data using power law fits (usually below 0.3 K) and shifted the curves rigidly so that the fits went through the origin. This is expected to be the case for a conventional superconductor with a nodeless gap. This might not be valid for more complicated gap structures, where impurity scattering can produce a residual non-zero value for the attenuation and other properties of the material. Heat capacity measurements on dirty samples [168] show a fast increase of the residual linear term which reaches about 25% for samples of quality similar to ours but is less than 10% for samples of the highest quality. This behavior of the residual linear term is qualitatively well described by p-wave [156] and f-wave models [74]. These same models predict a much smaller residual term for the ultrasound attenuation [212, 74] when considering resonant impurity scattering.[3] Therefore the extracted attenuation amplitude, using the method just described to find an origin, should

---

[3] Without resonant impurity scattering those models have a much smaller residual heat capacity at low temperature [70, 69] for the same effect on T_c.

Mode	$\bar{\eta}$	millipoise	dB/(cm GHz^2)	dB/cm	Frequency (MHz)
L100	η_{11}	7830	912	6.27	82.9
T110	$\frac{1}{2}(\eta_{11}-\eta_{12})$	7110	8080	12.0	38.555
L110	$\frac{1}{2}(\eta_{11}+\eta_{12}+2\eta_{66})$	274	30.0	0.694	152.2
T100	η_{66}	6.50	5.19	0.148	169
T100c	η_{44}	0.50	0.36	0.043	345.1

Table 5.4: Comparison of normal state attenuation amplitude in many units. The data is obtained from the temperature sweep at the specified frequency. The amplitude in dB/cm is only valid at that frequency. The others should be frequency independent in the hydrodynamic limit.

provide an amplitude for the normal state which is at worst 30% too small and probably better than 10%.

Looking at the values at T_c for the four in-plane modes, it is obvious that there is a very large in-plane anisotropy. Both L100 and T110 have roughly the same amplitude but the longitudinal anisotropy is about L100/L110 = 29 and the transverse one is much stronger T110/T100 = 1100. To the best of our knowledge, anisotropies this large have not been reported before. Such anisotropies cannot be explained with the free electron model of attenuation. We will come back with a possible explanation later.

5.2.1 Data quality

Because of the extreme variation in attenuation, not all the data is of the same quality. The most accurate data is for the L100 mode. The attenuation of that mode provided an easily measurable attenuation at 82.9 MHz which was quite accessible with our setup. We had up to 20 echoes at low temperature and the attenuation was strong enough to leave 4 echoes at T_c (see fig. (5.5)). On the other hand the T110 mode had a much higher attenuation (even if it has the same viscosity, this is due to the smaller sound velocity). It required a much lower frequency and this was more difficult with our setup. The small transducers we used produced large diffraction effects at low frequency and a large amount of parasitic signals were excited in the sample. Therefore the background was not flat because of all the coherent acoustic noise and at most two echoes could be used for a proper analysis (see fig. (5.6)). These problems taken together resulted in data that was more prone to systematic errors such as the saturation of the amplitude at T_c

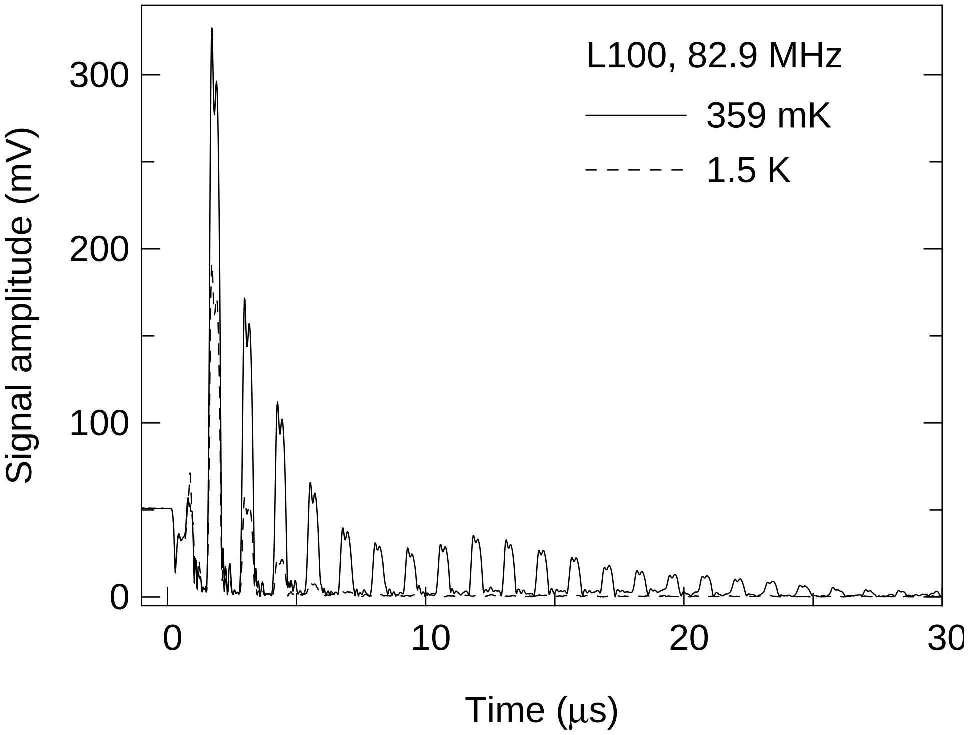

Figure 5.5: Echo signal example for the L100 mode.

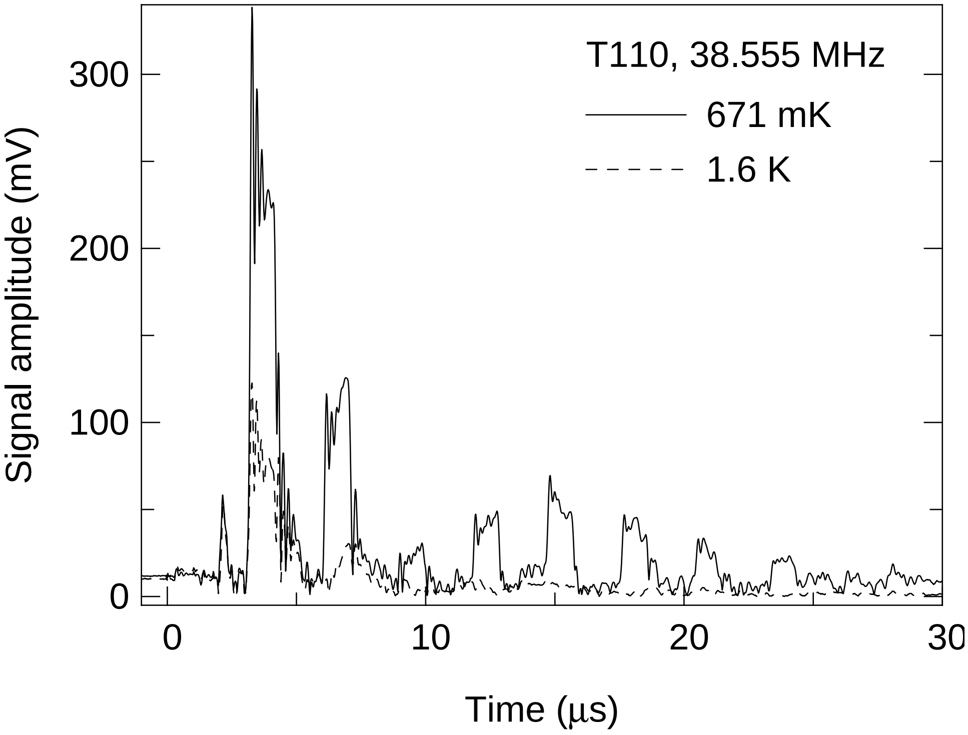

Figure 5.6: Echo signal example for the T110 mode.

due to incorrect background subtraction.

The other modes have a much weaker attenuation. The L110 mode was measured with 50 echoes at low temperature and still about 35 echoes at T_c with a rather flat background. The frequency needed was also easily achieved by our setup. This mode provided a good analysis except for the strong structure in the echo pattern (see fig. (3.5)). This pattern should be approximately temperature independent and since the late echoes have a strong change (they disappear) we have confidence in the analysis.

The T100 has even less attenuation. At the easily achievable frequency of 169 MHz we observed 60 echoes before the electronic window would close (140 μs) but the amplitude was still 1/4 of the first echoes (at 40 mK see fig. (3.6)), so many more echoes existed. Since the attenuation was weak, no echoes disappeared at T_c. Even though the change was small, the large number of echoes provided good statistics to reduce the noise and the background was very flat. The structure of the echo pattern was much weaker than for L110 and the raw attenuation therefore looked much more exponential. Measurements at other frequencies had a larger modulation of the echo amplitude, and this did introduce some systematic errors. The problem comes from assuming the structure factor to be rigorously temperature independent, because, when it is slightly temperature dependent, it produces some effective attenuation, and since the real attenuation is so small, this might be large enough to affect the measurement. But, as can be seen in fig. (3.6) for the 169 MHz data, this structure was weak and produced a random spread around the exponential fit. To be more accurate, the analysis of single echo, or pair of echoes, consistently gave the same curve and a similar amplitude (15% variation). Therefore we can trust the analyzed data, in particular for this frequency. At other frequencies, the echo structure is stronger, the exponential fit is much worse (many data points far away of the line) and the analysis of separate echoes with respect to the exponential analysis show stronger variation. In those cases the data is therefore affected by the systematic errors and we don't believe it to be accurate. Nonetheless it usually gives a very similar curve for the attenuation but with a significant variation in the amplitude of the curve.

The measurement of the T1x0c mode having an even weaker attenuation required much higher frequencies. The measurements of the T100c and the T110c modes should give the same results since they depend on the same elastic constant and viscosity component. But they are measured in 2 different samples and variation in the characteristics of the samples can produces differences. For the T100c measurement (like for the T100 above, it is also sample S1') the echo structure was not too strong and 60 echoes were

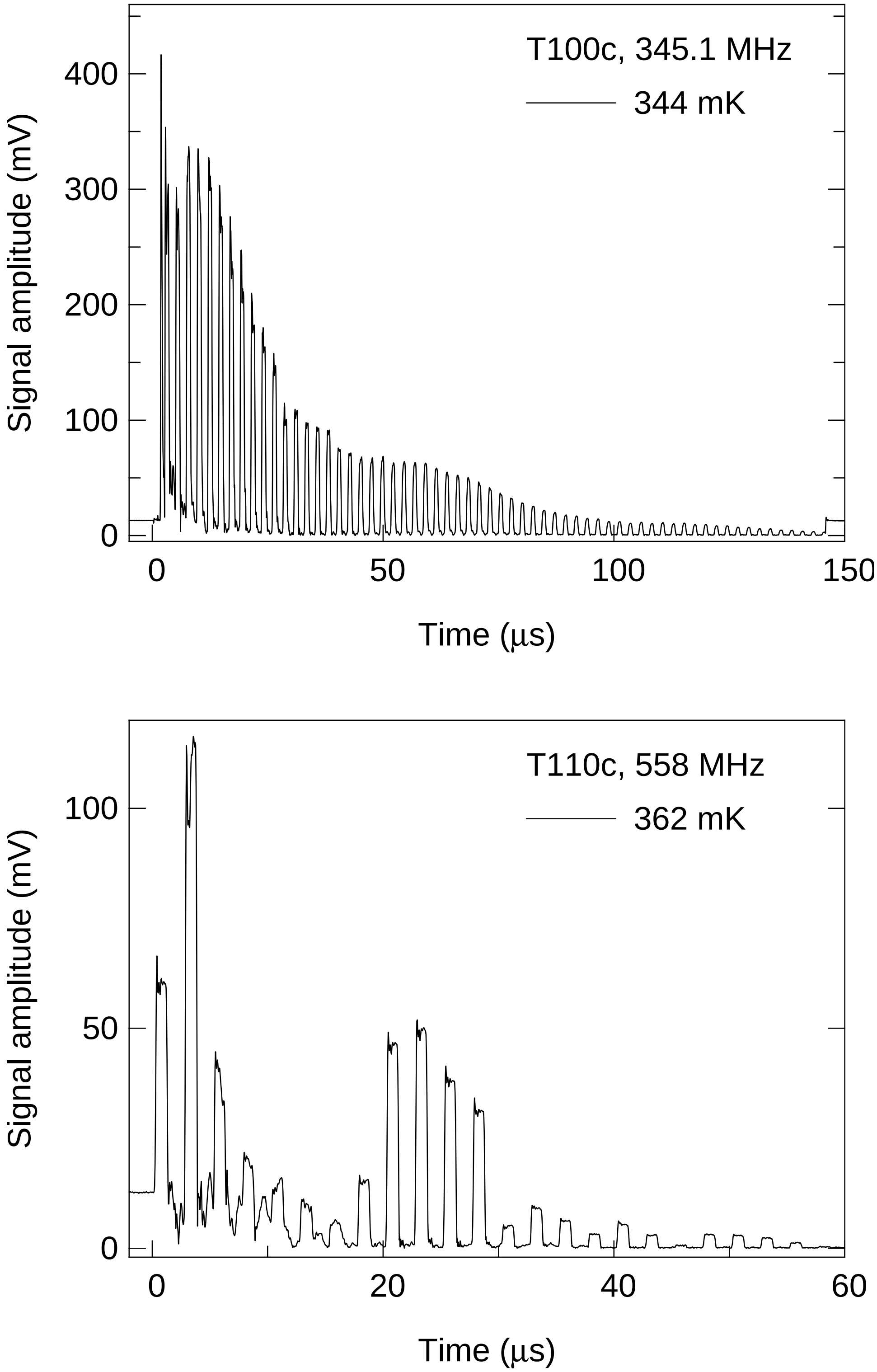

Figure 5.7: Echo signal example for the T1x0c mode. The top panel shows T100c, the bottom panel shows T110c. In both cases the last echoes are decreased by less than 20% at 1.5 K.

observable up to the window cutoff (see top panel of fig. (5.7)). The background was flat. The amplitude of the 60^{th} echo was about 1% of the first ones. But the crystal had a misalignment of the *c*-axis of about 0.3° and this will be seen later to cause some trouble. On the other hand the T110c mode was measured on the S3 crystal. Like the L110 mode, it also had a strong modulation structure of the echoes (see bottom panel of fig. (5.7)). About 20 echoes were observable and the background was flat (except of the first few echoes which were plagued with acoustic noise). These combine to produce a noisy curve, affected by some systematic errors. So in both cases for T1x0c, the measured values were affected by some systematic errors. The curves in fig. (5.4) were selected because they were the most consistent, reproducible and possessed the smallest amount of visible systematic error. They can be relied upon to give the approximate amplitude of the attenuation for this mode and hints at the intrinsic shape. The measurements were performed in the ^{3}He system and the data was extrapolated from 0.9 K (T100c) and 0.7 K (T110c) respectively in order to adjust the origin.

5.2.2 Other sources of attenuation

The discussion of data quality described how well the measured signal represents the attenuation of the crystal. We now need to verify that these measurements represent the intrinsic value of the *electronic* attenuation for the specified sound mode. In other words, we need to establish that other sources of attenuation we mentioned in section 2.2.1 are negligible.

The first effect that we can eliminate is the phonon-phonon interaction due to the anharmonicity of the atomic potential. In terms of viscosity we can write this source of attenuation as $\eta = \gamma^2 \kappa T / v_S^2$ where γ is the the Grüneisen parameter and is of order one[4] and κ is the thermal conductivity of the phonons. We are taking the low frequency limit where this source of attenuation is largest. Taking 1.5 K as the temperature, $\kappa = 20$ mW/K cm,[5] setting $\gamma = 1$ and using a sound velocity of 3 km/s we obtain $\eta = 3 \times 10^{-3}$ millipoise. This is much smaller (by a factor of at least 100) than even the T1x0c mode with 0.5 millipoise. This effect is therefore not important.

---

[4] The Grüneisen parameter can be obtained from $\gamma = \beta_V B / C_V$ where β_V is the coefficient of volume thermal expansion, B is the bulk modulus and C_V is the heat capacity per unit volume. Using a maximal value of $\beta_V = 0.1$ ppm/K (see further discussion in next paragraph), $B = 160$ GPa and $C_V = 1400$ J/m^3 (at 2 K) we estimate that γ is at most 11.

[5] $\kappa = 20$ mW/K cm is about 10% of the in-plane thermal conductivity which is mostly electronic and 10 times larger than the *c*-axis conductivity which is mostly due to phonons (see [207, 165, 213]).

Sound Mode	C (millipoise)	A (millipoise)	B (1/K^2)
L100	500 (0.06)	9300 (1.19)	0.13
T110	146 (0.02)	8800 (1.23)	0.13
L110	33 (0.14)	250 (1.02)	0.09
T100	2.0 (0.31)	5.4 (0.84)	0.10

Table 5.5: Parameters obtained from fitting the viscosity in the normal state to $C+A/(1+BT^2)$ (see fig. (5.8)). The values in parenthesis are for $\alpha(T)/\alpha(T_c)$.

The second effect we can estimate is the attenuation due to the thermoelastic effect. It is present only in the case of longitudinal waves and is caused by density variations which induce temperature variations in the sample. The viscosity is given by $\eta = \beta^2 \kappa T v_L^2 / C_p^2$ where β is the coefficient of linear thermal expansion, κ the thermal conductivity, v_L the longitudinal sound velocity and C_p the heat capacity. Taking values for $T = 1.5$ K, we have $\kappa = 20$ W/Km [165], $v_L = 6.4$ km/s, $C_p = \gamma_n T = 40 \times 1.5$ mJ/K mol $= 0.18$ J/kg K (see table (4.3)) and $\beta = 0.1$ ppm/K and they combine to give $\eta = 4$ millipoise. This is much smaller than the smallest longitudinal mode measured, *i.e.* the L110 mode with an amplitude of 274 millipoise. This value depends strongly on the thermal expansion coefficient β. The value of 0.1 ppm/K is an upper bound from our phase angle measurements. The measured phase change depends on both sound velocity and length variations. Some of the measured modes had a variation, when assigned to the sound velocity, of less than 0.1 ppm/K. That was the most probable source of change but if we assume the variation was due to the length then we arrive at an upper bound of 0.1 ppm/K for β. Also data from LSCO, with $\beta < 0.05$ ppm/K at low temperature [214], suggests that it could be smaller than 0.1 ppm/K for Sr_2RuO_4. No direct measurement of the thermal expansion of Sr_2RuO_4 has been published so far, except for neutron studies which don't have enough resolution for these small changes [102, 104]. In any case the upper bound obtained for this source of attenuation is at most 2% of the measured signal at T_c and should come down at low temperature. We can therefore also eliminate this source of attenuation.

The other sources of attenuation, mostly dislocations, are much harder to estimate. We therefore resort to a more general argument. In fig. (5.8) we show the measured attenuation for the four in-plane modes up to 4 K. We also include the measurement

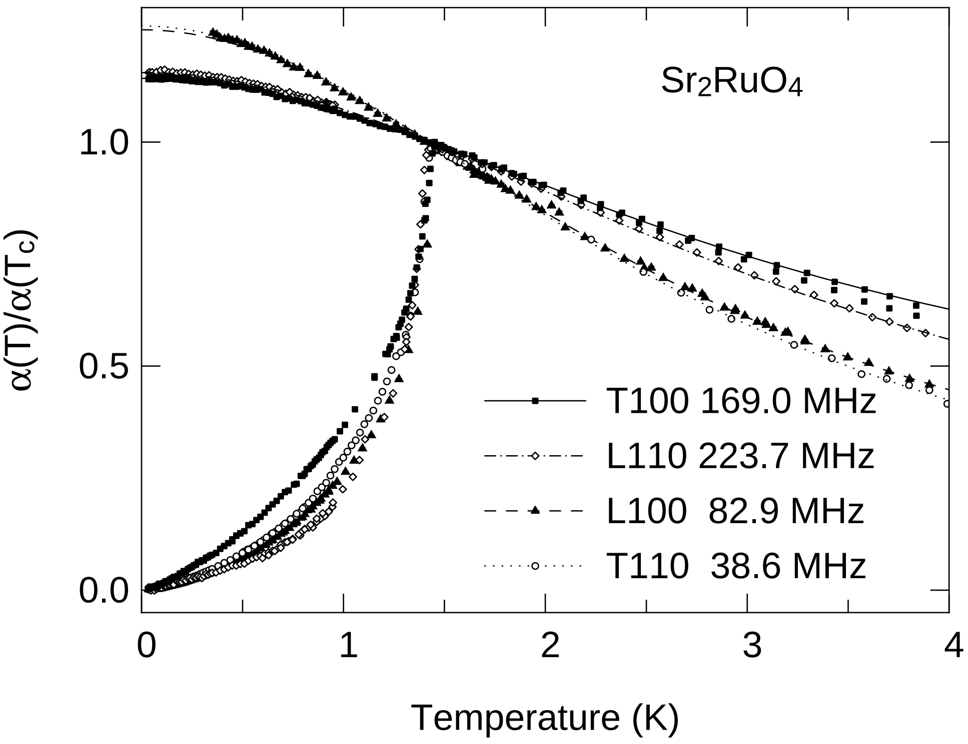

Figure 5.8: Comparison of in-plane modes normalized at T_c. The normal state data was obtained by applying a field of 1.5 T (greater than H_{c2}) approximately in-plane. The lines in the normal state data are obtained by fitting to $C + A/(1 + BT^2)$.

of the normal state for all but the T110 state, obtained by applying a field of 1.5 T approximately in plane and between 0 and 45° from the direction of propagation. In order to compare all the modes together they are normalized at T_c. The lines are fits to the normal state data (with field) and includes the data without field but above 1.5 K. The function that is fitted to is

$$\eta = C + \frac{A}{1 + BT^2}. \tag{5.1}$$

This functional form is what is expected if the attenuation is proportional to the electrical conductivity which has $C = 0$. The fits are rather good, so this form looks reasonable. The value of the parameters for the curves are given in table (5.5). The normal state separates in two groups. For the L100 and T110 modes, the offset C is small relative to the amplitude A and the curvature is $B = 0.13$. The other modes, L110 and T100, which have a much smaller absolute amplitude, also have a larger offset C and a smaller curvature $B \approx 0.10$. The number for B can be compared to a similar value obtained from the fit of the electrical resistivity where we obtained $B = 0.034$. This is about 3 to 4 times smaller than what is observed for the sound attenuation. As mentioned in section 2.3 this difference between the attenuation and the electrical conductivity can result from the different scattering times appropriate for the two properties. In this case the attenuation would be more sensitive than the electric conductivity to the electron-electron scattering that gives rise to the T^2 term. The difference between the two groups of sound waves could also be explained in similar terms. In this case the difference could be explained by different averages over the Fermi surface between the two groups.

The normal state attenuation therefore looks reasonably like what is expected from the electrical conductivity. The attenuation from dislocations is expected to increase with temperature. But over the whole measuring range from 0 to 4 K we do not observe an increase but a decrease. Therefore the attenuation from dislocations is not very strong. If it has any effect, it is to decrease the measured B value from the intrinsic value. This is a possible explanation for the smaller value for the L110 and T100 modes but it does not match with the low temperature data in the superconducting state where T100 is the largest and L110 is the smallest, while the above explanation would suggests they should both be similar and larger than the T110 and L100 mode. This assumes the dislocations are not affected by the superconducting state. Therefore, without being a very strong demonstration, the attenuation from dislocations is small and probably weaker than the $1/(1+BT^2)$ term of the electronic attenuation. This term changes by at most 3% between 0 and 0.5 K, which is smaller then the observed changes in the superconducting state as will be seen later. This estimate cannot be extended to the T1x0c mode because for that mode we have not measured the normal state under a magnetic field due to a strong field dependence (see section 5.5). The small segment of normal state data above T_c does not show an increase, which is an indication (even if weak) that the dislocations are not too important in this case also.

In summary, we have estimated some sources of attenuation and presented general arguments that indicate that the measured attenuation was purely electronic in origin.

5.2.3 Hydrodynamic limit and reproducibility

We have shown in the previous section that the measurements yields the electronic attenuation. In order to compare with theories we must find in which regime, hydrodynamic or quantum, we obtained the data. As was estimated before, $q\ell = 1$ around 500 MHz for the transverse modes, is a more stringent restriction than for the longitudinal waves where it is estimated to be around 1 GHz. The attenuation being smallest for the transverse T100 mode (and T1x0c), this requires a larger frequency to obtain a measurable

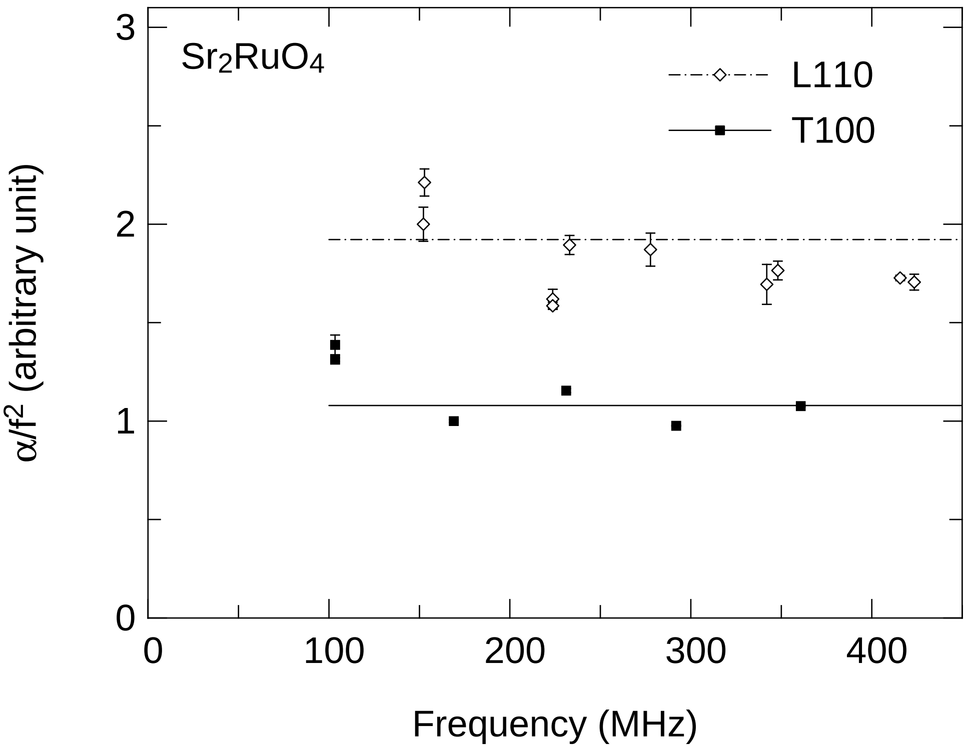

Figure 5.9: Frequency dependence of the attenuation for the L110 and T100 modes. The attenuation is the amplitude at 0.8 K for T100 and 0.7 K for L110 obtained from low temperature fits divided by the square of the frequency and should be a flat line in the hydrodynamic regime. The data are normalized by an arbitrary number. The line is a weighted average below 300 MHz for the L110 mode and between 150 and 300 MHZ for the T100 mode. The error bars represent the statistical (electronic) noise. The scattering is due to systematic errors.

signal which goes in opposition with the smaller limit for the hydrodynamic regime. For T100, with measurements at 169 MHz, we estimate $q\ell = 0.34$ which is not much less than one, but should be low enough to still represent the hydrodynamic limit.

In fig. (5.9) we present the amplitude as a function of frequency for the L110 and T100 mode. The amplitude is obtained from fits to the low temperature data in the superconducting state and represents the amplitude at a fixed temperature of 0.7 and 0.8 K, respectively. The amplitude of the attenuation is divided by the square of the frequency and is normalized to 2 and 1 respectively for the frequency shown previously (152.2 and 169 MHz respectively). It should show a flat line for data in the hydrodynamic regime and deviate into $1/f$ in the quantum limit (see section 2.2.3 and fig. (2.2)). A similar plot is obtained by looking at the frequency dependence of the attenuation amplitude at T_c. We have selected the L110 mode as representative of the longitudinal modes because it has the smallest amplitude, which allowed measurements over a wider range of frequency.

Also, showing it is in the in the hydrodynamic limit would then apply directly to the L100 mode where measurements were done at lower frequencies. The L100 mode with its very clean data has a very clean quadratic frequency dependence of the attenuation, but it is over a limited range of frequencies. We chose T100 to represent the transverse modes because the T110 mode is so attenuating we have very little data for its frequency dependence and also because it will be in the hydrodynamic limit if the T100 mode is. As for the T1x0c mode, the data is relatively noisy, we don't have low temperature data (below 350 mK) and only a limited set of high frequencies are available. We will come back to this mode later.

As seen in the graph, α/f^2 is roughly frequency independent, which suggests we are indeed in the hydrodynamic limit. In particular we want to show that the good curves, 152 MHz for the L110 mode and 169 MHz for the T100 mode, are in that regime. The lines are weighted fits (using statistical errors) of the low frequency data. The scattering around the line is larger than the statistical errors and thus is due to systematic errors. As was mentioned before, the T100 data at 169 MHz was selected because it is believed the systematics had a smaller effect there. On the other hand, the 103 MHz data had a stronger scatter of points in the exponential analysis and therefore was more strongly affected by the systematic problems, explaining why that point is so far away from the line. This would also explain the scattering in the L110 mode. In general, it was observed that for modes with a small attenuation, like L110 and T100, as the frequency is lowered below 100 MHz, the measurements would obviously become more noisy but they would also deviate from a constant α/f^2 and this is due to systematic errors. In particular, at low frequencies, it could be due in part to changes in the structure factor of the echo spectrum.

Since the data has so much scatter, it is not easy to see a downturn at higher frequency which is expected when $q\ell = 1$ is approached. Therefore while it suggests we are indeed in the hydrodynamic regime for the good curves, it is not possible to confirm our estimates of the value of $q\ell$. In order to sidestep this problem we compare the shape of the curve at the good frequency and at a higher frequency for both the L110 and T100 modes. As can be seen in fig. (5.10) the shape is quite stable.[6] The high frequency data was taken in the ^{3}He system (so only starts around 0.35 K) and was offset and scaled to match the good data, but their shape was not modified. The scaling factors of 0.95 for L110

---

[6] For T100 in particular we selected a frequency where systematic errors did not look too strong. Other frequencies with obvious systematic problems showed some modification in shape.

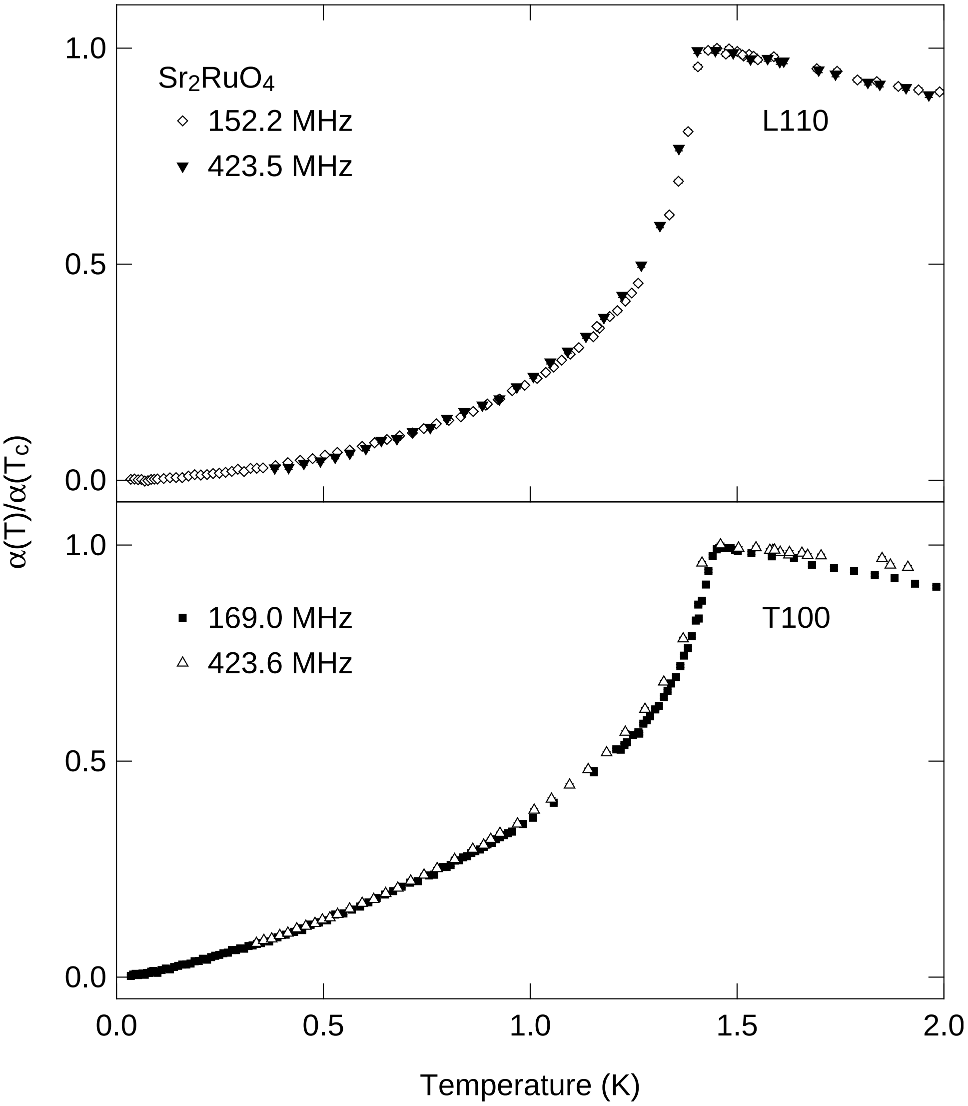

Figure 5.10: Shape of the attenuation of the L110 and T100 modes at different frequencies. The ratio of high frequency over low frequency viscosity at T_c is 0.95 for L110 and 0.84 for T100.

and 0.84 for T100 are not unreasonable considering the frequencies and the systematic errors. These facts combine to show that, even if we are not deep in the hydrodynamic regime (for T100 in particular), the shape of the curve is not frequency dependent and this shape is what will be analyzed to extract information about the superconducting state. Hence for most practical purposes we are in the hydrodynamic regime and theories valid for that range (for example based on viscosity calculations) should apply.

The T1x0c, as we have mentioned, was measured at much higher frequencies and the limited set of valid data does not permit us to look at its frequency dependence. The two frequencies in fig. (5.4) show a similar behavior and amplitude at low temperature, which suggests it is not too far from the hydrodynamic regime either. We will present a possible explanation for the difference in amplitude at T_c in the next section. It is also possible that the mean free path in this case is different (and shorter) since it includes some c-axis dependence, but we will not rely on this. In any case we will not use this mode alone for any conclusion so the identification of its regime is not crucial.

5.2.4 Normal state anisotropy

Before finally discussing the superconducting behavior we must describe the normal state anisotropy in more detail. We will restrict ourselves to the four in-plane modes (L100, L110, T110 and T100), because the small amplitude of the T1x0c mode can be understood as a result of the near two dimensionality of this material. The T1x0c includes some c-axis dependence and in a purely 2D model the c-axis should show no attenuation.

But the in-plane attenuation shows a large anisotropy while a free electron model would suggest none. Anisotropy has been observed before, *e.g.* a factor of 4 in tin at high frequency (quantum limit) [72] but a factor of 1000 is unheard of. We have not found any reference in the literature to such a large anisotropy for metals.

The four in-plane modes are linear combinations of three independent viscosity components (η_{11}, η_{12} and η_{66}). In order to describe the anisotropy more easily we select a different basis. We set $\eta_A = \eta_{11}$, $\eta_B = \frac{1}{2}(\eta_{11} + \eta_{22})$ and $\eta_C = \eta_{66}$. In this way we have $\bar{\eta}_{\mathrm{L100}} = \eta_A$, $\bar{\eta}_{\mathrm{T100}} = \eta_C$, $\bar{\eta}_{\mathrm{T110}} = \eta_A - \eta_B$ and $\bar{\eta}_{\mathrm{L110}} = \eta_B + \eta_C$. Comparing with the measured data at T_c we can see that the ratio between these viscosities is $\eta_A : \eta_B : \eta_C = 7800 : 270 : 6.5 = 1200 : 42 : 1$. From this we see that $\eta_A/\eta_B \approx 30$ so that $\bar{\eta}_{\mathrm{L100}} \approx \bar{\eta}_{\mathrm{T110}}$ (equivalently $\eta_{11} \approx -\eta_{12}$) which was obvious from the start. The actual difference between the two modes should be about 3% but the actual measured change is more of the order of 10%. This is a good comparison considering the T110 data is not very good, especially in terms of amplitude, and also because we are comparing measurements from two different samples which have slightly different T_c's. Hence they probably have different scattering rates (the T110 sample being dirtier) which would also affect the amplitude of the attenuation (smaller for dirtier samples). Another relation is that we can write $\bar{\eta}_{\mathrm{L110}} \approx \eta_B$ since η_C is so small. In this way $\bar{\eta}_{\mathrm{L110}}$ is a direct measurement of the difference between $\bar{\eta}_{\mathrm{L100}}$ and $\bar{\eta}_{\mathrm{T110}}$.

In some simple theories, considering only a 2D free electron gas [74], it is predicted that 1) $\bar{\eta}_{\mathrm{L100}} = \bar{\eta}_{\mathrm{T110}}$ and 2) $\bar{\eta}_{\mathrm{L110}} = \bar{\eta}_{\mathrm{T100}}$. In our language this would require $\eta_B = 0$ or at least $\eta_B \ll \eta_A$ and $\eta_B \ll \eta_C$. Since we do have $\eta_B \ll \eta_A$, the condition 1) is approximately obeyed by our data, but the fact the η_C is so small breaks 2). This is a consequence of the simple theories being unable to explain the large anisotropy between $\bar{\eta}_{\mathrm{T110}}$ and $\bar{\eta}_{\mathrm{T100}}$. If they were of the same order of magnitude, the two predictions would be satisfied. As for $\eta_B = 0$, it is easy to break this condition by considering models away from the simple 2D free electron gas. We will consider such an example in the next section.

The presence of the strong anisotropy causes some experimental difficulties. Considering the in-plane transverse modes, and assuming the modes to be purely transverse[7] we can write the angular dependence as:

$$\eta(\theta) = \bar{\eta}_{\mathrm{T100}} \cos^2(2\theta) + \bar{\eta}_{\mathrm{T110}} \sin^2(2\theta) \tag{5.2}$$

where θ is the in-plane angle of the direction of propagation with 0° being along [100] and 45° along [110]. Because $\bar{\eta}_{\mathrm{T100}}$ is 1000 times smaller than $\bar{\eta}_{\mathrm{T110}}$, a small misalignment angle can invalidate a measurement. For example $\eta(2^\circ) = \bar{\eta}_{\mathrm{T100}} + 0.0059\bar{\eta}_{\mathrm{T110}}$ and the measured signal will mostly be $\bar{\eta}_{\mathrm{T110}}$ and not the intrinsic $\bar{\eta}_{\mathrm{T100}}$. That was the problem with our initial [100] sample (S2) which had a misalignment of 2.2°. This misalignment angle explains the amplitude and shape of the transverse mode we measured on S2. This had no effect on the longitudinal measurement because the anisotropy is weaker and we were measuring the mode with the stronger attenuation anyway. This type of calculation applied to the original unaligned sample (S1) also estimated properly the measured amplitude. But this brings the question as to whether we have indeed measured the intrinsic T100 attenuation or that the data is still affected by other modes. We measured the misalignment angle for the S1' crystal several times by X-ray and obtained angles ranging from 0.2° to 0.3°. We therefore have that $1200 \sin^2(2 \times 0.3^\circ) = 0.13$, or at most 13% of the T110 mode could contaminate the measured T100 mode. This is a small modification as is seen in fig. (5.11). The figure also shows the effect of a larger misalignment of 0.5° and 0.7°. This demonstrates the trend of the correction that makes the data more linear at low temperature and to make the normal state flatter. For 0.7°, it also produces a bump at T_c and removes the temperature dependence in the normal state (it becomes flat). A larger angle of 0.9° would produce a negative attenuation. From those observations, and from the measured angle which is at the very worst 0.5°,

---

[7] As was noted before, the elastic constants show a weak anisotropy so the modes should be almost pure. Also we are mainly interested in possible deviations close to a high symmetry direction where deviations from pure modes should also be small.

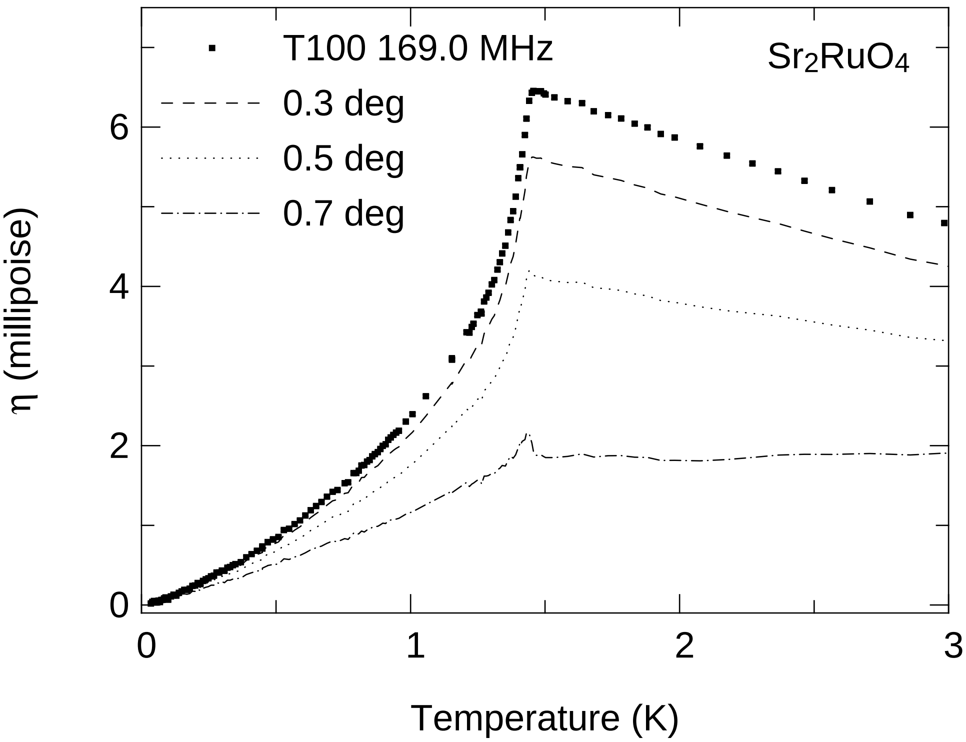

Figure 5.11: The measured T100 data is shown as points. The lines are the T100 data with a fraction of the L100 mode subtracted. The fraction is $\sin(2\theta)^2$ where θ is the angle given. The measured misalignment angle is no larger than 0.3° and that has a minor effect on the curve. The 0.5° and 0.7° curves are examples to display the general trend of making the curve more linear while 0.9° would produces a negative attenuation.

our measured attenuation is close to the intrinsic shape and amplitude of the T100 mode. We will use it uncorrected and assume it represents the real T100 attenuation.

Misalignment errors must also be considered for the T1x0c measurements. In this case an error of θ out of the plane gives the following angular dependence

$$\eta(\theta) = \bar{\eta}_{\mathrm{T1x0c}} \cos^2(2\theta) + \frac{\bar{\eta}_{\mathrm{L1x0}} + \eta_{33} - 2\eta_{13}}{4} \sin^2(2\theta) \tag{5.3}$$

where again we assume pure transverse modes. The η_{33} and η_{13} components have not been measured but since they include some c-axis attenuation and this is a highly 2D material we expect they will be much smaller than the in-plane longitudinal modes. Therefore for small angles we have approximately $\bar{\eta}_{\mathrm{T1x0c}} + (\bar{\eta}_{\mathrm{L1x0}}/4)\sin^2(2\theta)$. For the S3 sample (T110c) the out-of-plane misalignment is about 0.5°, while it is about 0.3° for the S1' sample (T100c). If we assume an intrinsic value for $\bar{\eta}_{\mathrm{T1x0c}}$ of 0.5 millipoise, we obtain $[\eta(\theta) - \bar{\eta}_{\mathrm{T1x0c}}]/\bar{\eta}_{\mathrm{T1x0c}} = 43\%$ for T100c and 4.2% for T110c. Therefore a large mixing of the longitudinal mode is expected for T100c and should be absent in T110c and this is a consequence of the in-plane anisotropy (×30) of the longitudinal modes. This mixing

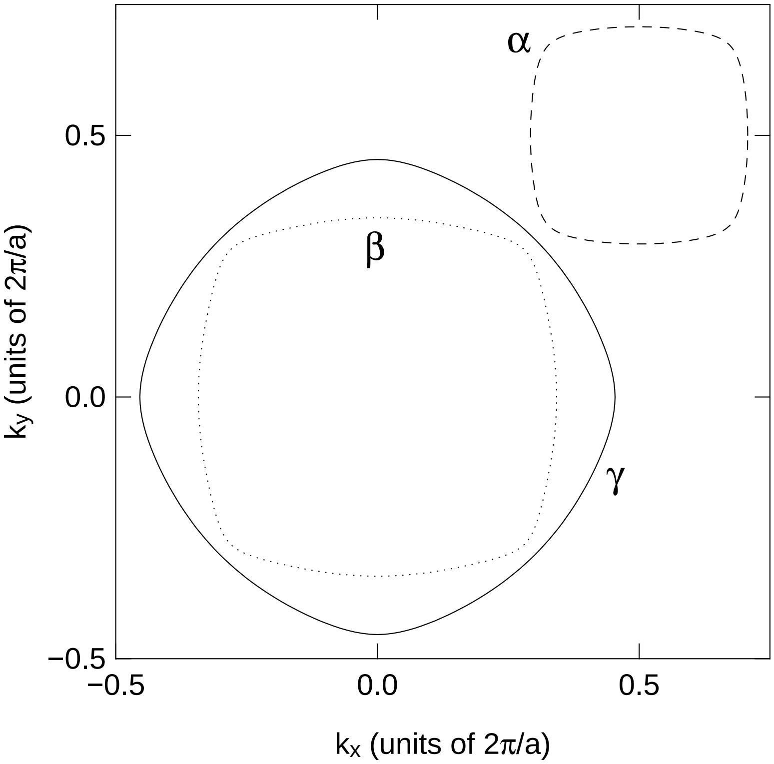

Figure 5.12: Fermi surface obtained from the tight binding model with the parameters of table (5.6)

for the T100c mode can explain the large difference between it and the T110c mode close to T_c as seen in fig. (5.4). Assuming the intrinsic attenuation is slowly and linearly decreasing away from T_c, the sudden drop would be from the quickly disappearing $\bar{\eta}_{\mathrm{L100}}$ component. At lower temperature, $\bar{\eta}_{\mathrm{L100}}$ is relatively small and both T1x0c modes show similar behavior. Therefore the intrinsic curve might be more like the T110c data. But it should be remembered that this is a very small attenuation which is noisy and also prone to systematic errors. Both curves are also taken at high frequency where it is possible to have an intrinsic jump in transverse wave at T_c because of the loss of the electromagnetic coupling in the superconducting state. Nonetheless, both curves seem to provide a consistent story when considering misalignment errors and are compatible with the other measured viscosity components.

5.2.5 Simulation of the normal state anisotropy

The angular dependence of the attenuation is not explained by the free electron model. In order to improve on this we need to consider a more realistic electron-phonon interaction. This was done recently by Walker *et al.* [76] who considered the interaction in a tight

Parameter	xy band	xz band	yz band
t_x (eV)	0.44	0.31	0.045
t_y (eV)	0.44	0.045	0.31
$t' = t'_{45^\circ} = t'_{-45^\circ}$ (eV)	-0.14	0.01	0.01
μ' (eV)	-0.50	0.24	0.24

Table 5.6: List of parameters for the tight binding model of $\mathrm{Sr_2RuO_4}$. t are nearest-neighbor-hopping, t' are next-nearest neighbor hopping and μ' is the band offset.

binding model of $\mathrm{Sr_2RuO_4}$. Using Green's function calculations of phonon lifetime, they obtained a longitudinal anisotropy of the correct magnitude and proposed an explanation for the transverse anisotropy. They also gave general symmetry arguments about the angular structure of the electron-phonon interaction which are useful in understanding superconducting state anisotropy. In this section we develop similar ideas but using the language of the deformation potential theory of section 2.3.

In order to proceed, a model of the Fermi surface is required. Following Morr *et al.* [143], we used a tight binding model with the following energy dispersion:

$$\varepsilon_b = -2t_x\cos(k_xa_x) - 2t_y\cos(k_ya_y) + 2t'_{45^\circ}\cos(k_xa_x + k_ya_y) + 2t'_{-45^\circ}\cos(k_xa_x - k_ya_y) - \mu' \tag{5.4}$$

where $a_x = a_y = a$ is the lattice dimension, b identifies the energy band and stands for xy, xz or yz. The parameters t_x and t_y are nearest-neighbor hopping integrals, the $t'_{\pm 45^\circ}$ are next-nearest-neighbor hopping integrals and μ' is the band offset. All these parameters depend on the band b and the values we used are given in table (5.6). The γ Fermi surface is determined from $\varepsilon_\gamma = \varepsilon_{xy} - \mu$ where μ is the chemical potential and is zero for the unstrained system. The α and β surfaces are the result of the hybridized xz and yz bands. They are given by

$$\varepsilon_{\substack{\alpha\\\beta}} = \frac{\varepsilon_{xz} + \varepsilon_{yz}}{2} \mp \sqrt{\left(\frac{\varepsilon_{xz} - \varepsilon_{yz}}{2}\right)^2 + t_\perp^2} - \mu \tag{5.5}$$

where the $-$ sign is for α and $+$ sign for β and $t_\perp$ is the parameter describing the hybridization and is set to 0.1 eV. Fig. (5.12) shows the resulting Fermi surface.

To calculate the viscosity we must obtain the deformation potential, which is given by eqn. (2.29) and which we repeat here

$$D_{ij} = \lim_{s_{ij}\to 0} \frac{\varepsilon(k_i - s_{ij}k_j, s_{ij}, \mu(s_{ij})) - \varepsilon(k_i, 0, \mu(0))}{s_{ij}} \tag{5.6}$$

which requires finding the change in energy for a point $\mathbf{k}$ when a strain s_{ij} is applied. The point $\mathbf{k}$ is modified by the strain and the chemical potential also needs to be adjusted to keep the number of electrons constant (see section 2.3) for longitudinal strains. Inspecting eqn. (5.4) we see that all the $\mathbf{k}$ dependence comes as either k_xa_x or k_ya_y and that these combination of factors are not changed under strain since k and a are modified in opposite ways. Therefore the strain has no effect on the Fermi surface and the deformation potential will be zero. So when considering only the shape of the Fermi surface, this tight binding model has no intrinsic attenuation. This is in contrast to the free electron system which provides non-zero attenuation when considering the Fermi surface alone. This model therefore seems to represent an opposite limit to the free electron model.

In this case, to obtain any attenuation we will need to modify the tight binding parameters. In order to simulate the in-plane modes we calculated the three in-plane deformation potentials: D_{11}, D_{22} and D_{12}. Actually D_{22} is the same as D_{11} but rotated by 90°. For D_{11} and D_{22} we decreased t_x and t_y respectively by 1% for all the bands. As the definition requires, we enforced particle conservation by adjusting the chemical potential. For D_{12}, a pure shear strain, we decreased t'_{45° by 1% and increased t'_{-45° by 1% for all the bands also. These kinds of changes assume the hopping parameters only depend on the longitudinal distance between two sites. This is a reasonable assumption considering the hopping parameters are determined by wave function overlap and are sensitive to bond lengths. The values of 1% for the changes was selected after some testing so that it was small enough to be in the linear regime (a change in the parameters produced a proportional change in the deformation potential) and not so small as to cause numerical difficulties. The calculation is simplified because the parameters of the cosine functions are independent of strain as seen above and this permits the use of a fixed square unit cell of unit dimensions.

We are not interested in the absolute value but in the relative value between the modes. The fractional change for a hopping parameter t under strain s_{ij} is given by $(\partial t/\partial s_{ij})s_{ij}/t$. To compare with the measured viscosities (η_A, η_B and η_C), we combined the deformation potentials in the required combination and the result are shown in fig. (5.13). These graphs represent the angular dependence of the integrand for calculating the viscosity. The angle is defined from the center of each respective Fermi sheet, *i.e.* the origin for the β and γ sheet and the (0.5, 0.5) point for the α sheet. The angle just parameterizes the point on the sheet, so doing the integration requires performing a line integral around the Fermi surface. It is evident from the figure that for our choice of variation in hopping

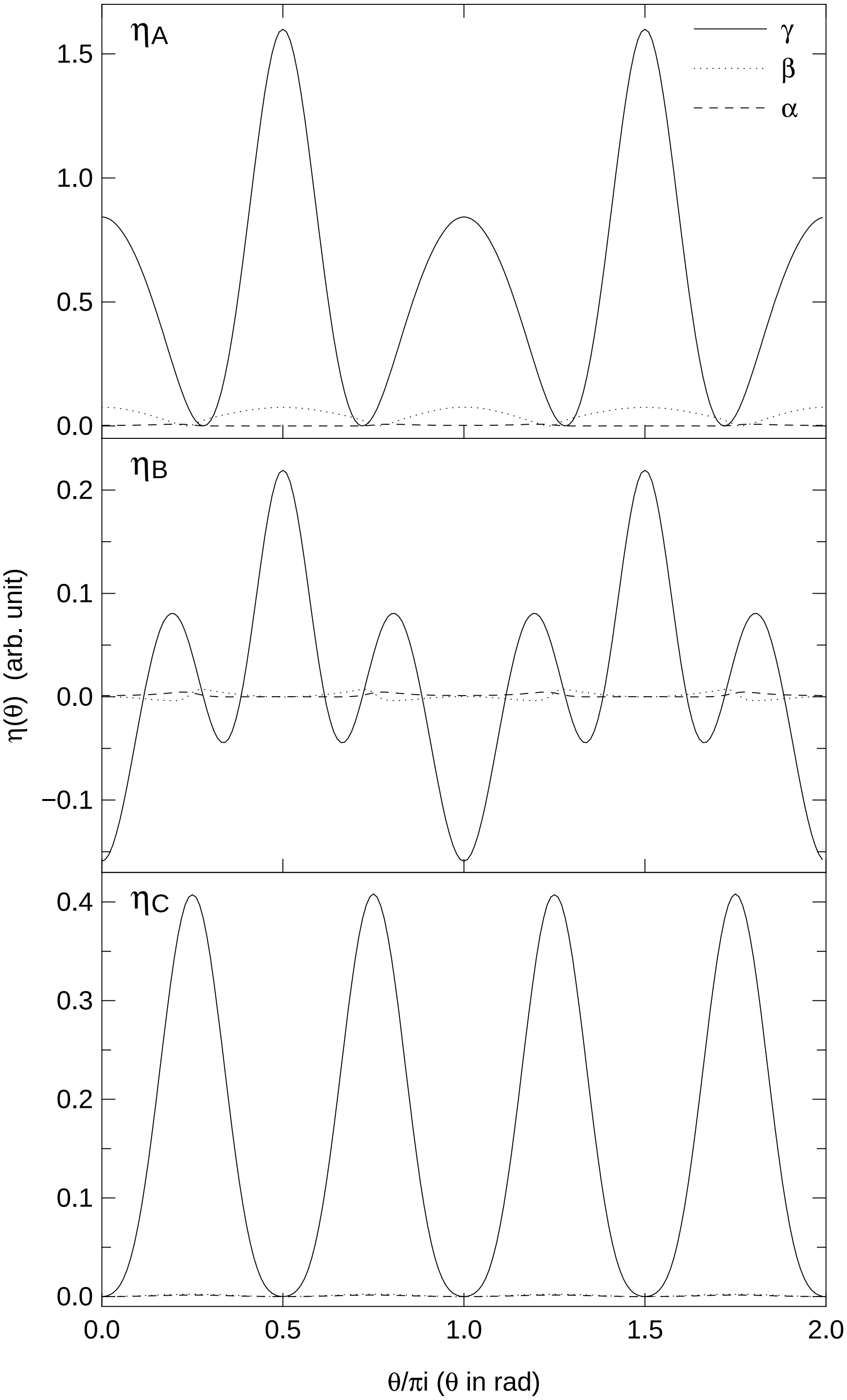

Figure 5.13: Angular dependence of the integrand for the three viscosities discussed in the text (η_A, η_B and η_C). For all the viscosities the integrand for the three Fermi surface sheets is displayed but the α and β sheets have a much smaller amplitude.

parameters, the γ sheet controls the amplitude of the viscosity since the α and β sheet have a much smaller dependence. When considering the approximate position of the minima and maxima, the angular dependence is similar to that expected for the free electron model for η_A ($\cos^2(2\theta)$) and for η_C ($\sin^2(2\theta)$). Performing the line integrals we obtain for the simulation that $\eta_A/\eta_B = 39$ which is of the right order of magnitude to explain the measured anisotropy (29). As stated before, a similar result was obtained by Walker *et al.* [76] using a different technique. We also obtain $\eta_A/\eta_C = 6$ which is very far from the measured 1200. Assuming the model is valid, this implies the sensitivity on strain of the t' parameter is much weaker than for the t parameter by a factor of about 14 (remember that the viscosity depends on the square of the deformation potential). Band calculations with applied strain are required to verify if this value of 14 is possible. Such calculations are not currently available.

The above model calculation seems to explain the η_A, η_B anisotropy and provides a possible explanation for the η_A, η_C anisotropy, but it was a simple model. Even keeping the tight binding model as is, the hopping parameter can have different dependences on strain for the different bands. For example the sensitivity on strain of the α and β Fermi surfaces can be increased relative to the γ Fermi surface so that their contribution to the viscosity becomes as large as for the γ sheet. This might be required in light of the results in the superconducting state (see next section). As a side effect this reduces the η_A–η_B anisotropy. The other parameters can also be adjusted. Even if simple, it is an interesting model that gives some insight into the possible behavior of this material.

5.3 Superconducting state

We have shown that the measured attenuation represents the intrinsic electronic attenuation of the hydrodynamic regime. We also looked at a simple model to describe the normal state attenuation. We are now ready to look at the superconducting state anisotropy. In terms of the simple theories [73, 74] we should compare the two transverse modes (T100 and T110). Transverse modes are preferred because they don't require vertex corrections (see section 2.5.4). But we have shown that the data for the T110 and L100 modes are similar and that the L100 date is much cleaner. Also since the difference between them, $\eta_B \approx \bar{\eta}_{\text{L110}}$, is small and has roughly the same shape in the superconducting state as T110 and L100 (see fig. (5.3) and fig. (5.8)) then they can be related to a good approximation by a scaling factor. When using normalized data (as

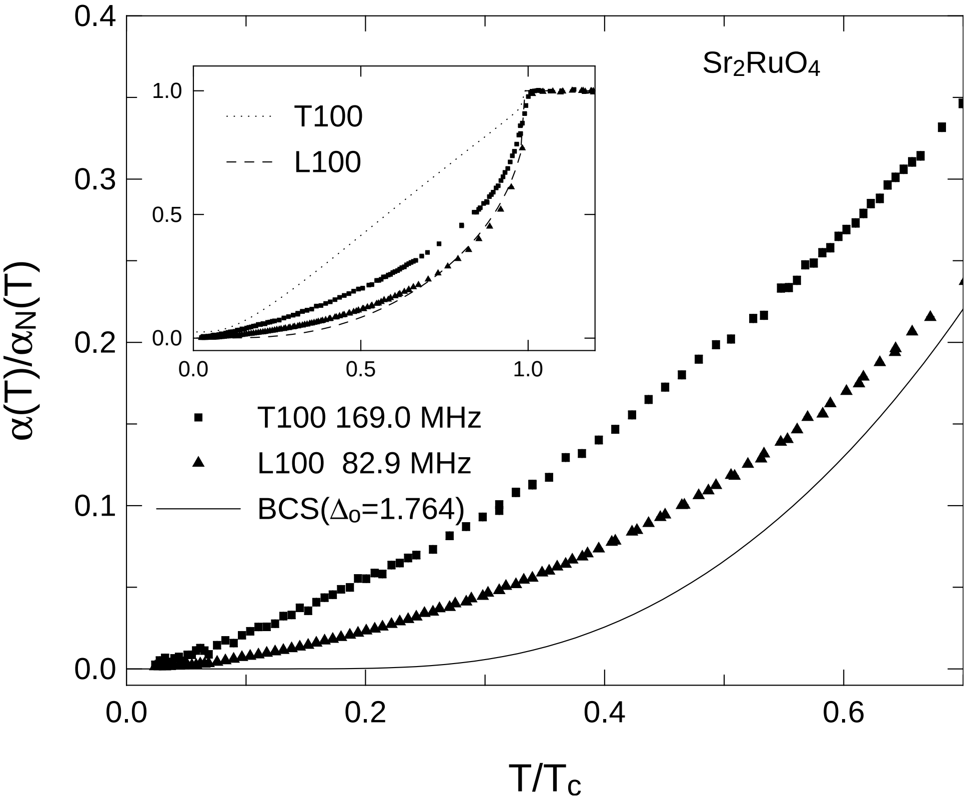

Figure 5.14: Normalized attenuation as a function of normalized temperature. The BCS result for a weak coupling s-wave gap ($\Delta_o = 1.764 k_B T_c$) is shown as a solid line in the main panel. The inset shows the data up to T_c and the curves are for the f-wave model from [74].

we will) this scaling is irrelevant. Therefore we will compare the L100 and T100 modes keeping in mind that it should be equivalent to comparing the T110 and T100 modes. This will also restrict the comparison to a single sample (S1'), so differences in sample purity will not be a concern.

In fig. (5.14) we show the L100 and T100 data at low temperatures down to 40 mK. We plot the attenuation normalized by the normal state curve with respect to the reduced temperature $t = T/T_c$. The inset shows the same data up to T_c. Very similar curves are obtained when the attenuation is normalized by the value at T_c (see fig. (5.8)) since the normal state curvature is small. It is immediately apparent that the data is not exponential at low temperatures but follows a power law. For comparison, the main panel shows the standard BCS result assuming the usual weak coupling BCS gap, $\Delta_0 = 1.764 k_B T_c$ at 0 K. Fitting a BCS curve by adjusting Δ_0 did not give good results. In order to have some temperature dependence down to low temperatures requires a smaller gap than the BCS one, but this makes the decrease below T_c much too slow. A BCS like curve is expected for the simple p-wave gap ($k_x + \mathrm{i}k_y$). Therefore we can *eliminate* that gap (and a s-wave gap) as a candidate for this material. The power laws at low temperature are indicative of line of nodes or, at the very least, of a very strong gap anisotropy.

Before considering gap with nodes, we should mention that a large variation in gap amplitude between sheets of the Fermi surface can be obtained in models that decouple the α and β Fermi surfaces from the γ Fermi surface. In these models [186, 189], depending on the coupling strength between Fermi surfaces, the gap would be the simple p-wave on all the surfaces but with different amplitudes. At very weak coupling this would be similar to two superconducting transitions. At large coupling the transitions merge together and it will be similar to the BCS result. In general it always has a minimum gap below which an exponential behavior is expected. We did not observe any sudden change (expected for weak coupling) or exponential behavior at low temperature so our data does not agree with these models.

The most probable explanation for the low temperature power laws is therefore the presence of nodes. This was an expected result since other probes have also seen power laws. These measurements are an additional confirmation and they extend to a very low temperature ($T/T_c \sim 30$ or 40 mK). Having identified the presence of nodes we can now try to find their position. To do so we must look at the anisotropy of the attenuation in the superconducting state. The T100 mode shows a larger attenuation than the L100 mode. This indicates it is sensing more quasiparticles. But the power laws are not very different. For a simple model consisting of vertical line nodes, the expected result is a T^2 change in power laws between the two directions. We present the result of that model in the inset of fig. (5.14). The curves are taken from Graf *et al.* [74] but we have rotated their result. They placed the nodes along the crystal axis (f_{xy}), while for the graph we placed the nodes on the diagonal ($f_{x^2-y^2}$). This change just swaps the identification of the two curves. The T100 curve has a weak power law, like the data, but the amplitude is much larger than the experimental result. The L100 curve is closer in amplitude but the low temperature power law is stronger than the measured data. This model is based on a free electron model so we must be careful when comparing it to our data. For example, it does not explain the large normal state angular dependence. But since the tight binding model we used before predicted a similar angular dependence of the deformation potential as for the free electrons, the prediction of this simple model might still apply. The anisotropy suggests that more quasi-particles are present on the diagonal

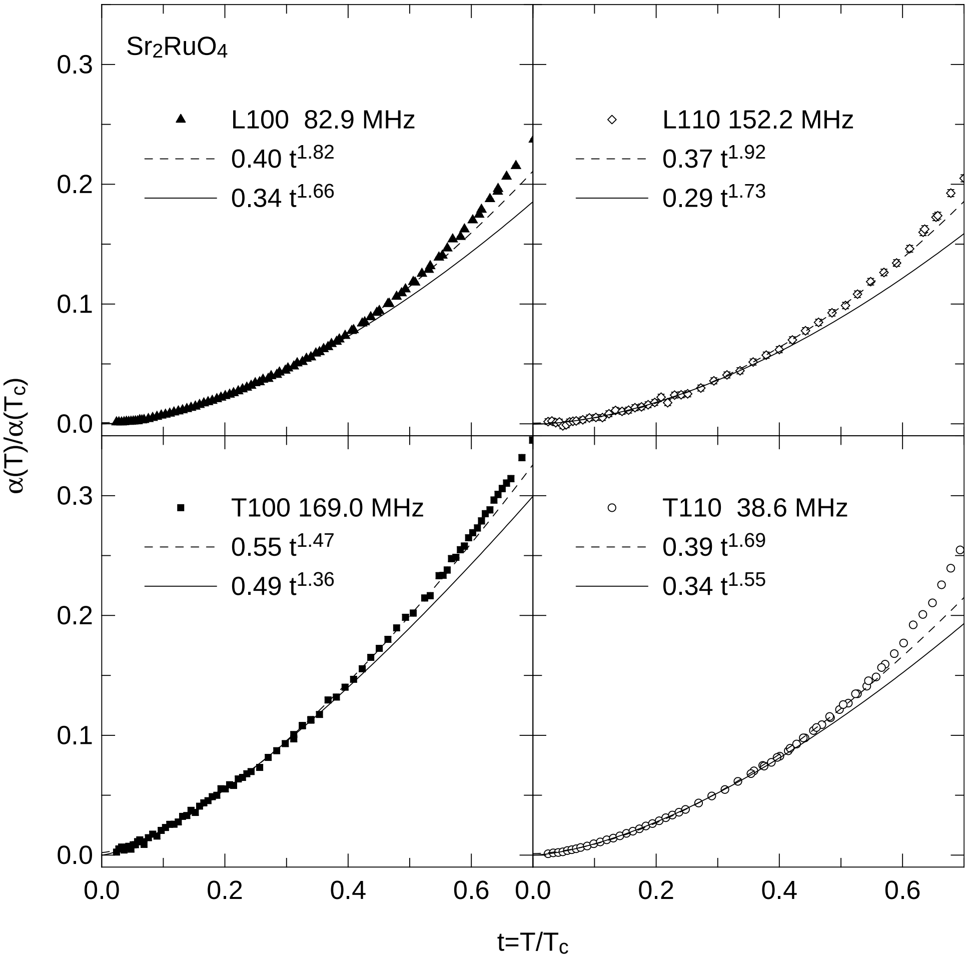

Figure 5.15: Low temperature power law fits of the normalized attenuation vs normalized temperature. The solid lines are fits for $t = T/T_c < 0.35$ and the dashed lines for $t < 0.55$.

then along the a-axis. But for a line of nodes on the diagonal the model would require a T^2 change in power which is not observed. More realistic calculations of the f-wave model are needed for a conclusive decision but our data tends to eliminate the f-wave gaps as a possibility for Sr_2RuO_4.

In fig. (5.15) we show the low temperature power laws for the four in-plane modes. We fitted the attenuation, normalized by the value at T_c, up to the reduced temperature $t = T/T_c = 0.35$ and $t = 0.55$. In table (5.7) we list the exponents for the L100 and T100 modes fitted over the same range ($t < 0.35$) and over another longer range ($T < 1.0$ K). It shows the difference between fits on unnormalized data (α, which is the same as $\alpha(T)/\alpha(T_c)$ and fits to data normalized by the normal state curve ($\alpha/\alpha(T)$). This change is very small (0.03) for the small fitting range and it is still relatively small (0.1) for the larger fitting range. Another observation is that the power laws increase as the

Sound mode	$T < 0.5$ K ($t < 0.35$)		$T < 1.0$ K ($t < 0.69$)	
	α	$\alpha/\alpha(T)$	α	$\alpha/\alpha(T)$
L100	1.63	1.66	1.82	1.93
T100	1.33	1.36	1.47	1.55

Table 5.7: Low temperature power fit exponent for L100 and T100. The fits are done below the listed temperature ($t = T/T_c$) and on the raw attenuation ($\alpha^{\mathrm{SC}}(T)$) or on the normalized attenuation ($\alpha^{\mathrm{SC}}(T)/\alpha^{\mathrm{N}}(T)$).

fitting range is lengthened so the data does not have a pure power law. For the fits with $t < 0.35$, the power varies from 1.36 for the T100 mode to 1.73 for the L110 mode. This is a small variation compared to the variation of 2 expected from the simple theories between directions with "active" and "inactive" nodes and observed in UPt_3 [29, 30]. Our power laws are close to the expected 1.5 for an active line of nodes [73]. Therefore, apparently, neither sound mode exhibited the behavior expected for inactive nodes. It should be noted that the T110 mode is not *exactly* like the L100 mode. It has similar amplitude and the power laws, even if smaller, are also similar. Part of this is just variations between experiments; different frequencies do show a variation in power laws due to noise and systematic errors. Another reason is that, as mentioned before, the data was of a lower quality and more prone to systematic errors. Therefore we reiterate that the L100 mode is preferred over the T110 for detailed comparisons.

The L110 mode is similar to the L100 mode but has a smaller amplitude and a larger power law which can also be seen in fig. (5.8). Considering the angular dependence of η_B in the tight binding simulation (see fig. (5.13)) is quite different than for the other modes, it could provide some additional discrimination between models when more careful calculations are performed. For low temperature, its maxima and zero crossings are similar to η_A (hence L100), so it should have similar power laws as is the case.

We have power laws indicative of nodes, but the anisotropy of the power and its value suggests we have active nodes in all directions. This would be observed if more than four nodes were present, or if the nodes were not at right angles to each other, breaking tetragonal symmetry. A simpler reason would be if there was horizontal lines of nodes. The anisotropy between the T100 and L100 modes would then be due to an anisotropy in the quasiparticle density and/or in the scattering time coupled with the deformation potential angular dependence. The power laws would be controlled by the presence of

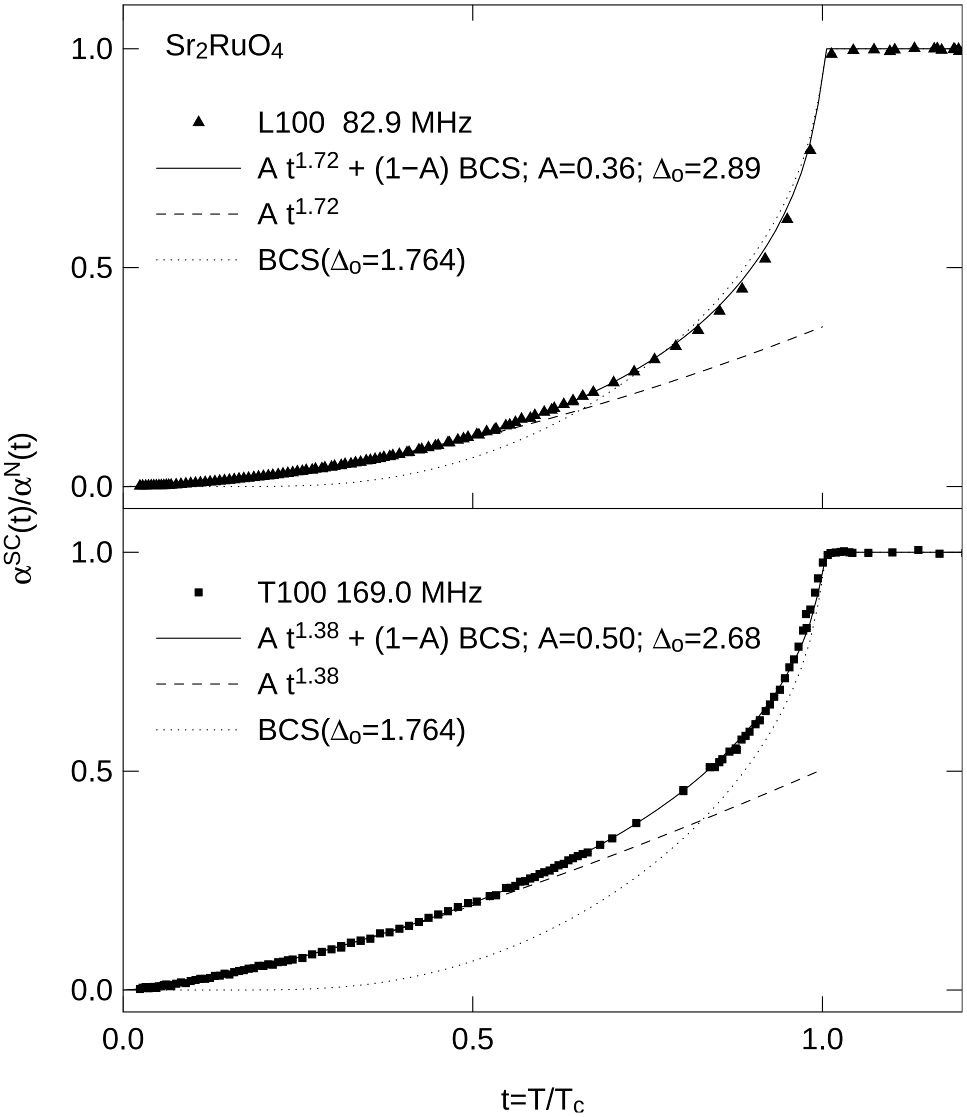

Figure 5.16: Fit to the L100 and T100 data of $At^{\delta} + (1 - A)\text{BCS}(\Delta_o)$ below $t = T/T_c = 1$. BCS stands for the standard BCS result for the attenuation, $2f(\Delta)$, but parametrized by a variable zero temperature gap (Δ_0). The three free fitting parameters (A, δ and Δ_0) are given. For comparison the power law part of the fit is shown and a BCS curve with the weak coupling gap ($\Delta_0 = 1.764k_BT_c$) is also displayed.

the nodes. A gap anisotropy, such as the one obtained in [140], with a minimum on the diagonal, would increase the density of quasiparticles in those directions relative to other directions and could provide the needed anisotropy.

A horizontal line node in a highly 2D system is not a comfortable idea. A purely 2D system could not have such a node and therefore we must include 3-dimensional effects. But this is a very 2D system (for example the electrical conductivity is 1000 times larger in-plane than along the c-axis) so it is strange that it would be so important to the superconductivity. Also we are still faced with the problem that the simple models usually have the roughly linear behavior of active nodes going to T_c (see [193]). In our case $\alpha(T)/\alpha(T_c)$ for T100 goes to about 0.5 instead of 1. This could be a problem with the simple calculations, but another solution is possible that can solve both problems. As stated before, the α and β Fermi surfaces are in principle somewhat decoupled from the γ FS. Considering the coupling between them, Zhitomirsky and Rice [188] have recently proposed that a p-wave gap ($k_x + \mathrm{i}k_y$) on the γ FS could induce a horizontal line of nodes on the α and β surfaces. The node would be at $k_z = \pm\pi/c$ but a small admixture of p-wave symmetry can shift the nodes vertically. This gives a mechanism to require the 3D dependence because the coupling depends on interlayer interaction which is related to the c-axis warping of the FS. It also explains the second observation because only a fraction of the quasi-particles are on a fully gapped FS. No calculations of the ultrasound attenuation for this model has been done yet but in order to test this model we fitted the data to a combination of a power law and the BCS curve:

$$\begin{aligned} \frac{\alpha_{\mathrm{SC}}(T)}{\alpha_{\mathrm{N}}(T)} &= A\left(\frac{T}{T_c}\right)^{\delta} + (1-A)2f(\Delta) \qquad && T < T_c \\ &= 1 && T \geq T_c \end{aligned} \tag{5.7}$$

where Δ is the standard BCS temperature dependent gap but parametrized by the zero temperature value of Δ_0. The fitting parameters are therefore A which is the fraction of the signal due to the FS with nodes, δ the exponent and Δ_0. The result of the fit is shown in fig. (5.16). For comparison purposes we also show a BCS curve with the weak coupling gap ($\Delta_0 = 1.764 k_B T_c$) and the power law part of the fit. We could have allowed different weights for the BCS and power law terms, and we could also have added a constant offset. But in order to minimize the number of adjustable parameters we did not consider such complications.[8] The fits reproduce the data almost perfectly. The value of Δ_0 for the two curves are similar and reasonable. The power law amplitudes and exponents are very similar to the low temperature fits we described above. Therefore this model looks quite interesting. We certainly cannot eliminate it, and it provides the best fit to our data so far. Of course it has more free parameters than the other models, so it must provide a better fit anyway. Nonetheless the fit is so good over the full temperature range and with reasonable parameters that it is a real candidate gap. The anisotropy (especially in power laws) we observed is not explained by the model but as we said above it might

---

[8] Including those extra parameters has a small effect on the fits. The offset stays close to zero and the sum of the amplitude of the two terms is still approximately 1.

come out of a more detailed calculations. It should be noted that a similar model as been proposed very recently which also includes some of the needed gap anisotropy [215].

The T1x0c mode should help to distinguish between different gap structures. But the data is not of a quality able to support strong conclusions, so we must content ourselves to see if it is consistent with the above model. As we said above, the difference between the two curves in fig. (5.4) is probably due to misalignment of the crystal for the T100c mode. Therefore the data looks like a linear power law all the way to T_c. No calculations for this mode have been performed but we can guess that it could be most sensitive to the β FS because dHvA measurements [109] have shown this sheet to be the most strongly warped. It therefore has the strongest 3D behavior and could dominate the other surfaces for the T1x0c attenuation assuming other parameters such as the density of states are not too different between the Fermi surfaces. For the above model, the β FS should have horizontal lines of nodes and if it is the main source of attenuation we could expect a linear power law all the way to T_c as long as the node is not inactive in this configuration. Hence the T1x0c looks consistent with the other data. Better data and calculations are required for further progress but the model of Zhitomirsky and Rice looks promising.

The measurements in the superconducting state have yielded power laws indicating the presence of nodes. The anisotropy of the power laws is weak pointing to horizontal instead of vertical nodes. A good fit to the data is achieved with the two band model of Zhitomirsky and Rice which includes both horizontal line nodes and a full gap on different Fermi surface sheets.

5.4 Sound velocity

Until now we have discussed the ultrasound attenuation data. But from the pulse echo technique we can also extract measurements of the changes in sound velocity. In fig. (5.17) we show the temperature dependence of the sound velocity. We present both the superconducting state and the normal state data taken with an applied field of 1.5 T approximately in-plane as before (the data was taken at the same time).

In order to extract the effect of the superconducting state we plot the difference between the superconducting state and the normal state in fig. (5.18). Both T110 and L100 behave similarly, except the change in T110 is bigger. In both cases the effect of the superconducting state is to change the slope at T_c and this can be related to the

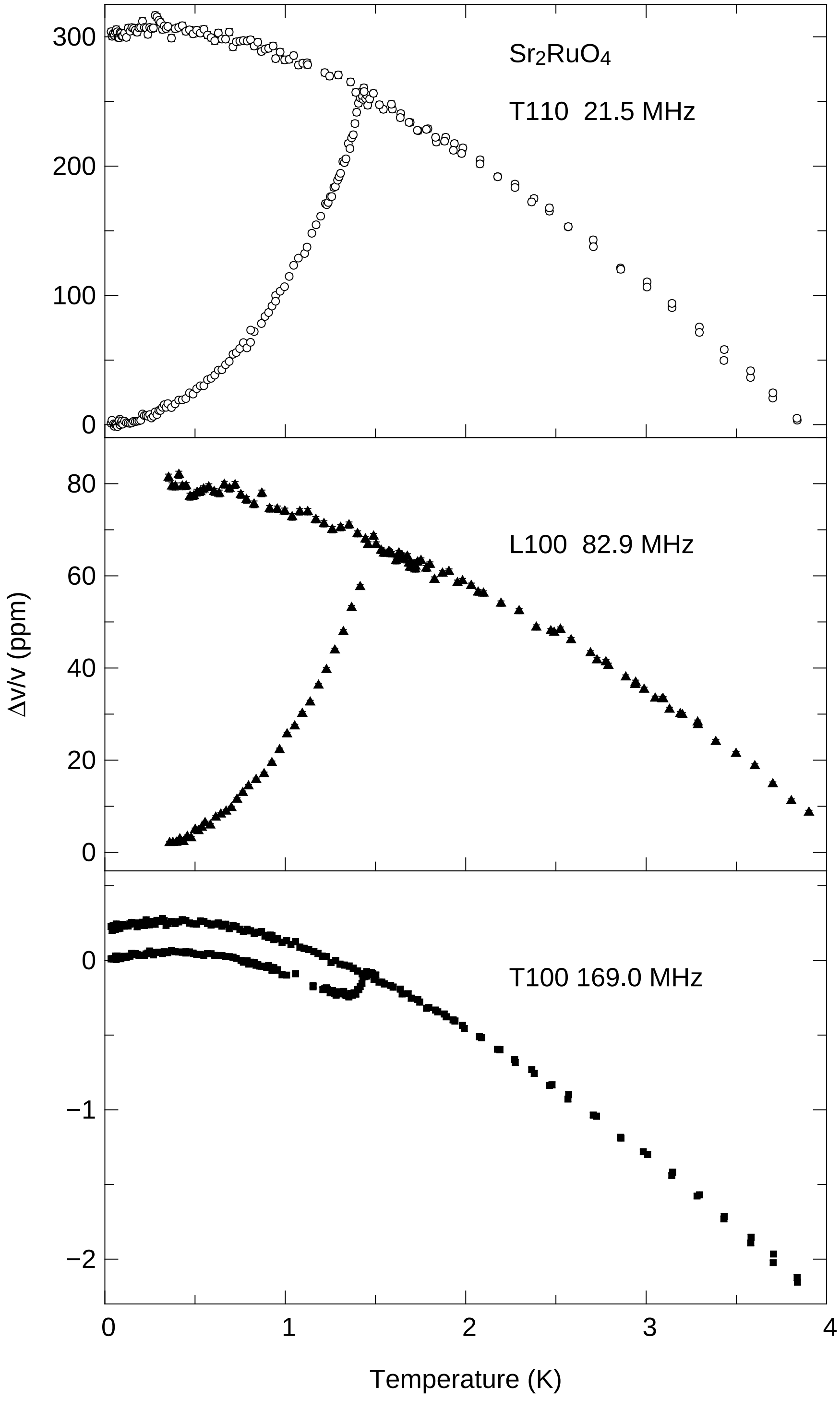

Figure 5.17: Temperature dependence of the sound velocity of the L110, T110 and T100 modes in the superconducting and normal states. The normal state is obtained by applying a field of 1.5 T approximately in the plane. See also fig. (5.18)

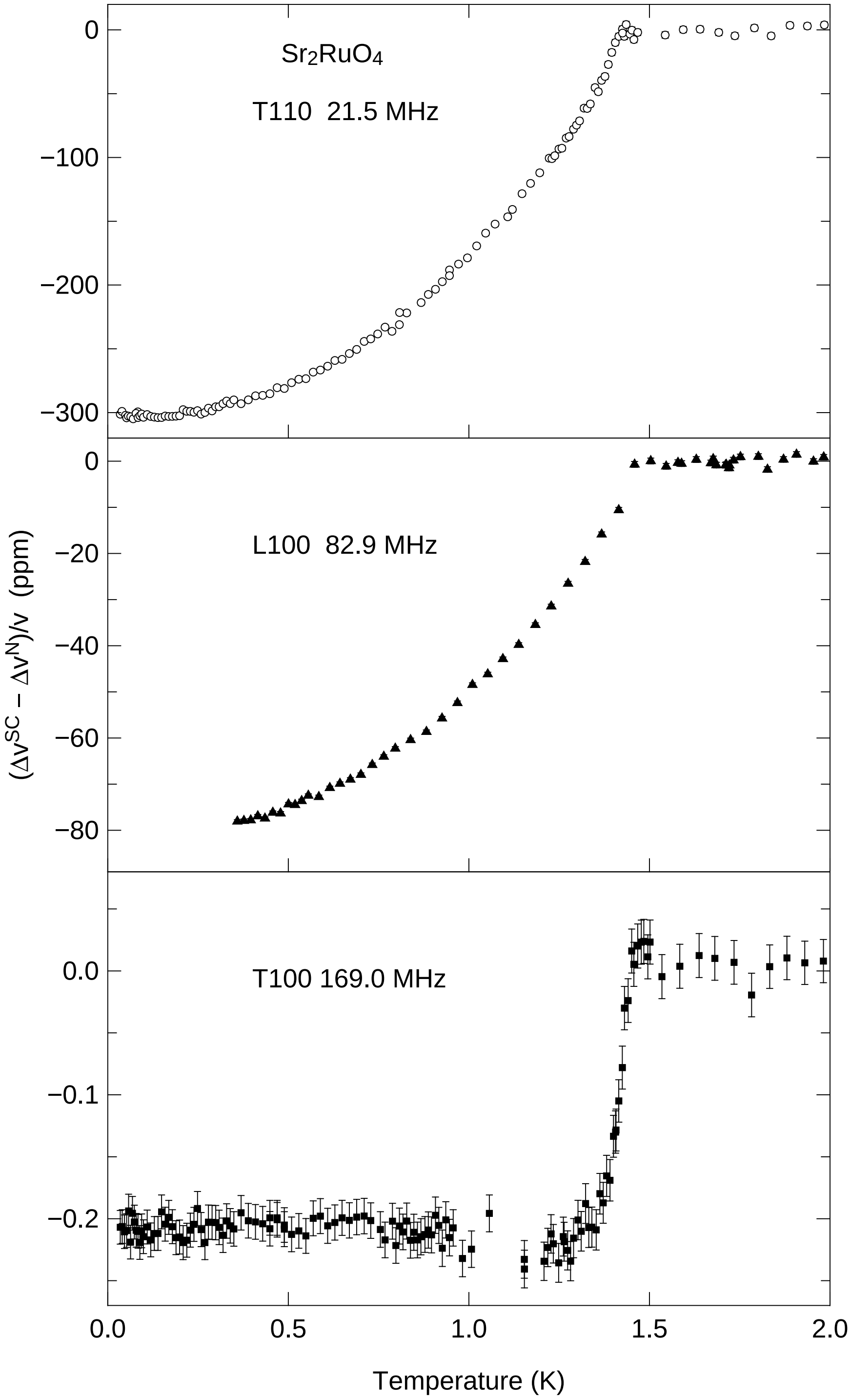

Figure 5.18: Difference in sound velocity between the superconducting and normal states. The results for L100 and T110 are similar to [117, 175]. See also fig. (5.17)

second derivative of T_c with strain. This was seen by Matsui *et al.* [117, 118, 175] and in particular we obtained the same size of change for the T110 mode.

The change for T100 is different. In this case the slope did not change but a very small step of 0.2 ppm is observable. A step is expected for longitudinal waves but not for transverse waves. The step in velocity is given by

$$\frac{\Delta v_S}{v_S} = \frac{1}{2}\frac{\Delta C_e}{T_c}\left(\frac{1}{v_S}\frac{\partial T_c}{\partial s}\right)^2 \tag{5.8}$$

where ΔC_e is the heat capacity jump at T_c per unit of mass, and s is the strain. In the case of longitudinal waves, $v_S \approx 6$ km/s, the heat capacity jump is about 0.75 of the normal state γ_N so $\Delta C_e/T_c \approx 0.1$ J/K^{2}kg. The strain dependence of T_c can be estimated from its pressure dependence of about 0.03 K/kbar = 0.3 K/GPa [216]. A hydrostatic pressure is composed of stresses in all 3 directions so for simplicity we assume they all contribute the same way to the change in T_c.[9] Therefore we have $\partial T_c/\partial s = B\partial T_c/\partial P = (1/3)(C_{11} + 2C_{12})\partial T_c/\partial P = 49$ K using $C_{11} = 230$ GPa and $C_{12} = 130$ GPa. Hence we estimate the jump to be $\Delta v/v = 3.3$ ppm which is much smaller than the overall change observed in the L100 mode and explains why we did not see it.

For transverse modes no step should be observable since $\partial T_c/\partial s_{\text{shear}} = 0$ by symmetry (a negative shear strain produces the same deformation as a positive shear strain). This argument can fail for multi-component order parameters [79] which could be the explanation here. The jump in T100 is very small but it was quite robust in the analysis and looks like a constant jump. Systematic errors in the velocity due the attenuation should have a shape reminiscent of the attenuation which is not the case here.[10] Therefore it seems to be a real effect, so that a multi-component (a vector instead of the usual scalar) order parameter is required. All triplet gap structures we discussed above (p-wave, f-wave, horizontal line node) have a multi-component order parameter. The longitudinal estimate of the step size is just one order of magnitude larger than the measured step but it does not apply directly to the transverse mode. Too many parameters are unknown, such as the coupling of the gap to the shear strain, to calculate an estimate to compare

---

[9] If measurements of the T_c dependence on uniaxial stress were available this assumption would be unnecessary, but none have been published so far.

[10] It is the case for the T110 and L100 modes that the attenuation and the phase have a similar shape but it is different enough (consider the same value at 0 K and 4 K is reached for the velocity which is not the case for the attenuation) and the systematic errors seem small enough that the measured velocity is the intrinsic one. This does not eliminate the possibility of some systematic effect due to the attenuation contaminating the curves but it should not affect them drastically.

with our 0.2 ppm. Nonetheless it is an intriguing result that is connected to the multi-component nature of the order parameter and that can probably be used to constrain some of the many parameters.

In addition to the modes discussed above, we also extracted the velocity for the L110 and T1x0c modes. In the case of L110 the data was somewhat unreliable because of systematic errors (from coupling to the attenuation) and noise. Considering such problems, we can put an upper limit of no significant change in slope and no observed jump larger than about 2 ppm. Looking at the elastic components of L110, this would require that the change in C_{11} (measured in L100) and C_{12} (measured in T110) cancel since C_{66} (T100) was measured to have a very small change. This is approximately the case since L100 has a velocity change of about 80 ppm which implies a relative change in C_{11} of 160 ppm and an absolute change of 0.037 GPa (using $C_{11} = 230$). Similarly the 300 ppm change in velocity for T110 implies a relative change of 600 ppm for $(C_{11} - C_{12})/2 \approx 50$ GPa hence an absolute variation of 0.030 GPa. Therefore T110 and L100 have about the same absolute change considering the measurements were done on different samples and that the T110 data is usually of lower quality (more sensitive to systematic errors). This makes the data consistent with the measurement of L110 that shows no large change.

In the case of T1x0c (hence for the C_{44} elastic constant) the data was more trustworthy so that no jump or change of slope was observable larger than about 0.2 ppm. This is in contrast to the result of Matsui *et al.* [118, 175] who measured a change of slope which correspond to a difference in velocity between T_c and 0 K of about -15 ppm. It should be mentioned that they do not quote the measured velocity and only the extracted elastic constants and that these are lower than ours. For example they have 42 GPa for C_{44} and 40 GPa for C_{66} [118] which are both about 62% of our values. We believe our measurements are more accurate in terms of sound velocity (and elastic constant) since they are similar to the resonant ultrasound spectroscopy results (see table (5.3)) and to measurements of the phonon dispersion by neutron scattering [105]. We also believe we measured the temperature dependence of the C_{44} elastic constant properly since, as will be seen in the next section, its field dependence is quite different than all the other modes. To explain the difference in results with Matsui *et al.* we must therefore suggest that their results were contaminated by another mode which could be caused by transducer misalignment among other possibilities.

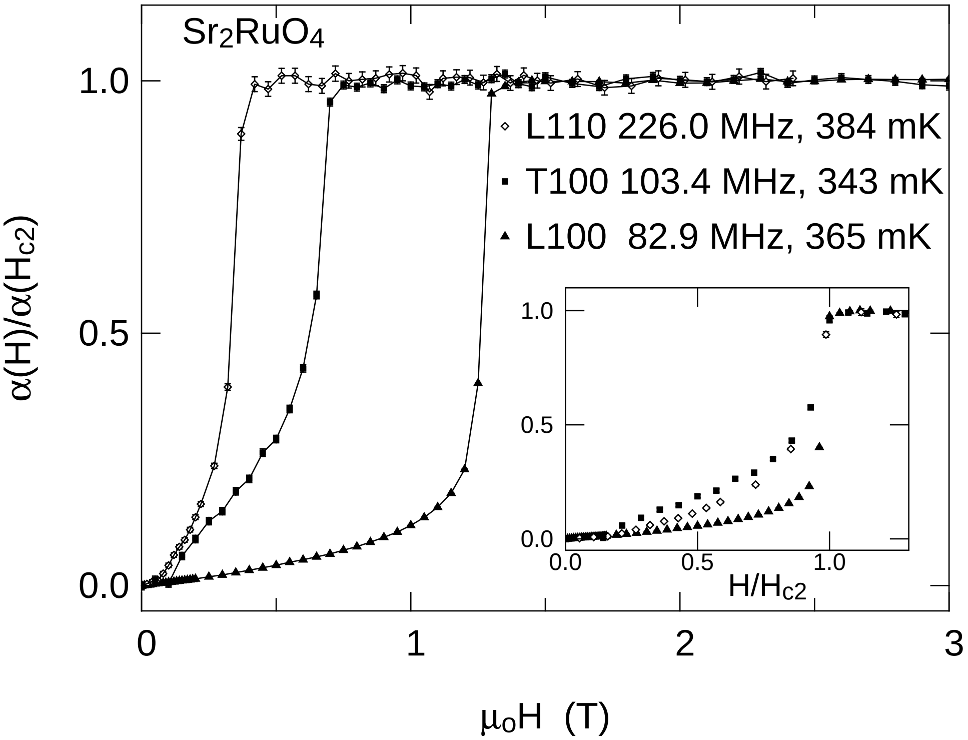

Figure 5.19: Field dependence of the attenuation for the L100, L110 and T100 modes. The attenuation has been normalized at H_{c2}. The inset shows the same data but with normalized field. The variation in critical field is caused by a misalignment of the field partially out of the plane. The data was taken at constant temperature around 350 mK.

5.5 Field sweeps

In order to complete our survey of results for the ultrasound attenuation and sound velocity of Sr$_2$RuO$_4$, we show the measurements under magnetic field. In fig. (5.19) we show the sound attenuation normalized above H_{c2} for the L100, L110 and T100 modes taken at around 350 mK. No data for T110 is shown simply because no believable field sweep data is available for that mode. The field was aligned approximately in-plane and close to the direction of propagation. It is obvious that the upper critical field varies between experiments on the different modes but this is caused by the out-of-plane misalignment of the field. The literature gives the in-plane critical field as 1.5 T while the c-axis H_{c2} is only 0.075 T. Therefore a small misalignment can strongly affect the observed critical field as we observed. Because of the sample shape and a lack of an in-situ sample rotation capability we were not able to have a consistent (precise) alignment. Since our main focus was on the zero field results we did not bother improving the alignment as that entailed warming to room temperature and which might destroy a good transducer bond.

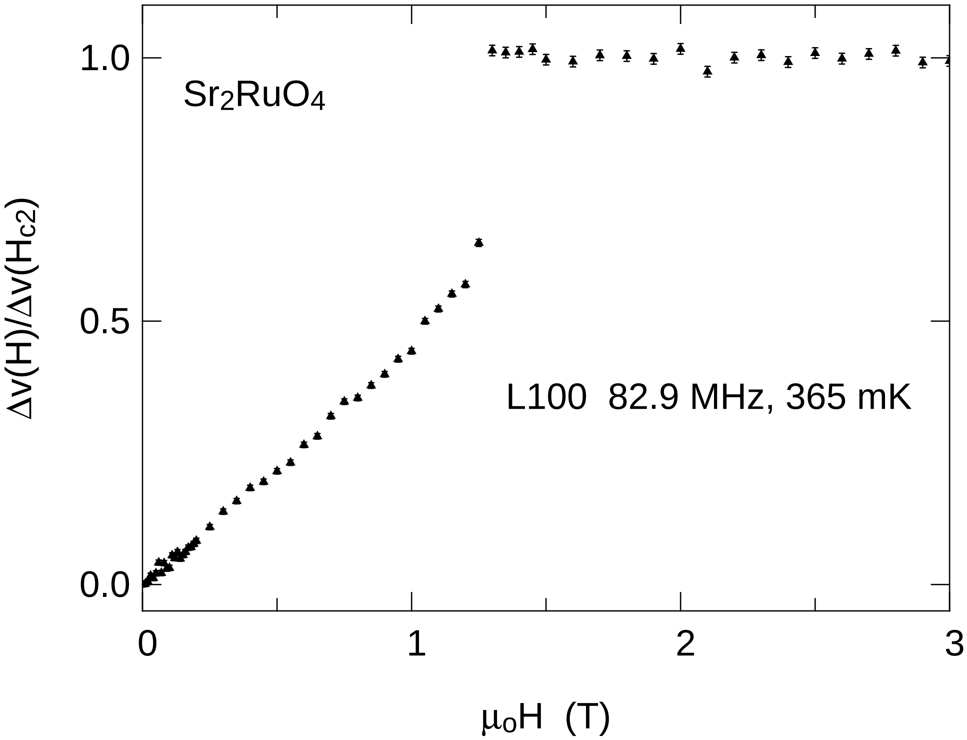

Figure 5.20: Field dependence of the sound velocity for L100 normalized at H_{c2}. Compare with the attenuation in fig. (5.19).

Aside from variation of the critical field (the highest measured H_{c2} is 1.3 T for the L100 mode) all the field dependences are roughly similar. They consist in roughly linear increase to a fraction of the normal state towards the upper critical field followed by a very fast increase close to H_{c2}. The actual fraction varies for different modes but this could be partially due to the change in H_{c2}. Because of the limited amount of data and the lack of control of the field orientation we cannot extract much information from these measurements except to say that it is similar to the temperature dependence. This would match with the view that the field can be used to sweep the energy in a way similar to temperature.

In a recent theoretical paper, Tewordt and Fay [194] calculated the field dependence of the attenuation for some candidate gap models and suggest that it could be a useful measurement to discriminate between them. But they used the free electron model, and moreover, it would require a more careful study then we have done. It is an interesting avenue of research for future study.

For comparison to the field dependence of the attenuation, we plot the field dependence of the velocity for the L100 mode in fig. (5.20). Data for the other modes was either too

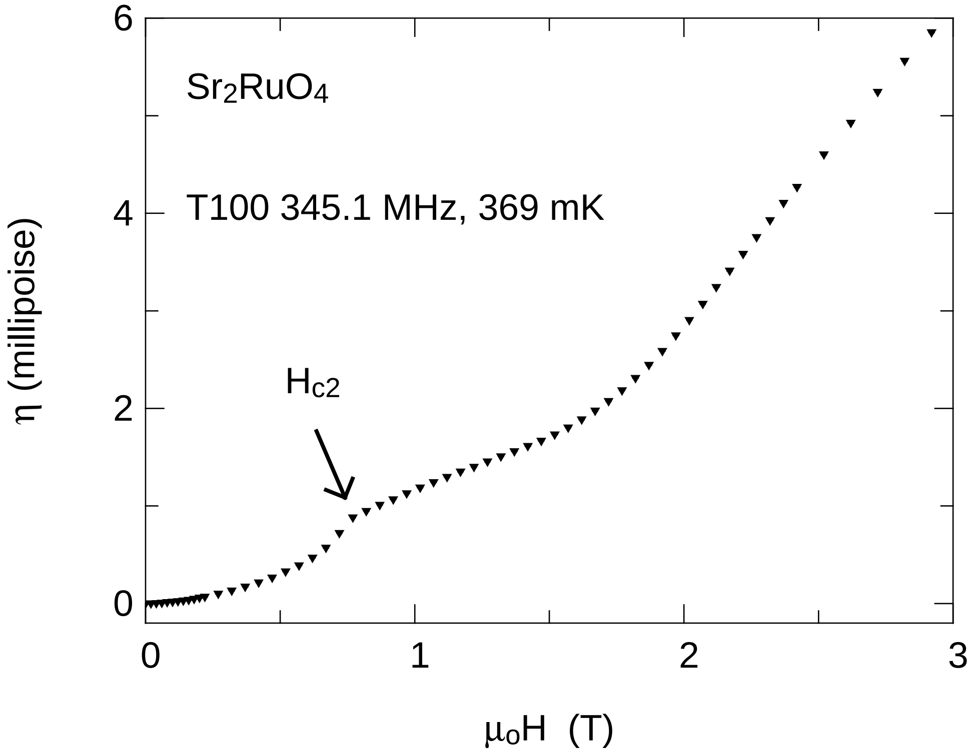

Figure 5.21: Field dependence of the viscosity for T100c. Compared to the in-plane modes (see fig. (5.19)), there is a strong dependence above H_{c2}.

noisy, of dubious quality, or had no perceptible changes, thus we do not show them. Here again there is a linear increase followed by a rapid increase near the critical field. Because of the even more limited amount of data, we will not say anything more except that the linear increase is stronger than for the attenuation and that the step at H_{c2} might be due to some contamination from the attenuation signal.

We have not mentioned the field sweep dependence of the T1x0c mode until now because it is quite different and needs to be discussed separately. In fig. (5.21) we show the attenuation and in fig. (5.22) we show the sound velocity. Compare them to the field sweep data for the in-plane modes fig. (5.19) and fig. (5.20). The differences are quite obvious. The in-plane modes have an essentially constant attenuation and velocity (at least for L100) above H_{c2}. This is definitively not the case for T1x0c. Also no signal of the superconducting state is observable in the sound velocity which is consistent with the observations of the temperature sweeps (see previous section). The difference between the modes, the quadratic shape of the sound velocity and the increase in the attenuation of T1x0c can be understood in terms of the theory described in section 2.4. It defines an additional source of attenuation in a magnetic field which is controlled by the parameter

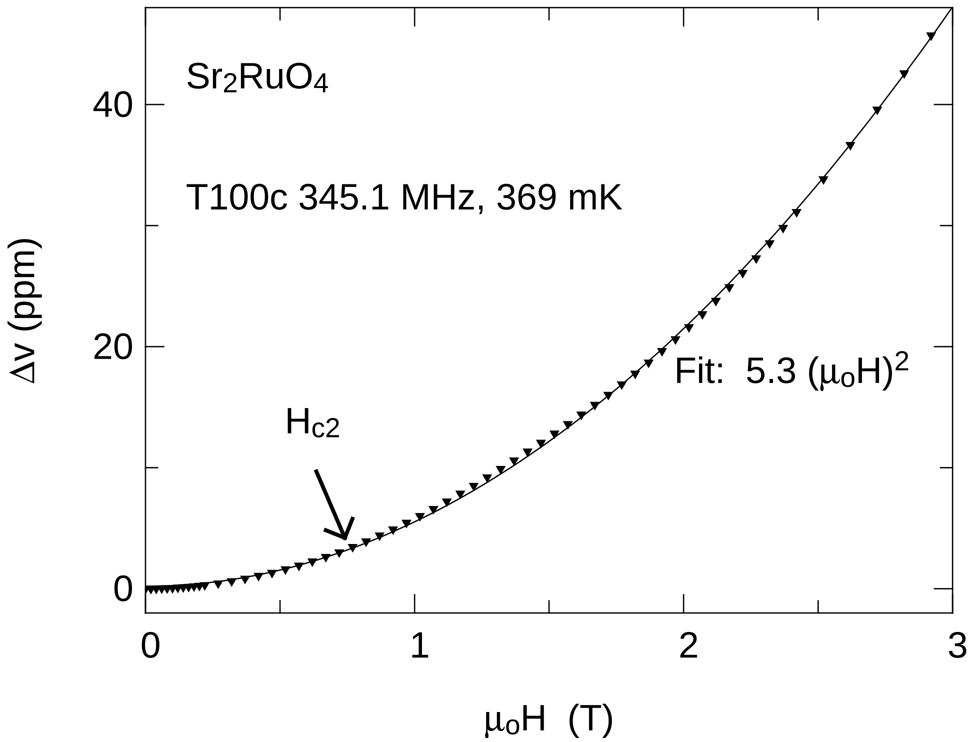

Figure 5.22: Field dependence of the sound velocity for T100c. The velocity has a large quadratic dependence on the field which is quite different to the in-plane modes (see fig. (5.20)).

$\beta_i = \omega/\sigma_{ii}\mu v_s^2$ where σ_{ii} is the ii component of the electrical conductivity tensor, μ is the magnetic permitivity of the material, $\omega = 2\pi f$ with f the sound frequency and v_S the sound velocity. Assuming $\mu \approx \mu_0 = 4\pi \times 10^{-7}$, and that the conductivity tensor is diagonal then $\beta_i = 50 f \rho_{ii}/v_s^2$ where f is in GHz, ρ_{ii} is the resistivity in $\mu\Omega$cm and the sound velocity v_S is in km/s. The effect on the sound velocity for transverse modes is given by

$$\frac{\Delta v_S}{v_S} = \frac{\mu}{2\mu_0^2 \rho v_S^2} \left(\frac{(\mu_0 H)^2}{1+\beta^2} \right) \tag{5.9}$$

where ρ is the density (5.95 g/cm^3) and $\mu_o H$ is the magnetic field (in Tesla) in the direction of propagation. Assuming $v_S = 3.3$ km/s we have $\Delta v/v$ (in ppm) $= 6(\mu_o H)^2/(1+\beta^2)$. In the case of in-plane modes $\beta^2 = \beta_z^2 = 46^2 = 2100$ using $\rho_c = 100$ $\mu\Omega$cm and $f = 0.1$ GHz while for T1x0c $\beta^2 = \beta_{xy}^2 = 0.22^2 = 0.05$ using $\rho_{xy} = 0.1$ $\mu\Omega$cm and $f = 0.5$ GHz. This explains very well the quadratic shape and the amplitude observed for the T1x0c mode. As for the in-plane transverse mode, the contributions from this effect should be negligibly small because of the factor of 1/2100. This can also be shown to be the case for the in-plane longitudinal modes if the field is aligned in-plane. This was approximately the case especially for the L100 mode which had the highest H_{c2}, the constant behavior in the normal state and absence of observable quadratic increase of the sound velocity (see fig. (5.20)).

The attenuation can be discussed in a similar way. This effect adds an extra attenuation which for transverse modes goes as

$$\alpha = \frac{(\mu/\mu_0)^2}{\rho v_S}\left(\frac{\sigma\beta^2(\mu_0 H)^2}{1+\beta^2}\right). \tag{5.10}$$

Using the same approximation as above this becomes η (in millipoise) $= 63(\rho_i/v_S^2)\frac{(\mu_0 H)^2}{1+\beta^2}$ and as before ρ_i is in $\mu\Omega$cm and v_S in km/s. Therefore for the T1x0c mode we have about $0.58(\mu_0 H)^2$ millipoise while for the in-plane modes we have $0.28(\mu_0 H)^2$ millipoise. Similar results are obtained for longitudinal modes if the field is in-plane. These values explain quite well the extra contribution present for T1x0c. For most of the other modes, the other source of viscosity is much bigger so it should not be possible to notice the effect except possibly for the T100 mode. As seen in fig. (5.19) T100 did not show visible signs of this effect and considering the amplitude at H_{c2} is about 10 millipoise, it requires this field effect to be less than 1 millipoise at 3 T. This is reasonable considering the above estimate gives 2.5 millipoise. The difference can be due to the direction of the applied field being more perpendicular (lowering the component along the sound propagation) and the c-axis resistivity could also be smaller. In particular the small misalignment angle of the sample, combined with the strong anisotropy of the resistivity could combine to produce a smaller effective resistivity than the 100 $\mu\Omega$cm we used.

As we mentioned before, the normal state of T1x0c was not measurable because of the magnetic field behavior. What was observed was a roughly linearly increasing viscosity changing by about 0.3 millipoise between 350 mK and 2 K under a field of 1.5 T. This effect was weaker and less linear under smaller magnetic fields (because of sample misalignment we had a critical field as low as 0.5 T for one experiment). The shape of the curve was inconsistent with the zero field data above T_c, and this is the reason we cannot use it. The effect described above adds a large component to the attenuation which is also proportional to the in-plane resistivity. Under a magnetic field this resistivity increases because of magneto-resistance. This magneto-resistance for Sr_2RuO_4 decreases as the temperature is increased so this should provide a decreasing signal in the normal state contrary to our osbervation. On the other hand, the usual source of attenuation is proportional to the conductivity. For the T1x0c mode it is probably related to the c-axis conductivity which has a larger magneto-resistance effect than the in-plane ones [106, 217, 218, 219]. In this case, the expected behavior is an increase as a function of temperature because it depends on the conductivity instead of the resistivity. This is probably the effect observed. To be sure would require more magnetoresistance data at lower temperatures and more attenuation field sweeps.

6

CONCLUSIONS

In this thesis we presented a comprehensive study of ultrasound attenuation in the unconventional superconductor Sr_2RuO_4. The primary goal of this research was to elucidate the nodal structure of the superconducting gap.

We measured the ultrasound attenuation and sound velocity using a standard pulse echo technique. The electronics and data analysis were tested by measuring a sample of tantalum, for which the standard BCS behavior with a gap of 1.75 ± 0.02 $k_B T_c$ was obtained, in good agreement with previous measurements.

The Sr_2RuO_4 crystals, kindly provided by Prof. Y. Maeno at Kyoto University, were carefully aligned and prepared for sound propagation along the [100] and [110] directions in the tetragonal crystal structure. Both longitudinal and transverse modes along each direction were studied at various sound frequencies. The definitive experiments were performed in a dilution refrigerator from 40 mK up to 4 K.

The first and unexpected result was a large normal state in-plane anisotropy. Transverse sound waves along the a-axis of the RuO_2 planes (T100) are found to be a thousand times less attenuated by electrons than the transverse waves along the diagonal (T110), both sound polarizations being in-plane. The longitudinal sound waves are less attenuated when traveling along the diagonal than along the a-axis, by a factor of 30 or so. Such large in-plane anisotropies, in particular for transverse waves, has not been reported in literature before, to the best of our knowledge. As an immediate effect it implies that theories based on the free electron model fail. These predict no anisotropy for the in-plane attenuation in the normal state for a cylindrical Fermi surface and relatively weak anisotropy for more realistic Fermi surfaces. Using the deformation potential theory and a simple tight-binding model of the Fermi surface, we can explain the longitudinal anisotropy. In that same model, the transverse anisotropy would come from a much weaker sensitivity of the next-nearest-neighbor versus the nearest-neighbor hopping parameter on the elastic strain. This explanation can be checked by doing band calculations for a strained crystal.

In the superconducting state, we observed power laws down to the lowest temperature measured, namely $T_c/30$ (40 mK). This is conclusive evidence for lines of nodes. We also observed some anisotropy of the low temperature power laws ($T^{1.4}$–$T^{1.7}$) which is too weak to be explained by vertical line nodes. This weak anisotropy is more consistent with horizontal line nodes. The best fit to the data was obtained using the two band model of Zhitomirsky and Rice. This model has horizontal line nodes on the α and β bands which can explain the observed power laws at low temperature and a p-wave (nodeless) gap on the γ Fermi surface which can explain the rapid decrease of attenuation observed below T_c that is reminiscent of s-wave BCS behavior. A definite conclusion awaits more careful calculations, including the effect of the normal state anisotropy, for the different proposed gaps.

We also measured the attenuation for transverse modes polarized along the c-axis. Because of the 2D character of this material, such a mode is expected to have a small attenuation, and this was indeed the case. The attenuation was smaller than the smallest in-plane mode by an order of magnitude. Because of this very weak attenuation the measurement was noisy but nonetheless the data in the superconducting state was consistent with the two band model of Zhitomirsky and Rice.

Finally, we also looked at the sound velocity. The results were consistent with previous measurements by another group except for the c-axis polarized mode. Our absolute sound velocity differed but were consistent with a resonant ultrasound spectroscopy measurement. We observed a small but interesting step at T_c for the T100 mode. This was unexpected because normally only longitudinal modes show this behavior. If it is confirmed as a real effect, it could prove useful in further identifying the order parameter since it is probably related to the multi-component nature of the order parameter.

Bibliography

[1] H. Kamerlingh Onnes. Further experiments with liquid helium .... *Communications from the Physical Laboratory at the University of Leiden*, 120b, 122b, 124c, 1911. 1

[2] W. Meissner and R. Ochsenfeld. Ein neuer effekt bei eintritt der supraleitfähigkeit. *Die Naturwissenschaften*, 21:787–788, 1933. 1

[3] F. London and H. London. The electromagnetic equations of the supraconductor. *Proceedings of the Royal Society of London*, A149:71–88, 1935. 1

[4] C. J. Gorter and H. B. G. Casimir. Zur thermodynamik des supraleitenden zustandes. *Physikalische Zeitschrift*, 35:963–966, 1934. 1

[5] A. B. Pippard. An experimental and theoretical study of the relation between magnetic field and current in a superconductor. *Proceedings of the Royal Society of London*, A216:547–568, 1953. 1

[6] V. L. Ginzburg and L. D. Landau. K teorii sverkhprovodnimosti. *Zhurmal Eksperimentalnoi i Theoreticheskoi Fiziki*, 20:1064, 1950. 1

[7] J. Bardeen, L. N. Cooper, and J. R. Schrieffer. Theory of superconductivity. *Physical Review*, 108:1175–1204, 1957. 1, 40

[8] L. P. Gor'kov. Microscopic derivation of the ginzburg-landau equations in the theory of superconductivity. *Soviet Physics. JETP*, 9:1364–1367, 1959. 1

[9] J. R. Schrieffer. *Theory of Superconductivity.* Advanced Book Classics. Perseus Books, Reading , MA, 1999. 2

[10] R. B. Laughlin. Anomalous quantum hall effect: An incompressible quantum fluid with fractionally charged excitations. *Physical Review Letters*, 50(18):1395–1398, May 1983. 2

[11] Robert B. Laughlin. *The Quantum Hall Effect*, chapter 7, pages 233–301. Graduate Texts in Contemporary Physics. Springer-Verlag, New York, second edition, 1990. 2

[12] R. D. Parks, editor. *Superconductivity*, volume 1&2. Marcel Dekker, New York, 1969. 3

[13] John C. Wheatley. Experimental properties of superfluid ^{3}He. *Reviews of Modern Physics*, 47(2):415–470, April 1975. 3

[14] Anthony J. Leggett. A theoretical description of the new phases of liquid ^{3}He. *Reviews of Modern Physics*, 47(2):331–414, April 1975. 3

[15] Jean-Pascal Brison, Loïc Glémot, Hermann Suderow, Andrew Huxley, Shinsaku Kambe, and Jacques Flouquet. Heavy fermion superconductivity. *Physica B*, 280:165–171, 2000. 4

[16] Robert Joynt and Louis Taillefer. The superconducting phases of UPt_3. To be published in Reviews of Modern Physics, January 2002. 4

[17] J. Wosnitza. *Fermi Surfaces of Low-Dimensional Organic Metals and Superconductors*. Springer-Verlag, Berlin, 1996. 4

[18] J. Singleton. Studies of quasi-two-dimensional organic conductors based on BEDT-TTF using high magnetic fields. *Reports on Progress in Physics*, 63(8):1111–1207, August 2000. 4

[19] J. G. Bednorz and K. A. Müller. Possible high T_c superconductivity in the Ba-La-Cu-O system. *Zeitschrift für Physik B*, 64(2):189–193, 1986. 4

[20] M. K. Wu, J. R. Ashburn, C. J. Torng, P. H. Hor, R. L. Meng, L. Gao, Z. J. Huang, Y. Q. Wang, and C. W. Chu. Superconductivity at 93 K in a new mixed-phase Yb-Ba-Cu-O compound system at ambient pressure. *Physical Review Letters*, 58(9):908–910, March 1987. 4

[21] S Hikami, T Hirai, and S Kagoshima. High transition temperature superconductor: Y-Ba-Cu oxide. *Japanese Journal of Applied Physics*, 26(4):L314–L315, April 1987. 4

[22] Zhongxian Zhao, Liquan Chen, Qiansheng Yang, Yuzhen Huang, Genghua Chen, Ruming Tang, Guirong Liu, Changgeng Cui, Lie Chen, Lianzhong Wang, Shuquan Guo, Shanlin Li, and Jianqing Bi. Superconductivity above liquid nitrogen temperature in Ba-Y-Cu oxides. *Kexue Tongbao (Science Bulletin)*, 32:661–664, 1987. 4

[23] M. B. Maple. High-temperature superconductivity. *Journal of Magnetism and Magnetic Materials*, 177–181:18–30, January 1998. 4

[24] Y. Maeno, H. Hashimoto, K. Yoshida, S. Nishizaki, T. Fujita, J. G. Bednorz, and F. Lichtenberg. Superconductivity in a layered perovskite without copper. *Nature*, 372:532–534, 1994. 5, 83, 89

[25] John J. Randall and Roland Ward. The preparation of some ternary oxides of the platinum metals. *Journal of the American Chemical Society*, 81:2629–2631, June 1959. 5, 83

[26] F. Lichtenberg, A. Catana, J. Mannhart, and D. G. Schlom. Sr_2RuO_4: A metallic substrate for the epitaxial growth of $YBa_2Cu_3O_{7-\delta}$. *Applied Physics Letters*, 60(9):1138–1140, March 1992. 5, 83

[27] T. M. Rice and M. Sigrist. Sr_2RuO_4: An electronic analogue of ^{3}He. *Journal of Physics: Condensed Matter*, 7:L643–L648, 1995. 6, 89, 99

[28] G. Baskaran. Why is Sr_2RuO_4 not a high T_c superconductor? electron correlation, Hund's coupling and p-wave instability. *Physica B*, 223 & 224:490–495, 1996. 6, 89, 99

[29] B. S. Shivaram, Y. H. Jeong, T. F. Rosenbaum, and D. G. Hinks. Anisotropy of transverse sound in the heavy-fermion superconductor UPt_3. *Physical Review Letters*, 56(10):1078–1081, March 1986. 7, 134

[30] Brett Ellman, Louis Taillefer, and Mario Poirier. Transverse ultrasound revisited: A directional probe of the A phase of UPt_3. *Physical Review B*, 64(13):9043–9046, October 1996. 7, 134

[31] J. H. Schon, C. Kloc, and B. Batlogg. Superconductivity in molecular crystals induced by charge injection. *Nature*, 406:702–704, August 2000. 8

[32] J. H. Schon, Ch. Kloc, R. C. Haddon, and B. Batlogg. A superconducting field-effect switch. *Science*, 288:656–658, April 2000. 8

[33] J. H. Schon, Ch. Kloc, and B. Batlogg. Superconductivity at 52 K in hole-doped C_{60}. *Nature*, 408:549–552, November 2000. 8

[34] J. H. Schön, Ch. Kloc, and B. Batlogg. High-temperature superconductivity in lattice-expanded C_{60}. *Science*, 293(5539):2432–2434, September 2001. 8

[35] Jun Nagamatsu, Norimasa Nakagawa, Takahiro Muranaka, Yuji Zenitani, and Jun Akimitsu. Superconductivity at 39 K in magnesium diboride. *Nature*, 410:63–64, March 2001. 8

[36] L. D. Landau and E. M. Lifshitz. *Theory of Elasticity*, volume 7 of *Course of Theoretical Physics*. Pergamon Press Ltd., London, 1959. 9, 16

[37] Neil W. Ashcroft and N. David Mermin. *Solid State Physics*. W. B. Saunders Company, 1976. 13

[38] Herbert Goldstein. *Classical Mechanics*. Adddison-Wesley Series in Physics. Adddison-Wesley, Reading, Massachusetts, second edition, 1980. 16, 17

[39] M. S. Steinberg. Ultrasonic attenuation and dispersion in metals at low temperatures. *Physical Review*, 111(2):425–429, July 1958. 16, 28

[40] Gerald D. Mahan. *Many-Particle Physics*. Physics of Solids and Liquids. Plenum Press, New York, second edition, 1990. 17

[41] Rohn Truell, Charles Elbaum, and Bruce B. Chick. *Ultrasonic Methods in Solid State Physics*. Academic Press, New York, 1969. 18

[42] A. B. Bhatia. *Ultrasonic Absorption*. Monographs on the Physics and Chemistry of Materials. Oxford University Press, 1967. 19, 22, 41

[43] F. Reif. *Fundamentals of Statistical and Thermal Physics*. Fundamentals of Physics. McGraw-Hill, New York, 1965. 22

[44] A. B. Pippard. Theory of ultrasonic attenuation in metals and magneto-acoustic oscillations. *Proceedings of the Royal Society of London*, A257:165–193, 1960. 23, 28, 29

[45] A. B. Pippard. Ultrasonic attenuation in metals. *The Philosophical magazine*, 46:1104–1114, 1955. 23, 28

[46] Eugene I. Blount. Ultrasonic attenuation by electrons in metals. *Physical Review*, 114(2):418–436, April 1959. 23, 27, 30

[47] T. Tsuneto. Ultrasonic attenuation in superconductors. *Physical Review*, 121(2):402–415, January 1961. 24

[48] F. S. Khan and P. B. Allen. Sound attenuation by electrons in metals. *Physical Review B*, 35(3):1002–1019, January 1987. 24, 27, 28

[49] F. S. Khan and P. B. Allen. Deformation potentials and electron-phonon scattering: Two new theorems. *Physical Review B*, 29(6):3341–3349, March 1984. 27

[50] E. Kartheuser and S. Rodriguez. Deformation potentials and the electron-phonon interaction in metals. *Physical Review B*, 33(2):772–779, January 1986. 27

[51] T. Holstein. Theory of ultrasonic absorption in metals: the collision-drag effect. *Physical Review*, 113(2):479–496, January 1959. 27

[52] M. S. Steinberg. Viscosity of the electron gas in metals. *Physical Review*, 109(5):1486–1492, March 1958. 28

[53] Morrel H. Cohen and Michael J. Harrison an Walter A. Harrison. Magnetic-field dependence of the ultrasonic attenuation in metals. *Physical Review*, 117(4):937–952, February 1960. 30

[54] R. A. Alpher and R. J. Rubin. Magnetic dispersion and attenuation of sound in conducting fluids and solids. *Journal of the Acoustical Society of America*, 26:452, 1954. 31

[55] G. A. Alers and P. A. Fleury. Modification of the velocity of sound in metals by magnetic fields. *Physical Review*, 129(6):2425–2429, March 1963. 31

[56] Y. Shapira and L. J. Neuringer. Effects of high magnetic fields on the ultrasonic velocity and attenuation in Nb-25% Zr. *Physical Review Letters*, 15(18):724–727, November 1965. 31

[57] Y. Shapira. Magnetoacoustic attenuation in liquid mercury. *Physical Letters*, 20(6):604–606, April 1966. 31

[58] Gerald Burns. *High-Temperature Superconductivity: an Introduction*. Academic Press, 1992. 33

[59] David R. Lide, editor. *CRC Handbook of Chemistry and Physics*. CRC Press, Florida, 81st edition, 2000. 33, 80, 84

[60] Michael Tinkham. *Introduction to Superconductivity*. International Series in Pure and Applied Physics. McGraw-Hill, New York, second edition, 1996. 35, 40

[61] C. J. Pethick and David Pines. Transport processes in heavy-fermion superconductors. *Physical Review Letters*, 57(1):118–121, July 1986. 39, 45

[62] Moises Levy. Ultrasonic attenuation in superconductors for $ql < 1$. *Physical Review*, 131(4):1497–1500, August 1963. 40

[63] L. P. Kadanoff and A. B. Pippard. Ultrasonic attenuation in superconductors. *Proceedings of the Royal Society of London*, A292:299–313, 1966. 40, 41

[64] Richard A. Ferrell. Minimal theory of ultrasonic attenuation in superconductors. *Physics*, 3(3):157–159, 1967. 40

[65] V. M. Bobetic. Evaluation of high-frequency ultrasonic attenuation in superconductors in the bardeen-cooper-schrieffer therory of superconductivity. *Physical Review*, 136(6A):A1535–A1538, December 1964. 42

[66] V. P. Mineev and K. V. Samokhin. *Introduction to Unconventional Superconductivity*. Gordon and Breach Science Publishers, Amsterdam, 1999. 42, 45, 94

[67] Kazushige Machida, Masa aki Ozaki, and Tetsuo Ohmi. Odd-parity pairing superconductivity under tetragonal symmetry – possible application to Sr_2RuO_4 –. *Journal of the Physical Society of Japan*, 65(12):3720–3723, December 1996. 43, 99

[68] Manfred Sigrist. Spin-orbit coupling and the in-plane anisotropy of the upper critical field in Sr_2RuO_4. *Journal of the Physical Society of Japan*, 69(5):1290–1293, May 2000. 43, 95

[69] P. J. Hirschfeld, W. O Putika, and D. J. Scalapino. *d*-wave model for microwave response of high-T_c superconductors. *Physical Review B*, 50(14):10250–10264, October 1994. 45, 111

[70] P. Hirschfeld, D. Vollhardt, and P. Wölfle. Resonant impurity scattering in heavy fermion superconductors. *Solid State Communications*, 59(3):111–115, 1986. 45, 111

[71] B. Arfi, H. Bahlouli, and C. J. Pethick. Transport properties of anisotropic superconductors: Influence of arbitrary electron-impurity phase shifts. *Physical Review B*, 39(13):8959–8983, May 1989. 46, 48

[72] J. M. Perz and E. R. Dobbs. Ultrasonic attenuation in white tin crystals. *Proceedings of the Royal Society of London*, 297:408–423, 1967. 47, 123

[73] J. Moreno and P. Coleman. Ultrasound attenuation in gap-anisotropic systems. *Physical Review B*, 53(6):R2995–R2998, February 1996. 47, 48, 130, 134

[74] Matthias J. Graf and A. V. Balatsky. Identifying the pairing symmetry in the Sr_2RuO_4 superconductor. *Physical Review B*, 62(14):9697–9702, October 2000. 47, 100, 102, 103, 111, 123, 130, 131, 132

[75] B. Arfi and C. J. Pethick. Thermal conductivity and ultrasonic attenuation in heavy-fermion superconductors. *Physical Review B*, 38(4):2312–2325, August 1988. 48

[76] M. B. Walker, M. F. Smith, and K. V. Samokhin. Electron-phonon interaction and ultrasonic attenuation in the ruthenate and cuprate superconductors. cond-mat/0105109, 2001. 49, 126, 130

[77] Warren P. Mason. *Physical Acoustics and the Properties of Solids.* The Bell Telephone Laboratories Series. D. Van Nostrand Company, Princeton, 1958. 49

[78] L. R. Testardi. Unusual strain dependence of T_c and related effects for high-temperature (A-15-structure) superconductors: Sound velocity at the superconducting phase transition. *Physical Review B*, 3(1):95–106, January 1971. 49

[79] G. Bruls, D. Weber, B. Wolf, P. Thalmeier, B. Lüthi, A. de Visser, and A. Menovsky. Strain–order-parameter coupling and phase diagrams in superconducting UPt_3. *Physical Review Letters*, 65(18):2294–2297, October 1990. 49, 50, 140

[80] S. Adenwalla, S. W. Lin, Q. Z. Ran, Z. Zhao, J. B. Ketterson, J. A. Sauls, L. Taillefer, D. G. Hinks, M. Levy, and Bimal K. Sarma. Phase diagram of UPt_3 from ultrasonic velocity measurements. *Physical Review Letters*, 65(18):2298–2301, October 1990. 50

[81] M. Boukhny, G. L. Bullock, and B. S. Shivaram. Thermodynamics of superconducting UPt_3. *Physical Review B*, 50(13):8985–8989, October 1994. 50

[82] M. Boukhny, G. L. Bullock, B. S. Shivaram, and David G. Hinks. Ultrasound study of the superconducting phases of UPt_3 under uniaxial stress. *Physica B*, 199&200:132–134, 1994. 50

[83] M. Boukhny, G. L. Bullock, and B. S. Shivaram. Tetracritical points and the superconducting phases of UPt_3: Uniaxial pressure effects. *Physical Review Letters*, 73(12):1707–1710, September 1994. 50

[84] Emmanuel P. Papadakis. *The Measurement of Ultrasonic Attenuation*, chapter 3, pages 108–156. Volume XIX of Thurston and Pierce [94], 1990. 51, 61

[85] Robert C. Richardson and Eric N. Smith, editors. *Experimental Techniques in Condensed Matter Physics at Low Temperatures.* Frontiers in Physics. Addison-Wesley, Redwood City, CA, 1988. 51

[86] O. V. Lounasmaa. *Experimental Principles and Methods Below 1 K.* Academic Press, London, 1974. 51

[87] Frank Pobell. *Matter and Methods at Low Temperatures.* Springer-Verlag, Berlin, second edition, 1996. 51

[88] Guy Kendall White. *Experimental Techniques in Low-Temperature Physics*. Monographs on the Physics And Chemistry of Materials. Oxford University Press, Oxford, third edition, 1979. 51

[89] Rohn Truell and William Oates. Effect of lack of parallelism of sample faces on the measurement of ultrasonic attenuation. *Journal of the Acoustical Society of America*, 35(9):1382–1386, September 1963. 60

[90] E. F. Carome and J. M. Witting. Theory of ultrasonic attenuation in cylindrical and rectangular waveguides. *Journal of the Acoustical Society of America*, 33(2):187–197, February 1961. 61

[91] Warren P. Mason. *Piezoelectric Crystals and Their Application to Ultrasonics*. The Bell Telephone Laboratories Series. D. Van Nostrand Company, Princeton, New Jersey, 1950. 62

[92] Valpey-Fisher. The user's guide to ultrasound & optical products. Technical documentation. Also available on the web at http://www.valpeyfisher-ud.com/vf.products.htm. 63

[93] A. A. V. Gibson, J. R. Owers-Bradley, I. D. Calder, J. B. Ketterson, and W. P. Halperin. Versatile pulsed rf heterodyne spectrometer. *Review of Scientific Instruments*, 52(10):1509–1516, October 1981. 64

[94] R. N. Thurston and Allan D. Pierce, editors. *Ultrasonic Measurement Methods*, volume XIX of *Physical Accoustics*. Academic Press, San Diego, 1990. 70, 157

[95] William H. Press, Saul A. Teukolsky, William T. Vetterling, and Brian P. Flannery. *Numerical Recipes in C: the Art of Scientific Computing*. Cambridge University Press, second edition, 1992. 78

[96] Moises Levy and Isadore Rudnick. Ultrasonic determination of the superconducting energy gap in tantalum. *Physical Review*, 132(3):1073–1080, November 1963. 81

[97] Yoshiteru Maeno, T. Maurice Rice, and Manfred Sigrist. The intriguing superconductivity of strontium ruthenate. *Physics Today*, pages 42–47, 2001. January. 83

[98] Leonhard Walz and Frank Lichtenberg. Refinement of the structure of Sr_2RuO_4 with 100 and 295 K X-ray data. *Acta Crystallographica*, C49:1268–1270, 1993. 83

[99] J. L. Martínez, C. Prieto, J. Rodríguez Carvajal, A. de Andrés, M. Vallet-Regí, and J. M. González-Calbet. Structural and magnetic properties of Sr_2RuO_4-type oxides. *Journal of Magnetism and Magnetic Materials*, 140–144:179–180, 1995. 83

[100] J. S. Gardner, G. Balakrishnan, and D. McK. Paul. Neutron powder diffraction studies of Sr_2RuO_4 and $SrRuO_3$. *Physica C*, 252:303–307, 1995. 83

[101] T. Vogt and D. J. Buttrey. Low-temperature structural behavior of Sr_2RuO_4. *Physical Review B*, 52(14):R9843–R9846, October 1995. 83

[102] J. S. Gardner, G. Balakrishnan, D. M^{c}K. Paul, and C. Haworth. Neutron diffraction and magnetisation studies of Sr_2RuO_4 below 2 K. *Physica C*, 265:251–257, 1996. 83, 84, 117

[103] M. Braden, A. H. Moudden, S. Nishizaki, Y. Maeno, and T. Fujita. Structural analysis of Sr_2RuO_4. *Physica C*, 273:248–254, 1997. 83

[104] O. Chmaissem, J. D. Jorgensen, H. Shaked, S. Ikeda, and Y. Maeno. Thermal expansion and compressibility of Sr_2RuO_4. *Physical Review B*, 57(9):5067–5070, March 1998. 83, 117

[105] M. Braden, W. Reichardt, S. Nishizaki, Y. Mori, and Y. Meano. Structural stability of Sr_2RuO_4. *Physical Review B*, 57(2):1236–1240, January 1998. 83, 141

[106] N. E. Hussey, A. P. Mackenzie, J. R. Cooper, Y. Maeno, S. Nishizaki, and T. Fujita. Normal-state magnetoresistance of Sr_2RuO_4. *Physical Review B*, 57(9):5505–5511, March 1998. 85, 146

[107] Yoshiteru Maeno, Koji Yoshida, Hiroaki Hashimoto, Shuji Nishizaki, Shin ichi Ikeda, Minoru Nohara, Toshizo Fujita, Andrew P. Mackenzie, Nigel E. Hussey, J. Georg Bednorz, and Frank Lichtenberg. Two-dimensional fermi liquid behavior of the superconductor Sr_2RuO_4. *Journal of the Physical Society of Japan*, 66(5):1405–1408, May 1997. 85

[108] A. W. Tyler, A. P. Mackenzie, S. NishiZaki, and Y. Maeno. High-temperature resistivity of Sr_2RuO_4: Bad metallic transport in a good metal. *Physical Review B*, 58(16):R10107–R10110, October 1998. 85

[109] C. Bergemann, S. R. Julian, A. P. Mackenzie, S. NishiZaki, and Y. Maeno. Detailed topography of the fermi surface of Sr_2RuO_4. *Physical Review Letters*, 84(12):2662–2665, March 2000. 86, 87, 137

[110] A. P. Mackenzie, S. R. Julian, A. J. Diver, G. J. McMullan, M. P. Ray, G. G. Lonzarich, Y. Maeno, S. Nishizaki, and T. Fujita. Quantum oscillations in the layered perovskite superconductor Sr_2RuO_4. *Physical Review Letters*, 76(20):3786–3789, May 1996. 85, 87

[111] Andrew P. Mackenzie, Shin ichi Ikeda, Yoshiteru Maeno, Toshizo Fujita, Stephen R. Julian, and Gilbert G. Lonzarich. The fermi surface topography of Sr_2RuO_4. *Journal of the Physical Society of Japan*, 67(2):385–388, February 1998. 87, 88

[112] A. P. Mackenzie, S. R. Julian, A. J. Diver, G. G. Lonzarich, N. E. Hussey, Y. Maeno, S. Nishizaki, and T. Fujita. Calculation of thermodynamic and transport properties of Sr_2RuO_4 at low temperatures using known Fermi surface parameters. *Physica C*, 263:510–515, 1996. 85, 87, 107

[113] Tamio Oguchi. Electronic band structure of the superconductor Sr_2RuO_4. *Physical Review B*, 51(2):1385–1388, January 1995. 85

[114] David J. Singh. Relationship of Sr_2RuO_4 to the superconducting layered cuprates. *Physical Review B*, 52(2):1358–1361, July 1995. 85

[115] I. I. Mazin, D. A. Papaconstantopoulos, and D. J. Singh. Tight-binding hamiltonians for Sr-filled ruthenates: Application to the gap anisotropy and hall coefficient in Sr_2RuO_4. *Physical Review B*, 61(8):5223–5228, February 2000. 85

[116] E. Ohmichi, H. Adachi, Y. Mori, Y. Maeno, T. Ishiguro, and T. Oguchi. Angle-dependent magnetoresistance oscillation in the layered perovskite Sr_2RuO_4. *Physical Review B*, 59(11):7263–7265, March 1999. 87

[117] Hiroshi Matsui, Masanori Yamaguchi, Yoshiyuki Yoshida, Atsushi Mukai, Rikio Settai, Yoshichika Ōnuki, Humihiko Takei, and Naoki toyota. Elastic anomalies

and acoustic de haas-van alphen effects in Sr_2RuO_4. *Journal of the Physical Society of Japan*, 67(11):3687–3690, December 1998. 87, 98, 109, 139, 140

[118] Hiroshi Matsui, Yoshiyuki Yoshida, Atsushi Mukai, Rikio Settai, Yoshichika Ōnuki, Humihiko Takei, Noriaki Kimura, Haruyoshi Aoki, and Naoki Toyota. Acoustic de haas-van alphen effect and elastic anomaly of transverse mode $(C_{11} - C_{12})/2$ in Sr_2RuO_4. *Journal of the Physical Society of Japan*, 69(12):3769–3772, December 2000. 87, 98, 109, 140, 141

[119] S. Hill, J. S. Brooks, Z. Q Mao, and Y. Maeno. Cyclotron resonance in the layered perovskite superconductor Sr_2RuO_4. *Physical Review Letters*, 84(15):3374–3377, April 2000. 87

[120] A. P. Mackenzie, N. E. Hussey, A. J. Diver, S. R. Julian, Y. Maeno, S. NishiZaki, and T. Fujita. Hall effect in the two-dimensional metal Sr_2RuO_4. *Physical Review B*, 54(10):7425–7428, September 1996. 87

[121] A. Damascelli, D. H. Lu, K. M. Shen, N. P. Armitage, F. Ronning, D. L. Feng, C. Kim, Z.-X. Shen, T. Kimura, Y. Tokura, Z. Q. Mao, and Y. Maeno. Fermi surface, surface states, and surface reconstruction in Sr_2RuO_4. *Physical Review Letters*, 85(24):5194–5197, December 2000. 87, 88

[122] D. H. Lu adn M. Schmidt, T. R. Cummins, S. Shuppler, F. Lichtenberg, and J. G. Bednorz. Fermi surface and extended van Hove singularity in the noncuprate superconductor Sr_2RuO_4. *Physical Review Letters*, 76(25):4845–4848, June 1996. 88

[123] T. Yokoya, A. Chainani, T. Takahashi, H. Ding, J. C. Campuzano, H. Katayama-Yoshida, M. Kasai, and Y. Tokura. Angle-resolved photoemission study of Sr_2RuO_4. *Physical Review B*, 54(18):13311–13318, November 1996. 88

[124] A. V. Puchkov, Z.-X. Shen, T. Kimura, and Y. Tokura. ARPES results on Sr_2RuO_4: Fermi surface revisited. *Physical Review B*, 58(20):R13322–R13325, November 1998. 88

[125] K. M. Shen, A. Damascelli, D. H. Lu, N. P. Armitage, F. Ronning, D. L. Feng, C. Kim, Z.-X. Shen, D. J. Singh, I. I. Mazin, S. Nakatsuji, Z. Q. Mao, Y. Maeno,

T. Kimura, and Y. Tokura. Surface electronic structure of Sr_2RuO_4. *Physical Review B*, 64:180502, 2001. 88

[126] Y. Maeno, S. Nakatsuji, and S. Ikeda. Metal-insulator transitions in layered ruthenates. *Materials Science and Engineering*, B63:70–75, 1999. 89

[127] O. Friedt, M. Braden, G. André, P. Adelmann, S. Nakatsuji, and Y. Maeno. Structural and magnetic aspects of the metal-insulator transition in $Ca_{2-x}Sr_xRuO_4$. *Physical Review B*, 63:174432, 2001. 89

[128] S. A. Carter, B. Batlogg, R. J. Cava, J. J. Krajewski, Jr. W. F. Peck, and Jr. L. W. Rupp. Mechanism for the metal-insulator transition in $Sr_2Ir_{1-x}Ru_xO_4$. *Physical Review B*, 51(23):17184–17187, June 1995. 89

[129] R. J. Cava, B. Batlogg, K. Kiyono, H. Takagi, J. J. Krajewski, Jr. W. F. Peck, Jr. L. W. Rupp, and C. H. Chen. Localized-to-itinerant electron transition in $Sr_2Ir_{1-x}Ru_xO_4$. *Physical Review B*, 49(17):11890–11894, May 1994. 89

[130] M. Minakata and Y. Maeno. Magnetic ordering in Sr_2RuO_4 induced by nonmagnetic impurities. *Physical Review B*, 63:180504, 2001. 89

[131] Shin-Ichi Ikeda, Yoshiteru Maeno, Satoru Nakatsuji, Masashi Kosaka, and Yoshiya Uwatoko. Ground state in $Sr_3Ru_2O_7$: Fermi liquid close to a ferromagnetic instability. *Physical Review B*, 62(10):R6089–R6092, September 2000. 89

[132] R. S. Perry, L. M. Galvin, S. A. Grigera, L. Capogna, A. J. Schofield, A. P. Mackenzie, M. Chiao, S. R. Julian, S. I. Ikeda, S. Nakatsuji, Y. Maeno, and C. Pfleiderer. Metamagnetism and critical fluctuations in high quality single crystals of the bilayer ruthenate $Sr_3Ru_2O_7$. *Physical Review Letters*, 86(12):2661–2664, March 2001. 89

[133] K. Yoshida, F. Nakamura, T. Goko, T. Fujita, Y. Maeno, Y. Mori, and S. NishiZaki. Electronic crossover in the highly anisotropic normal state of Sr_2RuO_4 from pressure effects on electrical resistivity. *Physical Review B*, 58(22):15062–15066, December 1998. 89

[134] Hidekazu Mukuda, Kenji Ishida, Yoshio Kitaoka, Kunisuke Asayama, Zhiqiang Mao, Yasumitsu Mori, and Yoshiteru Maeno. Novel character of spin fluctuations

in spin-triplet superconductor Sr_2RuO_4: ^{17}O-NMR study. *Journal of the Physical Society of Japan*, 67(11):3945–3951, November 1998. 89

[135] H. Mukuda, K. Ishida, Y. Kitaoka, K. Asayama, R. Kanno, and M. Takano. Spin fluctuations in the ruthenium oxides RuO_2, $SrRuO_3$, $CaRuO_3$, and Sr_2RuO_4 probed by NMR. *Physical Review B*, 60(17):12279–12285, November 1999. 89

[136] K. Ishida, Y. Kitaoka, K. Asayama, S. Ikeda, S. Nishizaki, Y. Maeno, K. Yoshida, and T. Fujita. Anisotropic pairing in superconducting Sr_2RuO_4: Ru NMR and NQR studies. *Physical Review B*, 56(2):R505–R508, July 1997. 89, 97

[137] T. Imai, A. W. Hunt, K. R. Thurber, and F. C. Chou. ^{17}O NMR evidence for orbital dependent ferromagnetic correlations in Sr_2RuO_4. *Physical Review Letters*, 81(14):3006–3009, October 1998. 89

[138] Y. Sidis, M. Braden, P. Bourges, B. Hennion, S. NishiZaki, Y. Maeno, and Y. Mori. Evidence for incommensurate spin fluctuations in Sr_2RuO_4. *Physical Review Letters*, 83(16):3320–3323, October 1999. 89

[139] F. Servant, S. Raymond, B. Fåk, P. Lejay, and J. Flouquet. Two-dimensional spin fluctuations in Sr_2RuO_4. *Solid State Communications*, 116(9):489–493, 2000. 89

[140] I. I. Mazin and D. J. Singh. Competitions in layered ruthenates: Ferromagnetism versus antiferromagnetism and triplet versus singlet pairing. *Physical Review Letters*, 82(21):4324–4327, May 1999. 89, 99, 135

[141] Takuji Nomura and Kosaku Yamada. Magnetic properties of quasi-two-dimensional ruthenates studied by mean field theoretical approach. *Journal of the Physical Society of Japan*, 69(6):1856–1864, June 2000. 89

[142] Kwai-Kong Ng and Manfred Sigrist. Anisotropy of the spin susceptibility in the normal state of Sr_2RuO_4. *Journal of the Physical Society of Japan*, 69(11):3764–3765, November 2000. 89

[143] Dirk K. Morr, Peter F. Trautman, and Matthias J. Graf. Resonance peak in Sr_2RuO_4: Signature of spin triplet pairing. *Physical Review Letters*, 86(26):5978–5981, June 2001. 89, 127

[144] K. Ishida, H. Mukuda, Y. Minami, Y. Kitaoka, Z. Q. Mao, H. Fukazawa, and Y. Maeno. Normal-state spin dynamics in the spin-triplet superconductor Sr_2RuO_4. *Physical Review B*, 64:100501(R), 2001. 89

[145] Z. Q. Mao, Y. Mori, and Y. Maeno. Supression of superconductivity in Sr_2RuO_4 caused by defects. *Physical Review B*, 60(1):610–614, July 1999. 90

[146] A. P. Mackenzie, R. K. W. Haselwimmer, A. W. Tyler, G. G. Lonzarich, Y. Mori, S. Nishizaki, and Y. Maeno. Extremely strong dependence of superconductivity on disorder in Sr_2RuO_4. *Physical Review Letters*, 80(1):161–164, January 1998. 90, 98

[147] Y. Maeno, T. Ando, Y. Mori, E. Ohmichi, S. Ikeda, S. NishiZaki, and S. Nakatsuji. Enhancement of superconductivity of Sr_2RuO_4 to 3 K by embedded metallic microdomains. *Physical Review Letters*, 81(17):3765–3768, October 1998. 91

[148] Takashi Ando, Takashi Akima, Yasumitsu Mori, and Yoshiteru Maeno. Upper critical fields of the 3-K superconducting phase of Sr_2RuO_4. *Journal of the Physical Society of Japan*, 68(5):1651–1656, May 1999. 91

[149] Z. Q. Mao, Y. Maeno, and H. Fukazawa. Crystal growth of Sr_2RuO_4. *Materials Research Bulletin*, 35:1813–1824, 2000. 91, 104

[150] Z. Q. Mao, Y. Maeno, Y. Mori, S. Sakita, S. Nimori, and M. Udagawa. Sign reversal of the oxygen isotope effect on T_c in Sr_2RuO_4. *Physical Review B*, 63:144514, 2001. 91

[151] K. Ishida, H. Mukuda, Y. Kitaoka, K. Asayama, Z.Q. Mao, Y. Mori, and Y. Maeno. Spin-triplet superconductivity in Sr_2RuO_4 identified by ^{17}O Knight shift. *Nature*, 396:658–660, December 1998. 92

[152] K. Ishida, H. Mukuda, Y. Kitaoka, Z. Q. Mao, H. Fukazawa, and Y. Maeno. Ru NMR probe of spin susceptibility in the superconducting state of Sr_2RuO_4. *Physical Review B*, 63:060507(R), 2001. 92

[153] J. A. Duffy, S. M. Hayden, Y. Maeno, Z. Mao, J. Kulda, and G. J. McIntyre. Polarized-neutron scattering study of the cooper-pair moment in Sr_2RuO_4. *Physical Review Letters*, 85(25):5412–5415, December 2000. 92

[154] K. K. Ng and M. Sigrist. The role of spin-orbit coupling for the superconducting state in Sr_2RuO_4. *Europhysics Letters*, 49(4):473–479, February 2000. 92

[155] G. M. Luke, Y. Fudamoto, K. M. Kojima, M. I. Larkin, J. Merrin, B. Nachumi, Y. J. Uemura, Y. Maeno, Z. Q. Mao, Y. Mori, H. Nakamura, and M. Sigrist. Time-reversal symmetry-breaking superconductivity in Sr_2RuO_4. *Nature*, 394:558–561, 1998. 93, 94

[156] K. Maki and E. Puchkaryov. Impurity effects in p-wave superconductors. *Europhysics Letters*, 50(4):533–539, May 2000. 94, 100, 111

[157] D. F. Agterberg. Vortex lattice structures of Sr_2RuO_4. *Physical Review Letters*, 80(23):5184–5187, June 1998. 94, 95

[158] D. F. Agterberg. Square vortex lattices for two-component superconducting order parameters. *Physical Review B*, 58(21):14484–14489, December 1998. 94

[159] T. M. Riseman, P. G. Kealey, E. M. Forgan, A. P. Mackenzie, L. M. Galvin, A. W. Tyler, S. L. Lee, C. Ager, D. McK. Paul, C. M. Aegerter, R. Cubitt, Z. Q. Mao, T. Akima, and Y. Maeno. Observation of a square flux-line lattice in the unconventional superconductor Sr_2RuO_4. *Nature*, 396:242–245, November 1998. 95

[160] T. M. Riseman, P. G. Kealey, E. M. Forgan, A. P. Mackenzie, L. M. Galvin, A. W. Tyler, S. L. Lee, C. Ager, D. McK. Paul, C. M. Aegerter, R. Cubitt, Z. Q. Mao, T. Akima, and Y. Maeno. Correction: Observation of a square flux-line lattice in the unconventional superconductor Sr_2RuO_4. *Nature*, 404:629, April 2000. 95

[161] P. G. Kealey, T. M. Riseman, E. M. Forgan, L. M. Galvin, A. P. Mackenzie, S. L. Lee, D. McK. Paul, R. Cubitt, D. F. Agterberg, R. Heeb, Z. Q. Mao, and Y. Maeno. Reconstruction from small-angle neutron scattering measurements of the real space magnetic field distribution in the mixed state of Sr_2RuO_4. *Physical Review Letters*, 84(26):6094–6097, June 2000. 95

[162] Z. Q. Mao, Y. Maeno, S. NishiZaki, T. Akima, and T. Ishiguro. In-plane anisotropy of upper critical field in Sr_2RuO_4. *Physical Review Letters*, 84(5):991–994, January 2000. 95

[163] D. F. Agterberg. In-plane upper critical field anisotropy in Sr_2RuO_4 and $CeIrIn_5$. *Physical Review B*, 64:052502, 2001. 95

[164] Shuji NishiZaki, Yoshiteru Maeno, and Zhiqiang Mao. Changes in the superconducting state of Sr_2RuO_4 under magnetic fields probed by specific heat. *Journal of the Physical Society of Japan*, 69(2):572–578, February 2000. 95, 96, 98

[165] M. A. Tanatar, S. Nagai, Z. Q. Mao, Y. Maeno, and T. Ishiguro. Thermal conductivity of superconducting Sr_2RuO_4 in oriented magnetic fields. *Physical Review B*, 63:064505, 2001. 95, 96, 116, 117

[166] Hiroshi Yaguchi, Takashi Akima, Zhiquiang Mao, Yoshiteru Maeno, and Takehiko Ishiguro. Detailed study of the ac susceptibility of Sr_2RuO_4 in oriented magnetic fields. cond-mat/0106491, 2001. 95

[167] Shuji Nishizaki, Yoshiteru Maeno, Snorre Farner, Shin ichi Ikeda, and Toshizo Fujita. Evidence for unconventional superconductivity of Sr_2RuO_4 from specific-heat measurements. *Journal of the Physical Society of Japan*, 67(2):560–563, February 1998. 96, 98

[168] Shuji NishiZaki, Yoshiteru Maeno, and Zhiqiang Mao. Effect of impurities on the specific heat of the spin-triplet superconductor Sr_2RuO_4. *Journal of Low Temperature Physics*, 117(5/6):1581–1585, 1999. 96, 111

[169] Y. Maeno, S. NishiZaki, and Z. Q. Mao. Experimental evidence for spin-triplet superconductivity in Sr_2RuO_4. *Journal of Superconductivity*, 12(4):535–541, 1999. 96

[170] H. Suderow, J. P. Brison, J. Flouquet, A. W. Tyler, and Y. Maeno. Very low temperature thermal conductivity in the layered perovskyte superconductor Sr_2RuO_4. *Journal of Physics: Condensed Matter*, 10:L597–L602, 1998. 96

[171] M. A. Tanatar, S. Nagai, Z. Q. Mao, Y. Maeno, and T. Ishiguro. Thermal conductivity of Sr_2RuO_4 in oriented magnetic field. *Physica C*, 341–348:1841–1844, 2000. 96

[172] I. Bonalde, Brian D. Yanoff, M. B. Salamon, D. J. Van Harlingen, E. M. E. Chia, Z. Q. Mao, and Y. Maeno. Temperature dependence of the penetration depth

in Sr_2RuO_4: Evidence for nodes in the gap function. *Physical Review Letters*, 85(22):4775–4778, November 2000. 96

[173] Ioan Kosztin and Anthony J. Leggett. Nonlocal effects on the magnetic penetration depth in *d*-wave superconductors. *Physical Review Letters*, 79(1):135–138, July 1997. 96

[174] K. Ishida, H. Mukuda, Y. Kitaoka, Z. Q. Mao, Y. Mori, and Y. Maeno. Anisotropic superconducting gap in the spin-triplet superconductor Sr_2RuO_4: Evidence from a Ru-NQR study. *Physical Review Letters*, 84(23):5387–5390, June 2000. 97

[175] H. Matsui, Y. Yoshida, A. Mukai, R. Settai, Y. Ōnuki, H. Takei, N. Kimura, H. Aoki, and N. Toyota. Ultrasonic studies of the spin-triplet order parameter and the collective mode in Sr_2RuO_4. *Physical Review B*, 63:060505(R), 2001. 98, 139, 140, 141

[176] Takashi Akima, Shuji NishiZaki, and Yoshiteru Maeno. Intrinsic superconducting parameters of Sr_2RuO_4. *Journal of the Physical Society of Japan*, 68(2):694–695, February 1999. 98

[177] I. I. Mazin and David J. Singh. Ferromagnetic spin fluctuation induced superconductivity in Sr_2RuO_4. *Physical Review Letters*, 79(4):733–736, July 1997. 98

[178] K. Miyake and O. Narikiyo. Model for unconventional superconductivity of Sr_2RuO_4: Effect of impurity scattering on time-reversal breaking triplet pairing with a tiny gap. *Physical Review Letters*, 83(7):1423–1426, August 1999. 98, 101

[179] Takeshi Kuwabara and Masao Ogata. Spin-triplet superconductivity due to antiferromagnetic spin-fluctuation in Sr_2RuO_4. *Physical Review Letters*, 85(21):4586–4589, November 2000. 99

[180] Masatoshi Sato and Mahito Kohmoto. Mechanism of spin-triplet superconductivity in Sr_2RuO_4. *Journal of the Physical Society of Japan*, 69(11):3505–3508, November 2000. 99

[181] Kazuhiko Kuroki, Masao Ogata, Ryotaro Arita, and Hideo Aoki. Crib-shaped triplet-pairing gap function for an orthogonal pair of quasi-one-dimensional Fermi surfaces in Sr_2RuO_4. *Physical Review B*, 63:060506(R), 2001. 99

[182] M. Eschrig, J. Ferrer, and M. Fogelström. Mixed-parity superconductivity in Sr_2RuO_4. *Physical Review B*, 63:220509(R), 2001. 99

[183] I. Eremin, D. Manske, C. Joas, and K. H. Bennemann. Electronic theory for superconductivity in Sr_2RuO_4: Triplet f-wave symmetry pairing due to spin-fluctuation exchange. cond-mat/0102074, 2001. 99

[184] Tetsuya Takimoto. Orbital fluctuation-induced triplet superconductivity: Mechanism of superconductivity in Sr_2RuO_4. *Physical Review B*, 62(22):R14641–R14644, December 2000. 99

[185] Manfred Sigrist and Michael E. Zhitomirsky. Pairing symmetry of the superconductor Sr_2RuO_4. *Journal of the Physical Society of Japan*, 65(11):3452–3455, November 1996. 99

[186] D. F. Agterberg, T. M. Rice, and M. Sigrist. Orbital dependent superconductivity in Sr_2RuO_4. *Physical Review Letters*, 78(17):3374–3377, April 1997. 99, 100, 132

[187] Yasumasa Hasegawa, Kazushige Machida, and Masa aki Ozaki. Spin-triplet superconductivity with line nodes in Sr_2RuO_4. *Journal of the Physical Society of Japan*, 69(2):336–339, February 2000. 99, 100

[188] M. E. Zhitomirsky and T. M. Rice. Interband proximity effect and nodes of superconducting gap in Sr_2RuO_4. *Physical Review Letters*, 87:057001, July 2001. 100, 101, 136

[189] D. F. Agterberg. Impurities and orbital-dependent superconductivity in Sr_2RuO_4. *Physical Review B*, 60(2):R749–R752, July 1999. 100, 132

[190] Kazumi Maki and Guolin Yang. Introduction to unconventional superconductivity. *Fizika A*, 8:345–356, 1999. 100

[191] H. Won and K. Maki. Possible f-wave superconductivity in Sr_2RuO_4. *Europhysics Letters*, 52(4):427–433, November 2000. 100

[192] Thomas Dahm, Hyekyung Won, and Kazumi Maki. Models of superconductivity in Sr_2RuO_4. cond-mat/0006301, 2000. 100, 102

[193] W. C. Wu and R. Joynt. Transport and the order parameter of superconducting Sr_2RuO_4. *Physical Review B*, 64:100507(R), 2001. 101, 102, 136

[194] L. Tewordt and D. Fay. Ultrasonic attenuation in magnetic fields for spin-triplet superconducting states with line nodes in Sr_2RuO_4. cond-mat/0108109, 2001. 101, 143

[195] F. Laube, G. Goll, H. v. Löhneysen, M. Fogelström, and F. Lichtenberg. Spin-triplet superconductivity in Sr_2RuO_4 probed by andreev reflection. *Physical Review Letters*, 84(7):1595–1598, February 2000. 101

[196] R. Jin, Yu. Zadorozhny, Y. Liu, D. G. Schlom, Y. Mori, and Y. Maeno. Observation of anomalous temperature dependence of the critical current in $Pb/Sr_2RuO_4/Pb$ junctions. *Physical Review B*, 59(6):4433–4438, February 1999. 101

[197] R. Jin, Y. Liu, Z. Q. Mao, and Y. Maeno. Experimental observation of the selection rule in josephson coupling between In and Sr_2RuO_4. *Europhysics Letters*, 51(3):341–347, August 2000. 101

[198] Z. Q. Mao, K. D. Nelson, R. Jin, Y. Liu, and Y. Maeno. Observation of andreev surface bound states in the 3-K phase region of Sr_2RuO_4. *Physical Review Letters*, 87(3):037003, 2001. 101

[199] V. B. Geshkenbein, A. I. Larkin, and A. Barone. Vortices with half magnetic flux quanta in "heavy-fermion" superconductors. *Physical Review B*, 36(1):235–238, July 1987. 101

[200] C. C. Tsuei and J. R. Kirtley. Pairing symmetry in cuprate superconductors. *Reviews of Modern Physics*, 72(4):969–1016, October 2000. 101

[201] Akira Furusaki, Masashige Matsumoto, and Manfred Sigrist. Spontaneous Hall effect in a chiral p-wave superconductor. *Physical Review B*, 64:054514, 2001. 101

[202] S. H. Pan, E. W. Hudson, K. M. Lang, H. Eisaki, S. Uchida, and J. C. Davis. Imaging the effects of individual zinc impurity atoms on superconductivity in $Bi_2Sr_2CaCu_2O_{8+\delta}$. *Nature*, 403:746–750, February 2000. 102

[203] E. W. Hudson, K. M. Lang, V. Madhavan, S. H. Pan, H. Eisaki, S. Uchida, and J. C. Davis. Interplay of magnetism and high-T_c superconductivity at individual Ni impurity atoms in $Bi_2Sr_2CaCu_2O_{8+\delta}$. *Nature*, 411:920–924, June 2001. 102

[204] Kazumi Maki and Stephan Haas. Impurity bound states and symmetry of the superconducting order parameter in Sr_2RuO_4. *Physical Review B*, 62(18):R11969–R11972, November 2000. 102

[205] L. Tewordt and D. Fay. Thermal conductivity near H_{c2} for spin-triplet superconducting states with line nodes in Sr_2RuO_4. *Physical Review B*, 64:024528, 2001. 102

[206] K. Izawa, H. Takahashi, H. Yamaguchi, Yuji Matsuda, M. Suzuki, T. Sasaki, T. Fukase, Y. Yoshida, R. Settai, and Y. Onuki. Superconducting gap structure of spin-triplet superconductor Sr_2RuO_4 studied by thermal conductivity. *Physical Review Letters*, 86(12):2653–2656, March 2001. 102

[207] M. A. Tanatar, M. Suzuki, S. Nagai, Z. Q. Mao, Y. Maeno, and T. Ishiguro. Anisotropy of magnetothermal conductivity in Sr_2RuO_4. *Physical Review Letters*, 86(12):2649–2652, March 2001. 102, 116

[208] F. Yu, M. B. Salamon, A. J. Leggett, W. C. Lee, and D. M. Ginsberg. Tensor magnetothermal resistance in $YBa_2Cu_3O_{7-x}$ via andreev scattering of quasiparticles. *Physical Review Letters*, 74(25):5136–5139, June 1995. See also comment in Phys. Rev. Lett. **77**, 3058 (1996). 102

[209] H. Aubin, K. Behnia, M. Ribault, R. Gagnon, and L. Taillefer. Angular position of nodes in the superconducting gap of YBCO. *Physical Review Letters*, 78(13):2624–2627, March 1997. 102

[210] K. Izawa, H. Yamaguchi, T. Sasaki, and Yuji Matsuda. Superconducting gap structure of κ-(BEDT-TTF)$_2$Cu(NCS)$_2$ probed by thermal conductivity tensor. cond-mat/0107537, 2001. 102

[211] K. Izawa, H. Yamaguchi, Yuji Matsuda, H. Shishido, R. Settai, and Y. Onuki. Angular position of nodes in the superconducting gap of quasi-2D heavy-fermion superconductor $CeCoIn_5$. *Physical Review Letters*, 87:057002, July 2001. 102

[212] Hae-Young Kee, Yong Baek Kim, and Kazumi Maki. Collective modes and sound propagation in a p-wave superconductor: Sr_2RuO_4. *Physical Review B*, 62(9):5877–5885, September 2000. 102, 111

[213] M. Suzuki, M. A. Tanatar, Z. Q. Mao, Y. Maeno, and T. Ishiguro. Quasiparticle density in Sr_2RuO_4 probed by the phonon thermal conductivity. cond-mat/0104493, 2001. 116

[214] M. Lang, R. Kürsh, A. Grauel, C. Geibel, F. Steglich, H. Rietschel, T. Wolf, Y. Hidaka nad K. Kumagai, Y. Maeno, and T. Fujita. Lattice instabilities in cuprate superconductors: A possible limiting mechanism for T_c. *Physical Review Letters*, 69(3):482–485, July 1992. 117

[215] James F. Annett, G. Litak, B. L. Györffy, and K. I. Wysokiński. Interlayer coupling and p-wave pairing in strontium ruthenate. cond-mat/0109023; see also cond-mat/0105376., September 2001. 137

[216] Naoki Shirakawa, Keizo Murata, Shuji Nishizaki, Yoshiteru Maeno, and Toshizo Fujita. Pressure dependence of superconducting critical temperature of Sr_2RuO_4. *Physical Review B*, 56(13):7890–7893, October 1997. 140

[217] R. Jin, Yu. Zadorozhny, Y. Liu, D. G. Schlom, F. Lichtenberg, and J. G. Bednorz. Normal-state magnetoresistance of Sr_2RuO_4 single crystals. *Journal of Physics and Chemistry of Solids*, 59(10–12):2215–2217, October 1998. 146

[218] R. Jin, Y. Liu, and F. Lichtenberg. Linear-field dependence of the normal-state in-plane magnetoresistance of Sr_2RuO_4. *Physical Review B*, 60(14):10418–10422, October 1999. 146

[219] E. Ohmichi, Y. Maeno, S. Nagai, Z. Q. Mao, M. A. Tanatar, and T. Ishiguro. Magnetoresistance of Sr_2RuO_4 under high magnetic fields parallel to the conducting plane. *Physical Review B*, 61(10):7101–7106, March 2000. 146